

High Efficiency Planar Microwave Antennas Assembled Using Millimetre Thick Micromachined Polymer Structures

Sumanth Kumar Pavuluri BTech, MSc

A thesis submitted for the degree of Doctor of Philosophy

Heriot-Watt University

School of Engineering and Physical Sciences

May 2011

This copy of the thesis has been supplied on condition that anyone who consults it is understood to recognise that the copyright rests with its author and that no quotation from the thesis and no information derived from it may be published without the prior written consent of the author or of the University (as may be appropriate).

Abstract

Communication systems at microwave and millimetre wave regimes require compact broadband high gain antenna devices for a variety of applications, ranging from simple telemetry antennas to sophisticated radar systems. High performance can usually be achieved by fabricating the antenna device onto a substrate with low dielectric constant or recently through micromachining techniques. This thesis presents the design, fabrication, assembly and characterisation of microstrip and CPW fed micromachined aperture coupled single and stacked patch antenna devices. It was found that the micromachining approach can be employed to achieve a low dielectric constant region under the patch which results in suppression of surface waves and hence increasing radiation efficiency and bandwidth. A micromachining method that employs photolithography and metal deposition techniques was developed to produce high efficiency antenna devices. The method is compatible with integration of CMOS chips and filters onto a common substrate. Micromachined polymer rims (SU8 photoresist) was used to create millimetre thick air gaps between the patch and the substrate. The effect of the substrate materials and the dimensions of the SU8 polymer rims on the performance of the antenna devices were studied by numerical simulation using Ansoft HFSS electromagnetic field simulation package. The antenna structures were fabricated in layers and assembled by bonding the micromachined polymer spacers together. Low cost materials like SU8, polyimide and liquid crystal polymer films were used for fabrication and assembly of the antenna devices. A perfect patch antenna device is introduced by replacing the substrate of a conventional patch antenna device with air in order to compare with the micromachined antenna devices. The best antenna parameters for a perfect patch antenna device with air as a substrate medium are ~20% for bandwidth and 9.75 dBi for antenna gain with a radiation efficiency of 99.8%. In comparison, the best antenna gain for the simple micromachined patch antenna device was determined to be ~8.6 dBi. The bandwidth was ~20 % for a microstrip fed device with a single patch; it was ~40 % for stacked patch devices. The best bandwidth and gain of 6.58 GHz (50.5%) and 11.2 dBi were obtained for a micromachined sub-array antenna device. The simulation results show that the efficiency of the antenna devices is above 95 %. Finally, a novel high gain planar antenna using a frequency selective surface (FSS) was studied for operation at ~60 GHz frequency. The simulation results show that the novel antenna device has a substantial directivity of around 25 dBi that is required for the emerging WLAN communications at the 60 GHz frequency band.

Acknowledgements

I would like to thank my supervisors, Dr. Changhai Wang and Prof. Alan Sangster for their help, guidance and patience during the construction of this thesis. They have been a significant source of encouragement and advice during the course of my research activities.

I would like to express my appreciation to Dr. George Goussetis and Prof. Marc Desmulliez, for their encouragement. I would also like to acknowledge my research colleagues from the MISEC group at Heriot-Watt University with whom I had shared quality discussions during the course of my research period.

Finally, my sincere appreciation goes to my family for their support and encouragement throughout my research career.

Sumanth Kumar Pavuluri
14 May 2011

ACADEMIC REGISTRY Research Thesis Submission



Name:	Sumanth Kumar Pavuluri		
School/PGI:	School of EPS		
Version: <i>(i.e. First, Resubmission, Final)</i>	Final	Degree Sought (Award and Subject area)	PhD (Electrical, Electronic and computing Engineering)

Declaration

In accordance with the appropriate regulations I hereby submit my thesis and I declare that:

- 1) the thesis embodies the results of my own work and has been composed by myself
- 2) where appropriate, I have made acknowledgement of the work of others and have made reference to work carried out in collaboration with other persons
- 3) the thesis is the correct version of the thesis for submission and is the same version as any electronic versions submitted*.
- 4) my thesis for the award referred to, deposited in the Heriot-Watt University Library, should be made available for loan or photocopying and be available via the Institutional Repository, subject to such conditions as the Librarian may require
- 5) I understand that as a student of the University I am required to abide by the Regulations of the University and to conform to its discipline.

* *Please note that it is the responsibility of the candidate to ensure that the correct version of the thesis is submitted.*

Signature of Candidate:		Date:	
-------------------------	--	-------	--

Submission

Submitted By <i>(name in capitals):</i>	
Signature of Individual Submitting:	
Date Submitted:	

For Completion in Academic Registry

Received in the Academic Registry by <i>(name in capitals):</i>			
Method of Submission <i>(Handed in to Academic Registry; posted through internal/external mail):</i>			
E-thesis Submitted (mandatory for final theses from January 2009)			
Signature:		Date:	

Declaration

I hereby declare that the work presented in this thesis was carried out by myself at Heriot Watt University, Edinburgh, and has not been submitted for any other degree, at this, or any other university.

Sumanth Kumar Pavuluri
14 May 2011

Table of Contents

ABSTRACT	II
ACKNOWLEDGEMENTS	III
DECLARATION	V
TABLE OF CONTENTS	VI
LIST OF FIGURES	XI
LIST OF TABLES	XXII
LIST OF PUBLICATIONS BY THE CANDIDATE FROM THE THESIS WORK	XXIV
CHAPTER 1 INTRODUCTION	1
1.1 BACK GROUND AND MOTIVATION	1
1.2 THESIS OUTLINE	3
CHAPTER 2 MICROMACHINED PATCH ANTENNAS	5
2.1 REVIEW OF MICROSTRIP PATCH ANTENNA DEVICES	5
2.2 BASIC PROPERTIES OF MICROSTRIP ANTENNA DEVICES	10
2.2.1 Resonant Frequency	10
2.2.2 Quality factor	11
2.2.3 Input Impedance and Bandwidth	13
2.2.4 Radiation Efficiency	16
2.2.5 Directivity and Gain	17
2.3 APPLICATIONS OF PATCH ANTENNA DEVICES	19
2.4 SUBSTRATES FOR PATCH ANTENNA DEVICES	20
2.4.1 Conventional substrates for microwave antenna applications	20
2.4.2 Polymer and ceramic composites for microwave applications	22
2.4.3 Liquid crystal polymer based antenna devices for SOP applications	24
2.5 MICROMACHINED PATCH ANTENNAS	25
2.5.1 Silicon micromachining	27
2.5.1.1 Microstrip edge feed	27
2.5.1.2 CPW feed	28

2.5.1.3	<i>Aperture coupled feed</i>	29
2.5.2	Polymer micromachining	31
2.5.2.1	<i>CPW fed THB151N based post supported patch antenna</i>	31
2.5.2.2	<i>Negative photoresist based microstrip fed patch antenna</i>	33
2.5.2.3	<i>Ultra thick SU8 based post supported antenna</i>	34
2.5.2.4	<i>SU8 based MEMS monopole antenna</i>	34
2.5.2.5	<i>SU8 based horn antenna devices</i>	35
2.5.2.6	<i>Polymer based reconfigurable antenna devices</i>	35
2.5.3	Millimetre wave antennas using low K Spin-on dielectric substrates	37
2.5.4	Synthesised low dielectric-constant substrates	38
2.5.5	Laser micromachining	39
2.5.5.1	<i>Patch antenna devices on micromachined glass substrates</i>	39
2.5.5.2	<i>Sacrificial substrate based meander monopole antenna</i>	40
2.5.6	LTCC micromachining	42
2.6	SUMMARY	44

CHAPTER 3 DESIGN AND MODELLING OF APERTURE COUPLED PATCH ANTENNA DEVICES **46**

3.1	INTRODUCTION	46
3.2	MODELLING TECHNIQUES FOR PATCH ANTENNA DEVICES	46
3.2.1	Full-wave analysis	47
3.2.2	Reduced analysis	48
3.3	THEORETICAL ANALYSIS OF APERTURE COUPLED PATCH ANTENNA DEVICES	48
3.3.1	Coupling mechanism	48
3.3.2	Input impedance	51
3.3.2.1	<i>Network model</i>	51
3.3.2.2	<i>Cavity model</i>	52
3.4	DESIGN METHODOLOGY	55
3.4.1	Assigning ports and boundaries	58
3.4.2	Solution setup	59
3.4.3	Validation check and simulation	59
3.4.3.1	<i>Mesh control and accuracy</i>	60
3.4.4	Extraction of simulation results	61
3.5	A MICROSTRIP FED MICROMACHINED APERTURE COUPLED PATCH ANTENNA DEVICE	61
3.5.1	Design and simulation	63

3.5.2	Results and discussion	66
3.5.2.1	<i>Field distribution</i>	66
3.5.2.2	<i>S parameters and study of the bandwidth</i>	67
3.5.2.3	<i>Normalised radiation patterns</i>	68
3.5.2.4	<i>Directivity and gain</i>	71
3.5.3	Effect of microstrip length	72
3.5.4	Effect of SU8 polymer rim dimensions	73
3.5.5	Effect of SU8 polymer rim thickness	76
3.5.6	Effect of SU8 polymer rim dielectric properties	77
3.6	A MICROSTRIP FED MICROMACHINED APERTURE COUPLED STACKED ANTENNA DEVICE	80
3.6.1	Antenna design and simulation	80
3.6.2	Results and analysis	83
3.6.2.1	<i>S parameters and study of the bandwidth</i>	83
3.6.2.2	<i>Normalised radiation patterns</i>	84
3.6.2.3	<i>Directivity and gain</i>	87
3.7	A CPW FED MICROMACHINED APERTURE COUPLED STACKED ANTENNA DEVICE	88
3.7.1	Antenna design and simulation	88
3.7.2	Results and discussion	91
3.7.2.1	<i>S parameters and study of the bandwidth</i>	91
3.7.2.2	<i>Normalised radiation patterns</i>	93
3.7.3	Effect of different substrate material	95
3.8	A MICROSTRIP FED MICROMACHINED APERTURE COUPLED SUBARRAY ANTENNA DEVICE	97
3.8.1	Antenna design and simulation	97
3.8.2	Results and discussion	101
3.8.2.1	<i>S parameters and study of the bandwidth</i>	101
3.8.2.2	<i>Normalised radiation patterns</i>	102
3.8.2.3	<i>Directivity and gain</i>	105
3.9	SUMMARY	105
CHAPTER 4 FABRICATION AND ASSEMBLY		108
4.1	INTRODUCTION	108
4.2	UV PHOTOLITHOGRAPHY	108
4.3	MATERIALS FOR MICROMACHINED ANTENNA DEVICES	109
4.3.1	SU8	109

4.3.2	Thin film substrates	110
4.3.2.1	<i>Polyimide film</i>	110
4.3.2.2	<i>Liquid Crystal Polymers</i>	110
4.4	OVERVIEW OF ANTENNA FABRICATION AND ASSEMBLY	111
4.5	PHOTOMASK DESIGN	114
4.6	FABRICATION	118
4.6.1	Fabrication of microstrip feed and aperture on the base substrate	119
4.6.1.1	<i>Photoresist deposition</i>	120
4.6.1.2	<i>Soft bake</i>	121
4.6.1.3	<i>UV exposure</i>	121
4.6.1.4	<i>Development and copper etch</i>	121
4.6.1.5	<i>Optimisation of photolithographic parameters for AZ 9260 photoresist</i>	123
4.6.2	Fabrication of patch elements on thin film substrates	125
4.6.3	Fabrication of micromachined spacers	126
4.6.3.1	<i>Spin coating</i>	127
4.6.3.2	<i>Prebake</i>	128
4.6.3.3	<i>UV exposure</i>	129
4.6.3.4	<i>Post bake and development</i>	129
4.6.3.5	<i>Optimisation of parameters for SU8 photoresist</i>	131
4.7	ANTENNA ASSEMBLY	133
4.8	SUMMARY	136

CHAPTER 5 MICROWAVE MEASUREMENTS AND CHARACTERISATION 137

5.1	THE EXPERIMENTAL METHOD	137
5.1.1	Reference plane and calibration method	137
5.1.1.1	<i>Reference plane</i>	137
5.1.1.2	<i>TRL calibration</i>	137
5.1.1.3	<i>The SMA connector</i>	138
5.2	ANTENNA RADIATION MEASUREMENTS	138
5.2.1	Anechoic chambers	138
5.2.2	Far field measurements	139
5.2.2.1	<i>Three antenna gain measurement method</i>	140
5.2.2.2	<i>Gain-transfer method</i>	142
5.3	RESULTS	144
5.3.1	Microstrip fed micromachined aperture coupled patch antenna device	144
5.3.2	Microstrip fed micromachined aperture coupled stacked antenna device	147

5.3.3	CPW fed micromachined aperture coupled stacked antenna device	150
5.3.4	Microstrip fed micromachined aperture coupled subarray antenna device	154
5.4	SUMMARY	155
CHAPTER 6 CONCLUSIONS		158
6.1	CONCLUSIONS	158
6.2	FUTURE WORK	161
APPENDIX		163
A1	A MICROMACHINED FSS BASED ANTENNA DEVICE	163
A1.1	Introduction	163
A1.2	Review of FSS based partially reflective arrays and antennas	163
A1.3	Design and modelling	166
A1.3.1	<i>Software tool for electromagnetic design and simulation</i>	166
A1.3.2	<i>Results and analysis</i>	168
A1.4	Fabrication and assembly	173
A1.5	Measurement	174
A1.6	Summary	175
A2	FABRICATION	177
A2.1	Thin film deposition	177
A2.2	Spin coating	177
A2.3	Soft baking	178
A2.4	UV exposure	179
A2.5	Development	180
A2.6	Copper etch	181
A3	THE NETWORK ANALYSER	184
REFERENCES		186

List of Figures

Figure 2.1 Illustration of feeding methods for microstrip antennas	7
Figure 2.2 Schematic diagrams showing the aperture coupled patch antenna.....	9
Figure 2.3 Illustration of a microstrip fed patch antenna device.....	10
Figure 2.4 Circuit model for the microstrip-fed patch antenna device.	14
Figure 2.5 Fabrication procedure for the proposed substrate.(a) PDMS is prepared by mixing silicone gel (b) procedure for ceramic adding and (c) schematic representation of the procedure [57].....	23
Figure 2.6 (a) Gain and (b) reflection coefficient for a 24 mm × 24 mm patch antenna placed on a BT/PDMS substrate (20% volume ratio), a MCT/PDMS substrate (10% volume ratio) and a pure PDMS substrate [57]	24
Figure 2.7 Multilayer implementations of the antenna arrays in LCP[68]	25
Figure 2.8 Layout of single-layer antenna array. The 2×2 patch antenna array, MEMS phase shifters, bias lines, and LNA pads are shown [68]	25
Figure 2.9 (a) Test fixture of the silicon micromachined antenna device (b) Geometry of the micromachined patch antenna with mixed air- substrate region that is laterally etched [4].....	28
Figure 2.10 (a) Patch antenna suspended over membrane (b) Photograph of the fabricated patch antenna [79]	28
Figure 2.11 (a) Insertion loss and reflection coefficient for a silicon micromachined antenna device (b) CPW-microstrip transition [79]	29
Figure 2.12 (a) Top view and (b) cross sectional view of the aperture-coupled micromachined microstrip antenna with all dimensions in microns [80]	30
Figure 2.13 Measured and simulated input impedance of the microstrip antenna on a full 100 μm thick silicon substrate [80].....	30

Figure 2.14 Proposed CPW-fed post-supported MEMS antenna devices for (a) Single post structure. (b) Additional supporting posts structure. (c) Half size structure with shorting wall [82]	31
Figure 2.15 (a) Fabricated 2×1 patch antenna array (b) Measured input reflection coefficient of 2×1 patch antenna array [82]	32
Figure 2.16 Fabrication steps of the multi-depth well integration scheme [83].....	33
Figure 2.17 Photo of fabricated elevated patch antenna, along with its mirror image on the ground [84]	34
Figure 2.18 (a) A photomicrograph of 3×3 monopole array (b) An SEM image of a single monopole antenna. (c) Measured and simulated S_{11} plots for monopole antenna for a height of 880 μm [86].....	35
Figure 2.19 (a) Top view of original MEMS antenna (b) Side view of MEMS antenna [91]	36
Figure 2.20 (a) Top view of frequency agile MEMS antenna (b) A fabricated geometry of MEMS antenna [91].....	37
Figure 2.21 (a) Geometry of millimetre wave CPA using low-k dielectric substrate (b) Reflection coefficient of mm wave CPA with the low-k dielectric substrate [94]. The red and blue curves show the measured and simulated results while the green curve shows the comparison (simulated results) with a ceramic substrate ($\epsilon_r = 9.8$)	38
Figure 2.22 Fabricated microstrip antenna on a localized low dielectric substrate [95]	39
Figure 2.23 (a) HFSS model of the folded shorted-patch antenna used for electrical analysis (b) Photograph of the antenna prototype [96].....	39
Figure 2.24 Simulated reflection coefficient of the FSPA (Folded short patch antenna) for different substrate thickness values [96].....	40
Figure 2.25 (a)3D MEMS monopole antenna top view (not scaled), (b) Process flow for 3D MEMS helical meander antenna [97].....	41
Figure 2.26 (a) Measured and simulated reflection coefficient for proposed antenna (b) Measured radiation patterns for the proposed meander monopole antenna [97].....	41

Figure 2.27 Exploded view of the 11 layer antenna structure in LTCC technology [55]	42
Figure 2.28 3-D layout of the antenna switch module in LTCC for SIP based antenna front-end [100].	43
Figure 2.29 Design architecture for the package level integration of an LTCC based antenna [56]	43
Figure 3.1 Side view (a) and top view (b) of a rectangular microstrip antenna aperture coupled to a microstripline [19]	49
Figure 3.2 Equivalent circuit model for an aperture coupled antenna device [111, 112]	52
Figure 3.3 (a) Top view of the aperture coupled antenna along with dimensions, (b) Side view of the antenna structure redrawn from [19]	53
Figure 3.4 Side view of the micromachined aperture coupled antenna device modelled in Ansoft HFSS [115]	56
Figure 3.5 Modified Ansoft HFSS 3D model and the design flow	57
Figure 3.6 Design modeller environment in Ansoft HFSS [115] and the 3D model of the micromachined aperture coupled antenna device	57
Figure 3.7 Mesh formation for the micromachined aperture coupled antenna model in HFSS	61
Figure 3.8 Geometry of the (a) cross-sectional view and (b) top view of microstrip fed micromachined aperture coupled patch antenna device	62
Figure 3.9 Field model showing the scalar and vector (a) electric and (b) magnetic fields at 13.5 GHz.	66
Figure 3.10 Simulated reflection coefficient and the VSWR parameters for the optimized microstrip fed micromachined aperture coupled patch antenna device	67
Figure 3.11 Simulated impedance parameters for magnitude, real and imaginary values	68

Figure 3.12 2D radiation patterns in E (x-z) plane and H (y-z) plane (a) and 3D (b) radiation patterns of a microstrip fed micromachined aperture coupled patch antenna device at 13.2 GHz	69
Figure 3.13 Simulated normalized E and H plane radiation patterns at different frequencies for the microstrip fed micromachined aperture coupled patch antenna device.....	70
Figure 3.14 Simulated gain, directivity and radiation efficiency of the optimized microstrip fed micromachined aperture coupled patch antenna device	71
Figure 3.15 Simulated reflection coefficient (S_{11}) parameters of the microstrip fed micromachined aperture coupled patch antenna device for different microstrip lengths	73
Figure 3.16 Simulated reflection coefficient (S_{11}) parameters of the microstrip fed micromachined aperture coupled patch antenna device for different SU8 polymer rim dimensions.....	73
Figure 3.17 Simulated gain, directivity parameters of the microstrip fed micromachined aperture coupled patch antenna device for different SU8 polymer rim dimensions. The solid lines represent directivity while the dotted lines represent antenna gain.....	74
Figure 3.18 Simulated radiation efficiency parameters of the microstrip fed micromachined aperture coupled patch antenna device for different SU8 polymer rim dimensions.....	75
Figure 3.19 (a) Simulated gain, directivity and efficiency parameters of the microstrip fed micromachined aperture coupled patch antenna device for different SU8 polymer rim dimensions at 13.1 GHz. A, B,C represents a polymer rim dimensions of 20mm×20mm, 16mm×16mm and 12mm×12mm respectively. (b) Simulated efficiency parameters of the micromachined patch antenna device for different SU8 polymer rim dimensions at 13.1 GHz.....	75
Figure 3.20 Simulated reflection coefficient (S_{11}) parameters of the microstrip fed micromachined aperture coupled patch antenna device for varying SU8 polymer rim thickness. The thickness of the polymer rim is denoted by 'h' in the plot.....	76
Figure 3.21 (a) Simulated gain and directivity parameters of the microstrip fed micromachined aperture coupled patch antenna device for different SU8 polymer rim dimensions at 13.1 GHz.(b) Simulated efficiency parameters of the micromachined patch antenna device for different SU8 polymer rim thickness at 13.1 GHz.....	77

Figure 3.22 Simulated reflection coefficient (S_{11}) parameters of the microstrip fed micromachined aperture coupled patch antenna device for varying SU8 dielectric constant.....	78
Figure 3.23(a) Simulated gain and directivity parameters of the microstrip fed micromachined aperture coupled patch antenna device varying SU8 dielectric constant at 13.1 GHz.(b) Simulated efficiency parameters of the micromachined patch antenna device for different SU8 polymer rim thickness at 13.1 GHz.....	78
Figure 3.24 Simulated reflection coefficient (S_{11}) parameters of the microstrip fed micromachined aperture coupled patch antenna device for varying SU8 dielectric loss tangent.	79
Figure 3.25 Simulated gain and directivity parameters of the microstrip fed micromachined aperture coupled patch antenna device varying SU8 dielectric loss tangent at 13.1 GHz.(b) Simulated efficiency parameters of the micromachined patch antenna device for different SU8 polymer rim thickness at 13.1 GHz.....	79
Figure 3.26 (a) Schematic cross-sectional views of the microstrip fed micromachined aperture coupled stacked antenna using micromachined polymer spacers. The top view of the apertures and feed lines on the substrate surface corresponding to (a) is shown in (b)	81
Figure 3.27 Simulated reflection coefficient and the VSWR parameters for the optimized microstrip fed micromachined aperture coupled stacked antenna device	83
Figure 3.28 Simulated impedance parameters for magnitude, real and imaginary values for the optimized microstrip fed micromachined aperture coupled stacked antenna device.....	84
Figure 3.29 (a) 2D radiation patterns in E (x-z) plane and H (y-z) plane (b) 3D radiation patterns at 9.82 GHz for the optimized microstrip fed micromachined aperture coupled stacked antenna device.....	85
Figure 3.30 Simulated normalized E and H plane radiation patterns at different frequencies for the optimized microstrip fed micromachined aperture coupled stacked antenna device.....	87
Figure 3.31 Simulated gain, directivity and radiation efficiency of the optimized microstrip fed micromachined aperture coupled stacked antenna device.....	88

Figure 3.32 Schematic cross-sectional views of the stacked CPW fed micromachined aperture coupled stacked antenna using micromachined polymer spacers, (a) CPW fed device. The top view of the apertures and feed lines on the substrate surface corresponding to (a) is shown in (b).....	90
Figure 3.33 Simulated reflection coefficient and the VSWR parameters for the optimized CPW fed micromachined aperture coupled stacked antenna	91
Figure 3.34 Simulated impedance parameters for magnitude, real and imaginary values for the optimized CPW fed micromachined aperture coupled stacked antenna.....	91
Figure 3.35 (a) 2D radiation patterns in E (x-z) plane and H (y-z) plane and (b) 3D radiation patterns for the optimized CPW fed micromachined aperture coupled stacked antenna at 8 GHz	92
Figure 3.36 Simulated normalized E and H plane radiation patterns at different frequencies for the optimized CPW fed micromachined aperture coupled stacked antenna device.....	94
Figure 3.37 Reflection coefficient (S_{11}) results of the CPW fed micromachined aperture coupled stacked antenna for different substrate configurations	96
Figure 3.38 Antenna efficiency results of the CPW fed micromachined aperture coupled stacked antenna for different substrate configurations	96
Figure 3.39 Antenna gain results of the CPW fed micromachined aperture coupled stacked antenna for different substrate configurations	97
Figure 3.40 Schematic of the microstrip fed micromachined aperture coupled subarray antenna device. The top view of the apertures and feed lines on the substrate surface corresponding to (a) is shown in (b). $W_{tp}=7$ mm, $L_{tp}=6.2$ mm, $L_{lp}=7.4$ mm, $W_{lp}=13$ mm, $L_s=20.1$ mm, $W_s=3.3$ mm, $W_a=9$ mm, $L_{sep}=6.8$ mm, $W_{sep}=4.6$ mm, $L_r=26$ mm, $W_r=28$ mm	99
Figure 3.41 Field model showing the scalar (a) electric and (b) magnetic fields for the microstrip fed micromachined aperture coupled subarray antenna device at 13 GHz.....	101
Figure 3.42 Simulated reflection coefficient and the VSWR parameters for the optimized microstrip fed micromachined aperture coupled subarray antenna.....	101

Figure 3.43 Simulated impedance parameters for magnitude, real and imaginary values for the optimized microstrip fed micromachined aperture coupled subarray antenna	102
Figure 3.44 (a) 2D radiation patterns in E (x-z) plane and H (y-z) plane and (b) 3D radiation pattern at 11 GHz for the microstrip fed micromachined aperture coupled subarray antenna	103
Figure 3.45 Simulated normalized E and H plane radiation patterns at different frequencies for the microstrip fed micromachined aperture coupled subarray antenna.....	104
Figure 3.46 Simulated gain, directivity and radiation efficiency of the microstrip fed micromachined aperture coupled subarray antenna device.....	105
Figure 4.2 Chemical structure of the Bisphenol A Novolak epoxy oligomer contained in SU8 formulation. [130].....	110
Figure 4.3 Illustration of the assembly method for fabrication of a generalised micromachined antenna device.	111
Figure 4.4 Schematic of the fabrication flow on (a) microwave substrate (b) polyimide film (c) assembly of the first patch (d) assembly of the second patch	112
Figure 4.5 Schematic of the microstrip fed micromachined aperture coupled antenna device from the top view.....	115
Figure 4.6 Schematic of the photomask designs for fabrication of the microstrip fed micromachined aperture coupled antenna device with the alignment marks. The photomasks shown are for (a) Microstrip feed line, (b) Ground plane and the aperture (c) Patch element and (d) Polymer rim	117
Figure 4.7 Schematic of the photomask designs for fabrication of the CPW fed micromachined aperture coupled stacked antenna device. The photomasks shown are for (a) CPW feed line, ground plane and the aperture (c) Top patch element and (d) Polymer rim.	118
Figure 4.8 Process flow of substrate fabrication for the microstrip fed micromachined aperture coupled antenna device.....	120
Figure 4.9 Optical images of (a) a feeding microstrip and (b) a coupling aperture on a substrate after fabrication for the microstrip fed micromachined aperture coupled antenna device	122

Figure 4.10 Optical diffraction patterns by various exposure situations reproduced from [136].....	123
Figure 4.11 Fabrication flow for the suspended patch elements for the micromachined aperture coupled antenna devices	125
Figure 4.12 Fabrication flow for the SU8 polymer rim for the microstrip fed micromachined aperture coupled antenna device.....	127
Figure 4.13 Temperature verses time plot for the prebake process for SU8 wafer.....	128
Figure 4.14 Illustration of tilted wafer and uneven SU8 photoresist	129
Figure 4.15 Illustration of SU8 layer peel off from the substrate due to excessive stresses during prebake.....	131
Figure 4.16 Illustration of the excessive development in the SU8 photoresist film	132
Figure 4.17 Photograph of a excessively developed SU8 polymer side wall	132
Figure 4.18 (a) Photograph of the fabricated microstrip fed micromachined aperture coupled antenna device after assembly. (b) Photo graph of the back side of the fabricated antenna.....	133
Figure 4.19 (a) Optical picture of the front side of a fabricated antenna (b) Optical picture of the reverse side of the antenna	134
Figure 4.20 (a) Photograph of a fabricated CPW line and aperture on the PTFE substrate, (b) Optical picture of a patch and a SU8 polymer rim on a LCP substrate and (c) Optical picture of an assembled device after stacking three patch layers on the PTFE base substrate	134
Figure 4.21 (a) Photograph of the microstrip fed micromachined aperture coupled stacked quad antenna after assembly. (b) Photograph of the lower patch element on LCP film and (c) Photograph of the upper quad array patch element on LCP film.....	135
Figure 5.1 A typical rectangular anechoic chamber [141]	139
Figure 5.2 Schematic showing the far field set up	141
Figure 5.3 Photograph of the far field measurement system in the anechoic chamber to measure the antenna radiation pattern and gain.....	144

Figure 5.4 Simulation and measurement results of the return loss for the microstrip fed micromachined aperture coupled patch antenna device	146
Figure 5.5 Simulated and measured E-plane (a) and H-plane (b) radiation patterns for microstrip fed micromachined aperture coupled patch antenna device at 12.1 GHz	146
Figure 5.6 Simulation and measurement results of the reflection coefficient for the microstrip fed micromachined aperture coupled stacked antenna device.....	147
Figure 5.7 Simulation results of the reflection coefficient for the microstrip fed micromachined aperture coupled stacked antenna device with the lower patch removed.	148
Figure 5.8 Simulated and measured E-plane (a) and H-plane (b) radiation patterns for the microstrip fed micromachined aperture coupled stacked antenna device at 9.5 GHz.....	149
Figure 5.9 Simulation and measurement results of the reflection coefficient for the CPW fed micromachined aperture coupled stacked antenna device....	151
Figure 5.10 Simulation results of the reflection coefficient for the CPW fed micromachined aperture coupled stacked antenna device with the lower and middle patch elements removed.....	152
Figure 5.11 Simulated and measured E-plane (a) and H-plane (b) radiation patterns for CPW fed micromachined aperture coupled stacked antenna device at 10 GHz.....	152
Figure 5.12 Frequency dependent peak gain for (a) microstrip fed and (b) CPW fed stacked patch antenna with respect to frequency	153
Figure 5.13 Simulation and measurement results of the reflection coefficient for the microstrip fed micromachined aperture coupled subarray antenna device.....	154
Figure 5.14 Simulated and measured E-plane (a) and H-plane (b) radiation patterns for the microstrip fed micromachined aperture coupled subarray antenna device at 12 GHz	155
Figure A.1 Schematic showing the FSS based antenna and the principle of operation [152]	164

Figure A.2 FSS based antenna device with multiple reflections between PRS screen and the ground plane [152].....	165
Figure A.3 Schematic of the cross-sectional view of the antenna design for 60 GHz operation.	167
Figure A.4 Layout of the micromachined FSS based antenna device in solid modeller within the Microstripes TM package[164].....	167
Figure A.5 Simulation results of reflection coefficient (S_{11}) for the micromachined FSS based antenna device.....	170
Figure A.6 Simulated radiation patterns of the micromachined FSS based antenna device at 60 GHz	170
Figure A.7 Simulation of the 3D radiation profile for the micromachined FSS based antenna device at 60.25 GHz.....	171
Figure A.8 3D radiation profile for the micromachined FSS based antenna device at 58.54 GHz.....	172
Figure A.9 3D radiation profile for the micromachined FSS based antenna device with SU8 filled inside the cavity	172
Figure A.10 Schematic of the fabrication flow for the micromachined FSS based antenna device on (a) microwave substrate (b) Taconic substrate (c) antenna assembly.....	173
Figure A.11 (a) Photograph of the micromachined FSS based antenna device after assembly (b) Photograph showing the FSS layer on the Taconic substrate along with the SU8 polymer rim.....	174
Figure A.12 Schematic showing the far field set up for the micromachined FSS based antenna device	175
Figure A.13 Photograph of the electron beam evaporator	177
Figure A.14 Photograph of the spin coating machine	178
Figure A.15 Photograph of the hot plate setup for pre-baking of the photoresist films.....	179
Figure A.16 Photograph of the Tamarac UV exposure system.....	180

Figure A.17 (a) Bungard Jet 34 d spray etching machine, (b) Ferric chloride solution with 50 g/l in the spray etch machine [169]	182
Figure A.18 General block diagram of a network analyzer [141].....	184
Figure A.19 Schematic of an S-parameter measurement system [141] `	184

List of Tables

Table 2.1 Antenna parameters for a conventional patch antenna device	18
Table 2.2 Applications of patch antenna devices	19
Table 2.3 Overview of microwave substrates (reprinted from [7] and measured at X band frequencies).....	21
Table 3.1 Summary of the parameters for the microstrip fed micromachined aperture coupled patch antenna device.....	65
Table 3.2 Summary of the design parameters for the microstrip fed micromachined aperture coupled stacked antenna	82
Table 3.3 Summary of electrical properties of substrates for microstrip fed micromachined aperture coupled stacked antenna device.....	83
Table 3.4 Summary of the design parameters for the CPW fed micromachined aperture coupled stacked antenna device	89
Table 3.5 Summary of the electrical properties of substrates for CPW fed micromachined aperture coupled stacked antenna device.....	90
Table 3.6 Summary of the antenna performance parameters for different antenna configurations	95
Table 3.7 Summary of the electrical properties of substrates for microstrip fed micromachined aperture coupled subarray antenna	98
Table 3.8 Summary of the design parameters for the microstrip fed micromachined aperture coupled subarray antenna device.....	98
Table 3.9 Summary of the antenna parameters for the micromachined aperture coupled antenna devices	107
Table 4.1 The composition of the SU8-5 photoresist.....	114
Table 4.2 Optimisation of photolithographic parameters for AZ 9260 photoresist	124
Table 4.3 Composition of the SU8-100 solution.....	126

Table 4.4 Processing steps and parameters for fabrication of AZ 9260 films for copper patterning and SU8 polymer rim for the micromachined aperture coupled antenna devices.....	130
Table 4.5 Processing steps and parameters for fabrication of SU8 polymer rims for the micromachined aperture coupled antenna devices	130
Table 5.1 Comparison of the measured antenna parameters for the micromachined antenna devices and the simulated conventional patch antenna device	156
Table A.1 Dimensions and electrical parameters for the micromachined FSS based antenna device	169
Table A.2 Physical and thermal properties of SU8 photoresist	182
Table A.3 Physical and thermal properties of DuPont Kapton polyimide film from Kapton [®] HN [120]	183
Table A.4 Physical and thermal properties of liquid crystal polymer (LCP) [133].	183

List of Publications by the candidate from the thesis work

Journal publications

1. S. K. Pavuluri, C. H. Wang, and A. J. Sangster "High Efficiency Wideband Aperture-Coupled Stacked Patch Antennas Assembled Using Millimeter Thick Micromachined Polymer Structures", *IEEE Trans. Antennas Propagat*, Vol. 58, No. 11, November 2010.
2. S. K. Pavuluri, C. H. Wang, and A. J. Sangster, "A High-Performance Aperture-Coupled Patch Antenna Supported by a Micromachined Polymer Ring," *IEEE Antennas Wireless Propag. Lett.*, vol. 7, pp. 283-286, 2008.

Book chapter

Sumanth K Pavuluri, Changhai Wang and Alan J Sangster "Micromachined high gain wideband antennas for wireless communications" published in the book "Mobile and Wireless Communications: Key Technologies and Future Applications", ISBN 978-3-902613-47-9.

Conference publications

1. S K Pavuluri, C H Wang, A J Sangster," A Cavity based High Gain MEMS Antenna for Microwave and Millimetre Wave Applications", The Second European Conference on Antennas and Propagation (EuCAP 2007)", 11 - 16 November 2007, EICC, Edinburgh, UK.
2. Changhai Wang, Sumanth Pavuluri," Fabrication and Assembly of High Gain MEMS Antennas for Wireless Communications" 27 - 30 May 2008, ECTC Buena vista, Florida, USA.
3. Sumanth Kumar Pavuluri, Feresidis Alexandros, George Goussetis, Changhai Wang, "A novel high gain 60 GHz antenna using a suspended frequency selective surface (FSS)", *Metamaterials*, 21-26 September 2008, Pamplona, Spain.

CHAPTER 1 INTRODUCTION

1.1 BACK GROUND AND MOTIVATION

The seemingly insatiable and growing demand for compact, multi-function, multi-frequency electronic systems for communications and other applications, is continuing to drive the search for devices offering more and more bandwidth. There is growing need for wideband, high gain communication systems in the X band (8 - 12 GHz) for terrestrial broadband communications and networking as well as for radar applications. Similarly, direct broadcast satellite (DBS) and various other applications in the K_u band (10 - 14 GHz) such as radio astronomy service, space research service, mobile service, mobile satellite service, radio location service (radar), amateur radio service and radio navigation, may require embedded antenna systems at different bands [1]. It would be ideal if efficient, broadband and cost effective planar microstrip based antenna and antenna array devices could be designed covering all these bands. Antennas operating in UWB scenarios face the difficulty to maintain invariable performances, i.e., phase linearity, radiation efficiency and impedance match over large bandwidth, frequency independent radiation patterns [2].

The majority of prediction models for cellular mobile radio, for instance are based on path loss that is inversely proportional to the gains of the transmitting and receiving antennas [3]. The benefit of reduced path loss is that the base station can transmit lower power and there will be less variation in the signal level throughout the cell in the case of a cellular system [3].

For these high frequency systems, compact size and high performance can usually be achieved by fabricating the antenna onto a low dielectric constant material and integrating it with the remaining circuitry implemented on a high dielectric constant substrate in neighbouring regions in the same package. This trend has serious implications for antennas, where these are required to be embedded within the system package, such as a mobile phone. Systems operating in the microwave and millimetre-wave frequency bands offer the possibility of high levels of integration of individual devices in high density layouts. The most compact circuit designs are invariably achieved by employing high dielectric constant substrates, but this is a requirement which is essentially incompatible

with the needs of an embedded planar antenna. Such antennas radiate most efficiently when fabricated onto substrates which exhibit low dielectric constant and low substrate losses. While it is not impossible to fabricate microstrip or coplanar circuits, together with planar antennas on the same high permittivity silicon substrate but the antenna gain and efficiency will inevitably be very poor [4]. The antenna gain and efficiency also decrease with loss tangent of the substrates as can be seen in Section 2.2.

Various schemes have been suggested, in recent years, aimed at overcoming the opposing substrate requirements of circuits and antennas. These largely involve the use of layered materials with high and low permittivity's in adjacent layers [5, 6]. However such methods tend to be of quite limited versatility and the trend now is toward selective removal of substrate in the vicinity of the antenna. This can be done by for example, bulk micromachining an air gap between the planar antenna (usually a conducting patch) and the ground plane. The advantages of doing so are as follows:

- Lower effective dielectric constant, hence wider circuit dimensions
- Ease of fabrication and relaxed dimensional tolerances
- Lower attenuation
- Enhanced radiation efficiency in case of antennas
- Eliminating surface waves

Micromachining technology continues to develop, and it is being applied in new ways to embedded antennas to improve their performance. The use of selective lateral etching based on micromachining techniques to enhance the performance of rectangular microstrip patch antennas printed on high-index wafers such as silicon, GaAs, and InP have been developed in the past decade [4]. Over the last decade several micromachining techniques have been developed for producing microwave wave and millimetre wave antennas. Devices using these procedures have achieved high performances compared to the conventional patches printed on to relatively high dielectric constant substrates. A post-foundry micromachining process is ideal for producing high efficiency communication systems by fabrication of components on thin dielectric membranes within the ICs, thus removing the substrate losses for critical components such as inductors and antennas by increasing the parallel resonant frequency of inductors and improving bandwidth and radiation properties of antenna structures.

This project aims at developing inexpensive micromachining processes for producing SU8 (photoresist) polymer rim based air suspended patch antenna devices. An improvement in the antenna bandwidth, gain and efficiency performance for the antenna devices is obtained. An aperture coupled feeding technique has been employed to reduce the feeding losses and a stacked patch configuration is used to improve the bandwidth of the micromachined patch antenna devices. The aperture coupled feeding technique has intrinsic properties which make it an attractive feature for millimetre wave applications. It has been found that antenna devices designed with this feeding technique can easily be impedance-matched by tuning the dimensions of the excitation aperture and adding a small tuning stub.

The contributions of this thesis are related to the design, fabrication and characterisation of novel micromachined aperture coupled antenna device prototypes. Several advantages have been shown for the proposed micromachined antenna devices including a simple feeding structure, a CMOS-compatible monolithic integration scheme, wide bandwidth and high efficiency.

1.2 THESIS OUTLINE

Chapter 2 contains a literature review for the design and simulation work undertaken for the micromachined antenna devices. A brief history of patch antenna devices and aperture coupled patch antenna devices is provided. This is followed by a review of the different substrate materials including the advanced polymer composites developed recently for the microwave and millimetre wave antenna application. Various micromachining techniques and micromachined antenna devices are also presented in this chapter.

Chapter 3 presents the electromagnetic analysis techniques for micromachined aperture coupled patch antenna devices. This is followed by the work on design, modelling and simulation of the micromachined antenna devices. The simulated results are presented for each of the antenna designs and compared for the reflection coefficient (S_{11}), radiation pattern, gain, directivity and efficiency. The effect of the substrate materials and the dimensions of the SU8 polymer rims on the performance of the microstrip and CPW fed micromachined aperture coupled antenna devices are discussed.

Chapter 4 describes the fabrication and assembly of the micromachined aperture coupled antenna devices. The processes, fabrication facilities and processing parameters are outlined. The fabrication of feeding and aperture features on the microwave substrates and radiating patch elements on polyimide and LCP (Liquid crystal polymer) substrates is presented.

Chapter 5 presents the results from the RF characterisation of micromachined antenna devices based on reflection and radiation measurements. The antenna gain and radiation pattern measurements were carried out in an anechoic chamber.

Chapter 6 presents the conclusions and future work.

Appendix A1 describes design and fabrication of a micromachined FSS (Frequency Selective Surface) based antenna device fabrication for high gain operation at 60 GHz. Full-wave simulation was carried out using commercially available software, MicrostripesTM, to predict the antenna performance.

CHAPTER 2 MICROMACHINED PATCH ANTENNAS

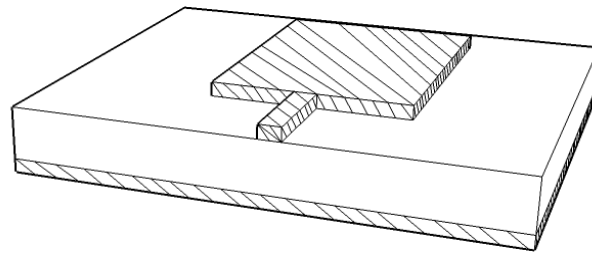
This chapter provides a description of previous work conducted within a number of research areas in the development of patch antennas and the micromachined patch antenna devices. A brief history of patch antenna devices and aperture coupled patch antenna devices is presented. This is followed by the progress in substrate materials including the advanced polymer composites developed recently for microwave and millimetre wave antennas. Various micromachining techniques and micromachined antenna devices are also presented in this chapter.

2.1 REVIEW OF MICROSTRIP PATCH ANTENNA DEVICES

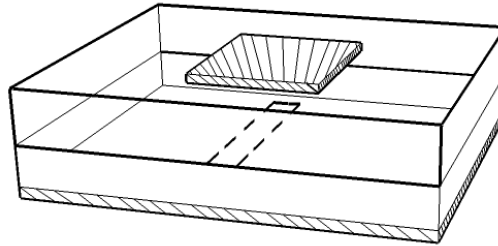
A comprehensive review of the microstrip antenna devices and technology has been presented by Carver *et al* [7]. “The microstrip antenna concept was developed 54 years ago and was first introduced in the US by Deschamps [7, 8] while at the same time in France by Gutton and Baissinot [9]. Striplines and stripline discontinuities and their radiation patterns were studied initially in 1970's when work on the radiating metallic strip separated from a ground plane by a dielectric substrate was reported by Byron [10]. The radiating element was half wavelength wide and several-wavelengths long and was fed by coaxial connections along both radiating edges at periodic intervals. In the project Camel, these radiating elements were used as an array”. The concept of a microstrip element was first patented by Munson [11]. Basic work on rectangular and circular microstrip patch antenna elements was first published by Howell [12]. Additional work on basic microstrip patch elements was reported by Garvin *et al* [13], and Howell [14] in 1975. Several microstrip geometries were developed by Weinschel for their use with cylindrical S-band arrays on rockets [15]. Sanford showed that the microstrip element could be used in conformal array designs for L-band communication from a KC-135 aircraft to the ATS-6 satellite [16]. Munson can be credited for the development of microstrip antennas for use as low-profile flush-mounted antennas on rockets and missiles [7]. These microstrip antenna devices served as a practical concept for use in many antenna system applications.

In recent years, the applications of patch antenna devices are wide spread and a number of the feeding methods and patch designs have been developed to meet the need of the different applications. The basic configuration of a microstrip antenna consists of a metallic patch printed on a thin, grounded dielectric substrate [1, 17, 18] as shown in Figure 2.1(a). The patch element was originally fed with either a coaxial feed through the substrate. An alternative type of excitation allows a feeding network on the substrate either by a microstrip line or a coplanar microstrip line. Figure 2.1 also shows the microstrip edge fed and aperture coupled configurations for the patch antenna. A microstrip antenna device has a low profile and it can be fabricated using printed circuit (photolithographic) techniques. The design of microstrip antennas at microwave and millimetre wave frequencies is closely related to the feeding technique. At these frequencies, there are several problems such as feed dimensions, soldering of probes associated with the classical feeding techniques, such as coaxial probe (Figure 2.1 (c)) or edge feeds (Figure 2.1 (a) and (b)). These considerations are even more important for wideband applications, which require thicker substrates. On the other hand, the aperture coupled feeding technique (Figure 2.1 (d)) has intrinsic properties which make it an attractive feature for millimetre wave applications.

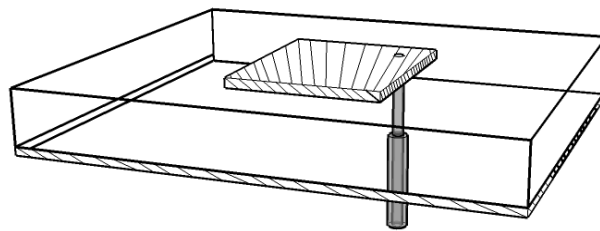
An aperture coupled feeding technique has been developed to decrease feeding loss and to improve the bandwidths of the patch antenna devices. The first aperture coupled microstrip antenna was fabricated and tested by a graduate student, Allen Buck, in 1984, at the University of Massachusetts. This antenna device was fabricated on a Duroid substrate with a circular coupling aperture and operated at around 2 GHz [19, 20]. Single layer probe or microstrip line-fed patch antenna devices are limited to bandwidths of 2%-5%. Aperture coupled antenna devices have been demonstrated to provide bandwidths up to 10 - 15% with a single layer [21-23], and up to 30-50% with stacked patch configurations [22, 24, 25]. The improvement in bandwidth is primarily a result of the additional degrees of freedom offered by the stub length and coupling aperture size. The tuning stub length can be adjusted to offset the inductive shift in impedance that generally occurs when thick antenna substrates are used, and the slot can be brought close to resonance to achieve a double tuning effect. Use of a stacked patch configuration also introduces a double tuning effect [5, 22, 24-32].



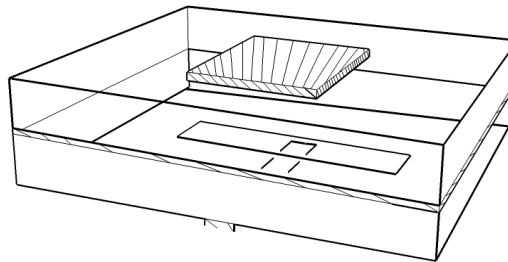
(a) Microstrip feed



(b) Buried line feed



(c) Coaxial feed



(d) Aperture coupled feed

Figure 2.1 Illustration of feeding methods for microstrip antennas

As a result, wide-band operation of this type of microstrip fed antenna has been demonstrated at microwave and millimetre wave frequencies using either single or stacked patch configurations. Although all of the coupling methods depicted in Figure 2.1 have been shown to give excellent bandwidth characteristics, the indirect methods (Figure 2.1(b) and (d)) give rise to a high back-radiation level. However this is only true for aperture coupling (Figure 2.1(d)) if the aperture is near resonance. The aperture coupled antenna

and normal CPW fed antenna devices can also be fabricated at microwave and millimetre wave frequencies in the 5-30 GHz region [29, 32-36]. It has been found that the CPW fed antennas can easily be impedance-matched by tuning the dimensions of the excitation aperture and by adding a small tuning stub in the ground plane. Numerous advantages arise for an aperture coupled configuration including those summarized previously [19] are listed below:

- (i) The configuration is suited for monolithic phased arrays, where active devices can be integrated on, for example, a gallium arsenide substrate with the feed network, and the radiating elements can be located on an adjacent (low dielectric constant) substrate, and coupled to the feed network through apertures in the ground plane separating the two substrates. The use of two substrates avoids the deleterious effect of a high-dielectric-constant substrate on the bandwidth and scan performance of a printed antenna array.
- (ii) No radiation from the feed network can interfere with the main radiation pattern, as the ground plane separates the two mechanisms.
- (iii) No direct connection is made to the antenna elements, so problems such as large probe self reactances or wide microstripline (relative to patch size), which are critical at millimetre-wave frequencies, are avoided.
- (iv) Ideal for micromachined antennas. The fabrication of a directly coupled feed probe would involve many fabrication steps.
- (v) The aperture coupled feeding technique has intrinsic properties which make it an attractive feature for millimetre wave applications.
- (vi) Wide-band operation of this type of microstrip antenna has been demonstrated at microwave frequencies (1 - 10 GHz) using either single or stacked patch configurations.
- (vii) A simple aperture coupled antenna structure gives rise to a high back-radiation level if the aperture is near resonance - this problem is eliminated by adopting a stacked antenna configuration.

A simple configuration of an aperture coupled microstrip antenna is shown in Figure 2.2. It consists of a radiating patch on one substrate coupled to a microstrip line feed on another parallel substrate, through an aperture in the intervening ground plane. It should be noted that the aperture coupled microstrip antenna can be used for both linear and circular

polarizations. It requires two co-located orthogonal apertures each one excited by a different feed line. Each aperture excites orthogonal linearly polarized resonances under the normally square patch. The polarisation of the radiation from the patch is then dependent on the relative magnitude and relative phase of the signals entering the independent feed lines. Circular polarisation is obtained when the signals are equal in magnitude and in quadrature phase.

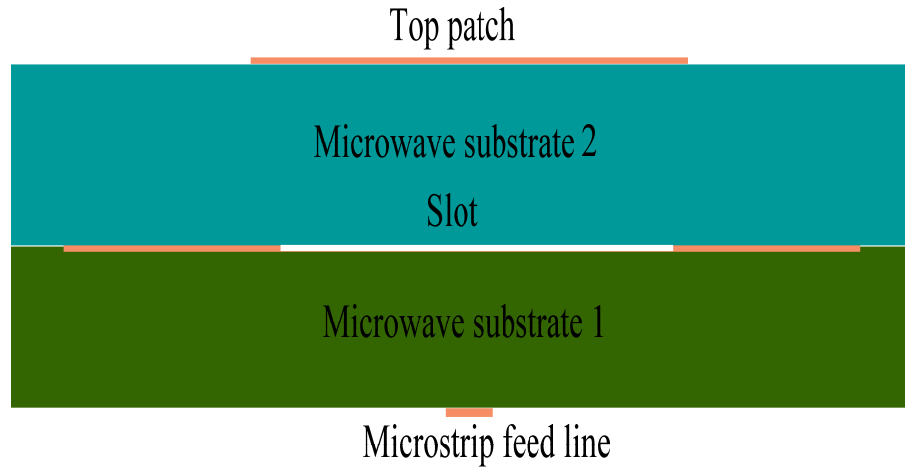


Figure 2.2 Schematic diagrams showing the aperture coupled patch antenna.

For conventionally fed patch antennas as in (Figure 2.1(a) to(c)) it is well known that to a very good approximation the patch resonant frequency is dictated largely by the size and shape of the patch. This is not the case in aperture coupled patches. The aperture also has a resonant frequency and the coupled resonators formed by the aperture and the patch resonates at a frequency determined by simple filter theory. In this section a micromachined microstrip fed aperture coupled antenna is studied in depth. We then examine micromachined aperture coupled stacked antenna devices fed both from microstrip and CPW line. Antenna performances are assessed for various antenna configurations. Reflection coefficient (S_{11}), VSWR, normalise radiation pattern, gain, directivity and efficiency parameters are presented for a range of design parameters with the results plotted as a function of frequency as necessary. The effects of these different design parameters on the antenna performance are discussed.

2.2 BASIC PROPERTIES OF MICROSTRIP ANTENNA DEVICES

The antenna analysis presented in this section is based on approximations of a rigorous solution by David R. Jackson [37]. The simplified theory provides a direct insight into the effect of the substrate parameters such as relative dielectric permittivity (ϵ_r) and substrate thickness on the behaviour of patch antennas [38]. The analytical expressions are used to provide initial design information for the micromachined antennas presented in this thesis.

2.2.1 Resonant Frequency

Figure 2.3 shows a schematic illustration of a microstrip patch antenna. The TM_{10} mode of operation gives a broadside radiation pattern for a rectangular patch and thus it is used extensively. This mode has no y variation and has a length of L that is approximately one-half wavelength in the dielectric medium. Thus the patch element acts as a wide microstrip line of width, W , that forms a transmission-line resonator of length L .

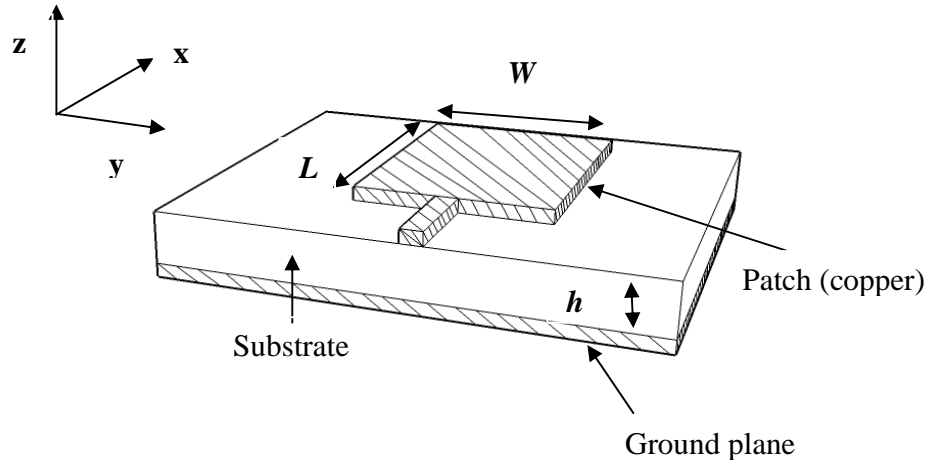


Figure 2.3 Illustration of a microstrip fed patch antenna device

For a rectangular patch antenna device, the TM_{mn} mode has a normalized electric field given by

$$E_z^{mn}(x, y) = \frac{k_0^2}{j\omega\epsilon_0\epsilon_r} \cos \frac{m\pi x}{L} \cos \frac{n\pi y}{W} \quad (2.1)$$

where ϵ_r is given by $\epsilon_r = \epsilon_r' - j\epsilon_r''$ and $\tan \delta = \frac{\epsilon_r''}{\epsilon_r'}$, ϵ_0 and μ_0 are the permittivity and permeability of free space, ϵ_r is the relative permittivity, $k_0 = \omega_0 \sqrt{\mu_0 \epsilon_0}$ and $\omega_0 = 2\pi f_0$ is the

angular frequency in free space. The resonant frequency f_{mn} (resonance frequency of (m, n) mode) is given by

$$f_{mn} = \frac{c}{2\pi\sqrt{\epsilon_r}} \sqrt{\left(\frac{m\pi}{L}\right)^2 + \left(\frac{n\pi}{W}\right)^2} \quad (2.2)$$

For TM_{10} mode, the resonant frequency f_{10} is given by

$$f_{10} = \frac{c}{\sqrt{\epsilon_r}} \left(\frac{1}{2L}\right) \quad (2.3)$$

$$\text{Where } c \text{ is the speed of light and is given by } c = 1/\sqrt{\mu_0\epsilon_0} \quad (2.4)$$

Due to the fringing fields at the ends of the patch element the electrical length of the element is effectively longer than the physical length. A formula for computing the length ΔL associated with the fringe fields has been derived by Hammerstad [39]

$$\frac{\Delta L}{h} = 0.412 \frac{(\epsilon_r + 0.3) \left(\frac{W}{h} + 0.264\right)}{(\epsilon_r - 0.258) \left(\frac{W}{h} - 0.8\right)} \quad (2.5)$$

The physical dimension, L (length as shown in Figure 2.3) of the patch can thus be approximated by

$$L = \frac{c}{2f_0\sqrt{\epsilon_r}} - 2\Delta L \quad (2.6)$$

Thus, a higher substrate permittivity allows for a smaller antenna (miniaturised) dimensions. The frequency f_0 represents the resonance frequency of the patch cavity.

2.2.2 Quality factor

The goal in antenna design is to produce an antenna system which has high efficiency and large bandwidth. These parameters are interrelated and it is hard to independently set these parameters. The stored energy in the cavity region, including the energy stored in the fringing fields around the structure, can be calculated and then compared with the various losses to compute the Q (quality) factor. The bandwidth and efficiency of an antenna device are related to the Q factor of the antenna device. For a resonant type of antenna such as the microstrip antenna, the Q factor is defined as

$$Q = \omega_0 \left(\frac{U_s}{P_{in}} \right) \quad (2.7)$$

where $\omega_0 = 2\pi f_0$ is the angular resonance frequency of the patch cavity, U_s is the energy stored inside the patch cavity, and P_{in} is the time average power going into the antenna device, which is equal to the average power being radiated plus dissipated. A microstrip antenna device has dielectric loss, conductor loss, and possibly surface-wave loss. The surface-wave loss depends on the environment surrounding the patch. If the substrate extends beyond the patch but ends at some distance away, the propagating surface wave will diffract at the edge of the substrate and convert into a radiation field. In this case the surface wave power is not actually a loss, but the diffracted fields will typically result in pattern degradation. The quality factor can be expressed as

$$Q = \omega_0 \left(\frac{U_s}{(P_{sp} + P_c + P_d + P_{sw})} \right) \quad (2.8)$$

where P_{sp} , P_c , P_d , P_{sw} denotes the average power radiated (space wave), the average power lost in the conductors, the average dielectric power loss (substrate) and the average power lost in the surface wave respectively. The sum of these powers is equal to the average power going into the antenna device. The total quality factor can be represented in terms of the individual quality factors as

$$\frac{1}{Q} = \frac{1}{Q_{sp}} + \frac{1}{Q_c} + \frac{1}{Q_d} + \frac{1}{Q_{sw}} \quad (2.9)$$

where Q_{sp} , Q_c , Q_d , and Q_{sw} denote the space-wave, surface-wave, dielectric, and conductor quality factors corresponding to the power radiated into space, launched into the fundamental TM_{10} surface-wave, dissipated by dielectric loss, and dissipated by conductor loss, respectively. The dielectric quality factor is given by

$$Q_d = \frac{1}{\tan \delta} \quad (2.10)$$

where $\tan \delta = \epsilon''/\epsilon'$, ϵ'' is the imaginary component and ϵ' is the real component of complex dielectric permittivity. If the ground plane and patch metal have surface resistances R_{sg} , R_{sp} , and R_s^{ave} denotes their average, then the conductor Q factor is given by

$$Q_c = \mu_r \left(\frac{\eta_0}{2} \right) \left(\frac{k_0 h}{R_s^{ave}} \right) \quad (2.11)$$

where $\eta_0 = 377\Omega$ is the free space impedance. The surface resistance is related to the conductivity of the metal, σ , and the skin depth δ is given by

$$\delta = \sqrt{\frac{2}{\omega \mu_0 \sigma}} \quad (2.12)$$

R_s^{ave} can then be expressed as

$$R_s^{ave} = \frac{1}{\sigma \delta} \quad (2.13)$$

The Q factor that accounts for the radiation into space is given as

$$Q_{sp} = \frac{3}{16} \left(\frac{\epsilon_r}{p_r c_1} \right) \left(\frac{L_e}{W_e} \right) \left(\frac{1}{h/\lambda_0} \right) \quad (2.14)$$

where $L_e = L + 2\Delta L$ and $W_e = W + 2\Delta W$ are the effective length and width of the patch. The fringing length, ΔL is given by equation 2.5, while the fringing width is approximately given by

$$\Delta W = h \left(\frac{\ln 4}{\pi} \right) \quad (2.15)$$

Thus, the space wave quality factor Q_{sp} of the antenna is inversely proportional to the substrate thickness h , for a given substrate material. The quality factor due to the surface wave is given by

$$Q_{sw} = Q_{sp} \left(\frac{e_r^{hed}}{1 - e_r^{hed}} \right) \quad (2.16)$$

where e_r^{hed} denotes the radiation efficiency of the patch when accounting for only surface-wave loss, and not dielectric or conductor loss. The value of e_r^{hed} can be obtained from equation 2.27.

2.2.3 Input Impedance and Bandwidth

From simple circuit theory, the input impedance of a patch antenna is given by [37]

$$Z_{in} = j\omega L_p + \frac{R}{1 + jQ(f_r - \frac{1}{f_R})} \quad (2.17)$$

where L_p represents the probe inductance (microstrip feed line) and the frequency ratio is defined as $f_R = f/f_0$, with f_0 being the resonant frequency of the patch cavity (the resonance frequency of the RLC circuit). The impedance resonance frequency of the patch (the frequency for which the input reactance is zero), is denoted by f_r , due to the presence of the feed line reactance. The term, R , represents the input resistance of the patch at the cavity resonance frequency f_0 ($f_R = 1$), at which the input resistance is a maximum. The total quality factor Q is given by equation 2.8. At the impedance resonance frequency f_r , the relation between the input resistance and the probe reactance is given approximately by [37]

$$R_{in} = \frac{R}{1 + \left(\frac{X_p}{R}\right)^2} \quad (2.18)$$

where $X_p = \omega_0 L_p$ and ω_0 is the angular frequency at f_0 . Thus from equation 2.18, at the impedance resonant frequency, f_r , the input resistance R_{in} will be slightly lower than the maximum value of R . Figure 2.4 shows the equivalent circuit model for the microstrip-fed patch antenna device where L_p represents the probe inductance (microstrip feed line) and R , L and C represents the resistance, inductance and capacitance of the patch resonator cavity respectively.

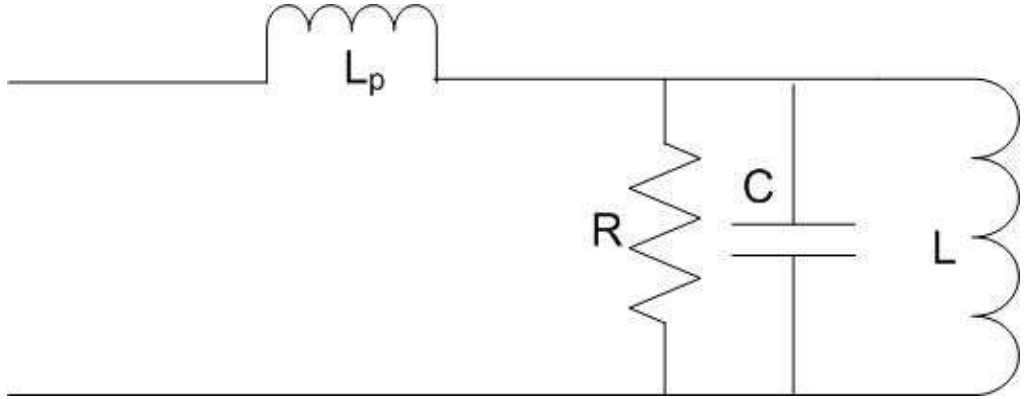


Figure 2.4 Circuit model for the microstrip-fed patch antenna device.

The probe reactance usually shifts the impedance resonance up from the cavity resonance by an amount $\Delta f = f_r - f_0$ given by the approximate relation as below [37]

$$\frac{\Delta f}{f} = (BW) \left(\frac{1}{\sqrt{2}} \right) \left(\frac{x_p}{R} \right) \quad (2.18)$$

The bandwidth of the patch element can be defined from the frequency limits at which the voltage standing-wave ratio (VSWR) reaches a certain value, assuming that the feeding transmission line that connects to the patch is perfectly matched at the resonant frequency. The impedance bandwidth is defined from the frequency limits f_1 and f_2 at which VSWR is equal to 2.0 (-10 dB impedance bandwidth)

$$BW = \frac{f_2 - f_1}{f_r} \quad (2.19)$$

where f_r is the impedance resonant frequency of the patch, and f_1 and f_2 are the low and high frequencies on either side of the resonance frequency at which VSWR (Voltage Standing Wave Ratio) = S, with S being a prescribed value. The bandwidth is given with respect to 'Q' of the patch antenna by

$$BW = \frac{S-1}{\sqrt{S}Q} \quad (2.20)$$

For the commonly used definition S = 2 (reflective coefficient of about -9.54 dB), we have

$$BW = \frac{1}{\sqrt{2}Q} \quad (2.21)$$

The relationship between the reflection coefficient (S_{11}) and VSWR is given by

$$VSWR = \frac{1 + S_{11}}{1 - S_{11}} \quad (2.22)$$

Where S_{11} is given by

$$S_{11} = \frac{Z_{in} - Z_0}{Z_{in} + Z_0} \quad (2.23)$$

where Z_0 is the characteristic impedance and is usually 50 ohms for a microwave circuit. By using equation 2.9 (total quality factor), the bandwidth can thus be defined as

$$BW = \frac{1}{\sqrt{2}} \left[l_d + \left(\frac{R_s}{\pi \eta_0} \right) \left(\frac{1}{h/\lambda_0} \right) + \left(\frac{16}{3} \right) \left(\frac{pc_1}{\epsilon_r} \right) \left(\frac{h}{\lambda_0} \right) \left(\frac{W}{L} \right) \left(\frac{1}{e_r^{hed}} \right) \right] \quad (2.24)$$

Where $l_d = \tan \delta$ is the loss tangent of the substrate. The width W of the patch element is usually larger than the length L in order to increase the bandwidth. From the relationship above, one can see that the bandwidth is inversely proportional to permittivity and directly proportional to the thickness (h) of the substrate.

2.2.4 Radiation Efficiency

The radiation efficiency is the ratio of power radiated into space to the total input power and is given by

$$e_r = \frac{P_r}{P_{tot}} = \frac{P_r}{P_r + (P_c + P_d + P_{sw})} \quad (2.25)$$

where P_r is the radiated power, P_{tot} is the total input power, P_c is the power dissipated by conductors, P_d is the power dissipated by dielectric and P_{sw} is the power launched into surface wave. The radiation efficiency is less than 100% due to the conductor, dielectric and surface-wave power losses. The radiation efficiency can also be written down as

$$e_r = \frac{e_r^{hed}}{1 + e_r^{hed} \left[l_d + \left(\frac{R_s}{\pi \eta_0} \right) \left(\frac{1}{h/\lambda_0} \right) \right] \left[\left(\frac{3}{16} \right) \left(\frac{\epsilon_r}{pc_1} \right) \left(\frac{L}{W} \right) \left(\frac{1}{h/\lambda_0} \right) \right]} \quad (2.26)$$

The above expression is obtained from the Sommerfeld solution for an x directed unit strength infinitesimal dipole located at the top of the substrate as described in [38, 40], where

$$e_r^{hed} = \frac{p_{sp}^{hed}}{p_{sp}^{hed} + p_{sw}^{hed}} = \frac{1}{1 + \frac{p_{sw}^{hed}}{p_{sp}^{hed}}} \quad (2.27)$$

where p_{sp}^{hed} is the power radiated into space and p_{sw}^{hed} is the power launched into the surface wave. This term is the radiation efficiency of a horizontal electric dipole (hed) on top of the substrate. This efficiency is approximated by that of a unit-amplitude infinitesimal horizontal electric dipole (hed) on the substrate. It can be shown that

$$p_{sp}^{hed} = \frac{1}{\lambda_0^2} (k_0 h)^2 (80\pi^2 c_1) \quad (2.28)$$

$$\text{and } p_{sw}^{hed} = \frac{1}{\lambda_0^2} (k_0 h)^3 \left(60\pi^3 c_1 \left(1 - \frac{1}{\epsilon_r} \right)^3 \right) \quad (2.29)$$

Hence we have,

$$e_r^{hed} = \frac{1}{1 + \frac{3}{4} \pi (k_0 h) \left(\frac{1}{c_1} \right) \left(1 - \frac{1}{\epsilon_r} \right)^3} \quad (2.30)$$

The constants are defined as

$$c_1 = 1 - \frac{1}{\varepsilon_r} + \frac{2}{5\varepsilon_r^2} \quad (2.31)$$

$$\text{and } p = 1 + \frac{a_2}{10}(k_0 W)^2 + (a_2^2 + 2a_4)\left(\frac{3}{560}\right)(k_0 W)^4 + c_2\left(\frac{1}{5}\right)(k_0 L)^2 + a_2 c_2\left(\frac{1}{70}\right)(k_0 W)^2(k_0 L)^2 \quad (2.32)$$

where $a_2 = -0.16605$

$c_2 = -0.0914153$

$a_4 = 0.00761$

2.2.5 Directivity and Gain

The directivity of the patch antenna elements is given by [37]

$$D = \left(\frac{3}{pc_1} \right) \left[\frac{e_r}{e_r + \tan^2(k_1 h)} \right] (\tan c^2(k_1 h)) \quad (2.33)$$

where

$$\tan c(k_1 h) = \tan(k_1 h)/(k_1 h) \quad (2.34)$$

The antenna gain is defined as

$$G = e_r D \quad (2.35)$$

To illustrate the effect of substrate properties on antenna performance, four antenna devices are designed. The performance parameters are calculated using the expressions presented in the previous section. The results and the design parameters are summarised in Table 2.1. For a low permittivity substrate such as air, $\varepsilon_r = 1$, $\tan \delta = 0$ and a good conductor like copper with $\sigma = 5.8 \times 10^7 \text{ S/m}$, the length of patch element of $L = 9.5 \text{ mm}$, width $W = 11.5 \text{ mm}$, ($W/L=1.21$) and substrate thickness of 1.5 mm , the antenna bandwidth is 8.59%, the directivity is about 9.8 dBi and the antenna gain is about 9.75 dBi with an efficiency of 99.8%. For a high permittivity substrate such as Rogers RO3010TM, $\varepsilon_r = 10.2$, with the length of patch element (L) = 2.5mm, width (W) = 3.025mm ($W/L=1.21$), the antenna bandwidth is 1.53%, the directivity is about 7.59 dBi, the antenna gain of 4.7 dBi with the antenna efficiency of 61.9%. Thus, increasing the permittivity of the substrate decreases the antenna efficiency considerably for the patch antenna device and hence the gain of the

antenna device. It also decreases the bandwidth of the antenna device. Micromachined aperture coupled patch antenna devices are presented in this thesis that are separated from the ground plane with a thickness (height) of up to 3 mm. For air, with substrate thickness of 3 mm, $\epsilon_r = 1$, with the length of patch element of 9.5mm, width of 11.5mm ($W/L=1.21$), the antenna bandwidth is 15.15%, the directivity is about 9.31 dBi, the antenna gain is about 9.25 dBi with the antenna efficiency of 99.8%.

Table 2.1 Antenna parameters for a conventional patch antenna device

	$\epsilon_r=1$, h = 1.5mm (W/L =1.21)	$\epsilon_r=1$, h = 3mm (W/L =1.21)	$\epsilon_r=10.2$, h = 1.5mm, (W/L =1.21)	$\epsilon_r=1$, h = 1.5mm (W/L =1.5)
Resonant frequency (GHz)	13.08	11.25	13.1	12.981
Bandwidth (%)	8.59	15.15	1.53	9.88
Directivity (dBi)	9.8	9.31	7.59	10.3
Radiation efficiency (%)	99.8	99.81	61.9	99.9
Gain (dBi)	9.75	9.25	4.7	10.28

Thus increasing the thickness of the substrate increases the bandwidth of the antenna device while no significant effect on the directivity of the patch antenna device. For air, with $\epsilon_r = 1$ and with the length of patch element of $L = 9.5\text{mm}$, width of $W = 14.25\text{mm}$ ($W/L=1.5$) and substrate thickness of 1.5 mm, the antenna bandwidth is 9.88%, the directivity is about 10.3 dBi, the antenna gain is about 10.25 dBi with the antenna efficiency of 99.9%. By increasing the W/L ratio the bandwidth of the antenna device, the bandwidth and gain increases minimally. The patch dimensions of $L = 9.5\text{mm}$, $W = 11.5\text{mm}$ ($W/L=1.21$) are chosen so that the antenna parameters can be compared with the micromachined aperture coupled patch antenna devices.

2.3 APPLICATIONS OF PATCH ANTENNA DEVICES

The applications of the microstrip antennas are numerous as they are light in weight and can be designed to operate over a large range of frequencies. These antenna devices can be integrated easily to form linear or planar arrays and can be used to generate linear, dual, and circular polarizations of electro-magnetic radiation. These antennas are inexpensive to fabricate using printed circuit board etching method. They are used in applications such as cellular and satellite communications, radars and GPS receivers. However, the narrow bandwidth (1-5%) of microstrip antennas restricts their application to single and narrowband frequencies [1]. An antenna is one of the largest components in the radar and millimetre wave systems, therefore reducing antenna size is increasingly important in order to make compact radar systems. Higher operation frequencies can be a solution for miniaturised light weight antenna systems. On the other hand, patch antennas have been a natural choice for integrated antennas because they are low profile, simple and low cost. Integrated antennas require good understanding of several different areas of microwave engineering (i.e. devices, antennas, circuits and component functions etc).

Table 2.2 Applications of patch antenna devices

Plat form	Systems
Aircraft	Radar, communications, navigation, altimeter, aircraft landing systems
Missiles	Radar, fusing, telemetry
Satellites	Communications, direct broadcast TV [41], remote sensing radars and radiometers [42]
Ships	Communications, radar, navigation
Land vehicles	Mobile satellite telephone, mobile radio [42]
Other	Bio-medical systems [43, 44], intruder alarms [45], cognitive Local Multipoint Distribution Service (LMDS), FWA (Fixed wireless access) [46], Wireless Personal Area Network (WPAN) [47], Millimetre wave and terahertz sensors [48], on chip communications [49] etc.

Antenna design considerations with these circuits, components and device combination effects are also important. Device biasing circuits disturb antenna radiation properties while the antenna configuration may degrade the component function characteristics. A complete RF design, simulation and integration approach is required that includes passive devices (antennas and filters etc) and active circuits (RFIC's, microcontrollers etc) for an integrated antenna system [49]. Some of the applications of microstrip antennas are summarised in Table 2.2.

2.4 SUBSTRATES FOR PATCH ANTENNA DEVICES

A substrate is a low loss rigid material that supports the radiating patch and the ground plane for a conventional patch antenna device. The rigid dielectric substrate makes the microstrip patch antennas to be distinctive to other non-conformal antenna devices like horn antennas and reflector antennas etc. The quality of a mass produced printed antenna is directly related to the substrate and connector materials.

2.4.1 Conventional substrates for microwave antenna applications

Substrate technologies and materials have been in development over the years. Plastic and alumina substrates have been extensively used in the past while the use of low loss and low permittivity substrates are more common in recent years [1, 17, 18]. Lower permittivity substrates reduce surface wave propagation effects but it is difficult to reduce the radiation from the feeding elements. Many substrate materials are available in today's market with dielectric constants in the range of 1.17-25 and that of loss tangents in the range of 0.0001-0.004. In general, the radiation efficiency of conventional microstrip patch antennas decreases with increase in substrate thickness or permittivity as a result of the losses due to surface wave propagation [37, 50-52]. The resonances (for example TM_{110}) cease to exist once the dielectric substrate thickness reaches 0.11λ and as a result the antenna radiation ceases to propagate [51, 53]. The various substrate materials that have been developed over the years are presented in Table 2.3. Apart from the dielectric constant and loss tangent, the other parameters that are critical for the substrates are dimensional stability and operating temperature range. The dimensional stability is critical for the sensitivity/reliability of the antenna device in terms of the frequency of operation since any change in dimensions is directly transformed into a change in frequency of operation for the

Table 2.3 Overview of microwave substrates (reprinted from [7] and measured at X band frequencies)

Substrate	ϵ_r (X band)	$\tan \delta$ (X band)	Dimensional stability	Temperature range in (°C)
PTFE unreinforced	2.10	0.0004	poor	-21 to +260
PTFE glass woven web	2.17	0.0009	excellent	-27 to +260
	2.33	0.0015		
	2.45	0.0018	very good	-27 to +260
	2.55	0.0022		
PTFE glass random fiber	2.17	0.0009	fair	-21 to +260
	2.35	0.0015		
PTFE quartz reinforced	2.47	0.0006	excellent	-21 to +260
Cross linked poly styrene/woven quartz	2.65	0.0005	good	-21 to +260
Cross linked poly styrene/ceramic powder-filled	3 to 15	from 0.00005 to 0.0015	fair	-27 to +110
Cross linked poly styrene/ glass reinforced	2.62	0.001	good	-21 to +110
Irradiated polyolefin	2.32	0.0005	poor	27 to +100
Irradiated polyolefin/ glass reinforced	2.42	0.001	fair	-27 to +100
Polyphenylene oxide (PPO)	2.55	0.00016	poor	-27 to +193
Silicone resin ceramic	3 to 25	from 0.0005	fair to medium	-27 to +268
Powder-filled Sapphire	9.0	0.0001	excellent	-24 to +371
Alumina ceramic	9.7 to 10.3	0.0004	excellent	to 1600
Glass bonded mica	7.5	0.0020	excellent	-27 to +593
Hexcell (laminates)	1.17 to 1.40 at 1.4 GHz	-	excellent	-27 to +260.
Air with/rexolite standoffs Fused quartz	3.78	0.001	excellent	-
FR4	4.2 at 8.4 GHz [54]	0.020 [122]		
LTCC- DuPont 943 material	7.3 at 40 GHz [55]	0.0004 [56]		

antenna device. The temperature range of operation determines the applications in which a particular substrate can be used. Comparative data on most substrates ($2.1 < \epsilon_r < 25$) are given in Table 2.3. One of the commonly used substrate for microwave applications is based on polytetrafluoroethylene (PTFE) with either glass woven web or glass random fibre because of (a) its desirable mechanical and electrical properties and (b) availability of the substrate in a wide range of sheet size and thickness. Glass fibers are available in thicknesses ranging from 0.508 mm to 3.175 mm. Due to the discontinuous nature of the fibre and relatively soft and deformable polymer matrix, this material can be coated on complex surfaces such as PTFE whereas heating the material accelerates the stress relief. Apart from sheets, this material is also available in shapes such as rods or cylinders. Alumina based ceramics ($9.7 < \epsilon_r < 10.3$) are often used for applications requiring high dielectric constants. Typical commercially available substrates are K-6098 teflon/glass cloth ($\epsilon_r \approx 2.5$), RT/duroid-5880 PTFE ($\epsilon_r \approx 2.2$), and Epsilam-10 ceramic-filled teflon ($\epsilon_r \approx 10$).

2.4.2 Polymer and ceramic composites for microwave applications

Polymers are gaining more importance, either in pure form or along with ceramic powders as substrates for RF and optoelectronic devices. For example, polymers have been used in the field of optoelectronics to produce mechanically flexible “electronic paper” [57, 58] and for high-efficiency light-emitting diodes [59]. Liquid crystal polymers (LCPs) have displayed attractive properties like low loss, low water absorption and low cost and have been proposed for system-on-package (SoP) applications [60]. The polymer ceramic composites were proposed as substrate materials for a scanning antenna by Yashchyshyn *et al* [61]. Hunt *et al* [62] have proposed the inclusion of metallic dopants within the substrate with no limitation on substrate thickness.

The most widely used silicone-based organic polymer is PDMS which is known for its unusual rheological/flow properties: It is non-flammable, water- and chemical resistant and stable at high temperature. It can be used as a substrate for patch antenna devices at microwave frequencies. BT-, BBNT-, and MCT-type powders possess a wide range of available dielectric constants among the various shades of commercial ceramic powders available namely LTCC and high-temperature co-fired ceramics (HTCC). Due to its ferroelectric properties, BT had shown to be widely employed in capacitor technology by

Popielarz *et al* [63]. It is usually mixed with polymers [64, 65] and depending upon its chemical form, grain size, environmental temperature and the added dopants, it demonstrates a wide range of attainable dielectric permittivity (from a few tens to a few thousands) values. BBNT is categorized under the LTCC group of ceramic powders and exhibits a dielectric permittivity of up to 100 [66] whereas the MCT powder is an HTCC which is commercially available in different dielectric constants ranging from 20 to 140.

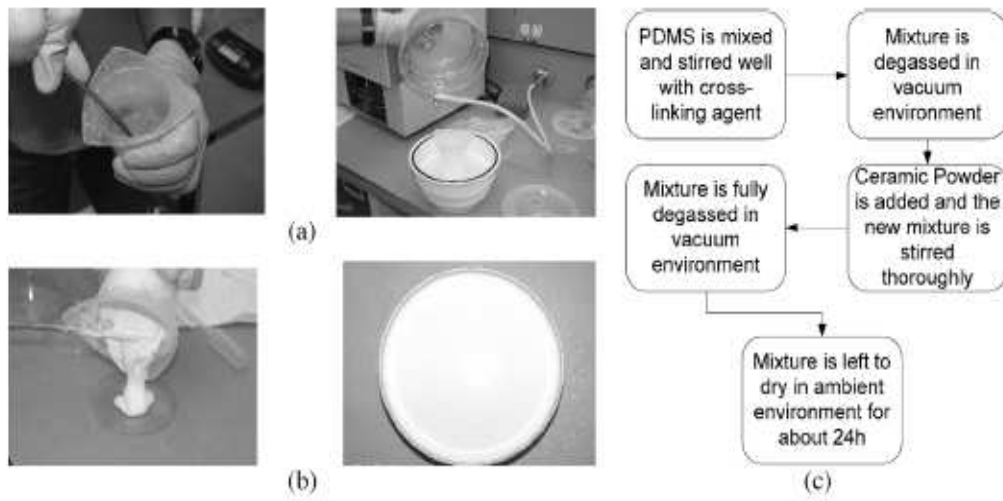


Figure 2.5 Fabrication procedure for the proposed substrate. (a) PDMS is prepared by mixing silicone gel (b) procedure for ceramic adding and (c) schematic representation of the procedure [57]

Patch antenna devices were fabricated by printing on a powder based substrate by Koulouridis *et al* [57]. Figure 2.5 shows the fabrication procedure for the proposed substrate. The rectangular patch elements were printed on a substrate with 20% BT volume and 10% MCT volume mixtures in PDMS. A 50 coaxial cable was used to feed the patches and Ansoft HFSS tool was used to carry out the simulations for comparison. As shown in Figure 2.6, the previously found dielectric constants are verified as the measured and simulated reflection coefficients for the three samples are in agreement. Figure 2.6 (a) shows the antenna gain measurements along with their corresponding simulated results for the three substrates. As expected, at bore sight, a higher BT/PDMS loss tangent results in a rather low gain of 0.5 dBi. In contrast, the gain is recovered and is near 5 dBi when the substrate is pure PDMS. Moreover high gain values of about 5dBi are achieved by MCT/PDMS substrates. A drawback of this method i.e. the low efficiency of the print

metal associated with the metal patterning on the PDMS substrate in the microwave and millimetre wave frequency regimes [67].

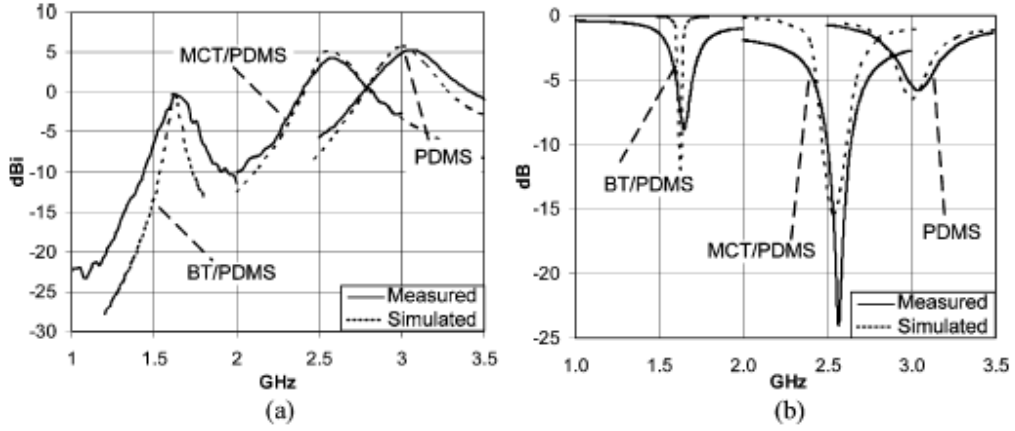


Figure 2.6 (a) Gain and (b) reflection coefficient for a $24 \text{ mm} \times 24 \text{ mm}$ patch antenna placed on a BT/PDMS substrate (20% volume ratio), a MCT/PDMS substrate (10% volume ratio) and a pure PDMS substrate [57]

2.4.3 Liquid crystal polymer based antenna devices for SOP applications

Organic materials such as Duroid [68, 69] and FR-4 [70] have been explored in the past for SOP (System on a package) applications. These materials are inexpensive and have low loss up to 10 GHz. Liquid crystal polymer (LCP) is a unique material for SOP applications. It is a low-cost, flexible material with low dielectric loss to well over 100 GHz [71]. It can be fabricated in large panels or on long rolls. Moreover, reliable RF MEMS circuits can be fabricated directly on the material. A 14 GHz phased array antenna for use in a NASA earth observing satellite system packaged using system-on-package technology and LCP has been demonstrated for the first time by Kingsley *et al* [68].

The fully-integrated array consists of a MMIC LNA, a MEMS phase shifter, a RF power distribution network, biasing circuits, and an antenna array [68]. The antenna geometry was designed using equations based on the design of the conventional patch antenna devices. The dielectric constant for the 100 μm thick LCP material used in the package is 2.95. The simulated directivity for the single patch antenna device on this package was 6.94 dB and it was 12.49 dB for the 2×2 antenna array.

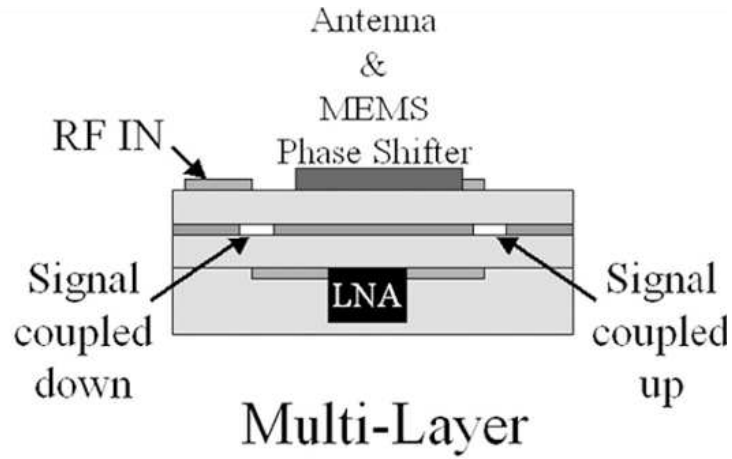


Figure 2.7 Multilayer implementations of the antenna arrays in LCP[68]

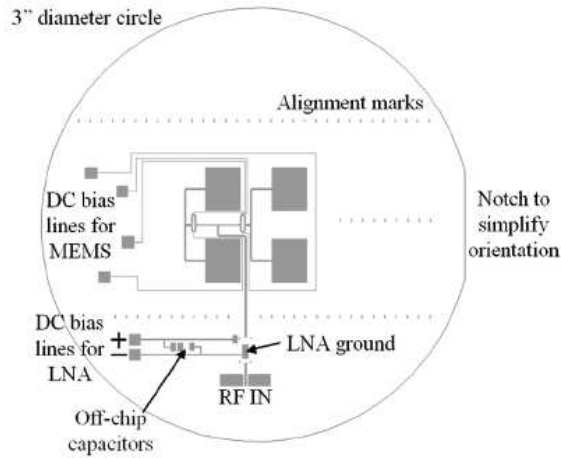


Figure 2.8 Layout of single-layer antenna array. The 2×2 patch antenna array, MEMS phase shifters, bias lines, and LNA pads are shown [68]

2.5 MICROMACHINED PATCH ANTENNAS

Microwave and millimetre wave design solutions with large density layouts require integration of individual devices, circuitry, and radiating elements that offer light weight, small size, and optimum performance. Compact circuit designs are typically achieved in high-index materials, which is in direct contrast to the low-index substrates imposed by antenna performance requirements [4]. Although one can directly fabricate microstrip, coplanar circuits and antennas on high resistivity silicon and MMIC (Monolithic microwave integrated circuits) substrates, the RF losses is high. A system of high-low dielectric constant layers have been proposed in the past to increase the efficiency and

bandwidth of the patch antenna elements [6]. A radiating patch antenna occupies a major portion of the surface area for a modern communication device or a sensor device. The high dielectric constant of these substrates, leads to the possibility of excitation of surface waves and degrading the radiation efficiency of the patch antenna devices. These problems can be overcome by introducing a small air gap between the microstrip line, radiating patch element and the ground plane. The air gap can be easily created using a bulk micromachining technique [72]. In addition, micromachining is also a viable method for fabricating resonators, waveguides, filters etc at millimetre wave frequencies [73-75].

Patch antenna based systems have major operational disadvantages at microwave and millimetre wave regions of the electromagnetic spectrum such as narrow bandwidth and low gain due to their inherent low efficiency. Compact size and high performance can be achieved at these frequencies by integrating a patch antenna on a low dielectric constant material substrate with the remaining circuitry on the high dielectric constant substrates within the same package. As the micromachining technology is being developed, it has been applied to antenna elements to improve the overall system performance. The use of selective lateral etching based on micromachining techniques to enhance the performance of rectangular microstrip patch antennas printed on high-index silicon, GaAs, and InP based substrate wafers have been developed in the past decade. Other techniques such as ultra thick photoresist micromachining and spin-on low dielectric constant photoresists have been proposed for millimetre wave antennas. All of these approaches have achieved high gain and efficiency performances compared to the conventional printed patch antennas on a high dielectric constant substrate. The various micromachining methods for patch antenna devices from the available literature can be categorised as follows:

- Silicon micromachining
- Polymer micromachining
- Millimetre wave antennas using low K Spin-on dielectric substrates
- Integrated chip-size antennas using Laser micromachining:
- LTCC Micromachining

These micromachined methods are outlined in the rest of the chapter. This PhD thesis was aimed at developing low cost micromachining processes for producing air suspended patch

antenna devices. The chapter emphasizes improvement in the antenna bandwidth, gain and efficiency performance for the antenna devices fabricated using these methods. An overview of the available micromachining methods and techniques will enable to compare these methods with the performances achieved by the micromachining method developed.

2.5.1 Silicon micromachining

In order to integrate patch antennas into the circuit designs on high index substrates without substantial loss of the advantages, the radiating elements should be housed in the low-index regions of the substrates that possess low index of refraction. This is achieved by utilising micromachining of a portion of the substrate material. The silicon material was removed laterally underneath the patch antenna to produce a cavity that consists of a mixture of air and substrate with equal or unequal thicknesses has been implemented in [4, 76-78]. In the following section, the silicon micromachined devices are described based on the patch antenna feeding techniques.

2.5.1.1 Microstrip edge feed

One particular silicon micromachined antenna device as presented by Thompson *et al* [4] consists of a rectangular patch centred over an air filled cavity, with the patch elements sized according to the effective index of the cavity region and is fed by a microstrip line. Figure 2.9 shows the test fixture and geometry of the micromachined patch antenna with mixed air-substrate region that is laterally etched. To produce the mixed substrate region (air cavity), silicon micromachining was used to laterally remove the material from underneath the specified cavity region resulting in two separate dielectric regions of air and silicon. The amount of silicon removed varies from 50 to 80% of the original substrate thickness underneath the patch. The walls of the hollow cavity were in general slanted due to the anisotropic nature of the chemical etching. A traditional modelling technique such as a cavity model can estimate the reduced dielectric index value. The resultant antenna has shown superior performance over conventional designs where the bandwidth and the efficiency have increased by as much as 64% and 28% respectively.

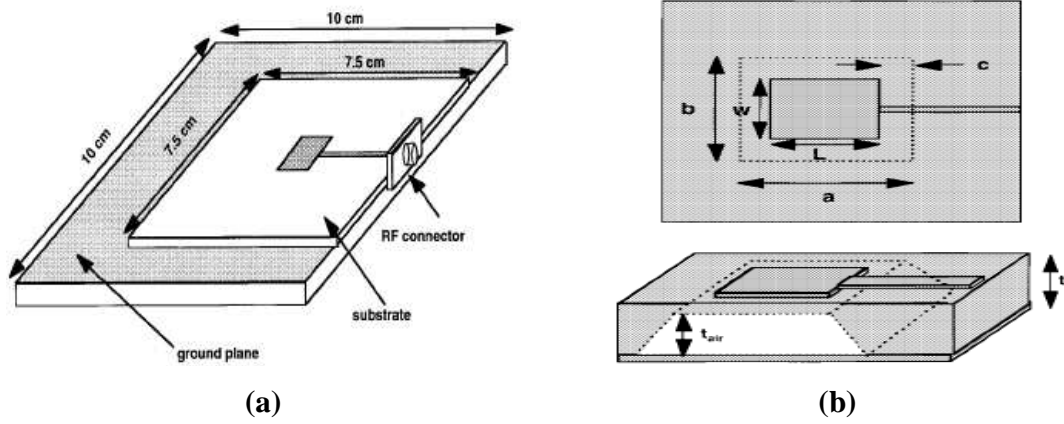


Figure 2.9(a) Test fixture of the silicon micromachined antenna device (b) Geometry of the micromachined patch antenna with mixed air-substrate region that is laterally etched [4].

2.5.1.2 CPW feed

A CPW feeding technique in principle eliminates the need for thicker substrates at microwave and millimetre wave frequencies. This feeding technique also simplifies the photoresist based micromachining processes. Abdel-Aziz *et al* have presented a 26.6 GHz patch antenna using MEMS technology [79]. A patch is suspended over a thin dielectric layer (membrane), which is deposited on a high index silicon substrate. In addition, the silicon substrate is fully etched under the patch, creating an air cavity region of very low dielectric constant ($\epsilon_r = 1$).

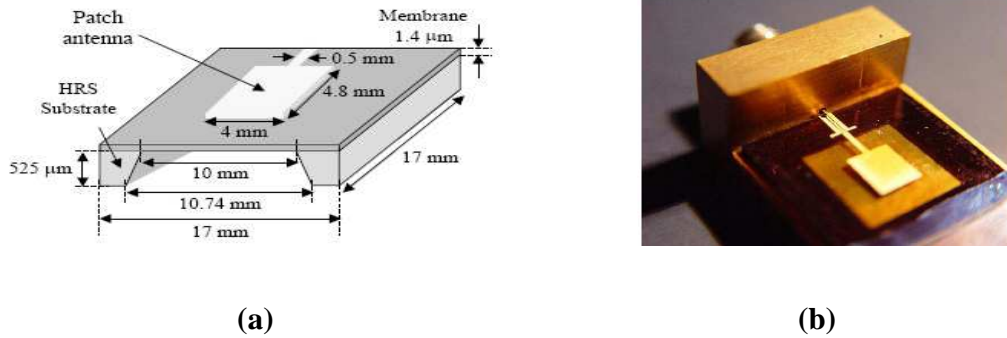


Figure 2.10 (a) Patch antenna suspended over membrane (b) Photograph of the fabricated patch antenna [79]

The antenna is directly fed using a microstrip line while a CPW-microstrip transition was used for probe measurements of the antenna reflection coefficient. The design was performed using the 3D electromagnetic simulator HFSS. The measured antenna reflection coefficient was -17dB at 26.6 GHz, and the bandwidth was 4.5%. The antenna had a

radiation efficiency of 61.7% and directivity of 7.9 dBi. The measured antenna cross-polarization level was less than -20 dB in both the E- and H-planes [79].

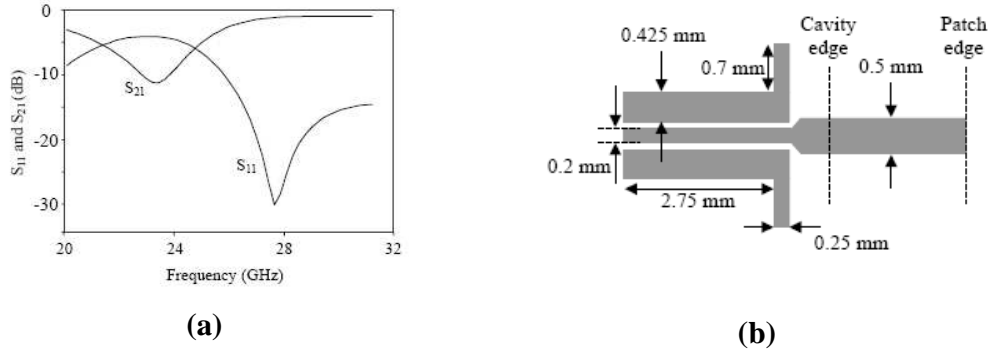


Figure 2.11 (a) Insertion loss and reflection coefficient for a silicon micromachined antenna device (b) CPW-microstrip transition [79]

2.5.1.3 Aperture coupled feed

Silicon micromachining has also been employed for aperture coupled patch antenna configuration at millimetre wave frequencies. An aperture-coupled micromachined microstrip antenna at an operation frequency of 94 GHz was studied by Gauthier *et al* [80]. The design consists of two stacked silicon substrates. The top substrate which carries the microstrip antenna was micromachined to improve the radiation performance of the antenna whereas the bottom substrate was used as a carrier for the microstrip feed line and the coupling slot. The cross-section view along with the dimensions of the silicon wafers are shown in Figure 2.12.

For an antenna built on a 100 μm thick silicon wafer, reflection coefficient was measured to be about -35 dB at 92.5 GHz with a -10 dB bandwidth of 4%. A reflection coefficient of < -18 dB at 94 GHz with a -10 dB bandwidth of 10%, were obtained for the micromachined microstrip antenna respectively.

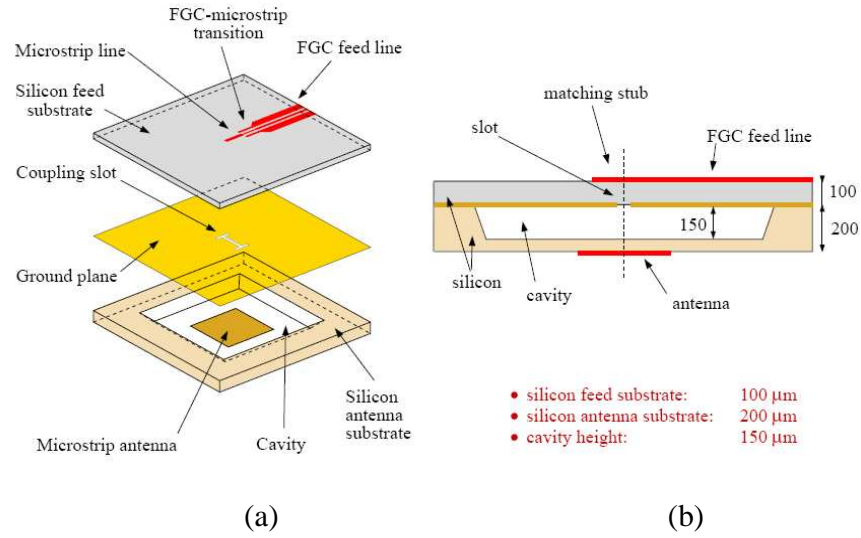


Figure 2.12 (a) Top view and (b) cross sectional view of the aperture-coupled micromachined microstrip antenna with all dimensions in microns [80]

A 2.5% frequency shift was observed between the measured and simulated response, which could be attributed to minute variations in the silicon wafer thickness and the general inaccuracies of numerical packages in high-Q structures at millimetre-wave frequencies. A maximum efficiency of 58.5% was measured and the radiation patterns show a measured front to back ratio of -10 dB at 94 GHz. Due to the integration of small 50 μm silicon beams between the antennas, the measured mutual couplings were below -20 dB in both E and H plane directions.

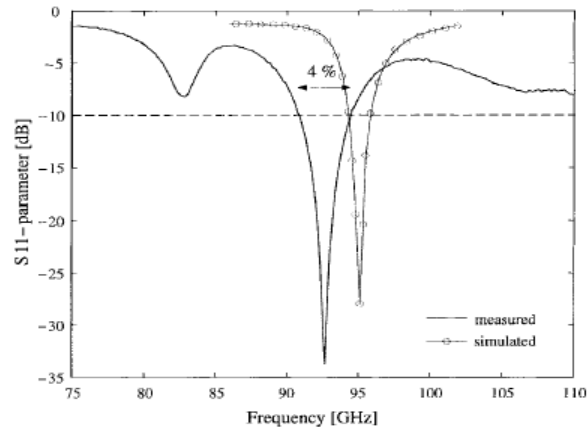


Figure 2.13 Measured and simulated input impedance of the microstrip antenna on a full 100 μm thick silicon substrate [80]

2.5.2 Polymer micromachining

A photoresist based micromachining method can be employed to fabricate an air suspended patch antenna by either using metallic supporting posts or polymer posts. Antenna structures at different frequency bands require different air cavity thicknesses to achieve optimum antenna performance and better impedance matching. Photoresist based polymers such as SU8 and THB151N can be used to obtain ultra-thick supporting posts and can also be used as moulds for fabricating ultra-thick electroplated metal posts. One such polymer micromachining method has been reported by Ryo-Ji *et al* [81]. Other polymer micromachined processes are described below.

2.5.2.1 CPW fed THB151N based post supported patch antenna

A CPW-fed post supported patch antenna array at 60 GHz that is fully compatible with commercial CMOS process has been fabricated by Hyung Suk Lee *et al* [82]. The antenna device is supported in air and thus shows broadband characteristics.

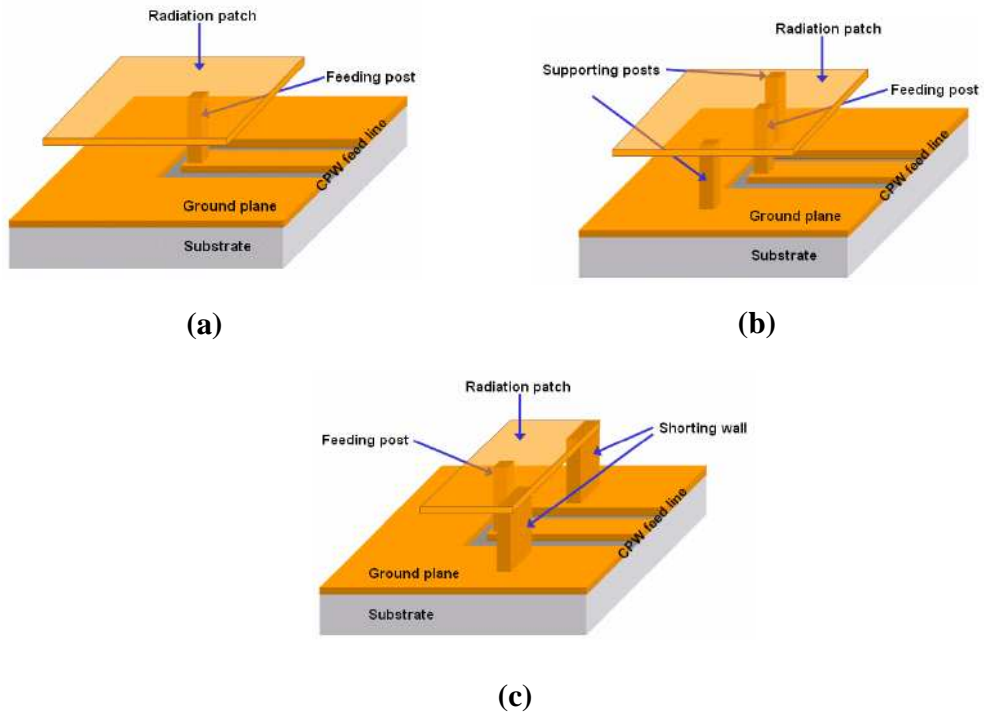


Figure 2.14 Proposed CPW-fed post-supported MEMS antenna devices for (a) Single post structure. (b) Additional supporting posts structure. (c) Half size structure with shorting wall [82]

In addition, a 2×1 patch array antenna without $\lambda/4$ impedance transformer (a $\lambda/4$ transmission line) was designed with a simple feeding network. The structure of the proposed antenna is shown in Figure 2.14. The antenna device consists of a CPW feed line, a feeding post, two supporting posts and a radiating patch. Better performance is observed by the CPW feed line than the microstrip line at millimetre wave frequency. Due to the placement of ground planes in the vicinity of the signal line, the electromagnetic field can be guided more efficiently. While maintaining the same characteristic impedance, adjustments can be made to the width of the CPW signal line and the gap between the signal line and the ground. The CPW feed line is on the substrate with a high dielectric constant, whereas the radiating patch is suspended in air. Therefore the radiating patch and the feed line can be optimised separately. The patch is supported with two metal posts which are located at the virtual ground of the patch (the centre of E-plane); the electrical performance of the antennas is not affected by the additional supporting posts. A simple feed line network design can be used, when it is designed as a patch antenna array.

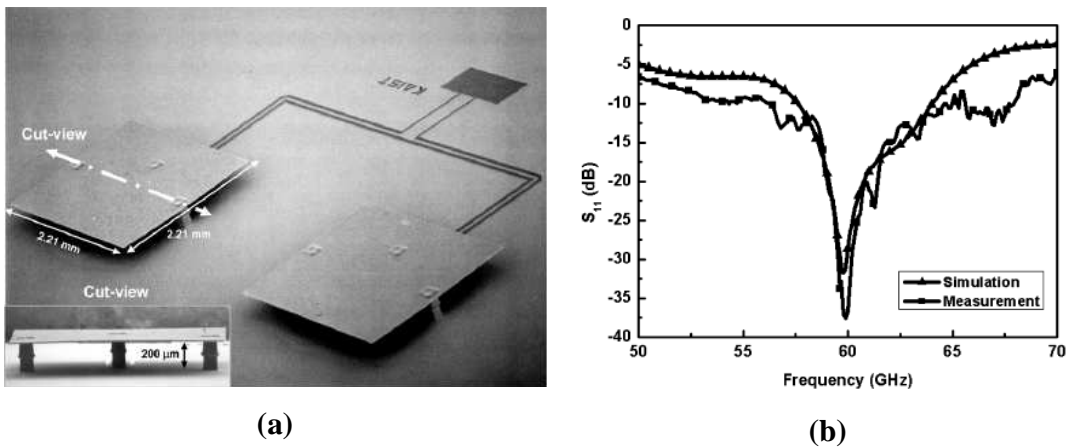


Figure 2.15 (a) Fabricated 2×1 patch antenna array (b) Measured input reflection coefficient of 2×1 patch antenna array [82]

The antenna device was fabricated on the glass substrate of Corning 7740 with a thickness of 800 μm and a dielectric constant of 4.6. Copper was used for metallisation. The feed line of the antenna was fabricated using a thick film photoresist (AZ9260) and in order to form the posts of the antenna using THB151N photoresist, a two-step coating process was performed. The simulated antenna gain and radiation efficiency were obtained from 5.6 dBi to 9.0 dBi and from 92.8% to 97.4% for single patch antennas, respectively. In the case of a 2×1 patch antenna array, the simulated antenna gain and the radiation efficiency were from 5.8 dBi to 11.2 dBi and from 93.6% to 95.3% respectively. The suspension of the

patch in air increases the bandwidth as the effective dielectric constant of the space between the patch and the ground plane decreases thus decreasing the Q factor of the device and thereby increasing the bandwidth. The relationships between the Q factor, the relative permittivity, the bandwidth and efficiency for a conventional rectangular patch antenna device are outlined in Section 2.2.

2.5.2.2 Negative photoresist based microstrip fed patch antenna

A combination of substrate micromachining and SU8 photoresist based micromachining has been proposed by Pan *et al* [83]. In order to elevate the feeding lines and the antennas, multiple wells with stepped depths are fabricated into the wafer. A positive photoresist NR 9000 has also been used. To maximize the radiation, the microstrip fed patch antenna is required to be air-lifted by several hundred microns. However, a 50Ω microstrip line will be several millimetres wide when it is being elevated into air by the same height. This width is comparable with the size of the patch antenna in Ka-band, thus the parasitic radiation generated from the feeding microstrip cannot be ignored.

To reduce the radiation, microstrip feeding lines were put into the shallow wells while the patch antennas used deeper wells to enhance radiation in order to obtain optimal performances. Since the feeding network and the antenna array were at the same level of height, only polymer posts were needed for this integration scheme. This in turn has reduced the fabrication complexity significantly. The fabrication steps are shown in Figure 2.16. Full wave simulation predicts a -10 dB bandwidth of 7%. A nearly constant broadside radiation pattern has been demonstrated, with a directivity 10.4 dBi at the centre frequency and low side/back lobes (< -20 dB).

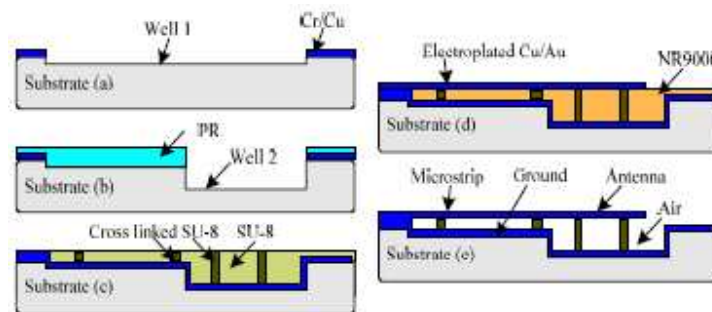


Figure 2.16 Fabrication steps of the multi-depth well integration scheme [83]

2.5.2.3 Ultra thick SU8 based post supported antenna

Pan *et al* have presented for the first time an air-lifted patch antenna by means of surface micromachining technology [84]. SU8, a relatively new negative tone photoresist, was used to fabricate an elevated patch antenna with micromachined posts of around 800 μm in height. In order to provide mechanical support as well as electrical feeding (metal posts), both of the metal and polymer posts were used.

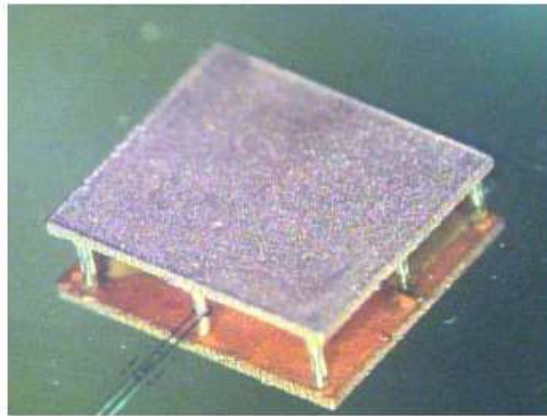


Figure 2.17 Photo of fabricated elevated patch antenna, along with its mirror image on the ground [84]

The fabricated prototype is shown in Figure 2.17. A 7% -10 dB bandwidth, centered at 25 GHz was observed. In terms of bandwidth, efficiency and lower side lobe, the proposed structure is superior to the conventional patch. In case of the traditional patch antenna directly printed on substrate, it usually provides a 3 - 5% bandwidth and about 70%-80% radiation efficiency, whereas in case of the proposed elevated patch, the fractional bandwidth is doubled and as a result of eliminating the substrate loss, gives a theoretical 97% radiation efficiency [84, 85].

2.5.2.4 SU8 based MEMS monopole antenna

A W-band micromachined monopole vertically mounted on a variety of substrates, was also reported by Pan *et al* [86]. A 2-D to 3-D conversion based feeding scheme was also proposed and optimised. A chromium coated soda-lime glass (Telic Co.) was used as the substrate. The chromium film was patterned for the monopole column definition using a standard photolithography. A SU8 epoxy film (800 μm) was coated on the substrate to define the monopole height. Deposition of titanium and copper using a DC sputterer was

performed to produce a conformal seed layer. A thin (5 μm) SU8 film was spin-coated on the substrate and patterned to define the signal path as well as ground pads using a proximity photolithography due to the uneven surface. A gold layer of up to 2 μm of thickness was electrodeposited through the bottom mould as well as column surface. The thin SU8 film, the seed layer and the bottom chromium layer were removed sequentially to complete the fabrication process. Both the simulation and measurement results demonstrate the broadband nature of this kind of antenna structure. Reflection coefficient of -16 dB and -50 dB were measured for two monopoles resonating at 85 GHz and 77.5 GHz respectively. . The difference in the simulation and the measurement results in Figure 2.18 (c) is attributed to fabrication tolerance in the monopole height. Upper-band loss shown is caused by fabrication variance, or more specifically due to the defective conductive path (metal thickness, also electrical connection between monopole and CPW center line) on that sample [86].

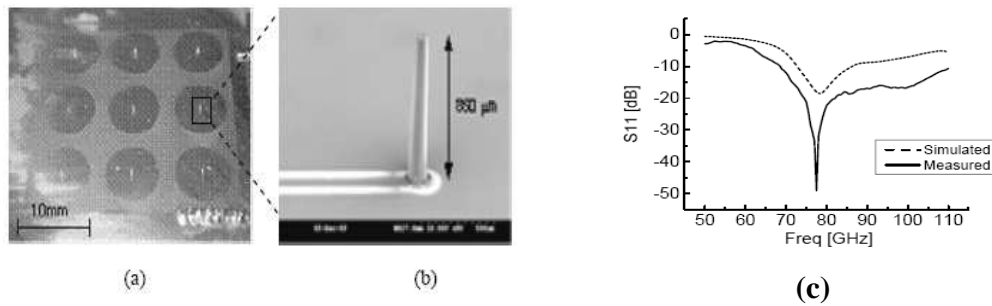


Figure 2.18 (a) A photomicrograph of 3×3 monopole array (b) An SEM image of a single monopole antenna. (c) Measured and simulated S_{11} plots for monopole antenna for a height of 880 μm [86]

2.5.2.5 SU8 based horn antenna devices

A V-band SU8 micromachined horn antenna device has been reported by Bo Pan *et. al* [87]. Murad *et. al* have presented a SU8 based micromachined horn antenna device that is fed by a V band waveguide [88].

2.5.2.6 Polymer based reconfigurable antenna devices

The polymer based fabrication technology has been also extended to the patch antenna arrays and reconfigurable antennas. A surface micromachined, fully integrated planar 4×4 phased array antenna operating at 36 GHz has been demonstrated by Lukic *et al* [89, 90]. The array element is a cavity backed patch fed by a rectangular coaxial probe and

supported by two metallic posts. The array element is an all copper, recta-coax fed, air-cavity backed patch and is built using a sequential micro-fabrication technique, the PolyStrata™ process. The complete structure was built from ten layers having an overall height of about 760 μm above the silicon. The impedance bandwidth of the individual elements is about 5.1% at around 36 GHz. The simulated results with a finite element method (FEM) based software Ansoft HFSS™ and a finite integration technique (FIT) based software CST Microwave Studio™ show that the element radiation patterns are symmetric in both E- and H- planes, each having efficiency above 95% and a gain of 6.8 dBi with ultra-low cross-polarization levels. The higher efficiency is attributed to the air cavity backed patch configuration.

A novel air suspended integrated antenna with frequency reconfigurability for compact integration with active devices has been presented by Cho *et al* [91]. The floating patch on an HRS (high resistive substrate) substrate gives wideband and high efficiency characteristics for antennas. An HRS wafer with $\epsilon_r = 11.2$ and $g_2 = 300 \mu\text{m}$ is used to build up the MEMS antennas. The parameters, g_1 , t , and l as shown in Figure 2.19 are set to be 300 μm , 10 μm , and 0.29 mm respectively. The MEMS antenna was designed for the BWA (Broadband Wireless Access) of IEEE 802.16 at 42 GHz initially.

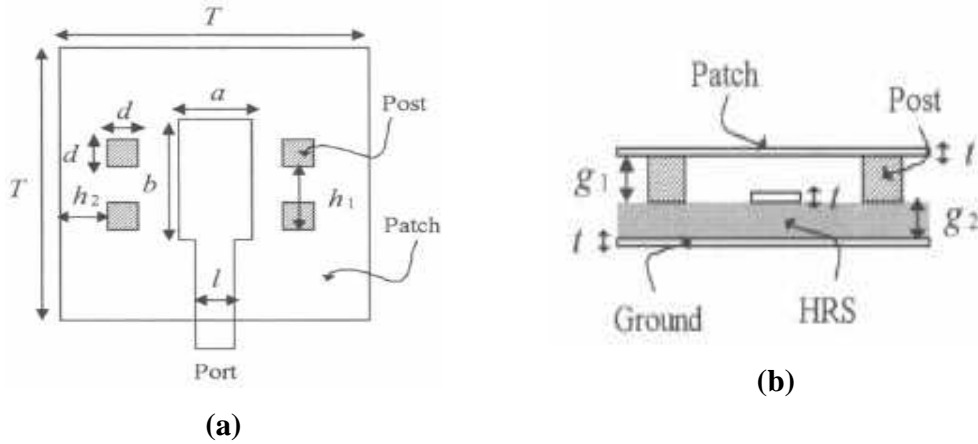


Figure 2.19 (a) Top view of original MEMS antenna (b) Side view of MEMS antenna [91]

The design shown in Figure 2.19 (a) is modified by moving a metallic post close to the radiating edge of the patch as shown in Figure 2.20 (a) in order to achieve frequency agility. Here, h_1 denotes the gap between the metallic posts and h_2 denotes the spacing between the metallic posts and the non radiating edge of the patch as shown in Figure 2.20

(a). To verify the designs, the floating-patch MEMS antenna devices are fabricated using the surface micromachining and the thick photoresist (THB-15INT) lithography process. The bandwidth is almost 6 GHz (40 to 46 GHz). The measured antenna gain and the 3 dB beam width are 12 dBi and 30° at 42 GHz, respectively while the simulated antenna gain is 13.2 dBi. The increase in strip length, h_1 , results in a decrease in the resonant frequency. This is due to the increase in capacitive loading at a radiation edge. The frequency shifting characteristics have been proposed and can be implemented for a reconfigurable antenna with the RF MEMS switch.

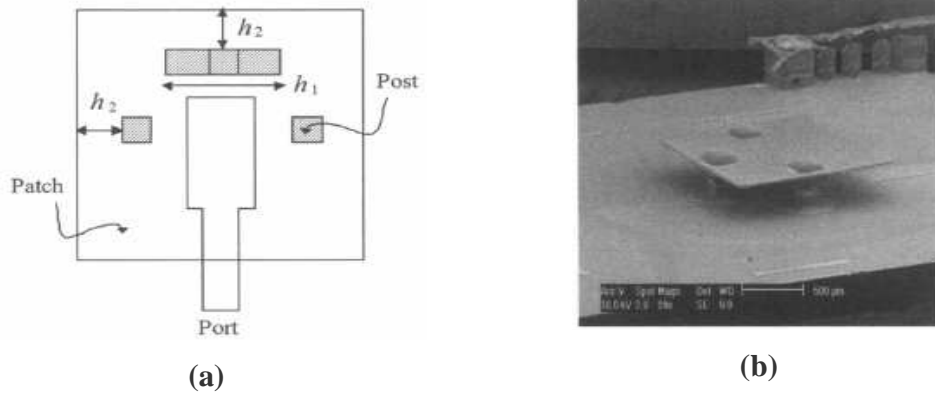


Figure 2.20 (a) Top view of frequency agile MEMS antenna (b) A fabricated geometry of MEMS antenna [91]

2.5.3 Millimetre wave antennas using low K Spin-on dielectric substrates

Low K spin-on dielectric substrates are efficient for guiding EM fields at microwave and millimetre wave frequencies [92] and have been used to fabricate microwave filters to reduce insertion loss on silicon substrates [93].

These antenna devices that use low-k dielectric substrates have a wider impedance bandwidth and a higher gain than those using ceramic dielectric substrates. K.F. Tong *et al* have presented the simulation and measurement results for the millimetre-wave coplanar patch antennas (CPA) using spin-on low-k dielectric substrate [94]. The geometry of a typical CPA is shown in Figure 2.21. The antenna device consists of a gold ground plane at the bottom, two layers of BCB dielectric material ($\epsilon_r = 2.7$ $\tan \delta = 0.002$ at 20GHz) in the middle and a CPA pattern on the top. The total thickness of the BCB layers is 30 μm . BCB is spun onto a silicon wafer with a 3-inch ground plane. The deposition technique is similar to the commonly used photoresist coating technique and the metal CPA pattern was

deposited onto the BCB dielectric layer. The thickness of the ground plane and the CPA pattern are both about 1.5 μm .

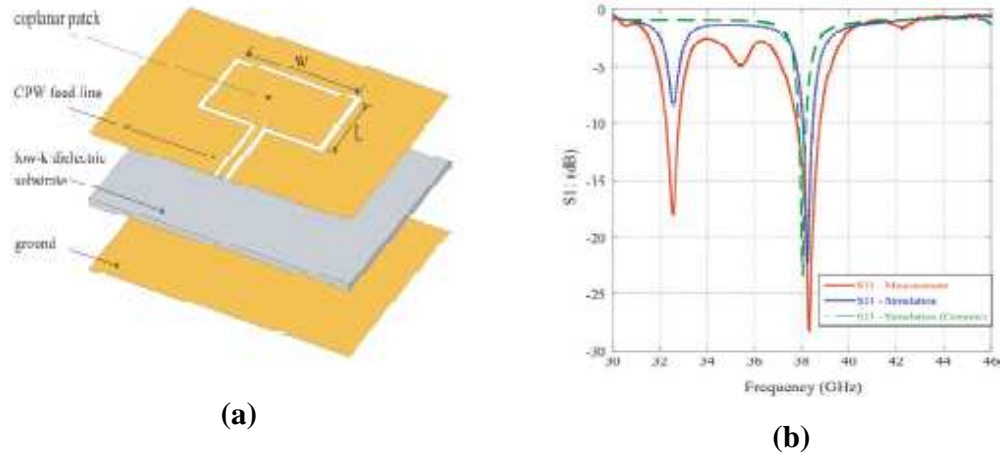


Figure 2.21 (a) Geometry of millimetre wave CPA using low-k dielectric substrate (b) Reflection coefficient of mm wave CPA with the low-k dielectric substrate [94]. The red and blue curves show the measured and simulated results while the green curve shows the comparison (simulated results) with a ceramic substrate ($\epsilon_r = 9.8$)

The simulated and measured impedance bandwidths are about 1.2% and 2.6% respectively. The measured resonant frequency of the antenna is 38.3 GHz. The difference in the measured and simulated results can be attributed to the fabrication errors of the BCB layers.

2.5.4 Synthesised low dielectric-constant substrates

A synthesised low dielectric constant substrate method has been presented by Gauthier *et al.* Closely spaced holes were micromachined underneath a microstrip antenna on a high dielectric-constant substrate so as to obtain a synthesised, localised low dielectric-constant environment ($\epsilon_r = 2.3$) [95]. The holes were drilled using a numerically controlled machine (NCM) underneath the microstrip antenna and the hole pattern was extended at least 3.5 mm beyond the edge of the antenna in all directions.

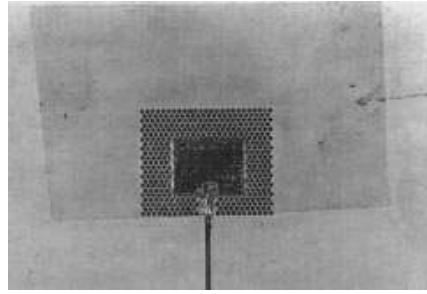


Figure 2.22 Fabricated microstrip antenna on a localized low dielectric substrate [95]

The substrate was Duroid 6010 material with a thickness of 1.25 mm. The measured radiation efficiency of a microstrip antenna on a micromachined Duroid 6010 substrate ($\epsilon_r = 10.8$) increased from 48.3% to 73.3% over the 12.8 to 13.0 GHz of frequency region.

2.5.5 Laser micromachining

2.5.5.1 Patch antenna devices on micromachined glass substrates

Integrated antennas fabricated by laser micromachining techniques on glass substrates are compact due to the reduced size and owing to the relatively higher dielectric constant. P. M. Mendes *et al* and others have reported on-chip integrated, folded short-patch antenna as shown in Figure 2.23 [96]. The antenna device consists of three horizontal metal sheets that are electrically connected by two vertical metal walls. Since it is embedded in a glass substrate having certain electrical permittivity and dielectric losses, the antenna geometry, design and its actual dimensions determine its radiation characteristics and overall performance.

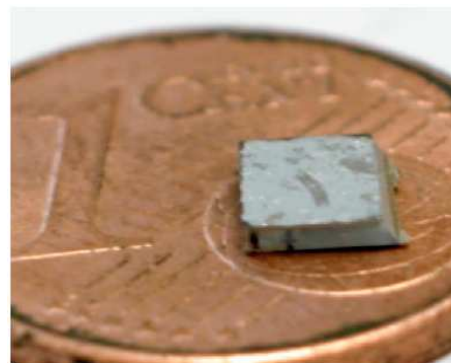
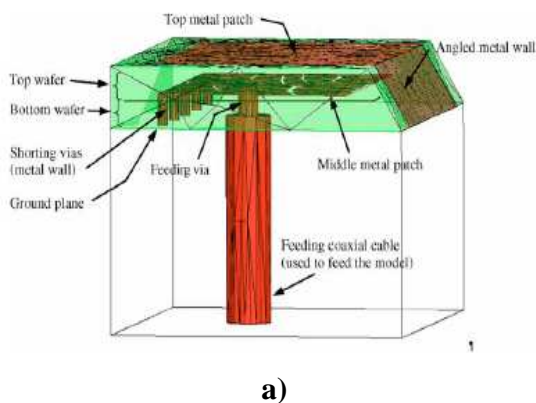


Figure 2.23 (a) HFSS model of the folded shorted-patch antenna used for electrical analysis (b) Photograph of the antenna prototype [96]

For better performance, the metal sheets should have a minimum resistivity and the dielectric should be a low-loss material in order to achieve high efficiency. High antenna efficiency requires thicker substrates ($>300\text{ }\mu\text{m}$) and therefore high aspect ratio vias in glass are required. At frequencies above 1 GHz, glass becomes a very attractive option. Its main advantages are low losses, reasonable ϵ_r and availability in a form of wafers with any required dimensions at low cost. There is also sufficient experience in processing of glass wafers for MEMS and WLP (wafer level packaging) applications. The antenna was designed to operate at 5.1 GHz, a frequency chosen to be inside the 5–6 GHz ISM band. The fabricated antenna has dimensions of $4\times4\times1\text{ mm}$, a measured operating frequency of 5.05 GHz with a bandwidth of 200 MHz and a simulated radiation efficiency of 60%. The simulated reflection coefficient of the FSPA (Folded short patch antenna) for different substrate thickness values is shown in Figure 2.24.

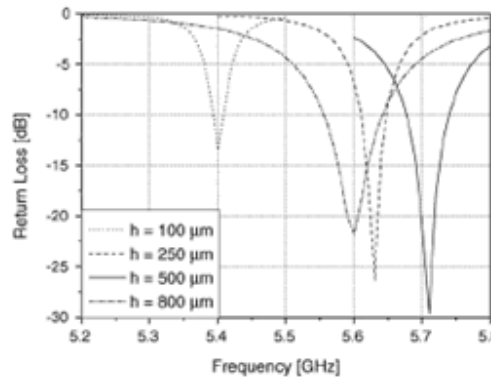


Figure 2.24 Simulated reflection coefficient of the FSPA (Folded short patch antenna) for different substrate thickness values [96]

2.5.5.2 Sacrificial substrate based meander monopole antenna

The idea of applying laser micromachining technologies to fabricate a compact, high performance and low-cost 3D monopole antenna was proposed by C. U. Huang *et al* [97]. The coplanar waveguide fed configuration was used owing to its simple structure, wide bandwidth, and the ability of multi-band operation. To reduce the size, the meander monopole antenna was fabricated on both sides of a Pyrex 7740 glass wafer, and the metal lines were connected through via holes as shown in Figure 2.25. The via holes were micromachined using an ArF excimer laser micromachining technique. The entire antenna was constructed with electroplated copper to lower its total resistance and hence to enhance its performance. The computed and measured input reflection coefficient S_{11} of the

fabricated MEMS monopole antenna is illustrated in Figure 2.26(a). The resonant frequency and bandwidth are 2.4 GHz and 190 MHz (7.9%). The radiation characteristics of this monopole antenna system at 2.45 GHz for the three plane cuts (x-z, y-z and x-y) are shown in Figure 2.26(b). A maximum gain of 3.4 dBi was obtained for the antenna.

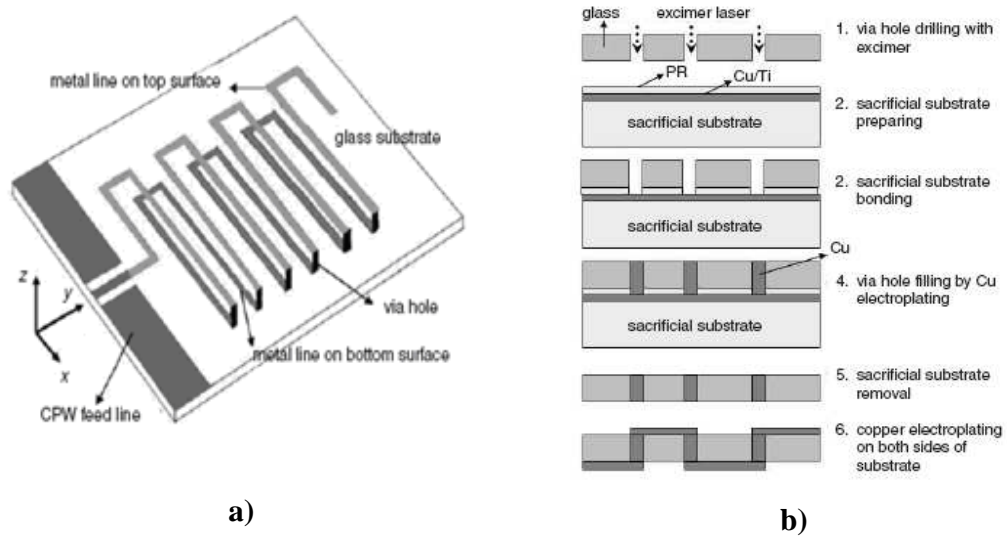


Figure 2.25 (a) 3D MEMS monopole antenna top view (not scaled), (b) Process flow for 3D MEMS helical meander antenna [97]

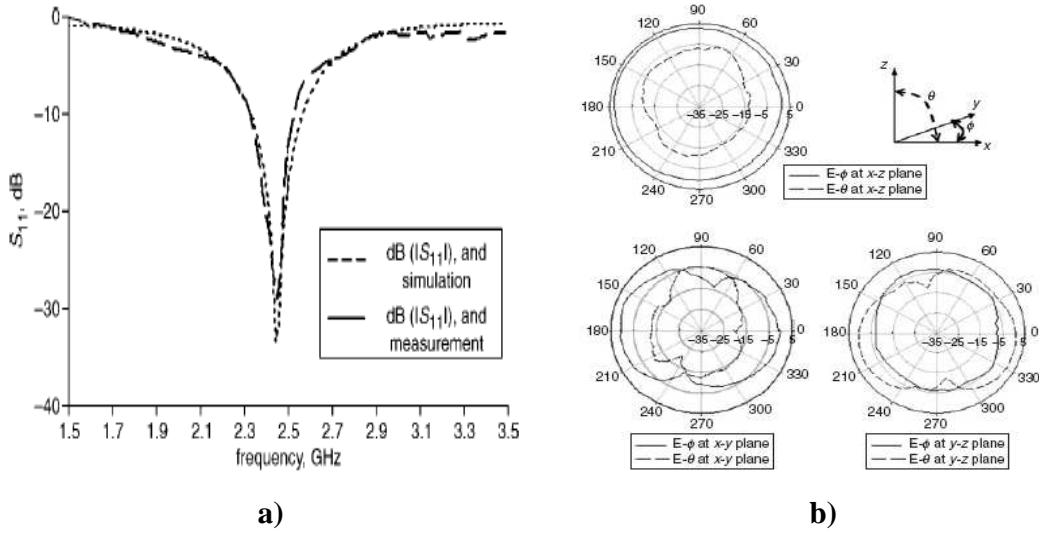


Figure 2.26 (a) Measured and simulated reflection coefficient for proposed antenna (b) Measured radiation patterns for the proposed meander monopole antenna [97]

2.5.6 LTCC micromachining

LTCC multilayer technology can be used to build RF front end modules, antenna based sensors and antenna arrays. The technology provides the necessary degree of vertical integration for the high-density microwave circuit and a packaging solution such as SIP (System in Package) [55, 56, 98-101]. LTCC is based on a ceramic substrate system with printed gold, copper and silver conductors or alloys with platinum or palladium onto ceramic layers stacked and fired to obtain a package. The metallisation pastes are screen printed layer by layer on the un-fired or “green” ceramic foil, followed by stacking and lamination under pressure. The multilayer ceramic stack then is fired (sintered) in the final manufacturing step. The temperature of sintering is below 900°C. This relative low temperature enables the co-firing of gold and silver conductors.

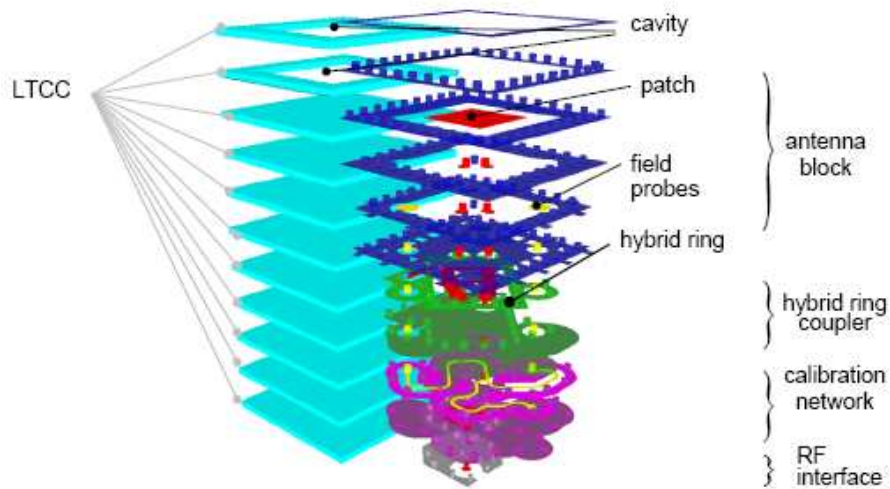


Figure 2.27 Exploded view of the 11 layer antenna structure in LTCC technology [55]

It is essential to have a low loss material with good microwave performance for LTCC multilayer packages. Low permittivity ceramic layers are certainly an advantage for microwave antennas [91]. Figure 2.27 shows a complete architecture of such an antenna element. The structure consists of eleven layers of FERRO A6 LTCC substrates. The system consists of four different functional blocks namely, (a) the antenna block (first 6 layers from the top), (b) the hybrid ring coupler block with 2 layers, (c) the calibration network (2 layers) and finally (d) the RF-to-antenna interface (1 layer). The high relative permittivity of LTCC of about 7.7 is a disadvantage of this material in antenna design. It supports the propagation of substrate modes and suppresses radiation from a travelling wave antenna because the electromagnetic field remains concentrated in the substrate.

Moreover the resulting miniaturisation due to high permittivity requires an additional effort in circuit realisation.

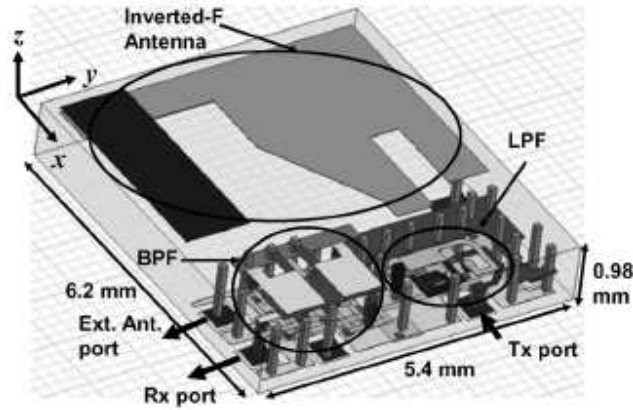


Figure 2.28 3-D layout of the antenna switch module in LTCC for SIP based antenna front-end [100].

To optimise the material properties and thus to reduce the relative permittivity of LTCC, a material modulation based on punched air holes into the substrate is performed. Thereby, the relative permittivity of the material is replaced by the relative permittivity of the modulated material [102]. Other schemes such as cavity backing have been employed in the fabrication process to obtain suspended antennas to improve efficiency [103]. Figure 2.28 shows an antenna front end module in an LTCC SIP package. Figure 2.29 shows an LTCC packaged patch antenna that is air suspended and with integrated chips embedded in the air cavity.

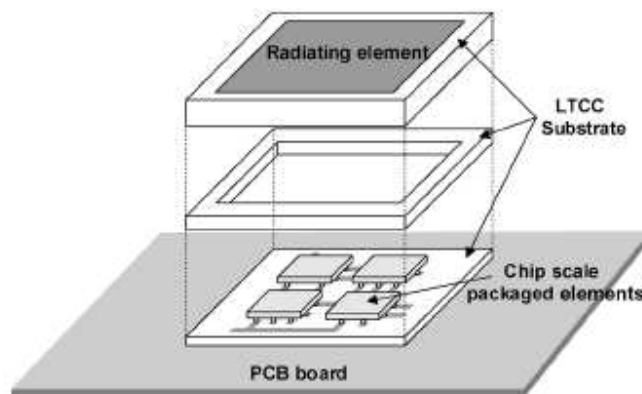


Figure 2.29 Design architecture for the package level integration of an LTCC based antenna [56]

2.6 SUMMARY

Patch antennas have been a common choice for integrated antennas in a communication system. They are low profile, simple, and inexpensive. Various feeding methods exist for the microstrip patch antenna devices. The buried line feed and aperture coupled feed methods can be employed for increasing the bandwidths of the antenna device but usually give rise to a high back-radiation level. However this is only true for aperture coupling if the aperture is near resonance. The patch antenna devices have found various applications at microwave and millimeter wave frequency regimes. Various substrate materials have been developed for the microwave and millimeter wave patch antenna applications. These substrates are engineered for low relative dielectric constant values for improving the bandwidths, minimizing the possibility of excitation of surface waves thus improving radiation efficiency of the patch antenna devices. The substrate materials are also engineered for low loss tangent values for improving the antenna radiation efficiencies. Another way of obtaining the above two desirable characteristics for the patch antenna devices is by micromachining of the substrate materials. Micromachining is particularly important in the MMIC (for active components) based integrated RF communication systems. Micromachining is also a viable method for fabricating resonators, waveguides, filters etc at millimetre wave frequencies and beyond. Although one can directly fabricate microstrip, coplanar circuits and antennas on high resistivity silicon, MMIC (Monolithic microwave integrated circuits) substrates, the substrate losses will be high. These problems can be overcome by introducing a small air gap between the microstrip line, radiating patch element and the ground plane. Silicon micromachining technique where in the silicon material is removed underneath the patch antenna was developed recently. This method is used to produce a cavity that consists of a mixture of air and substrate with equal or unequal thicknesses. Owing to the complicated silicon etching techniques, photoresist based micromachining methods were developed to fabricate suspended patch antenna devices either by supporting metallic posts or polymer posts. Low relative dielectric constant substrates had also been synthesized in the past by using low dielectric constant dielectric substrates by spin coating. Methods such as laser micromachining is employed for reducing the high relative permittivity of LTCC or by a material modulation based on punched air holes into the substrate.

All of the micromachining techniques outlined above involve significant processing of the substrates and may lack repeatability in performance. In the work described in this thesis, a novel fabrication technique based on photoresist based micromachining has been successfully developed for fabricating suspended aperture coupled patch antenna devices. The antenna element is usually fabricated on a separate substrate and integrated with the rest of the RFIC transceiver chip. The new developed technique requires minimal integration of RFIC chip with the antenna substrate. Highly efficient micromachined aperture coupled patch antenna devices have been demonstrated by this method.

CHAPTER 3 DESIGN AND MODELLING OF APERTURE COUPLED PATCH ANTENNA DEVICES

3.1 INTRODUCTION

Electromagnetic analysis techniques for micromachined aperture coupled patch antenna devices are presented in this chapter. The detailed studies in the design and simulation of the micromachined antenna devices are described. The RF simulated results are presented for the different micromachined aperture coupled antenna devices and compared. Particular attention is given to the reflection coefficient (S_{11}), radiation pattern, gain, directivity and efficiency for each of the micromachined aperture coupled patch antenna devices. The effect of the substrate materials and the dimensions of the SU8 polymer rims on the performance of the basic microstrip and CPW fed aperture coupled micromachined antenna devices are discussed.

3.2 MODELLING TECHNIQUES FOR PATCH ANTENNA DEVICES

Analytical and numerical modelling techniques for a wide variety of microstrip antennas have been developed over the years as reviewed in [1, 7, 104]. The CAD (Computer Aided Design) models that can deal with any arbitrary planar shapes but need homogeneous dielectric in the third axis are called 2D CAD models. The CAD models that can handle any arbitrary planar shapes and can accommodate dielectric inhomogeneities are called 3D CAD models. A 2.5D CAD models exist that can accommodate inhomogeneous dielectrics but only if the layers are stacked. Certain microstrip antenna geometries are relatively difficult to model due to the presence of dielectric inhomogeneities and a wide variety of feeding techniques and other geometrical features. A good antenna model or theory can calculate all of the necessary electrical parameters of the antenna device such as impedance, reflection coefficient (S_{11}), radiation pattern, gain, directivity etc with enough accuracy in a computationally efficient and user-friendly manner. Certain CAD models such as FEM based models can treat dynamic variations in the antenna geometry and can optimise a

particular performance variable such as impedance or gain against one or more design parameters.

A simple microstrip element consists of few parameters and the CAD models can simulate the radiation pattern, gain or bandwidth of the microstrip antenna devices accurately. Complex designs requires design optimisation and some of these designs include proximity coupled elements, stacked patches and aperture coupled patches and elements designed for circular polarization. The aperture coupled patch antenna geometry has a large number of design variables that involve at least two substrate layers, their thicknesses, dielectric constant variation, the patch dimensions, the feed line dimensions and offset. The presence of these design variables complicates the optimisation of an aperture coupled antenna device. Thus, modelling of the aperture coupled antenna device requires a full-wave solution. On the other hand, the analytical analysis of microstrip antennas and arrays is difficult due to different design parameters and different complex geometries involved and as a result many solutions and analysis methods have been proposed but most models can be divided into two groups: simplified (or reduced) analysis and full wave methods.

3.2.1 Full-wave analysis

Full wave methods can model the patch geometry and the dielectric substrate simultaneously for the microstrip antenna devices. Full wave analysis methods include (a) moment method solutions that use Green's functions for the dielectric substrates, (b) solutions based on the finite difference time domain (FDTD) approach and (c) the finite element (FE) method. These full wave models are highly accurate and have the ability to calculate all of the electrical parameters for any complex antenna geometries. The complexity includes multilayer configurations, arrays with feed networks and different element coupling configurations. The computational cost for these full wave analysis methods is generally high but high level of agreement is obtained between the experimental and simulated results. The advent of computationally faster computers with ever increasing computational power, memory and accuracy has made the use of these models widespread.

The moment method solutions were widely implemented before the year 2000 [104]. The solutions are in general specific to antenna geometries. The solutions assume the substrate to be of infinite extent and model the currents or fields on the patch elements and feed networks with the sub-sectional basis functions. These models are time consuming due to

numerical integrations of Sommerfield type integrals, in either spectral domain or space domain to form solutions when compared with the reduced analysis approach. The FDTD and FE methods are more rigorous approaches by modelling the entire antenna, including dielectric and metal components and the surrounding volume in terms of the radiation boundary. These methods allow a high degree of accuracy to be obtained when modelling arbitrary geometries, including multilayer and in homogeneous dielectrics. The drawbacks for these methods are the computational time involved that is even longer than the moment method for a comparable geometry. However, adaptive mesh refinement techniques have been developed that uses tangential vector finite elements for reduced computational time and increased accuracy for the FE methods [105].

3.2.2 Reduced analysis

Reduced analysis models generally possess one or more significant approximations to simplify the simulation. The most widely used reduced models are (a) cavity models that use a magnetic wall boundary approximation for the radiating edge of the patch element, (b) transmission line models that model the element as a transmission line equivalent lumped circuit elements at the radiating edges, and (c) multiport network models which are the generalised cavity models. Though initially all the above models were developed for microstrip antennas, later they were very useful in areas of practical design as well as for providing a good understanding of the operation of the microstrip patch antennas. These models are generally inaccurate for thick substrates and cannot handle certain parameters like mutual coupling, feed network effects, surface wave effects and multilayer substrate configurations [104]. Some of the reduced analysis models for microstrip fed aperture coupled antenna devices were introduced by El Yazidi *et al* and Himidi [106-109].

3.3 THEORETICAL ANALYSIS OF APERTURE COUPLED PATCH ANTENNA DEVICES

3.3.1 Coupling mechanism

A schematic cross-sectional diagram of the aperture coupled microstrip antenna configuration is shown in Figure 3.1 [19]. It consists of a radiating patch on a substrate is coupled to a microstrip line feed on another parallel substrate through an aperture in the ground plane which separates the two substrates. An aperture coupled microstrip antenna

can be used for linear and circular polarizations. Two uncoupled apertures can be excited separately by a different feed line providing a separate linear polarization of the emitted electromagnetic wave. In this manner dual linear polarizations or circular polarization arrays can be designed. In probe-fed patch elements and at a very good approximation in microstrip line fed ones, the natural frequency of the patch coincides with the resonant frequency of the whole structure. However this is not the case in aperture coupled patches. The input impedance of the patch as seen by the feeding line consists of two electromagnetically coupled equivalent circuits for the patch and the aperture.

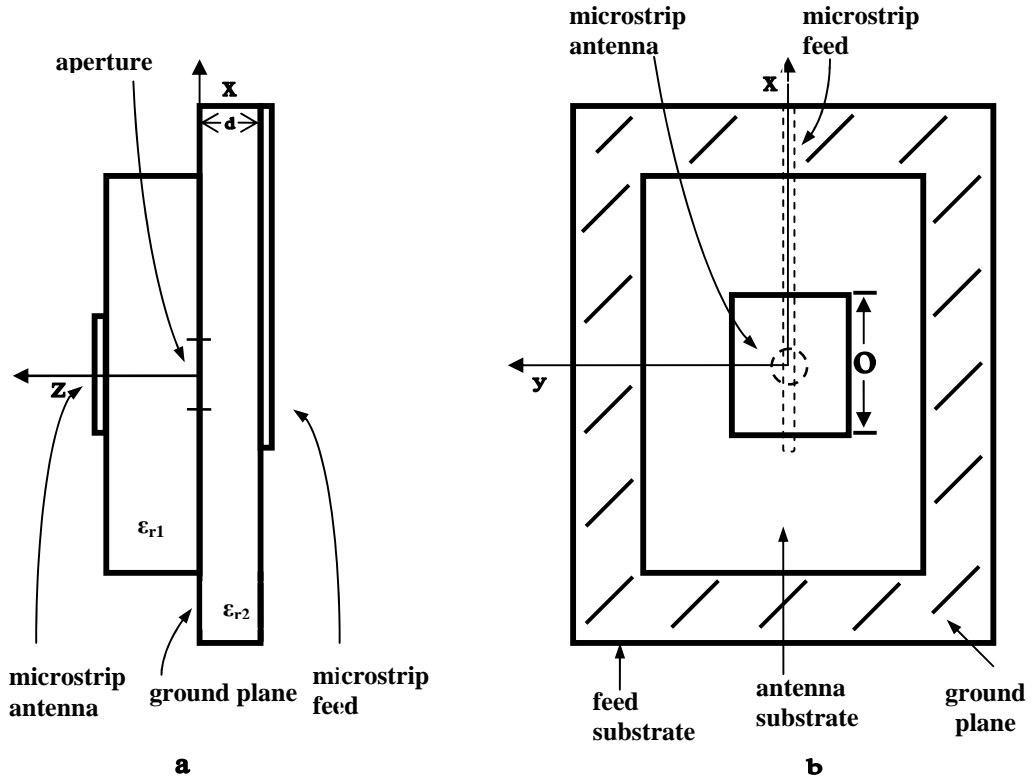


Figure 3.1 Side view (a) and top view (b) of a rectangular microstrip antenna aperture coupled to a microstripline [19]

Pozar *et al* has modelled the structure through a combination of small-hole coupling theory and the cavity method (reduced analyses) for patch antennas [19]. It was based on a simplified theory of the coupling of the microstrip antenna through an aperture to the microstrip line. The objective was to deduce the appropriate coupling mechanism and the aperture position for efficient coupling. It was considered that the patch is resonating in its dominant TM_{100} mode. To a good approximation, the fields inside the cavity formed by the patch and the magnetic walls around the periphery of the patch can be expressed as

$$E_z(x) = \frac{k_0^2}{j\omega\epsilon_o} \cos \frac{\pi x}{a} \quad (3.1)$$

$$H_y(x) = \frac{\pi}{a} \sin \frac{\pi x}{a} \quad (3.2)$$

where a is the resonant dimension of the antenna (along x-axis), and $k_0 = 2\pi / \lambda_0$. If the aperture is located at $(x_0, y_0, 0)$, polarisation currents are excited in the aperture according to

$$P_z = \epsilon_0 \epsilon_{r1} \alpha_e E_z(x_0) \quad (3.3)$$

$$M_y = -\alpha_m H_y(x_0) \quad (3.4)$$

where α_e and α_m are the electric and magnetic polarisabilities of the aperture respectively.

For a small circular aperture of radius r_0 , α_e and α_m are given by

$$\alpha_e = -\frac{2}{3} r_0^3 \quad (3.5)$$

$$\alpha_m = \frac{4}{3} r_0^3 \quad (3.6)$$

By moving the aperture along the x-axis, the dominant coupling mechanism can be shifted from a pure electric dipole, to a combination of electric and magnetic dipoles, or to a pure magnetic dipole coupling effect. If an aperture to microstrip line coupling for an infinitely long microstrip feed line of width W is assumed, the fields under this feed line to first order, can be approximated as

$$E_z = e^{-jk_0 x_0} \quad (3.7)$$

$$H_y = \frac{d}{WZ_c} e^{-jk_0 x_0} \quad \text{for } |y| < W/2 \quad (3.8)$$

Where k_0 is the effective propagation constant of the line, d is the feed line substrate thickness and Z_c is the line's characteristic impedance. The coupling coefficients between the cavity fields and the feed line can then be calculated as

$$C_P = \frac{2r_0^3 \epsilon_r k_0^2}{3P_{10}} \cos \frac{\pi x_0}{a} \quad (3.9)$$

$$C_M = \frac{-4jk_0 Z_0 r_0^3 \frac{\pi d}{aW}}{3P_{10} Z_c} \sin \frac{\pi x_0}{a} \quad (3.10)$$

where C_P and C_M denote the coupling factors via electric dipole and magnetic dipole coupling, respectively, are $Z_0 = 377 \Omega$ and P_{10} is a normalisation constant representing the total power flow in the microstrip line.

When the approximation $a = \lambda_o / 2\sqrt{\epsilon_e}$ is used (where ϵ_e is the effective dielectric constant of the antenna substrate), equations (3.9) and (3.10) show that, for $\epsilon_r = 2.55$ and $Z_c = 50 \Omega$ and $d/W = 0.34$, the coupling due to the magnetic dipole is about three times greater than the electric dipole coupling. Thus if the magnetic dipole coupling mechanism is the preferred one, then the aperture should be located at $x_0 = a/2$ to maximize this effect.

$$C_P^{\max} = A \quad (3.11)$$

$$C_M^{\max} = \frac{2jZ_0 d \sqrt{\epsilon_e}}{\epsilon_r Z_c W} A \quad (3.12)$$

Calculations for elliptical apertures show that, for long and thin elliptical apertures of the same area as a circular aperture, the coupling can be in the order of ten times greater than the circular aperture coupling. It has been concluded that a thin rectangular slot (oriented with its long dimension along y) is the optimum aperture shape.

3.3.2 Input impedance

3.3.2.1 Network model

The effective input impedance (frequency dependent) for a patch antenna device gives the bandwidth and reflection (S_{11}) characteristics. The input impedance for an aperture coupled antenna device is derived through network analysis technique [110]. The simplified equivalent circuit model for an aperture coupled antenna device based on the above technique is shown in Figure 3.2 [111, 112]. The turn ratios n_1 and n_2 are found from [112] by deducing the scattering coefficients. This is done by approximating an induced electric field across the aperture and then determining the magnetic vector from it.

The aperture admittances can be found by a transmission line technique [113]. The radiation resistance and fringing field effects are approximated by appropriate admittances from [114] and adding them to the equivalent microstrip line admittances for patch obtained from [113] to give the patch admittances.

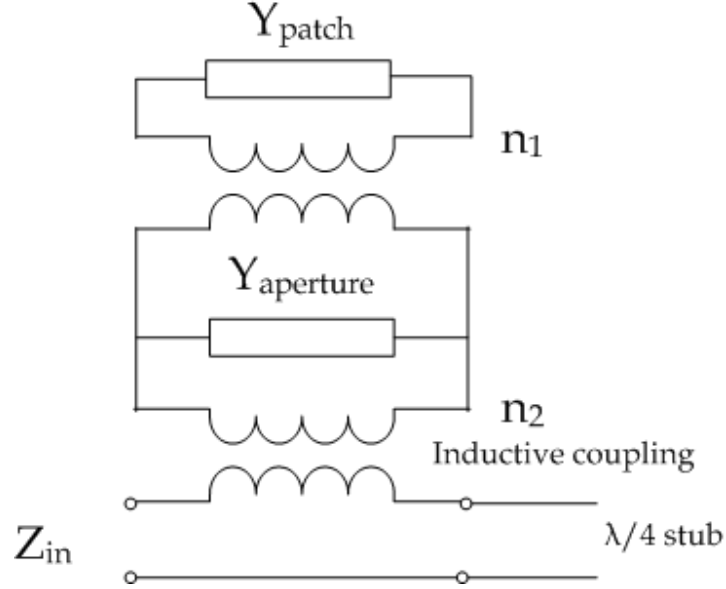


Figure 3.2 Equivalent circuit model for an aperture coupled antenna device [111, 112]

The draw back of the above technique is the need for accurate approximation of the electric field along the aperture to determine the turn ratios and the ability to predict the input impedance response of the antenna device due to other types of resonator couplings such as the patch coupling in a stacked aperture coupled antenna device.

3.3.2.2 Cavity model

In order to obtain the input impedance for the aperture coupled antenna device, a cavity based model has been developed by Himidi *et. al* [107]. The structure has been described and analysed based on the moment method. The main objective was to obtain a physical model of the phenomenon. In this context only dominant thin cavity was considered in a first approximation, therefore it is sufficient enough to consider the TM_{100} mode.

The first step is to consider the microstrip antenna as a cavity bounded by four perfect magnetic walls and two electric walls at $z = 0$ and t as shown in Figure 3.3. A magnetic current source M located in the aperture is determined using the principle of equivalence: $M = 2E^a \times \bar{z}$. E^a is the aperture electric field and is expressed by

$$E_a = \frac{V_0}{W_a} \frac{\sin k_a (L_a / 2 - |y - y_0|)}{\sin(k_a L_a / 2)} \bar{x} \quad (3.13)$$

$$x_0 - w_a / 2 \leq x \leq x_0 + w_a / 2, y_0 - L_a / 2 \leq y \leq y_0 + L_a / 2 \quad (3.14)$$

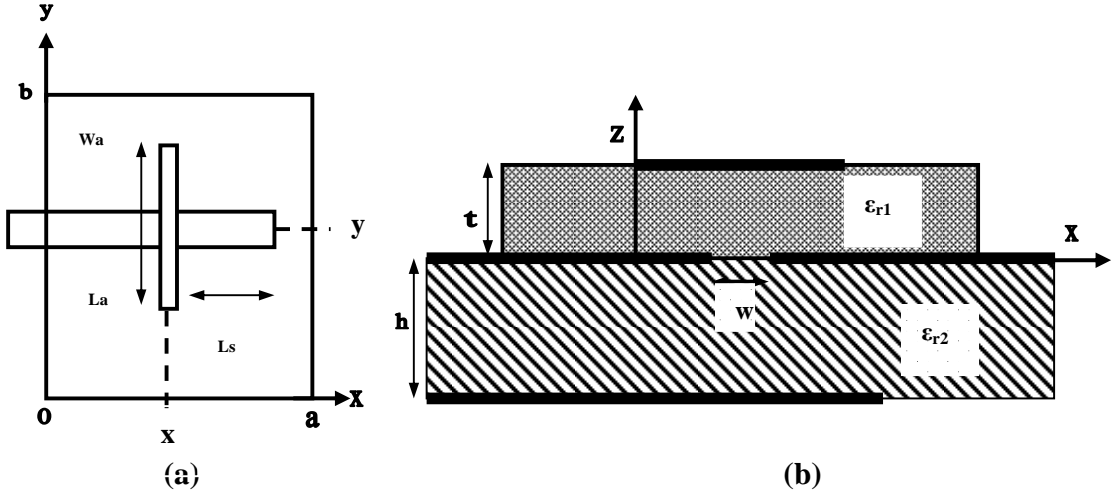


Figure 3.3 (a) Top view of the aperture coupled antenna along with dimensions, (b) Side view of the antenna structure redrawn from [19]

To obtain the z -component of the electric field into the overall volume cavity, the magnetic current source is assumed to be uniformly distributed in the volume above the slot. The other electric field components near the slot are considered by evaluation of the reactive power of the slotline. The equivalent magnetic current density can be written as

$$J_m = \frac{2V_0}{tW_a} \frac{\sin k_a (L_a / 2 - |y - y_0|)}{\sin(k_a L_a / 2)} \bar{y} \quad (3.15)$$

where $k_a = j \frac{2\pi}{\lambda} \sqrt{\frac{\epsilon_{r1} + \epsilon_{r2} - 2}{2}}$ is the propagation constant and V_0 is the modal voltage above the aperture parallel to the x axis

$$x_0 - w_a / 2 \leq x \leq x_0 + w_a / 2, y_0 - L_a / 2 \leq y \leq y_0 + L_a / 2 \quad 0 \leq z \leq t \quad (3.16)$$

Simple expressions for E_i and H_i can be obtained for the dominant mode TM where E_i and H_i represent electromagnetic fields in the cavity and are solutions of the propagation equation with perfect magnetic walls,

$$E_i = A \cos\left(\frac{\pi x}{a}\right) \bar{z} \quad (3.17)$$

$$H_i = B \sin\left(\frac{\pi x}{a}\right) \bar{y} \quad (3.18)$$

where A and B are given by

$$A = \frac{8\pi V_0}{k^2 - (\pi/a)^2} \sin\left(\frac{\pi x_0}{ba^2}\right) \frac{\sin(\pi w_a/2a)}{tk_a \sin(k_a L_a/2)} \times [1 - \cos(k_a L_a/2)] \quad (3.19)$$

$$B = j\left(\frac{a}{\pi}\right) \omega \epsilon_{r1} \epsilon_0 A \quad (3.20)$$

The second step deals with the radiation of the magnetic current source $H(x, y) = t E_i(x, y) \times \bar{z}$ at the edges of the cavity. This source is allowed to radiate into space given by (P_{rad}) while the losses in the copper (P_{cu}) and the dielectric (P_{cu}) can be computed by integrating the fields inside the cavity. Similarly the radiation losses and the electric (W_{elec}) , magnetic (W_{elec}) stored power can be calculated. Now $\delta_{eff} = 1/Q$ where Q is the quality factor is given by

$$\delta_{eff} = \frac{1}{Q} = \frac{P_{rad} + P_{cu} + P_d}{2\omega W_{elec}} \quad (3.20)$$

Now replacing k in equation (3.19) by K_{eff} where $K_{eff} = K_0 \sqrt{[\epsilon_{r1}(1 - \delta_{eff})]}$, where k_0 is the free space wave number. The admittance of the antenna at the aperture is given by

$$Y_{ant} = [P_{rad} + P_{cu} + P_d + 2j\omega(W_{elec} - W_{mag})] \times |V_0|^{-2} \quad (3.21)$$

The susceptance component due to the stored energy of the local field near the slot can be simply obtained from the two short-circuit slot lines (with proper characteristic impedance Z_{ca} and wave number K_a by

$$Y_{ap} = -\frac{2j}{Z_{ca}} \cot(k_a \frac{L_a}{2}) \quad (3.22)$$

The total admittance at the aperture is given by $Y_{at} = Y_{ap} + Y_{ant}$

The input impedance seen at the input of the transmission line is given by

$$Z_{in} = Z_l - Z_{ca} \cot(k_l L_s) \quad (3.23)$$

$$\text{where } Z_l = Y_l = \frac{Y_{at}}{\Delta V^2} \quad (3.24)$$

$$\text{and } \Delta V = \int_{slot} E_a \times H_l \cdot ds \quad (3.25)$$

where H_l is the normalized magnetic field for a microstrip line, L_s is the length of the open-circuited stub and k_l is the wave number of the microstrip line.

Sophisticated input impedance models like the transmission-line model and the cavity model (implemented using the Eigen function expansion method) are outlined in the above Sections for the aperture coupled antenna devices. These models are useful for illustration of principle of operation of aperture based antennas. However, these models are based on the same thin-substrate approximation as the circuit model (presented in Section 2.2) and improvement in accuracy is questionable and in practice not widely used in design and modelling of the antenna devices. For thicker substrates and for complex feed coupling mechanisms for a patch antenna device, a full-wave simulator like Ansoft HFSSTM is recommended for maximum accuracy. In order, to obtain some design criteria to judge the performance of the micromachined aperture coupled antenna devices, the CAD formulas presented in Section 2.2 are used for determining the initial resonant frequency, bandwidth and gain.

3.4 DESIGN METHODOLOGY

The simulation technique used in the thesis work is based on 3D full wave analysis of electromagnetic fields using Ansoft HFSSTM [105, 115] based on the finite element method for solving Maxwell's electromagnetic equations. The analysis is performed in the driven mode and the results for impedance, admittance, efficiency, gain and polarisation graphs as a function of frequency are extracted from the analysis.

For a Driven Solution, Ansoft HFSS solves the following matrix equation [115]:

$$Sx + k_0^2 Tx = b \quad (3.26)$$

Where:

S and T are matrices that depend on the geometry and the mesh.

x is the electric field solution.

K_0 is the free-space wave number.

b is the value of the source defined for the problem.

To calculate the S-matrix associated with a structure, the system does the following:

- a) Divides the structure into a finite element mesh.

- b) Computes the modes on each port of the structure that are supported by a transmission line having the same cross-section as the port.
- c) Computes the full electromagnetic field pattern inside the structure, assuming that one mode is excited at a time (usually fundamental mode is assumed).
- d) Computes the generalized S-matrix from the amount of reflection and transmission that occurs.

The final result is an S-matrix that allows the magnitude of transmitted and reflected signals to be computed directly from a given set of input signals, as opposed to the input impedance (lumped element) models presented in Section 3.3.

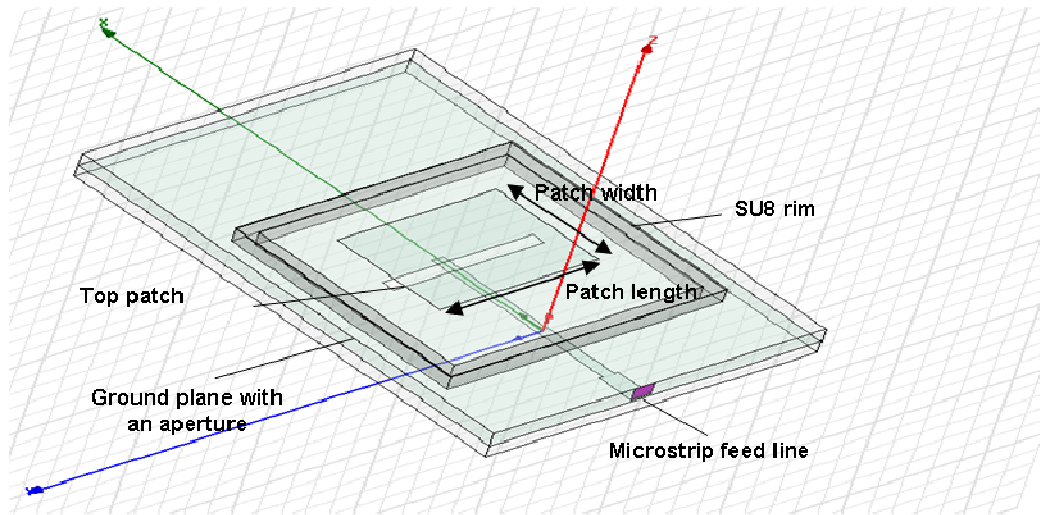


Figure 3.4 Side view of the micromachined aperture coupled antenna device modelled in Ansoft HFSS [115]

Schematic diagram of the modelled micromachined aperture coupled antenna device is shown in Figure 3.4. A schematic diagram for antenna design and simulation flow is shown in Figure 3.5. In Ansoft HFSS, the device of interest is drawn as a 3D structure using the graphical user interface and various 2D and 3D drawing objects. The material properties are assigned with the internal HFSS database. New materials are created and added to the library if necessary.

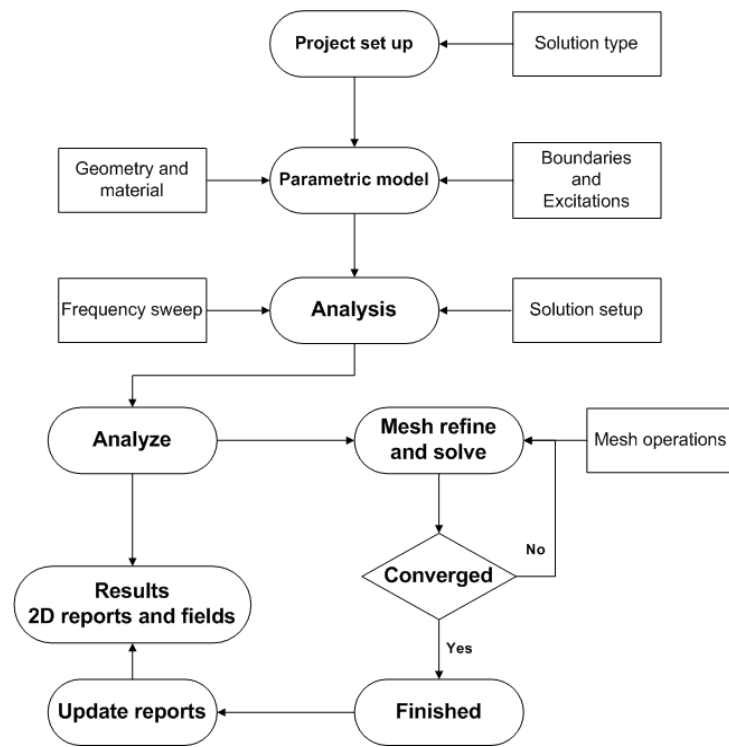


Figure 3.5 Modified Ansoft HFSS 3D model and the design flow

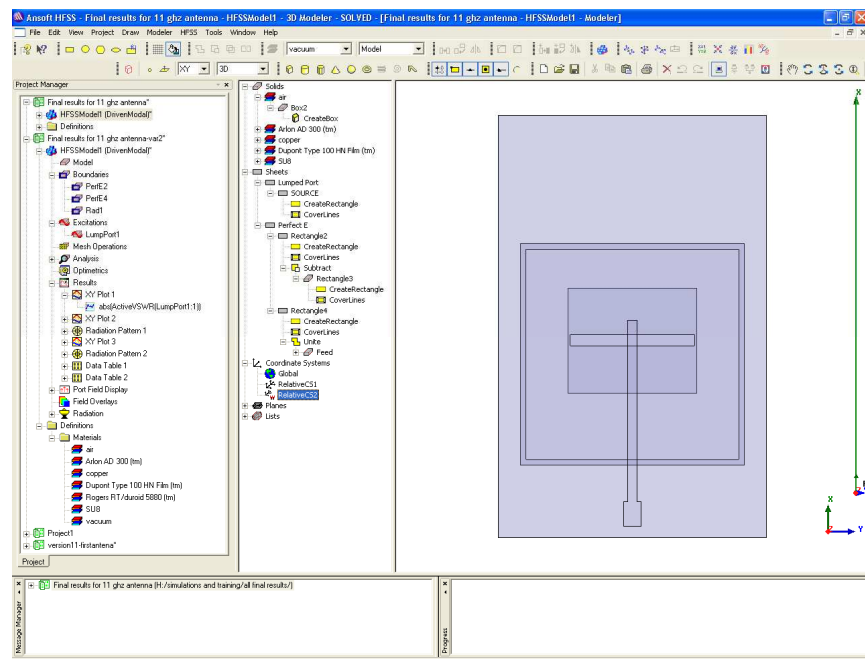


Figure 3.6 Design modeller environment in Ansoft HFSS [115] and the 3D model of the micromachined aperture coupled antenna device

The boundary conditions for the 2D metallic structures and radiation boundaries are assigned through the boundary assigning tool. Finally, ports are assigned as lumped ports

for antenna designs and an integration line is set up for the port. The metal elements in the design are meshed automatically and the ports are excited with a voltage potential. The devices are also modelled for various dimensions of the air cavities, dimensions of the polymer rim and for various substrates. The results are then compared and further design iterations are carried out in order to achieve optimized designs. Figure 3.6 shows a typical example of an antenna structure created in the HFSS design environment.

3.4.1 Assigning ports and boundaries

Ports are the boundary conditions in Ansoft HFSS that allow energy to flow into and out of the structure [116]. Ports can be assigned to any 2D object or a face. It is necessary to determine the excitation field pattern at each port before the full three-dimensional electromagnetic field inside the structure can be calculated. Ansoft HFSS uses an arbitrary port solver to calculate the natural field patterns or modes that can exist inside a transmission structure with the same cross-section as the port. The resulting 2D field patterns serve as the boundary conditions for the full three dimensional problem. Lumped and wave ports are widely used in HFSS for defining the ports. A wave port is assigned to the structure where energy enters and leaves within a conductive shield while voltages are defined for the lumped port [115]. Lumped ports are assigned at the edge of the microstrip feed lines for the microstrip fed micromachined aperture coupled antenna device as shown in Figure 3.7 while a wave-port is defined for the CPW fed micromachined antenna device presented in Section 3.7. Figure 3.7 shows the perfect E boundaries, radiation boundaries and the assigned lumped port for the micromachined antenna device. There are two types of boundaries in HFSS, the perfect E boundary and the radiation boundary. The perfect E boundary represents a perfect electric boundary (or wall) where the E-field is forced to be normal to the assigned boundary. In HFSS the perfect E boundary is optional and is generally used to represent perfect conducting surfaces. Copper cladded PTFE substrates are extensively used in the fabrication of antenna devices. In order to understand the effect of conductivity of copper metal on the antenna device performance, the copper metal is assigned as a solid block with a conductivity of 5.8×10^7 S/m instead as a perfect E boundary. When calculating radiation fields, the values of the fields over the radiation surface are used to compute the fields in the space surrounding the device. This space is typically set up by a boundary called radiation boundary (surface) which is typically an air region that is extended by approximately $\lambda/4$ from the radiating element on all sides. The

radiation boundary represents a perfect magnetic boundary where the H-field is forced to be normal to the assigned boundary. As shown in Figure 3.7, the perfect radiation boundary assigned to the antenna model form a cubic box enclosing the antenna and its substrate. The electromagnetic field within this box is solved in the field simulation.

3.4.2 Solution setup

A solution setup is needed in order to perform an analysis of the device / structure in Ansoft HFSS. HFSS takes the frequency sweep parameters (in a driven mode) and obtains the field solutions (from propagation constant) by solving the boundary value problem of Maxwell equations as shown in [105]. The solution setup stage consists of the solution frequency which is the frequency used by the adaptive mesher to automatically refine the mesh to obtain the electrical performance of the device and this is generally the centre frequency of the frequency sweep. The adaptive solution consists of the maximum number of passes the adaptive mesh routine will perform as it attempts to satisfy the convergence criteria. It also consists of the maximum delta S per pass which defines the convergence criteria for the adaptive meshing process [116]. The sweep setting specifies the characteristics of input signals: start frequency, end frequency, frequency step, voltage level, current level and waveform shape etc. These parameters are defined by the operation frequency of the antenna device. For instance, for the antenna devices studied in the thesis, the sweep is set at the start frequency of 10 GHz and stop frequency of 16 GHz with a step size of 0.1 GHz. The delta S per pass is set at around 0.005.

3.4.3 Validation check and simulation

After the micromachined antenna model was created and the ports and boundaries were assigned to the model, validation check was carried out to ensure that the model settings were correct for simulation. Within Ansoft HFSS this is executed automatically by the validation check tool. Any errors associated with the design and settings which can lead to failure of the numerical simulation would be reported. When the validation check is completed, 3D electromagnetic field analysis is carried out on the antenna to obtain the characteristics of the device through the simulation engine of HFSS. After obtaining a generalized S-matrix, it will be normalized to an impedance of $50\ \Omega$ to compute reflection and transmission directly from the resultant data. To renormalize a generalized S-matrix to specific impedance, HFSS first calculates a unique impedance matrix Z for the structure

under consideration. A typical simulation process takes about 30 ~ 200 minutes depending on the size and complexity of the antenna design.

3.4.3.1 Mesh control and accuracy

In general, the analysis problem space is divided into thousands of smaller regions in the finite element method and each sub-region (element) is represented with local functions to eliminate spurious modes [105]. In the case of HFSS, the geometric model is automatically divided into smaller regions called tetrahedra, where a single tetrahedron is a four-sided pyramid. This collection of tetrahedra is referred to as the finite element mesh. There is a trade-off between the size of the mesh, the desired level of accuracy and the amount of available computing resources in Ansoft HFSS [115]. Each of the individual elements (tetrahedral) is equally responsible for the accuracy of the solution. The visual image of the mesh allocation in Ansoft HFSS for a microstrip fed micromachined aperture coupled antenna device is shown in Figure 3.7. Each element must occupy a region that is small enough for the field to be adequately interpolated from the nodal values in order to generate an accurate description of a field quantity [105, 117]. However, generating a field solution involves inverting a matrix with approximately as many elements as there are tetrahedra nodes.

For meshes with a large number of elements, such an inversion requires a significant amount of computing power and memory. Therefore, it is desirable to use a mesh fine enough to obtain an accurate field solution but not too much that it cannot be handled by the available computer memory and processing power. An iterative process called an adaptive (meshing) analysis is used by HFSS to produce an optimal mesh, in which the mesh is automatically refined in critical regions. Firstly a solution is obtained based on a coarse initial mesh. Then, the mesh is refined in areas of high error density and new solution is generated [105, 116]. This process is repeated until the selected parameters converge to within a desired limit (ΔS). If the solution has converged, then the previous mesh is as good as the current mesh. HFSS will then use the previous mesh to perform frequency sweeps for driven mode and obtains the field solutions at all the frequencies.

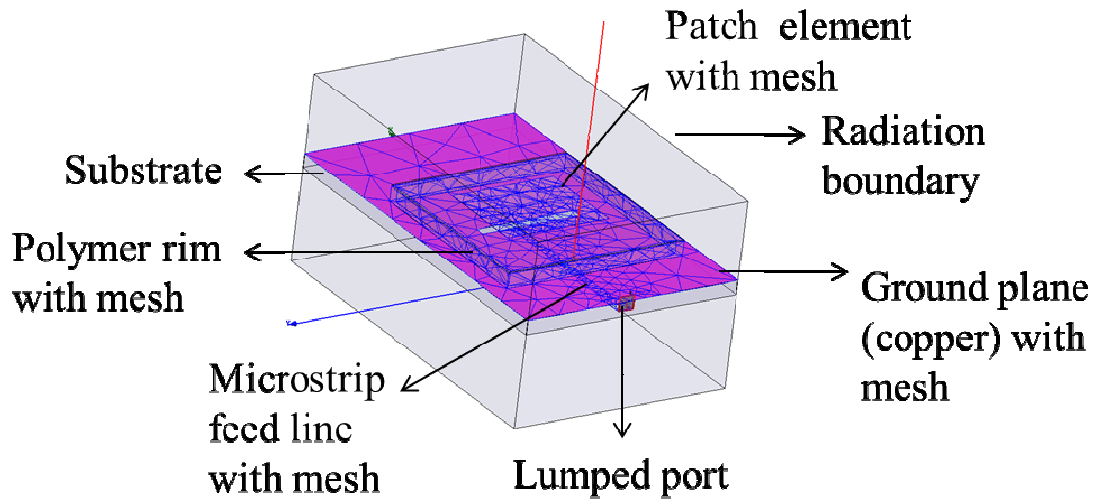


Figure 3.7 Mesh formation for the micromachined aperture coupled antenna model in HFSS

3.4.4 Extraction of simulation results

After simulation, the electromagnetic field solution for the antenna device is obtained. The post processor of HFSS allows the user to view the data and extract the desired device characteristics from the solution data. The results can be displayed in tabular forms or a variety of 2D/3D plots. The bandwidth, gain and efficiency are the most important factors for antenna devices. In order to obtain the value of the bandwidth, the reflection scattering parameter (S_{11}) of the antenna device was extracted from the field solution as presented in [116]. The bandwidth is determined by the difference between the upper and lower frequencies at which the magnitude of the reflection scattering parameter is -10 dB. The radiation pattern and gain along with the radiation efficiency at different frequencies are the critical factors for antenna devices.

3.5 A MICROSTRIP FED MICROMACHINED APERTURE COUPLED PATCH ANTENNA DEVICE

Figure 3.8 shows schematics of a microstrip fed patch antenna device using a micromachined polymer ring. The suspended patch design is studied for high efficiency operation.

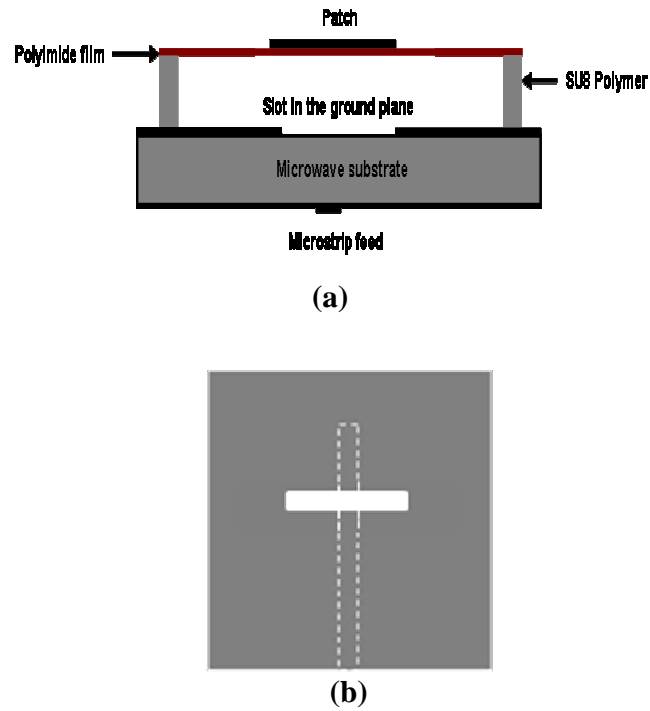


Figure 3.8 Geometry of the (a) cross-sectional view and (b) top view of microstrip fed micromachined aperture coupled patch antenna device

In order to create a sealed air cavity between the microwave substrate and the polyimide thin film substrate, a square polymer ring (SU8 rim) is used. Therefore there is an improvement in the radiation frequency when the slot (aperture) based feeding method is used and also it allows wide band operation which uses the double tuning effect of the slot when compared to the other feeding techniques [24, 118]. Hence by incorporating the air cavity and the slot in the antenna device, high gain and wide band operation can be achieved simultaneously.

A frequency range of around 10 GHz is more suitable to produce devices on the 3 inch wafers. The height of the air cavity is chosen to be at least 1.5 mm and equal to the height of the lower substrate which also depends on constraints in producing uniform thick polymer films. Furthermore it is much easier to produce SU8 films of thicknesses between 1 μm to 1.5 mm otherwise it is difficult to control the surface uniformity. The effect of different supporting substrates has also been conducted in order to determine an optimum substrate to support the patches for the microstrip fed micromachined aperture coupled patch antenna device. Ideally, the substrate should be thin, flexible and low cost. Taconic thin film substrates of different thickness and Kapton polyimide substrates have been

modelled in HFSS for optimum performance. The study revealed that there is not much variance in the performance of the antenna fabricated on the above two different substrates suggesting that the flexible and cheaper polyimide substrate can be used to support the patch element.

3.5.1 Design and simulation

For the ease of characterisation, the device was designed to operate at around 12 GHz using in-house facilities. The approximate resonant frequency for the micromachined antenna devices depends on the dimensions of the resonant patch element primarily [119] and is given by

$$f_0 = \frac{k_{mn}c}{2\pi\sqrt{\epsilon_{eff}}} \quad (3.26)$$

$$k_{mn}^2 = \left(\frac{m\pi}{a}\right)^2 + \left(\frac{n\pi}{b}\right)^2 \quad (3.37)$$

where c is the velocity of light, a is the patch width and b is the patch length. ϵ_{eff} is the effective dielectric constant and m, n denotes the modes. The resonant frequency can be approximated for the TM_{10} mode. The effective permittivity is given by [4]

$$\epsilon_{eff} = \frac{\epsilon_{air}\epsilon_{polyimide}}{\epsilon_{air} + (\epsilon_{sub} - \epsilon_{air})x_{air}} \quad (3.28)$$

Where ϵ_{air} is the relative permittivity of air, $\epsilon_{polyimide}$ is the relative permittivity of polyimide film, x_{air} is the ratio of the polymer rim thickness to the sum of the polymer film thickness and the polymer rim thickness. Due to the fringing fields at the ends of the patch elements the electrical length of the element is longer than the physical length. A formula for computing the length ΔL associated with the fringe fields has been derived by Hammerstad [39].

$$\frac{\Delta L}{h} = 0.412 \frac{(\epsilon_{eff} + 0.3) \left(\frac{b}{h} + 0.264 \right)}{(\epsilon_{eff} - 0.258) \left(\frac{b}{h} - 0.8 \right)} \quad (3.29)$$

where b is the length of the patch element, h is the sum of the thickness of the polymer rim

and the thickness of the polyimide substrate. The width of the patch element for this micromachined antenna device was fixed at 11.5 mm for a compact micromachined antenna device. The physical dimension a (width as shown in Figure 3.4) of the patch can thus be approximated by

$$a = \frac{c}{2f_r \sqrt{\epsilon_{eff}}} - 2\Delta L \quad (3.30)$$

The aperture length controls the resistive part of the input impedance where as the open circuit stub length controls the reactance part of the input impedance [119]. Increasing the length of the aperture also decreases the resonant frequency of the antenna device slightly. Thus, this has an effect on the function of the antenna device with respect to the resonant frequency and the bandwidth. Moreover, the aperture coupling is predominantly magnetic from equation 3.12.

After obtaining the approximate dimension of the patch element, optimisation of the design parameters such as the dimensions of the open circuit microstrip stub, aperture and top patch was performed using the Ansoft HFSS electromagnetic simulation package. As the aperture is operated at close to resonance for this antenna device, the initial length of the aperture can be approximated from (3.30) by replacing the dimension a by aperture length (l_{ap}). ΔL is replaced by Δl_{ap} and ϵ_{eff} by ϵ_{subeq1} . ϵ_{subeq1} is given by

$$\epsilon_{subeq1} = \frac{\epsilon_{sub} + 1}{2} + \frac{\epsilon_{sub} - 1}{2} \left[1 + 12 \frac{t_{ap}}{w_{ap}} \right] \quad (3.31)$$

where t_{ap} is the thickness of the Arlon substrate, w_{ap} is the width of the aperture which is fixed at approximately 1/10 of its length. ϵ_{sub} is the dielectric constant of the Arlon substrate.

Table 3.1 Summary of the parameters for the microstrip fed micromachined aperture coupled patch antenna device

Parameter	Unit (mm)
Patch width	9.5
Patch length	11.5
Patch thickness	0.007
Aperture length	11
Aperture width	1.1
Microstrip length	18.84
Microstrip width	0.85
Inner length of cavity	19
Inner width of cavity	19
Cavity height	1.5
Polyimide thickness	0.125

Δl_{ap} is obtained from equation 3.29 by substituting the values of the aperture width and the thickness of the Arlon substrate. The width of the microstrip line is approximated using the transmission line calculator from AWR[®] microwave officeTM while a stub equivalent to $\lambda_g/4$ is used initially. λ_g is the guided wavelength for the Arlon substrate in this case. The optimisation of the aperture resulted in the aperture resonating close to resonant frequency of the patch and hence the double tuning effect was utilized to obtain a wide bandwidth for the antenna device [25]. The height of the cavity is chosen not only to achieve optimum bandwidth and gain but also for the ease of fabrication. The antenna dimensions of the polymer rim were chosen so as to achieve high efficiency and compact size in the HFSS simulation. The dielectric constants of the polyimide film, the SU8 polymer and the microwave substrate (AD300A, Arlon MED) are 3.5 [120], 4.2 [121] and 3 [122] while the corresponding loss tangents are 0.0026 [120] and 0.042 [123] and 0.003 [122] respectively. The tolerances (variations) experienced due to the unevenness of the SU8 polymer rims should be taken into account while simulating the micromachined antenna device. After an initial height of 1.5 mm is fixed for the air cavity, the height is varied in steps of 50 μ m in the Ansoft HFSS modeller so as to study the effect of the variance of height in the shift in

resonance of the antenna structure and also the bandwidth. It has been verified that a tolerance of 100 μm is acceptable for $< 1\%$ variance in simulated bandwidth. A small rectangular overlay on the end section of the microstrip line where the connector would normally be attached was modelled in order to incorporate the effect of the SMA connector into the antenna design and simulate. The dimensions (3x1.5 mm) of the overlay were chosen such that they matched the length and diameter of the pin of the SMA connector. Table 3.1 gives a summary of the optimized design parameters of the antenna device.

3.5.2 Results and discussion

3.5.2.1 Field distribution

Figure 3.9 (a) and (b) show the electric and magnetic fields for the micromachined aperture coupled patch antenna structure at 13 GHz. The fields are plotted in vector and magnitude form.

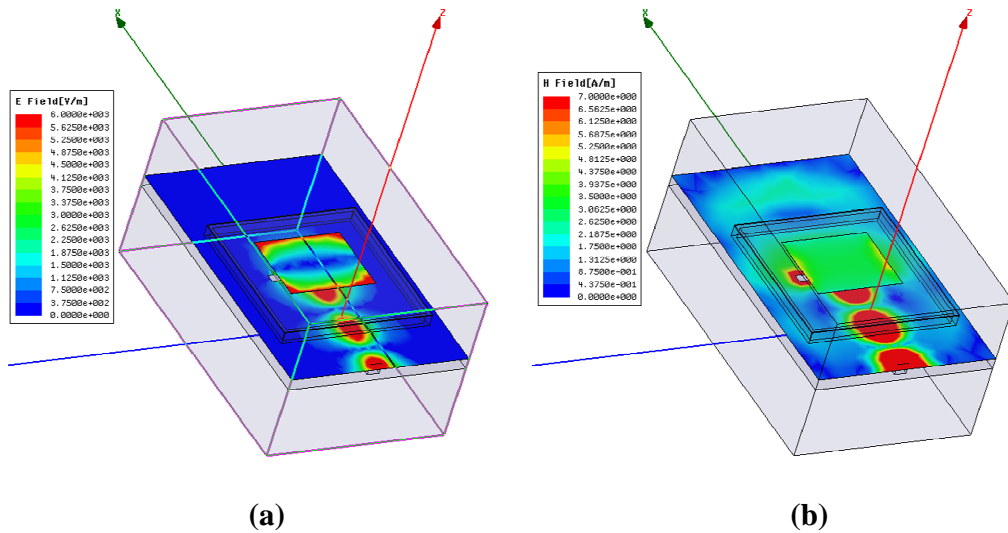


Figure 3.9 Field model showing the scalar and vector (a) electric and (b) magnetic fields at 13.5 GHz.

The field plot show that at the frequency of interest, 13 GHz, which is the efficient radiating frequency for the antenna structure. It can be seen that the fields satisfy the TM_{100} mode at this resonant frequency. The plot also shows that, there are electric and magnetic fields on the ground plane that correspond to the propagating TEM mode on the microstrip transmission line underneath the ground plane. The distribution of electric and magnetic fields also indicate the presence of backward radiation.

3.5.2.2 S parameters and study of the bandwidth

To determine the performance of the aperture coupled antenna device as described in Section 3.4, the reflection coefficient (S_{11}) and VSWR parameters are plotted to determine the -10 dB bandwidth after optimising the antenna performance. The reflection coefficient (S_{11}) and VSWR parameters are plotted as a function of frequency as shown in Figure 3.10.

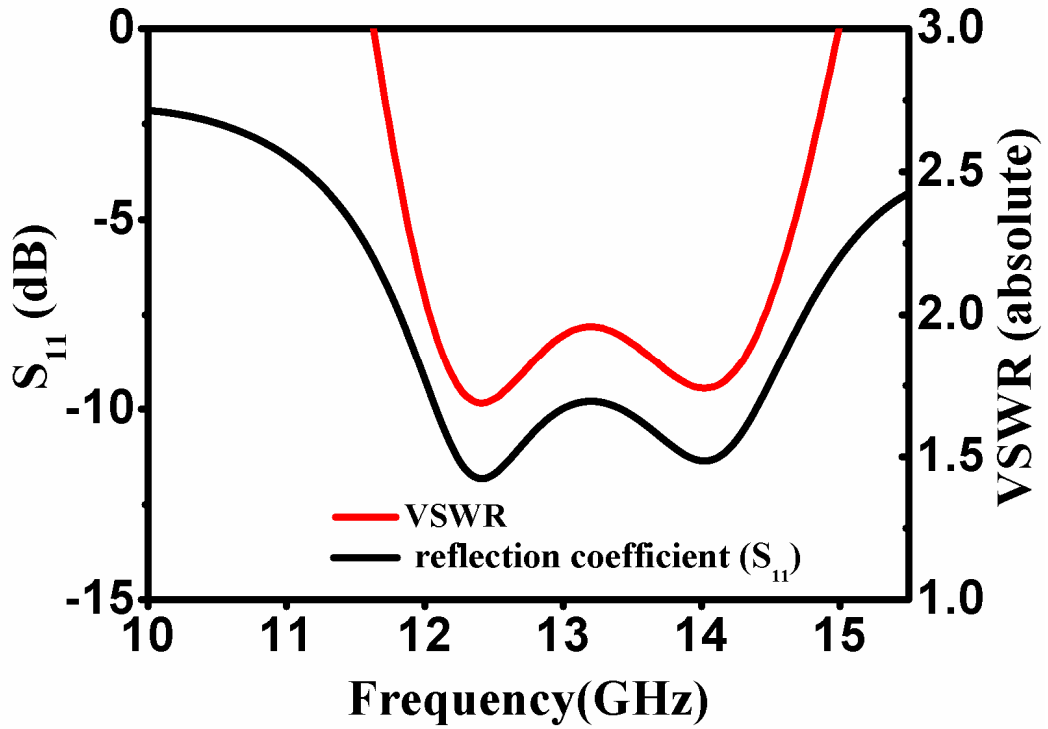


Figure 3.10 Simulated reflection coefficient and the VSWR parameters for the optimized microstrip fed micromachined aperture coupled patch antenna device

The impedance parameters are plotted in Figure 3.11. It can be seen from the plot that the reflection coefficient (S_{11}) is lower than -10 dB from around 11.5 GHz and the VSWR are lower than a value of 2. The plot also shows that the reflection coefficient (S_{11}) is less than -5 dB from around 11.5 GHz to 15.5 GHz that corresponds to attenuation or a loss of 30% power. Although the antenna structure can be used as a radiating element within this frequency range, it can be seen in the later sections that the gain and directivity of the structure is below 5 dBi even though the radiation efficiency is above 95%. The radiation plots also show that there is significant back radiation for frequencies below 12 GHz and above 15.5 GHz.

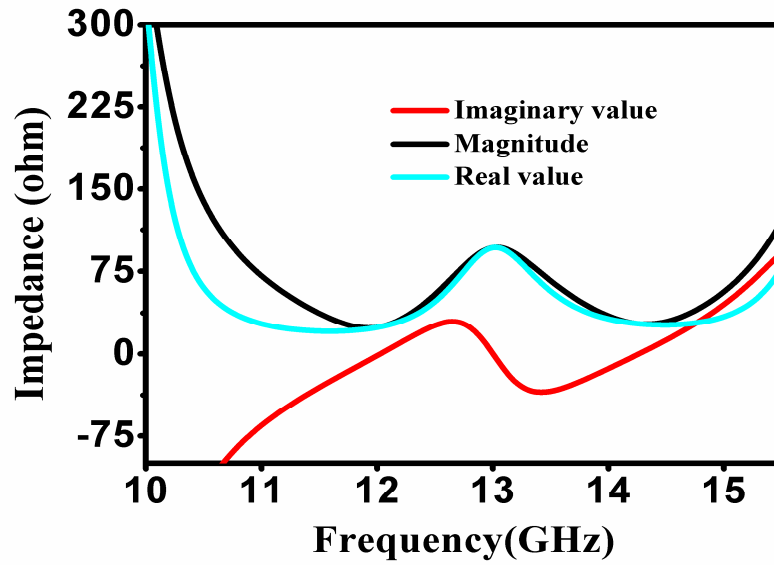


Figure 3.11 Simulated impedance parameters for magnitude, real and imaginary values

3.5.2.3 Normalised radiation patterns

The radiation patterns for the antenna device were obtained from the field solution and are plotted as a function of frequency from the far field plotter interface in Ansoft HFSS. Normalized radiation patterns for the E plane and H plane of the 3 D radiation pattern are plotted at different frequencies from the radiation pattern interface in Ansoft HFSS. Figure 3.12 shows the 2D and 3D far-field radiation patterns for the microstrip fed patch antenna device at 13.2 GHz near to the centre frequency of the operating band. The patterns show that there is significant backward radiation and significant side lobes in the E plane.

Figure 3.13 shows the polar radiation pattern curves from 11.5 GHz to 15 GHz. The plots show the E plane and H plane radiation patterns for the antenna device. The back to front radiation ratio and the side lobes can be studied at different frequencies from these plots. The E plane plot shows that there is a minimal side lobe in the front side and increasing with frequency while the pattern possesses two significant side lobes at around 15 GHz. The peak backward radiation for both the E plane and H plane for the aperture coupled device is around -8 dB in magnitude (normalised) and also increases with frequency.

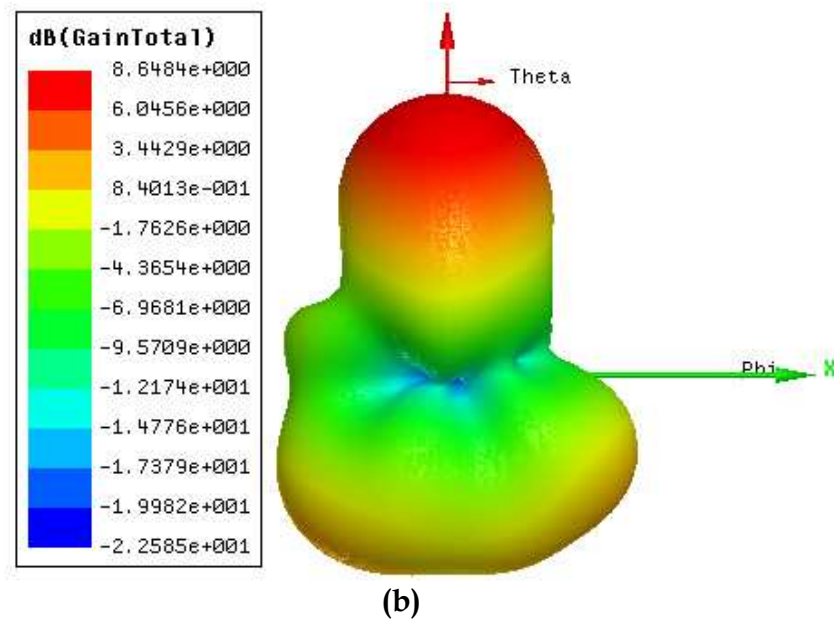
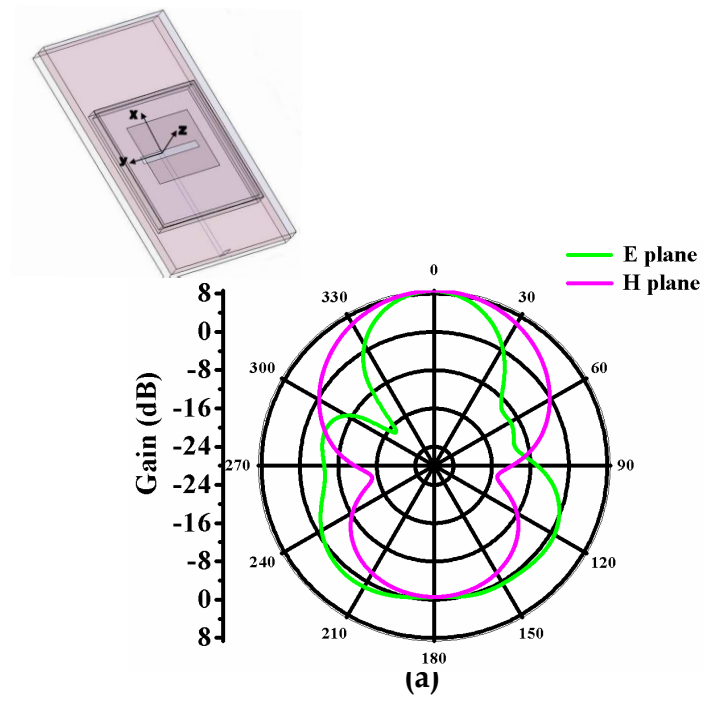
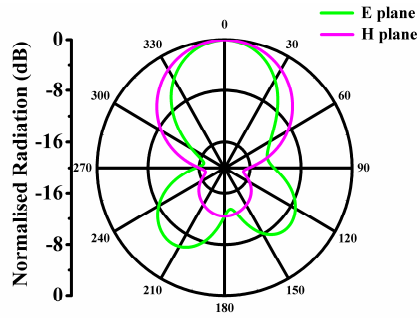
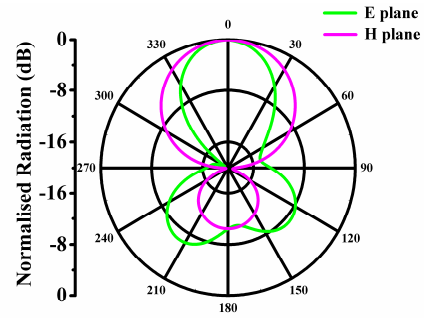


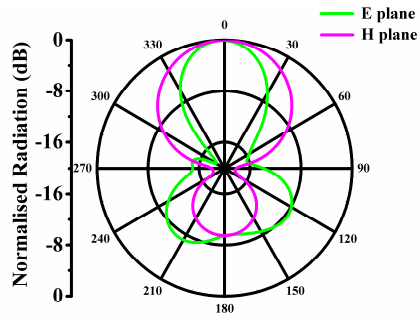
Figure 3.12 2D radiation patterns in E (x - z) plane and H (y - z) plane (a) and 3D (b) radiation patterns of a microstrip fed micromachined aperture coupled patch antenna device at 13.2 GHz



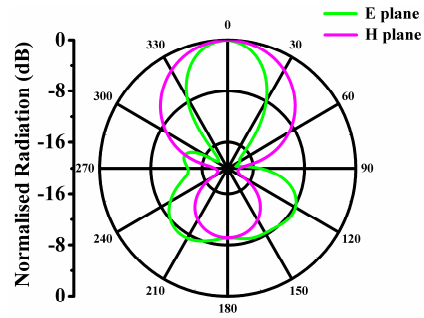
11.5 GHz



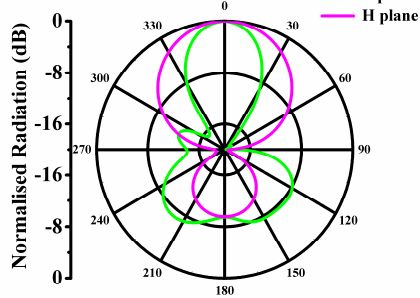
12 GHz



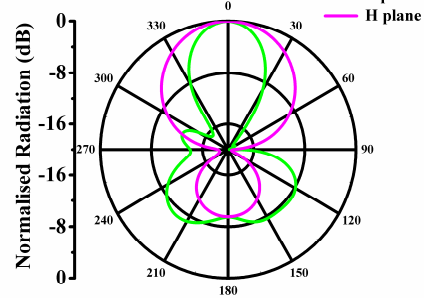
12.5 GHz



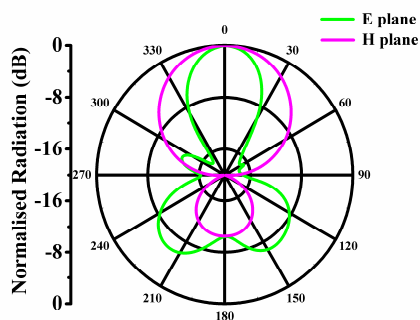
13 GHz



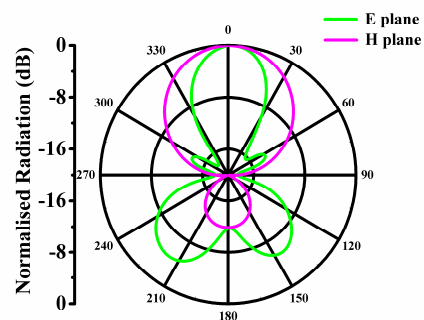
13.5 GHz



14 GHz



14.5 GHz



15 GHz

Figure 3.13 Simulated normalized E and H plane radiation patterns at different frequencies for the microstrip fed micromachined aperture coupled patch antenna device

It can also be seen that, the backward radiation in the E plane for the antenna device varies from -4 dB at 11.5 GHz to around -10 dB at 13 GHz and increases again to around -4 dB at 15 GHz. It can be concluded that the microstrip fed micromachined aperture coupled patch antenna device has a poor front to back ratio in terms of radiation and which can be attributed to the radiation from the microstrip feed line.

3.5.2.4 Directivity and gain

Figure 3.14 shows the time of directivity, gain and efficiency for the microstrip fed aperture coupled antenna device with respect to frequency. The left 'y' axis gives the magnitude of antenna directivity and gain where as the right 'y' axis gives the absolute efficiency. It can be seen easily from the plot the gain curve follows the directivity curve suggesting almost 100% radiation efficiency within the radiation bandwidth region.

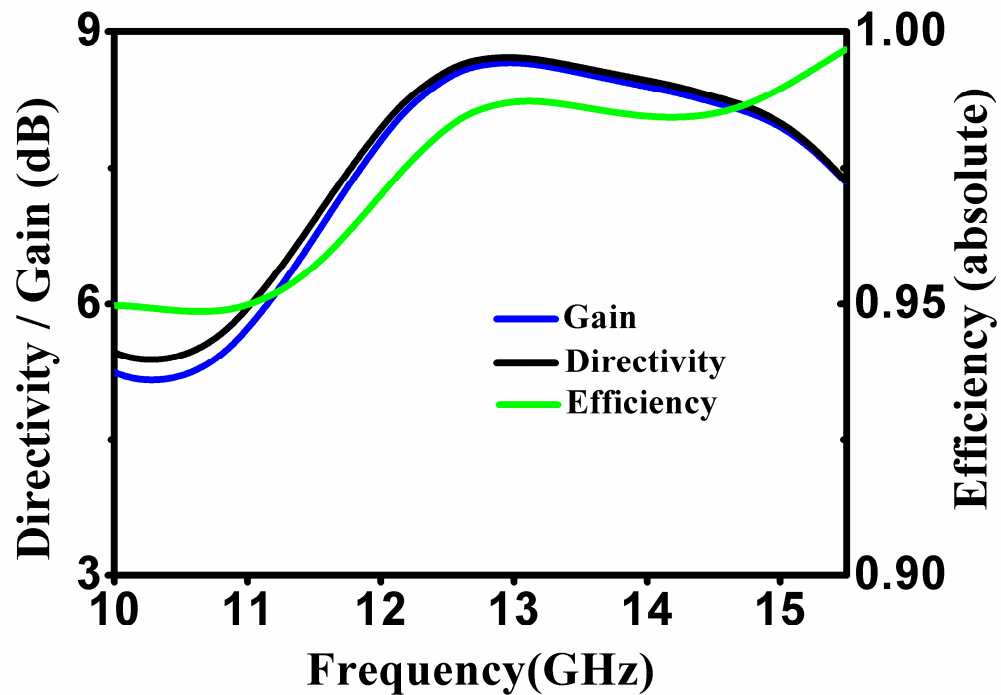


Figure 3.14 Simulated gain, directivity and radiation efficiency of the optimized microstrip fed micromachined aperture coupled patch antenna device

The gain and bandwidth varies from about 5 dBi at 10 GHz to around 8.3 dBi at 13 GHz and falls back below 6 dBi after 15.5 GHz. The variance of directivity and gain within the radiation bandwidth is below 1 dBi while it varies significantly out of the radiation bandwidth. Radiation efficiency is the ratio of the total power radiated by the antenna

device to the power input. The radiation efficiency for this antenna varies from about 0.95 to close to 1 at 15.5 GHz.

3.5.3 Effect of microstrip length

The effect of microstrip feed length on the impedance and therefore the S_{11} results were studied. Simulations in Ansoft HFSS were carried out to determine the S_{11} factor as a function of frequency for different values of the microstrip length while keeping all the other dimensions constant. The geometrical parameters and substrate properties of the aperture coupled antenna are the same as that in Table 3.1.

The length of the microstrip line is varied to study the change in bandwidth and the gain of the antenna device. The length of the microstrip line is varied from 18.05 to 18.84 mm to obtain the corresponding simulated S_{11} -parameters as shown in Figure 3.15. The effect of the microstrip length is to change the impedance seen at the end of the microstrip line thereby changing the -10 dB bandwidth of the device deduced from the S_{11} plots. Figure 3.15 show that the -10 dB bandwidth decreases as the length of the microstrip line decreases while the bandwidth increase with the length. An optimum length of the microstrip line is around 18.84 mm after which the antenna behaves as a dual band device when considering the -10 dB bandwidth. Further decrease of the length of the microstrip line from 18.05 mm decreases the bandwidth to a larger extent while maintaining good reflection coefficient (S_{11}). The efficiency of the antenna device on the other hand is almost constant for all different microstrip lengths. In antenna design, a device is usually aimed for larger bandwidth while having optimum gain and efficiency. The optimal conductor thickness is in the region of 7 ~ 10 μm . From equation (3.23) it can be seen that the input impedance at the end of the microstrip line for an aperture coupled antenna design is a function of the transmission line length and the characteristic impedance, Z_c . By changing the length of the microstrip line, the impedance changes which is related to the bandwidth of the antenna device. This method of design optimisation is more suitable for applications where the patch dimensions and the spacer (polymer rim) height are fixed but a large bandwidth is required.

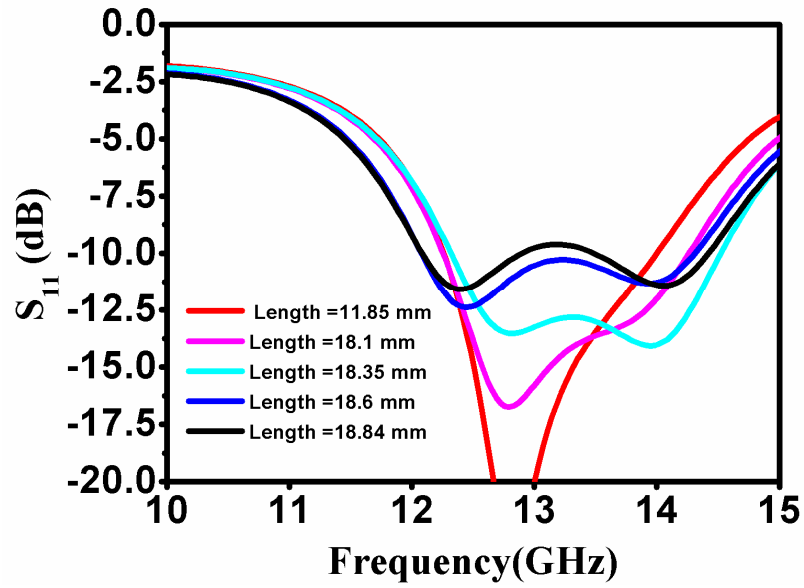


Figure 3.15 Simulated reflection coefficient (S_{11}) parameters of the microstrip fed micromachined aperture coupled patch antenna device for different microstrip lengths

3.5.4 Effect of SU8 polymer rim dimensions

The effect of SU8 polymer rim dimensions on the S_{11} characteristics are studied for three different rim designs. Simulations using Ansoft HFSS are carried out to determine the S_{11} factor as a function of frequency for different width and length of the polymer rim while keeping all the other dimensions constant.

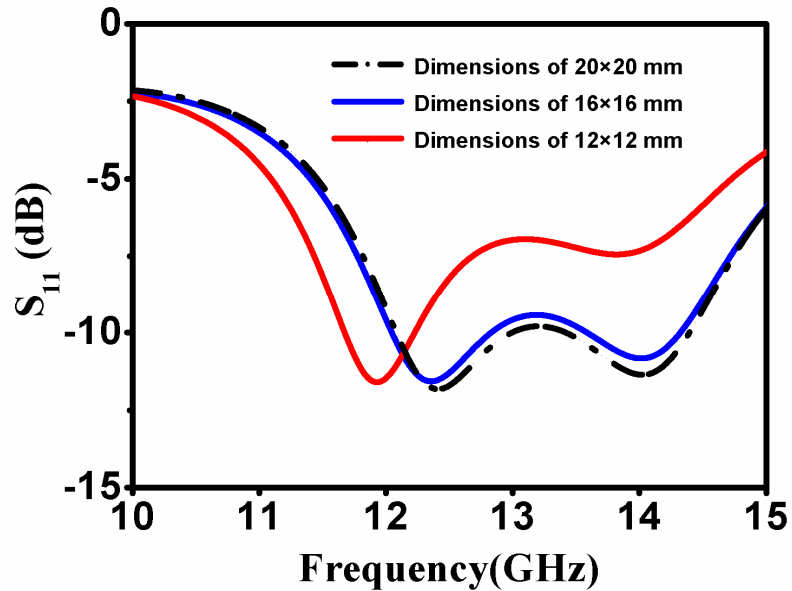


Figure 3.16 Simulated reflection coefficient (S_{11}) parameters of the microstrip fed micromachined aperture coupled patch antenna device for different SU8 polymer rim dimensions

The dimensions of the rim were varied to study the change in bandwidth and the gain of the antenna device. The dimensions studied were 20 mm \times 20 mm, 16 mm \times 16 mm, 12 mm \times 12 mm respectively and the corresponding simulated S_{11} parameters are shown in Figure 3.17. The width of the rim is 1 mm as can be seen in Figure 3.4. All of the polymer rims are centred with respect to the patch element. The effect of the polymer rim dimensions is the change of the impedance seen at the end of the microstrip line thereby changing the -10 dB bandwidth of the device deduced from the S_{11} plots and also the efficiency of the antenna device. The optimum dimensions were found to be around 16 mm \times 16 mm. The dimensions of 20 mm \times 20 mm were chosen for the final design. The effect of the polymer rim dimensions on the gain and directivity were studied and the results are as shown in Figure 3.17. The effect of the polymer rim dimensions on the radiation efficiency are shown in Figure 3.18 while the effect of rim dimensions on gain, directivity and efficiency at centre frequency of 13.1 GHz is presented in Figure 3.19. The gain, directivity and efficiency are similar for the dimensions of 16 mm \times 16 mm and 20 mm \times 20 mm while a reduction in the above parameters is observed for the dimensions of 12 mm \times 12 mm. This means that the effect of the dielectric constant and loss tangent of the SU8 polymer rim is more significant in the case of the smallest polymer rim.

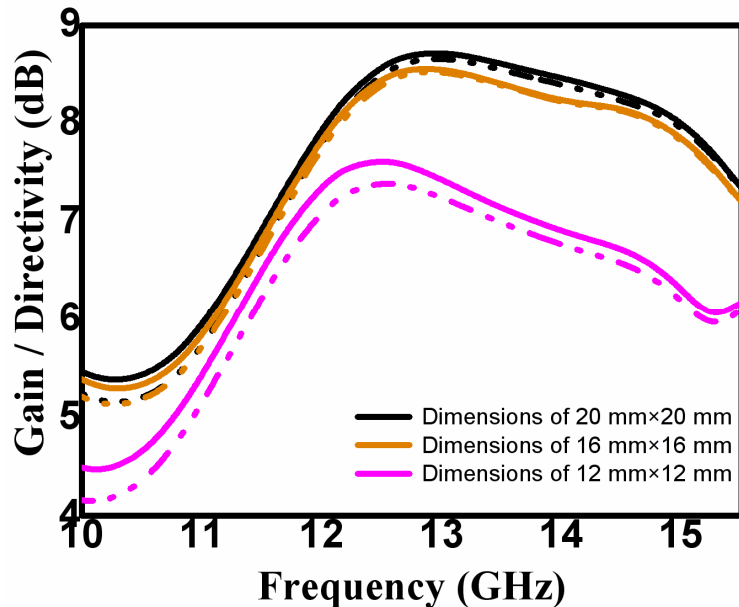


Figure 3.17 Simulated gain, directivity parameters of the microstrip fed micromachined aperture coupled patch antenna device for different SU8 polymer rim dimensions. The solid lines represent directivity while the dotted lines represent antenna gain.

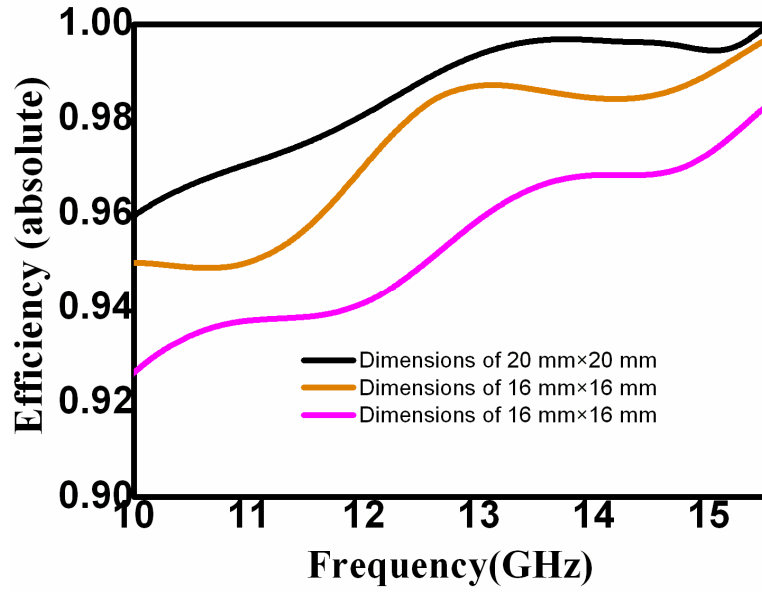


Figure 3.18 Simulated radiation efficiency parameters of the microstrip fed micromachined aperture coupled patch antenna device for different SU8 polymer rim dimensions

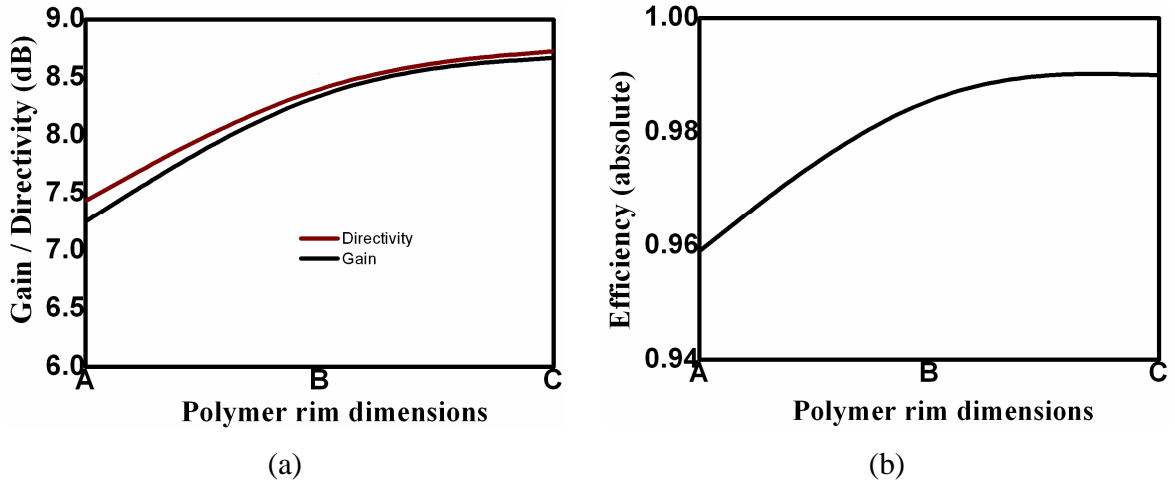


Figure 3.19 (a) Simulated gain, directivity and efficiency parameters of the microstrip fed micromachined aperture coupled patch antenna device for different SU8 polymer rim dimensions at 13.1 GHz. A, B, C represents a polymer rim dimensions of 20mm x 20mm, 16mm x 16mm and 12mm x 12mm respectively. (b) Simulated efficiency parameters of the micromachined patch antenna device for different SU8 polymer rim dimensions at 13.1 GHz

From Section 3.3.1, the dominant resonance for this antenna device is through complex electric and magnetic coupling of the aperture to the radiating patch element and thus it is difficult to estimate the effect of polymer rim on the dominant resonance but this could be studied with the Ansoft HFSS full wave simulations. With reduced polymer rim dimensions, one would expect an increase in effective dielectric constant beneath the

radiating patch element thus reducing the resonant frequency which can be seen in Figure 3.16. The variation in directivity and gain is about 1 dB with the polymer rim dimensions. The directivity is about 7.5 dBi with smallest rim dimensions and almost unaffected at about 8.5 dBi for the polymer rim dimensions of 16mm×16mm and 20mm×20mm. The variation in antenna efficiency is minimal and is about 0.03%.

3.5.5 Effect of SU8 polymer rim thickness

The effect of SU8 polymer rim thickness on the S_{11} characteristics are studied in order to understand the effect of manufacturing tolerances on the performance of the micromachined aperture coupled antenna device. It is anticipated that the manufacturing tolerances of about 70 μm are likely in the fabrication of the SU8 polymer rims as presented in Section 4.6.3. Simulations in Ansoft HFSS are carried out to determine the S_{11} factor as a function of frequency by varying the height of the polymer rim from 1.3 mm to 1.7 while keeping all the other dimensions (including polymer rim dimensions of 20mm×20mm) constant. The corresponding simulated S_{11} -parameters are shown in Figure 3.20.

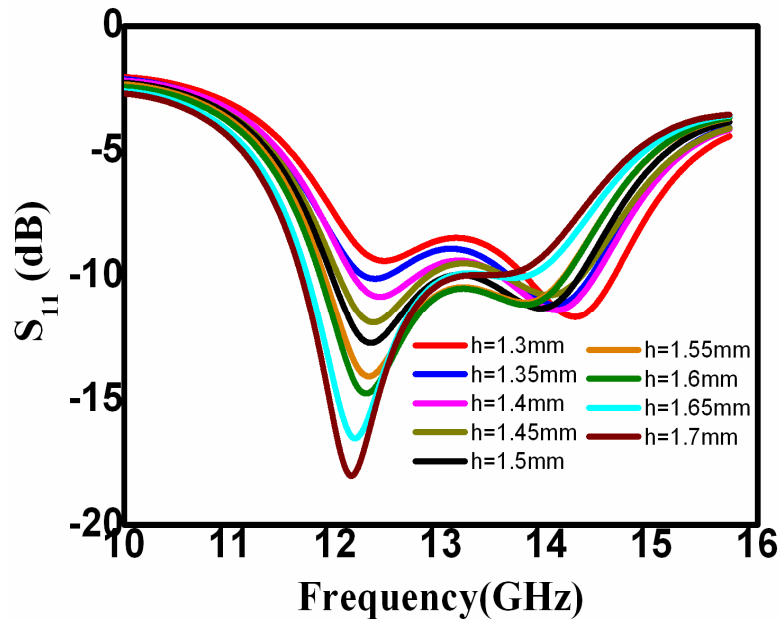


Figure 3.20 Simulated reflection coefficient (S_{11}) parameters of the microstrip fed micromachined aperture coupled patch antenna device for varying SU8 polymer rim thickness. The thickness of the polymer rim is denoted by 'h' in the plot.

The variation of polymer rim thickness has an effect on the reflection characteristics and there by the achievable bandwidth for the antenna device the impedance seen at the end of

the microstrip line thereby changing the -10 dB bandwidth of the device. From Figure 3.20 one can see that for the polymer rim height from 1.4 mm to 1.6 mm the variation in bandwidth is less than 2% and a similar variation in central frequency while for the variation from 1.3 to 1.4 mm and 1.6 mm to 1.7 mm shows a variation of greater than 5% and similar variation in central frequency. This shows that an optimally stable bandwidth and central frequency can be maintained for the micromachined antenna device fabricated with a tolerance less than 100 μm . The variation in directivity and gain is about 0.3 dB with the variance in polymer rim dimensions as shown in Figure 3.21 (a). The directivity is about 8.5 dBi with a polymer rim height of 1.3 mm and is about 8.8 dBi with the polymer rim height of 1.7 mm showing a small increase with the increase in height of the polymer rim. The variation in antenna efficiency is minimal and is about 0.02%.

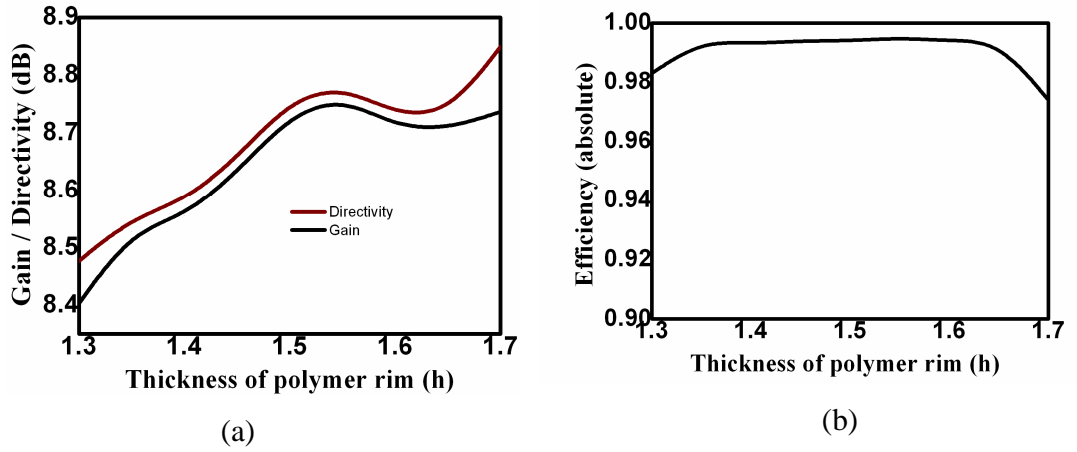


Figure 3.21 (a) Simulated gain and directivity parameters of the microstrip fed micromachined aperture coupled patch antenna device for different SU8 polymer rim dimensions at 13.1 GHz. (b) Simulated efficiency parameters of the micromachined patch antenna device for different SU8 polymer rim thickness at 13.1 GHz

3.5.6 Effect of SU8 polymer rim dielectric properties

There is a variation in the dielectric properties of the SU8 polymer reported in the literature primarily due to the variation in the composition of SU8 from the supplier and due to the viscosity of the SU8 material. The relative dielectric constant of the SU8 polymer of 2.9 and the corresponding loss tangent of 0.04 are reported for a cured SU8-25 formulation at 10 GHz in [40]. The dielectric constant of 3.35 and the corresponding loss tangent of 0.015 are reported for the cured SU8-25 formulation at 10 GHz in [124]. The dielectric constant for SU8-100 polymer of 4.2 at 10 GHz derived from [121] while the corresponding loss tangent of 0.042 [123] are used in the modelling of the micromachined antenna devices at

10 GHz. Thus, different types of SU-8 are available whose dielectric properties are sensitive to processing conditions [40]. The SU8-100 material used for the micromachined antenna devices is formulated in house and thus it is likely that the material properties may vary from that reported in the literature and also due to the processing conditions. In order to understand the effects of the dielectric properties of the SU8 material on the antenna properties, antenna simulations are performed by varying the dielectric constant of the SU8-100 material from 3.5 to 5 in steps of 0.5. Thus, a dielectric constant of 4 and a loss tangent of 0.042 give better agreement between the simulated and measured S_{11} coefficient for the micromachined antenna device as shown in Figure 3.22. The SU8 polymer rim dimensions are 20mm×20mm for the simulations.

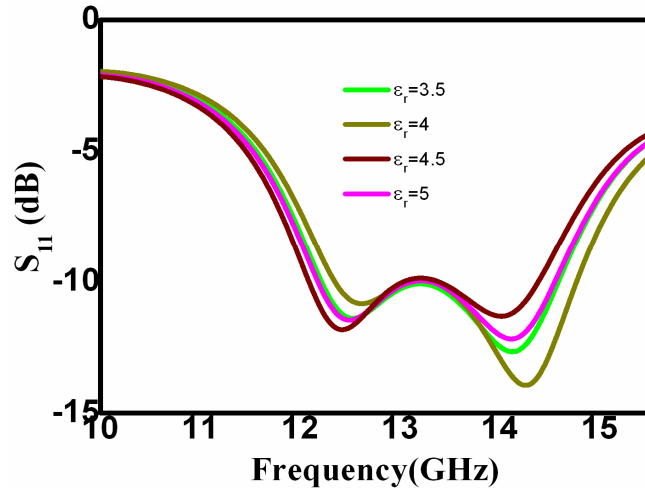


Figure 3.22 Simulated reflection coefficient (S_{11}) parameters of the microstrip fed micromachined aperture coupled patch antenna device for varying SU8 dielectric constant.

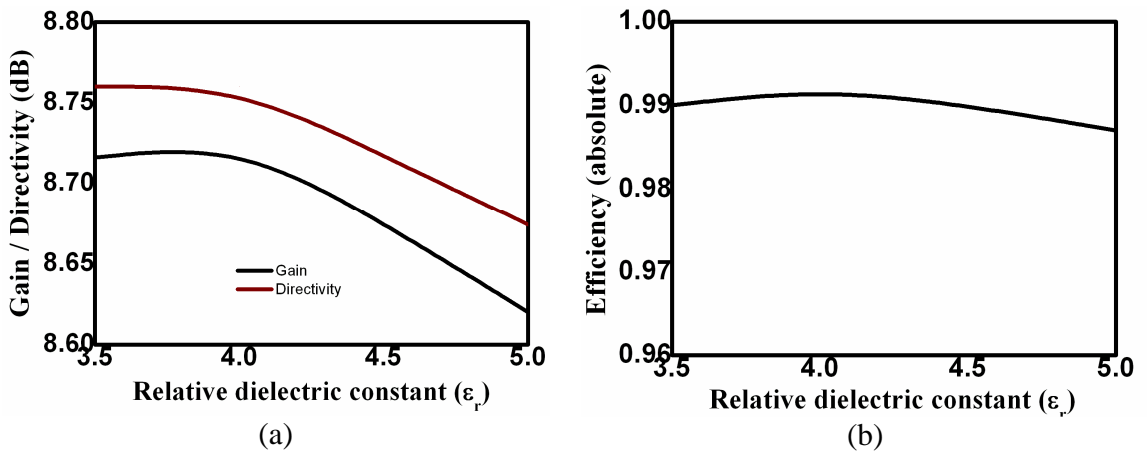


Figure 3.23(a) Simulated gain and directivity parameters of the microstrip fed micromachined aperture coupled patch antenna device varying SU8 dielectric constant at 13.1 GHz. (b) Simulated efficiency parameters of the micromachined patch antenna device for different SU8 polymer rim thickness at 13.1 GHz

The variation in directivity and gain is about 0.05 dB with the variance in polymer rim dimensions as shown in Figure 3.23 (a). The variation in antenna efficiency is minimal and is about 0.01%. This shows that the variation in relative dielectric constant has an effect on the reflection coefficient characteristics of the micromachined aperture coupled antenna device but minimal effect on the radiation characteristics.

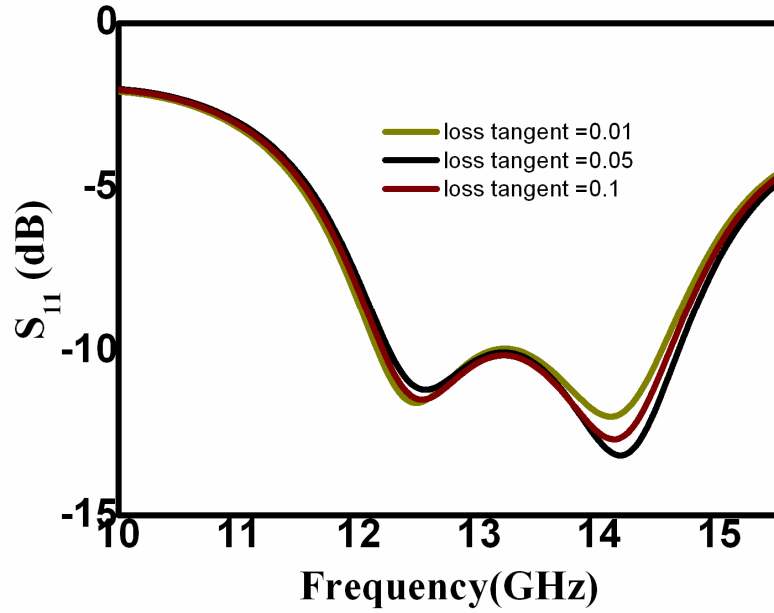


Figure 3.24 Simulated reflection coefficient (S_{11}) parameters of the microstrip fed micromachined aperture coupled patch antenna device for varying SU8 dielectric loss tangent.

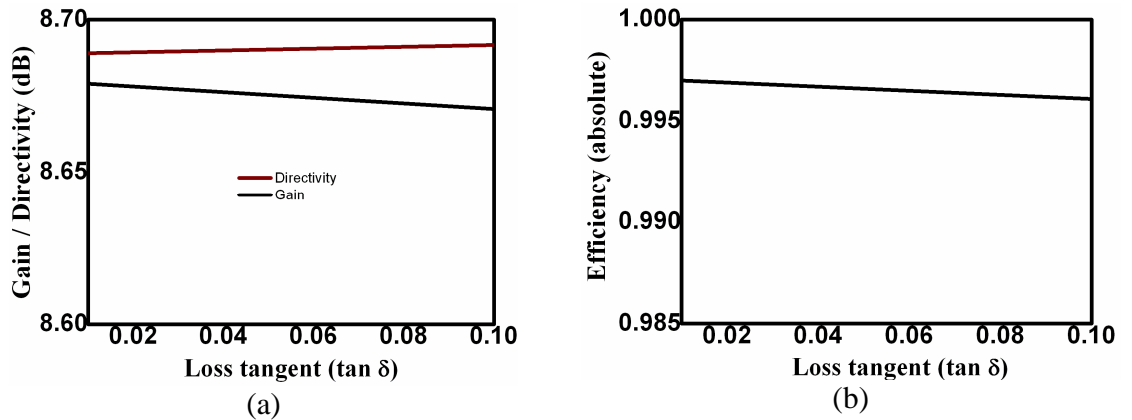


Figure 3.25 Simulated gain and directivity parameters of the microstrip fed micromachined aperture coupled patch antenna device varying SU8 dielectric loss tangent at 13.1 GHz. (b) Simulated efficiency parameters of the micromachined patch antenna device for different SU8 polymer rim thickness at 13.1 GHz

Antenna simulations are also performed by varying the dielectric loss tangent of the SU8-100 material from 0.01 to 0.1. The variation in directivity and gain is about 0.02 dB with the variation in polymer rim dimensions as shown in Figure 3.23 (a). The variation in antenna efficiency is minimal and is about 0.01%. This shows that the variation in loss tangent has a minimal effect on the antenna characteristics of the micromachined antenna device.

3.6 A MICROSTRIP FED MICROMACHINED APERTURE COUPLED STACKED ANTENNA DEVICE

A microstrip fed micromachined aperture coupled stacked antenna device has been designed and will be analysed in this section. The aperture coupled device is impedance matched for wideband operation.

3.6.1 Antenna design and simulation

Figure 3.26 (a) and (b) show the cross sectional view of a microstrip fed micromachined aperture coupled stacked antenna and the top view of the coupling aperture and the microstrip on the substrate surfaces. In order to improve the bandwidth and efficiency of the resultant antenna device, suspended patches were used. The device consists of a double cladded microwave PCB substrate and two suspended patches which forms a stacked antenna device. The microstrip feed line on the bottom surface of the microwave substrate feeds the device through a rectangular coupling aperture in the ground plane on the top surface of the substrate. Table 3.3 shows a summary of the physical dimensions of the structure layers for the microstrip fed micromachined aperture coupled stacked antenna. The thickness, dielectric constant and loss tangent of the substrates are given in Table 3.4. The patches on thin film substrates are supported by micromachined polymer spacers to reduce the loss and hence to improve the gain of the device. The antenna elements are protected from moisture and environment by the cavities formed by the bonded polymer rings. A microwave PCB material (AD300A, Arlon MED) [122] was used as the base substrate and polyimide thin films (Du Pont) were used as the supporting substrates for the two suspended patches. The antenna device was designed for operation in the 8 – 12 GHz of frequency region with 40% of bandwidth.

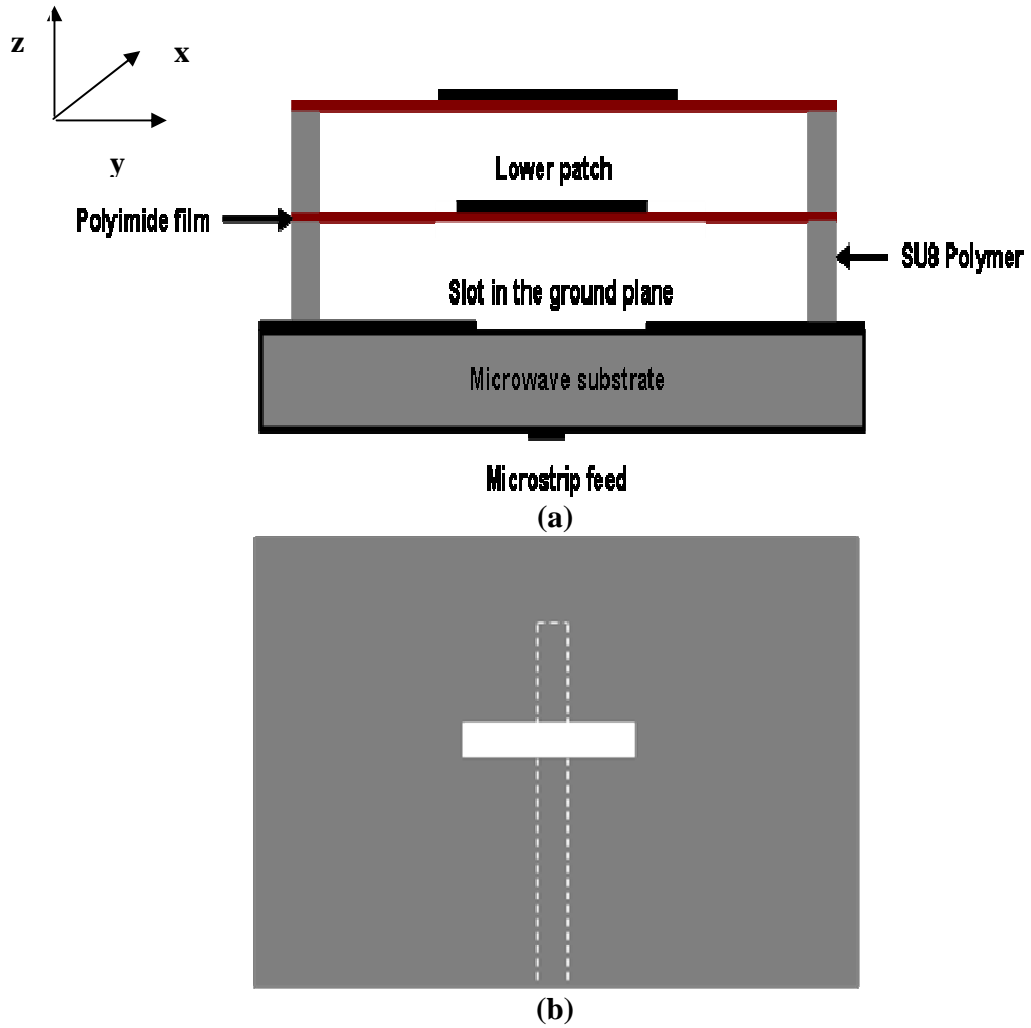


Figure 3.26 (a) Schematic cross-sectional views of the microstrip fed micromachined aperture coupled stacked antenna using micromachined polymer spacers. The top view of the apertures and feed lines on the substrate surface corresponding to (a) is shown in (b)

The design and modelling work for optimizing the antenna device was similar to that for the single patch device described in Section 3.5. For wideband operation the height of the top resonant patch to the ground is increased by stacking polymer rims. The top patch width is approximated by keeping a constant length from equation 3.30. For this stacked micromachined aperture coupled antenna device configuration, the air gaps between the upper patch element and the substrate (Figure 3.26) was chosen to increase the antenna bandwidth and at the same time to maintain a low profile (including fabrication challenges) for the overall antenna structures. For the microstrip fed device, the top patch and the aperture were designed to be in close resonance while the microstrip line and the lower patch was used as the impedance tuning element for wideband operation. The aperture

length was chosen to have a close resonance with that of the top patch again and the width was about one tenth of the length. The length of the feed line was then varied to obtain sufficient bandwidth. In order to obtain fixed band performance, the lengths of the top patch and the aperture were modified to tune the band of operation. Fine impedance tuning was achieved by adjusting the dimensions of the lower patch

Since the SU8 polymer is a lossy microwave material, the shape and dimensions of the SU8 spacer rings were chosen carefully to ensure good antenna performance. The dimensions of the SU8 rims were determined to obtain a small footprint and high gain for the resultant antenna devices. It was necessary to carry out several iterations of the above steps to obtain an optimized antenna structure for high gain wideband operation.

Table 3.2 Summary of the design parameters for the microstrip fed micromachined aperture coupled stacked antenna

Parameter	Dimensions (mm)
Lower patch width	5.8
Lower patch length	9
Upper patch width	9.6
Upper patch length	10.6
Patch thickness	0.009
Slot length	9.8
Slot width	0.98
Microstrip length	15.00
Microstrip width	0.82
Inner length of cavity	19
Inner width of cavity	19
Lower cavity height	2.2
Thickness of polymer rim	1.0
Upper cavity height	0.67

Table 3.3 Summary of electrical properties of substrates for microstrip fed micromachined aperture coupled stacked antenna device.

Substrate	Thickness (mm)	Dielectric constant	Loss tangent
Arlon substrate	1.51	3.0 [122]	0.003
Polyimide film	0.125	3.5 [120]	0.0026

3.6.2 Results and analysis

3.6.2.1 S parameters and study of the bandwidth

Figure 3.27 shows the results of S_{11} and VSWR parameters as a function of frequency. The impedance parameters are plotted in Figure 3.28.

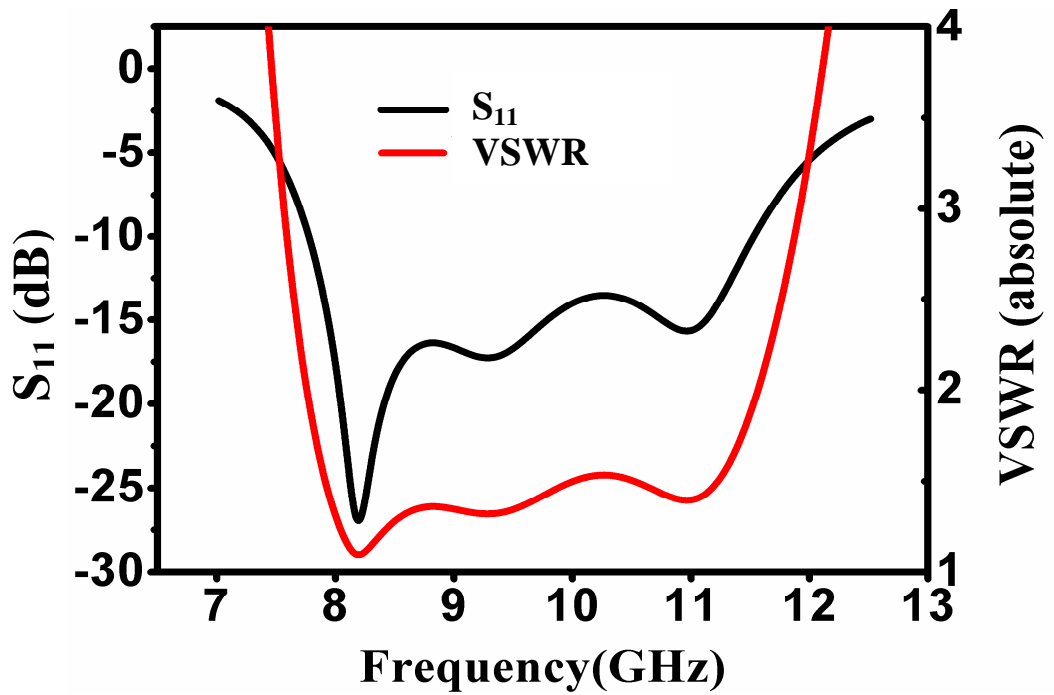


Figure 3.27 Simulated reflection coefficient and the VSWR parameters for the optimized microstrip fed micromachined aperture coupled stacked antenna device

It can be seen from the plot that the reflection coefficient (S_{11}) is lower than -10 dB from around 7.8 GHz and the VSWR are lower than a value of 2. The plot also shows that the reflection coefficient (S_{11}) is less than -5 dB from around 7.5 GHz to 12.5 GHz that corresponds to attenuation or a power loss of ~30%. The imaginary part of the input impedance curve from Figure 3.28 shows that the reactance switches from capacitive to

inductive twice indicating a double coupling mechanism for the aperture. The increase in bandwidth for this stacked micromachined patch antenna device is primarily due to the multiple resonance effects that include the TM_{10} resonances due to both magnetic and electric coupling (outlined in Section 3.3.1) between the top radiating patch and the aperture in the ground plane of the antenna device. The wide bandwidth characteristic for the antenna device has also been explained by both the electric and magnetic coupling of aperture to the top patch element in [19, 125].

Although the antenna structure can be used as a radiating element within this frequency range, it will be shown in the later sections that the gain and directivity of the structure is below 5 dBi even though the radiation efficiency is above 95%.

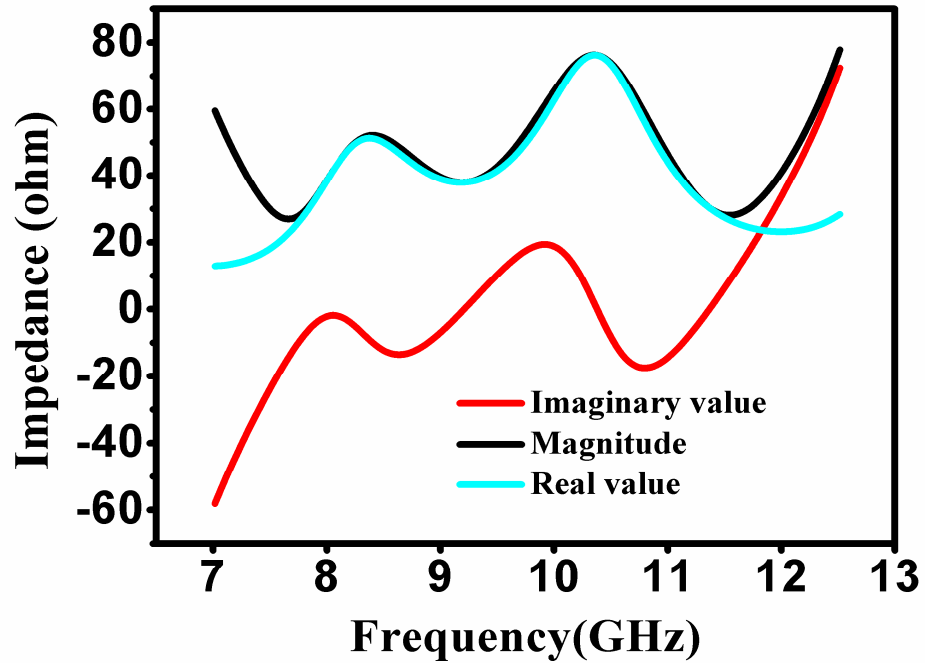
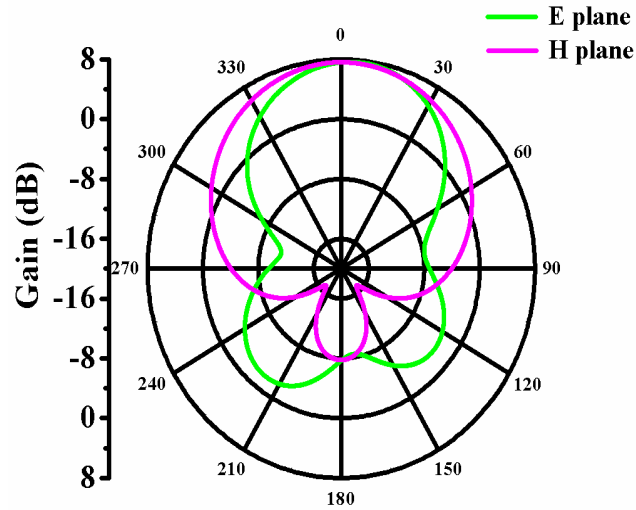


Figure 3.28 Simulated impedance parameters for magnitude, real and imaginary values for the optimized microstrip fed micromachined aperture coupled stacked antenna device

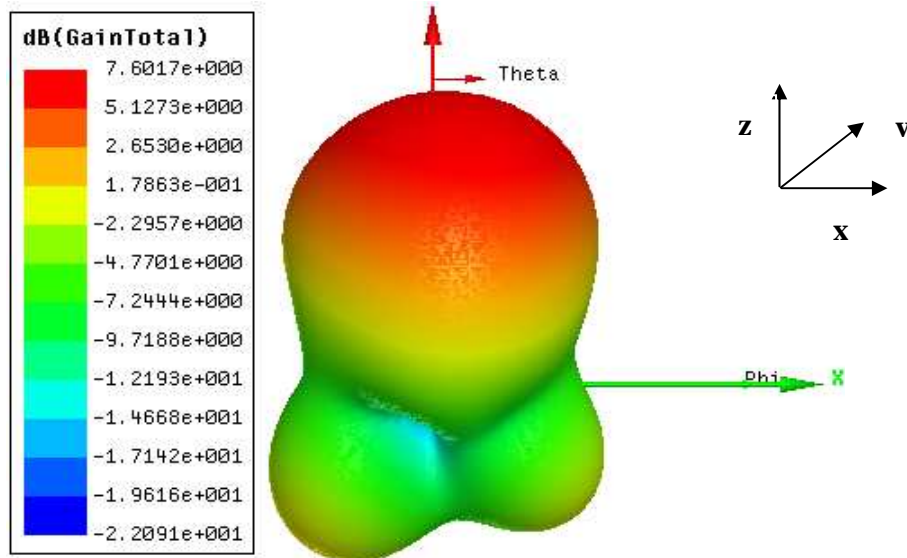
3.6.2.2 Normalised radiation patterns

Figure 3.29 shows the 2D and 3D far field patterns for the microstrip fed micromachined stacked patch antenna device. Normalised 3D radiation patterns for E plane and H plane are plotted at different frequencies. A complex coupling between the microstrip line and the radiating patch element through the aperture exists for this antenna device as presented in Section 3.3.1. The uncoupled fields to the patch element are radiated in the backward direction and hence the bulges in the radiation pattern on the backward direction. Figure

3.30 shows the polar radiation pattern curves from 7 GHz to 12 GHz. The E plane results show that there is an insignificant side lobe at the front side at lower frequencies but increasing with frequency. It is most significant at around 10 GHz. The radiation plots also show that there is significant back radiation for frequencies below 8 GHz and above 10 GHz. The minimum backward radiation for both E plane and H plane is around -12 dB in relative magnitude within the radiation bandwidth.

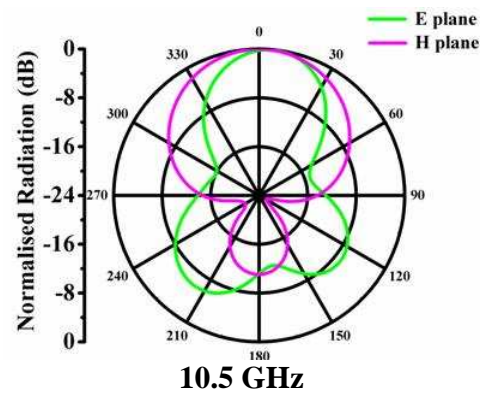
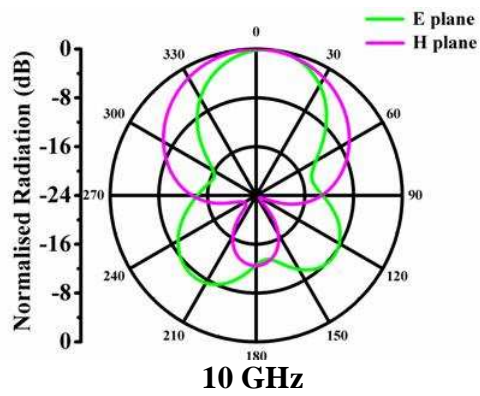
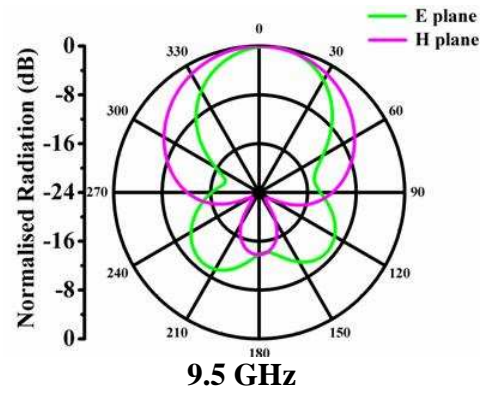
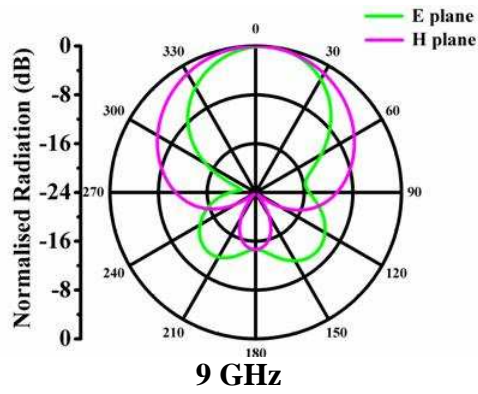
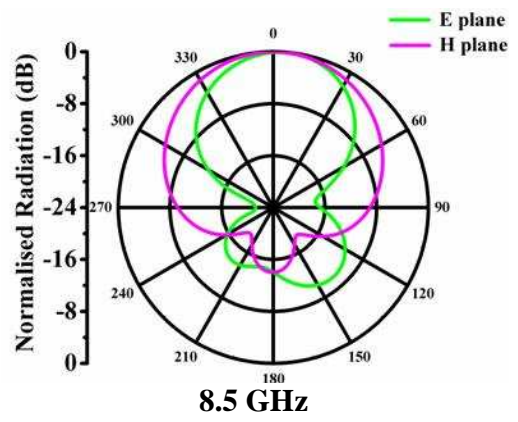
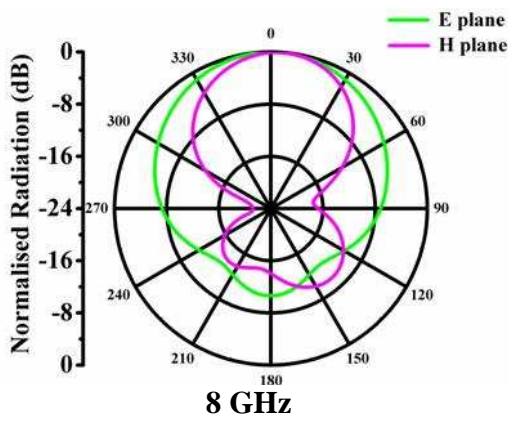
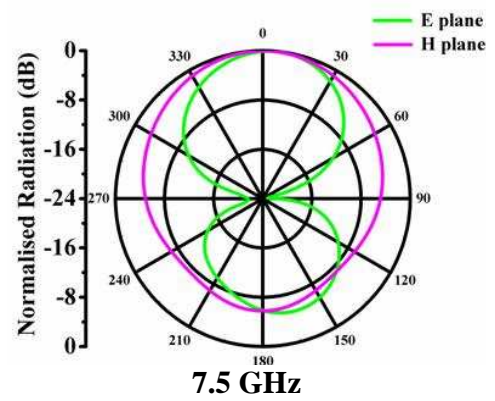
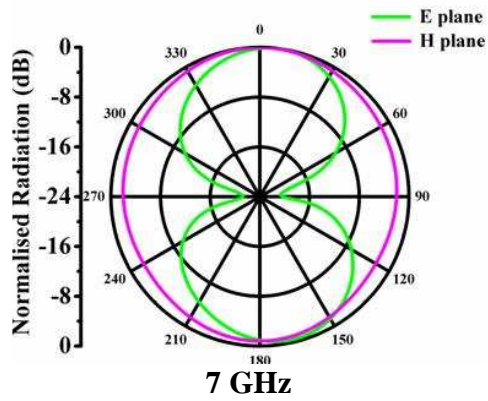


(a)



(b)

Figure 3.29 (a) 2D radiation patterns in E (x-z) plane and H (y-z) plane (b) 3D radiation patterns at 9.82 GHz for the optimized microstrip fed micromachined aperture coupled stacked antenna device



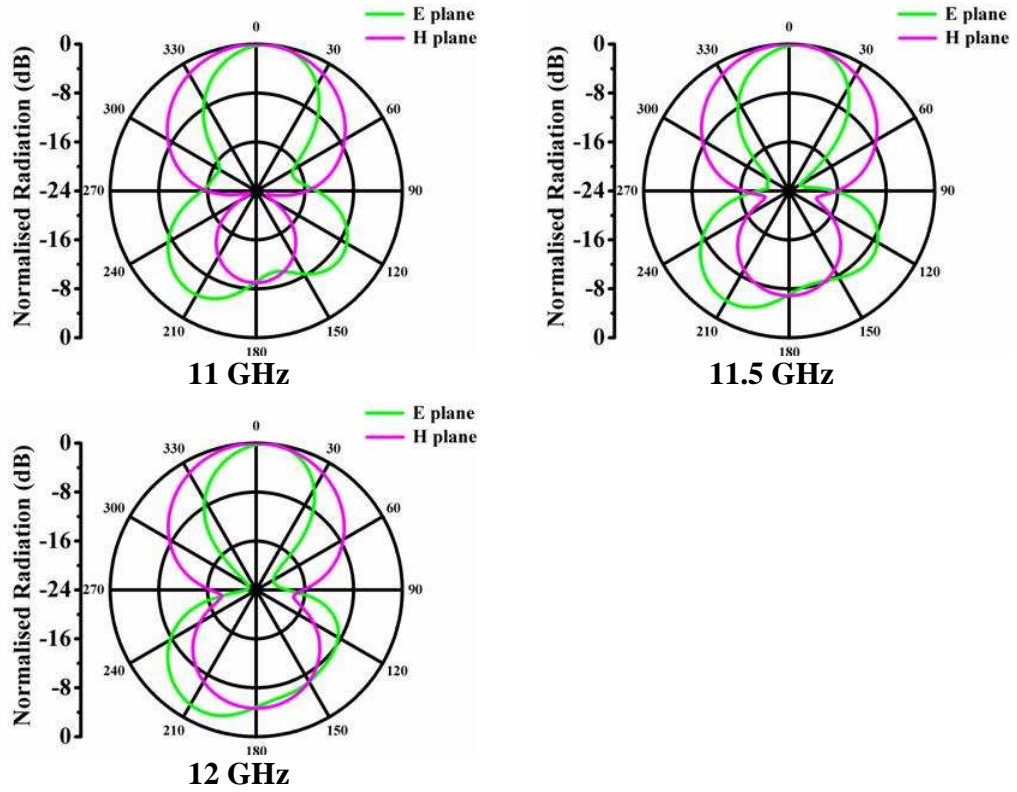


Figure 3.30 Simulated normalized E and H plane radiation patterns at different frequencies for the optimized microstrip fed micromachined aperture coupled stacked antenna device

It can also be seen that, the backward radiation in the E plane for the antenna device varies from 0 dB at 7 GHz to around -12 dB at 9.5 GHz and increases again to around -4 dB at 12 GHz. It can be concluded that the microstrip fed micromachined aperture coupled stacked antenna device possesses an improved front to back ratio in terms of radiation than with a micromachined aperture coupled single patch device.

3.6.2.3 Directivity and gain

Figure 3.31 shows the variation of directivity, gain and efficiency for the microstrip fed micromachined aperture coupled stacked antenna device with respect to frequency from 7 GHz to 12 GHz. It can be seen from the plot that the gain curve follows the directivity curve suggesting almost 96% radiation efficiency within the radiation bandwidth region. The gain and efficiency vary from about 2 dBi at 7 GHz to around 7.8 dBi at around 9.5 GHz and falls back below 7 dBi at 12 GHz. The variation of directivity and gain within the radiation bandwidth is below 1 dBi while it varies significantly out of the radiation bandwidth. The radiation efficiency varies from about 0.91 to close to 0.96 at 10 GHz.

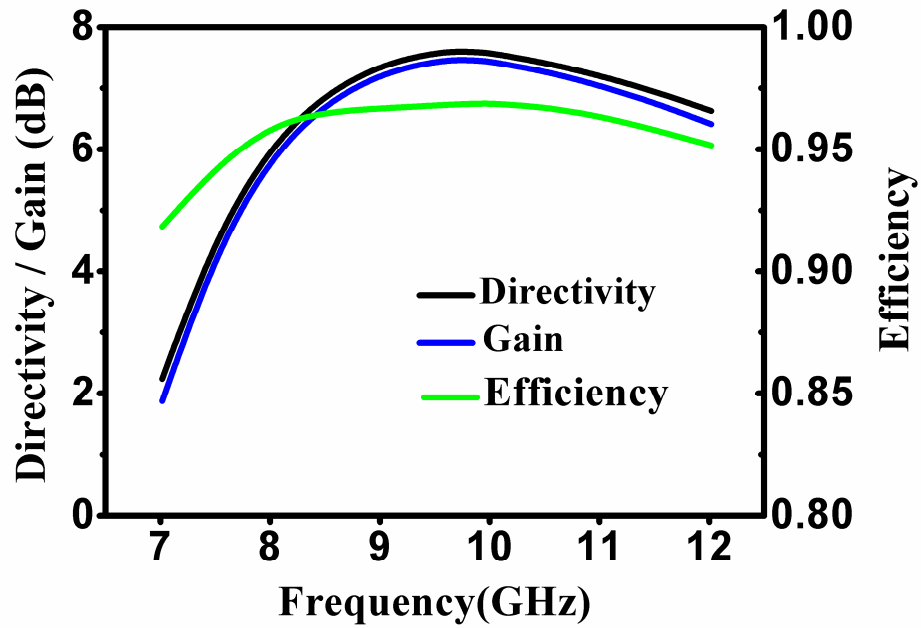


Figure 3.31 Simulated gain, directivity and radiation efficiency of the optimized microstrip fed micromachined aperture coupled stacked antenna device

3.7 A CPW FED MICROMACHINED APERTURE COUPLED STACKED ANTENNA DEVICE

3.7.1 Antenna design and simulation

A CPW feed will reduce the backward radiation for an aperture coupled antenna device. Also the feeding scheme will be easier for integration with other passive devices. Hence a CPW fed micromachined aperture coupled stacked antenna device was designed. The design follows a methodology similar to that of the microstrip fed antenna device. The layout of the CPW feed, aperture and the schematic of the antenna device are shown in Figure 3.32. The CPW feed line and the ground plane is on the same side of the microwave substrate and there is no further ground plane on the bottom side of the substrate. The antenna device was designed for operation in the 7 – 10 GHz of frequency region with >40% of bandwidth. The design procedure is similar to in Section 3.5.1. The bandwidth for the antenna device is to be increased by coupling of the top patch elements possessing identical dimensions. It was known that a coupling of stacked identical patch elements produces two separate resonant frequencies one higher and the other lower than that of the resonant frequencies of the individual elements [25]. Thus, the aperture and the top two patches were designed to be in close resonance. The bottom patch and the $\lambda/4$ stub are

adjusted to obtain impedance matching operation with wide bandwidth. The top patch and the middle patch width are approximated by Equations 3.29 and 3.30. For this CPW fed stacked micromachined aperture coupled antenna device configuration, the top patch elements and the aperture were designed to be in close resonance while the microstrip line stub and the lower patch was used as the impedance tuning element for wideband operation. Fine impedance tuning was achieved by adjusting the dimensions of the lower patch. Table 3.5 shows a summary of the physical dimensions of the structure layers for CPW antenna device. The thickness, dielectric constant and loss tangent of the substrates are given in Table 3.6.

Table 3.4 Summary of the design parameters for the CPW fed micromachined aperture coupled stacked antenna device

Parameter	Dimensions (mm)
Lower patch width	9.4
Lower patch length	18
Upper patch width	12.6
Upper patch length	18
Patch thickness	0.009
Aperture length	16.5
Aperture width	1.6
Microstrip length	18.2
Microstrip width	1.4
Inner length of cavity	18.2
Inner width of cavity	18.2
Lower cavity height	1.0
Thickness of polymer rim	1.0
Upper cavity height	1.0

In this device, three stacked patches were used to increase the bandwidth. A single cladded PTFE material (Taconic TLY-3-0200-CH/CH) [126] was used as the substrate for the CPW line and the coupling aperture.

Table 3.5 Summary of the electrical properties of substrates for CPW fed micromachined aperture coupled stacked antenna device

Substrate	Thickness (mm)	Dielectric constant	Loss tangent
Taconic PTFE substrate	0.5	2.2 [126]	0.0009
LCP film	0.10	3.2 [71]	0.002

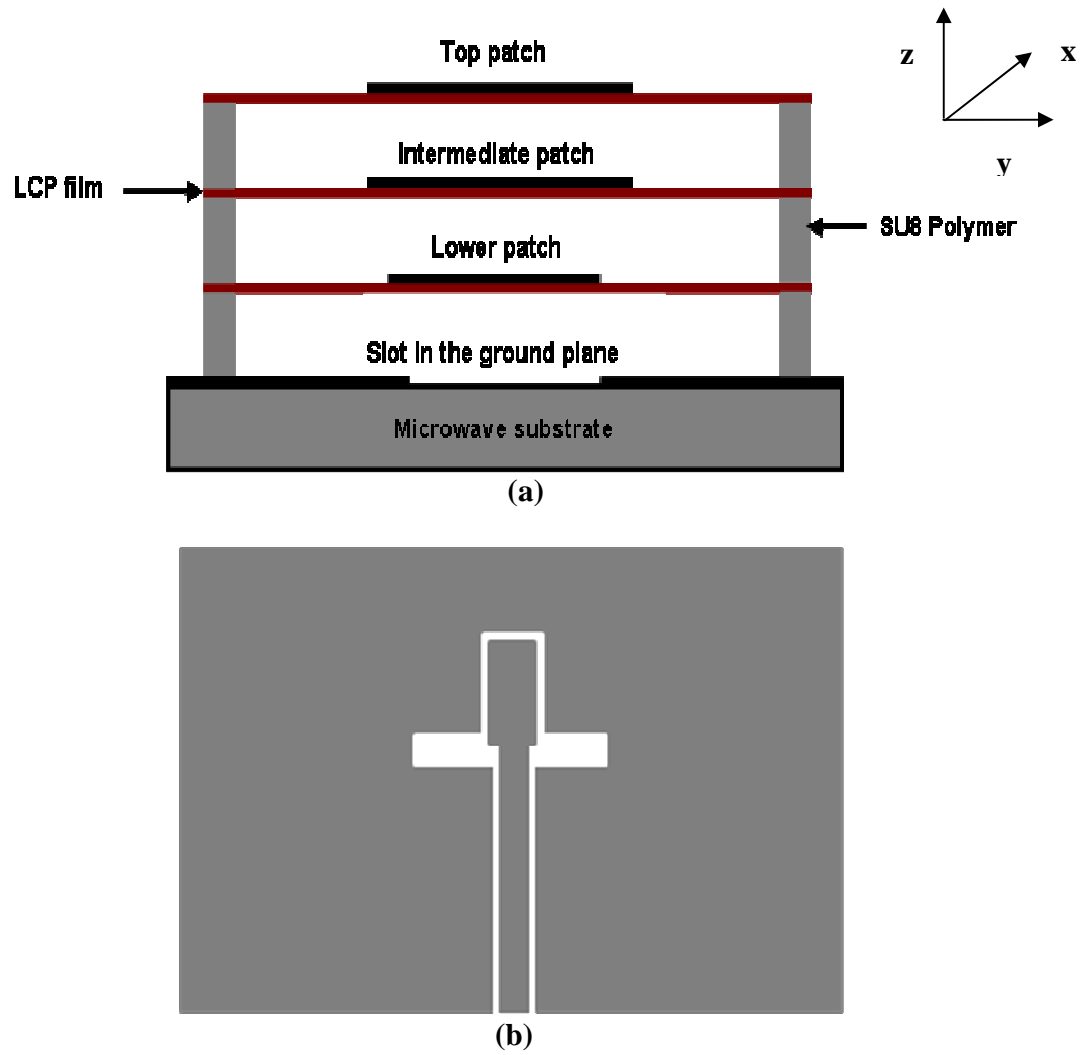


Figure 3.32 Schematic cross-sectional views of the stacked CPW fed micromachined aperture coupled stacked antenna using micromachined polymer spacers, (a) CPW fed device. The top view of the apertures and feed lines on the substrate surface corresponding to (a) is shown in (b)

3.7.2 Results and discussion

3.7.2.1 *S* parameters and study of the bandwidth

The stacked patches are suspended symmetrically above the aperture using micromachined SU8 polymer rims. The reflection coefficient (S_{11}) and VSWR parameters are plotted as a function of frequency from 6 – 10.5 GHz as shown in Figure 3.33. The impedance parameters are plotted in Figure 3.34. It can be seen from the plot that the reflection coefficient (S_{11}) is lower than -10 dB and the VSWR lower than a value of 2 at 6.5 GHz. The plot also shows that the reflection coefficient (S_{11}) is less than -5 dB from around 6 GHz to 10 GHz that corresponds to attenuation or a loss of 30% power.

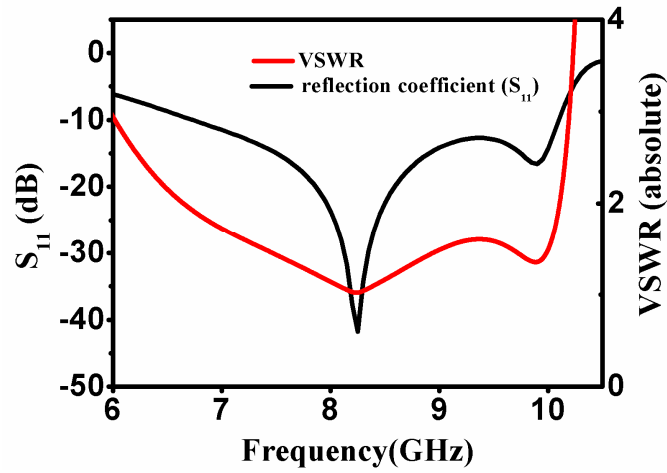


Figure 3.33 Simulated reflection coefficient and the VSWR parameters for the optimized CPW fed micromachined aperture coupled stacked antenna

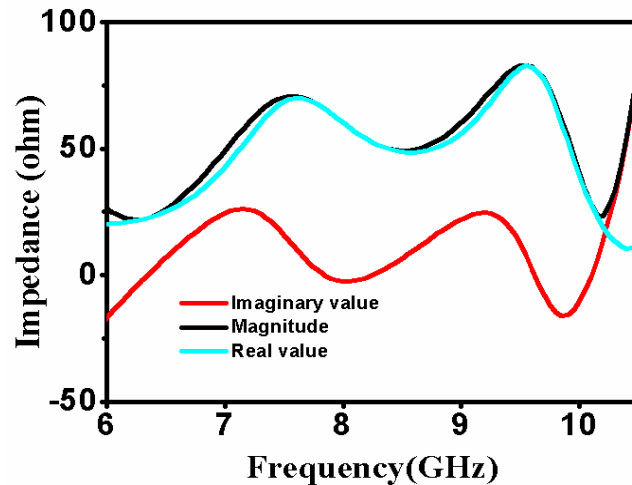


Figure 3.34 Simulated impedance parameters for magnitude, real and imaginary values for the optimized CPW fed micromachined aperture coupled stacked antenna

The imaginary part of the input impedance curve from Figure 3.34 shows that the reactance switches from capacitive to inductive twice indicating a double coupling mechanism. The wide bandwidth characteristic for the antenna device can be explained by the magnetic coupling of aperture to the top patch element and the mutual coupling between the patch elements [25]. The electric field coupling between the aperture and the top patch element is not present as it is seen that the bandwidth reduced when the middle patch element is removed. The simulated bandwidth for the antenna device is 3.29 GHz.

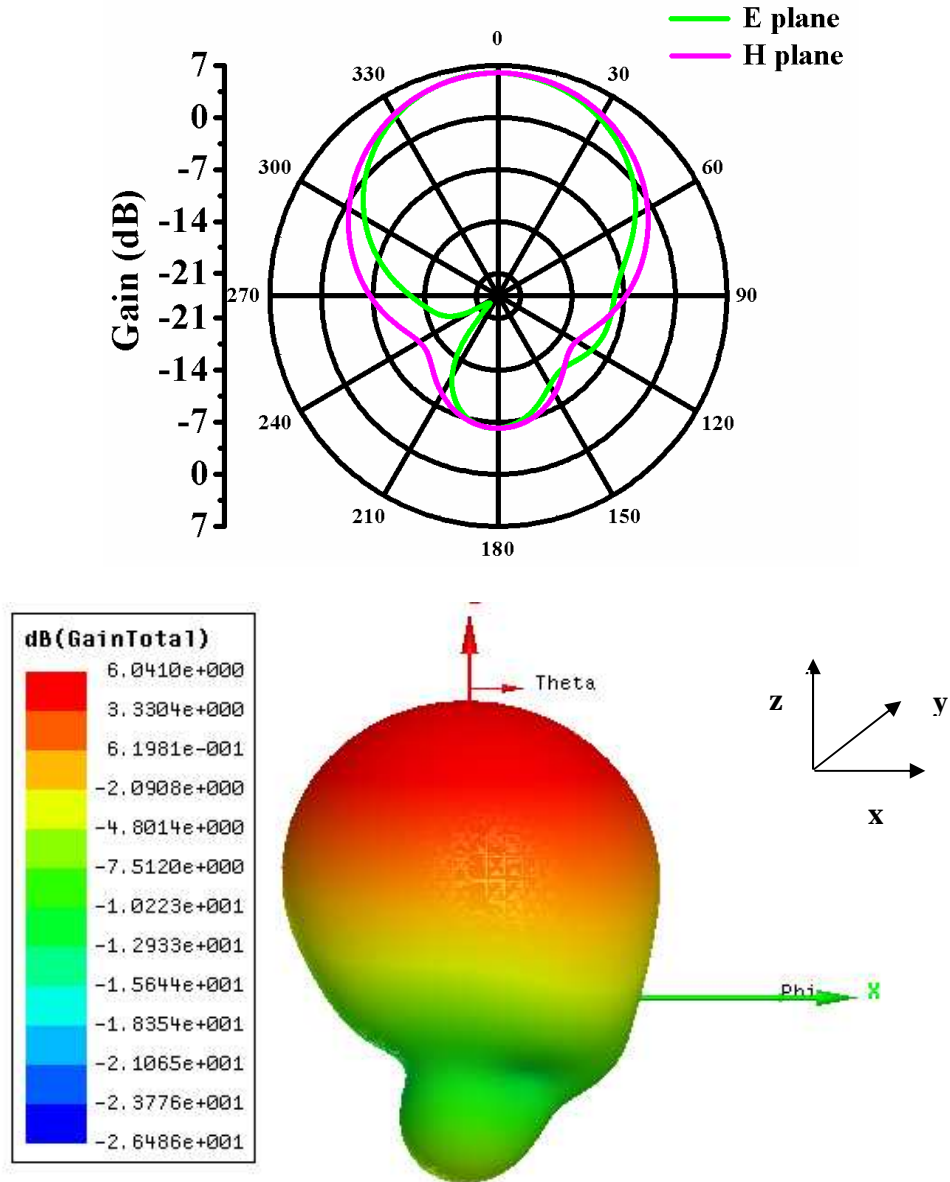
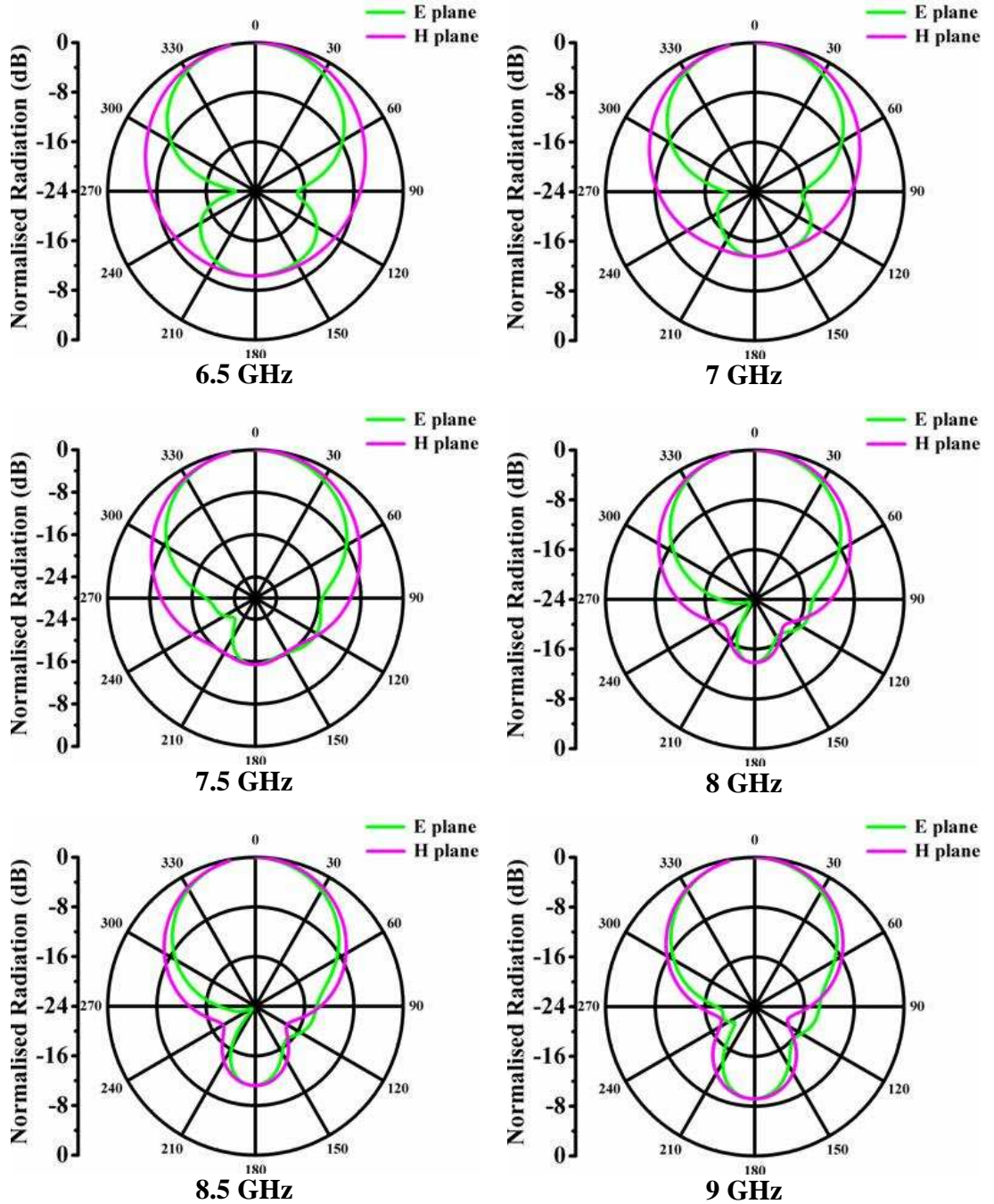


Figure 3.35 (a) 2D radiation patterns in E (x-z) plane and H (y-z) plane and (b) 3D radiation patterns for the optimized CPW fed micromachined aperture coupled stacked antenna at 8 GHz

3.7.2.2 Normalised radiation patterns

Figure 3.35 shows the 2D and 3D far field pattern for the CPW fed micromachined aperture coupled stacked antenna device. The normalised radiation patterns for the E plane and H plane of the 3 D radiation pattern are plotted at different frequencies.



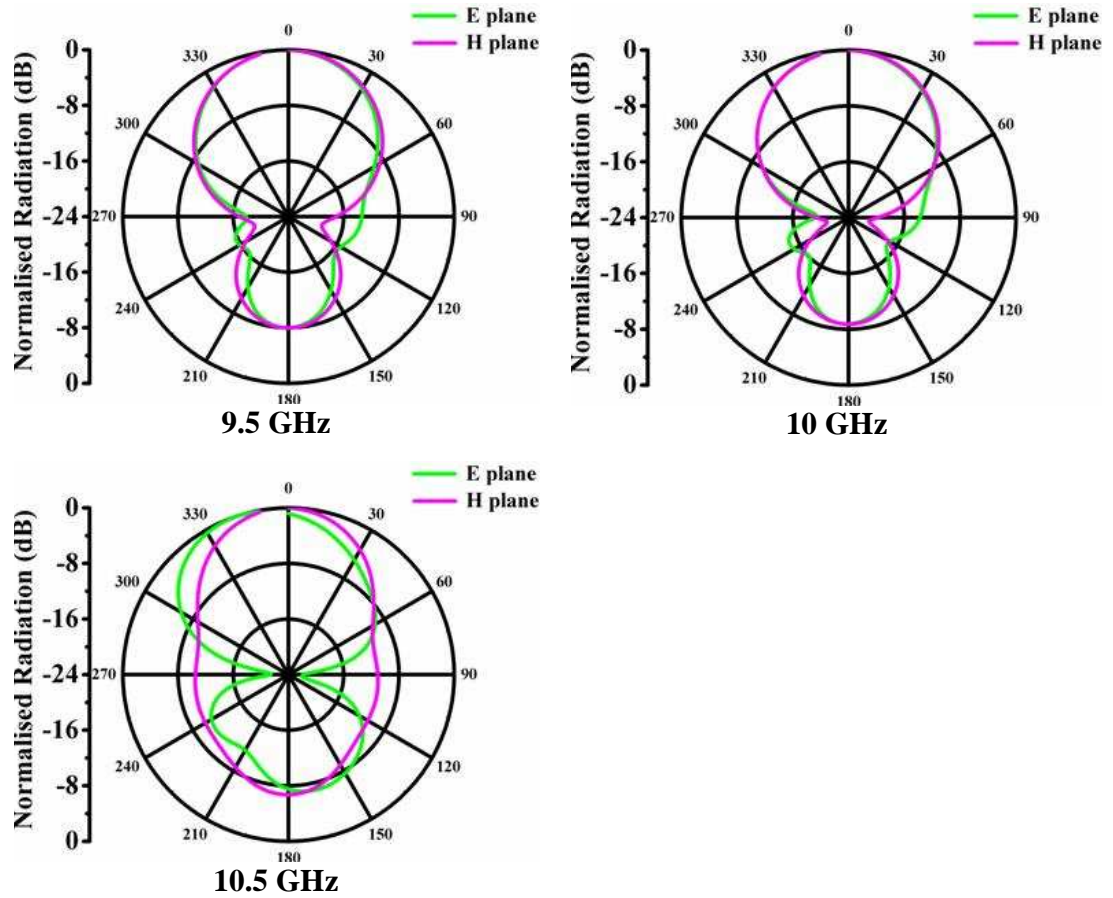


Figure 3.36 Simulated normalized E and H plane radiation patterns at different frequencies for the optimized CPW fed micromachined aperture coupled stacked antenna device

Figure 3.36 shows the polar radiation pattern curves from 6.5 GHz to 10.5 GHz. The E plane curve shows that there is no side lobe at the front side. The radiation plots also show that there is backward radiation for frequencies below 7 GHz and above 10 GHz. The minimum backward radiation for both E plane and H plane is around -17 dB within the radiation bandwidth. It can also be seen that, the backward radiation in the E plane for the antenna device varies from -12 dB at 6.5 GHz to around -17 dB at 7.5 GHz and increases again to around -8dB at 10.5 GHz. The variation in the radiation pattern can be attributed to the variation in the current distribution on the radiating patch elements with respect to frequency due to the electromagnetic coupling between the aperture and the radiating patch elements. From Section 3.3.1, the coupling mechanism is complex for an aperture coupled antenna device that involves combination of electric and magnetic coupling with respect to frequency. The field coupling is thus efficient from 7 GHz to 10 GHz that shows a backward radiation less than -8dB while it is inefficient below 7 GHz and 10 GHz. It can

also be concluded that the CPW fed micromachined aperture coupled stacked antenna device provides an improved front to back ratio in terms of radiation than the microstrip fed antenna devices.

3.7.3 Effect of different substrate material

In order to determine the effect of spacer material on stacked patch antennas, and PTFE based stacked CPW antenna designs with similar dimensions as that of the CPW antenna shown in Figure 3.32, were designed and optimized for impedance matched performance. These two devices consist of 4 layers of FR4 or PTFE material with three stacked patches. The dielectric constant and the loss tangent for the FR4 material were taken as 4.2 and 0.020 respectively [54]. Figure 3.37, Figure 3.38 and Figure 3.39 shows the reflection coefficient, efficiency and gain as a function of frequency for the three CPW fed micromachined aperture coupled stacked antenna configurations. The rapid decrease of gain above 9 GHz of the FR4 based device is due to the increased reflection coefficient as the frequency is out of the band of operation.

Table 3.6 Summary of the antenna performance parameters for different antenna configurations

CPW fed antenna design	Bandwidth (%)	Peak gain (dBi)	Efficiency (%)
Suspended patches on PTFE substrate	38.3	7.8	97.5
Stacked PTFE substrates	30.1	7.9	99
Stacked FR4 substrates	32.7	3.6	75

It can be seen that there is little difference between the gain values of the stacked patch antenna based on multiplayer PTFE material and the device with suspended patch elements since the dielectric loss is low in both designs. However, the micromachined device has a larger bandwidth. The performance of the FR4 based multilayer antenna is much poor due to the well known lossy behaviour of the FR4 material beyond the GHz frequency region. Table 3.7 gives a summary of the performance parameters. The bandwidth of the antennas was determined from the simulation results of the reflection characteristics. The antenna device with suspended patches showed the best bandwidth of about 38% close to that

required for ultra-wide band applications. The present CPW fed micromachined aperture coupled antenna device and the stacked taconic based antenna device are more efficient than the stacked FR4 or the antenna with FR4 as the base substrate. This is due to the higher substrate dielectric losses because of the higher dielectric and loss tangent values for the FR4 substrate. The effects of dielectric properties on the quality factor and there by the performance on the patch antenna device are outlined in Section 2.2.2.

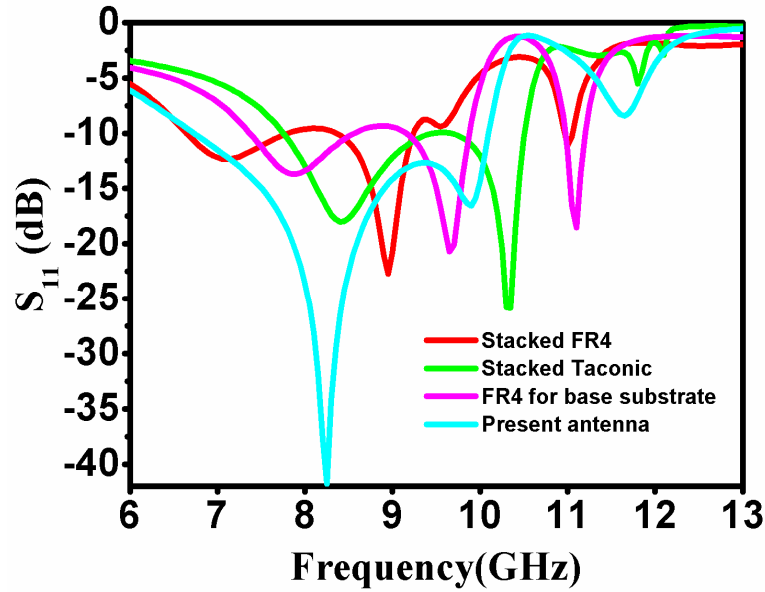


Figure 3.37 Reflection coefficient (S_{11}) results of the CPW fed micromachined aperture coupled stacked antenna for different substrate configurations

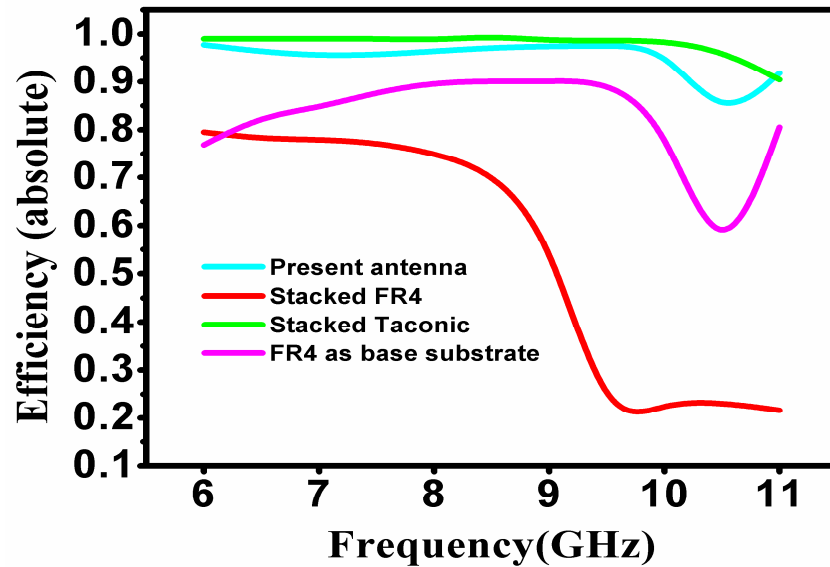


Figure 3.38 Antenna efficiency results of the CPW fed micromachined aperture coupled stacked antenna for different substrate configurations

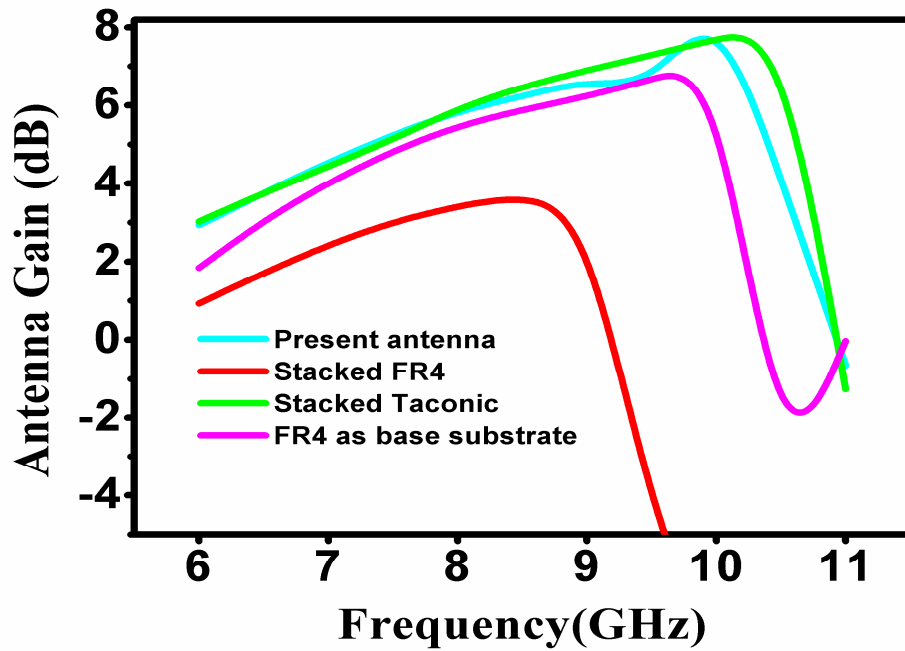


Figure 3.39 Antenna gain results of the CPW fed micromachined aperture coupled stacked antenna for different substrate configurations

3.8 A MICROSTRIP FED MICROMACHINED APERTURE COUPLED SUBARRAY ANTENNA DEVICE

A microstrip fed micromachined aperture coupled subarray configuration has been developed to achieve higher antenna gain values for the microstrip based planar patch antenna array configurations with a fewer number of elements and smaller array size [127-129]. This concept can be extended for micromachined devices to achieve efficient subarray antenna configurations. Micromachining of SU8 has been employed to fabricate compact, efficient higher gain and bandwidth antenna device at microwave frequencies. A microstrip fed stacked patch antenna with a 2 x 2 subarray of patches is studied in this section.

3.8.1 Antenna design and simulation

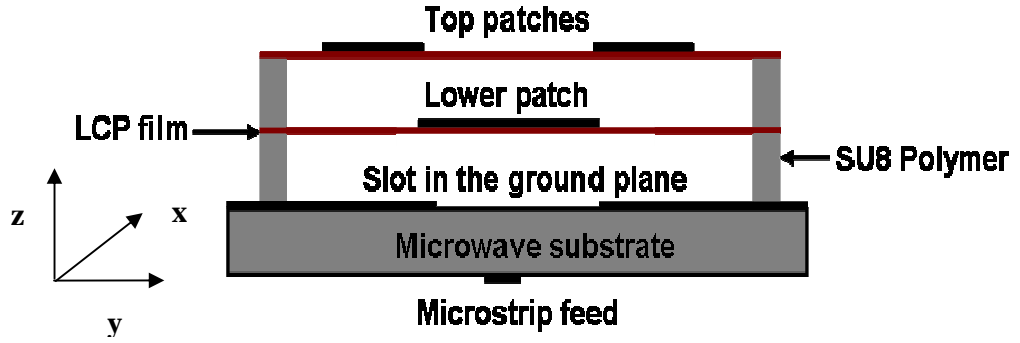
The microstrip fed micromachined aperture coupled subarray antenna device was designed for compactness and enhanced antenna.

Table 3.7 Summary of the electrical properties of substrates for microstrip fed micromachined aperture coupled subarray antenna

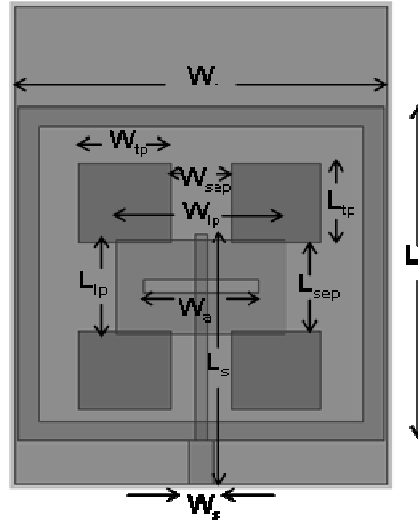
Substrate	Thickness (mm)	Dielectric constant	Loss tangent
Arlon substrate	1.51	3.0 [122]	0.003
LCP film	0.1	3.2 [71]	0.002

Table 3.8 Summary of the design parameters for the microstrip fed micromachined aperture coupled subarray antenna device

Parameter	Microstrip fed device (mm)
Lower patch width	7.4
Lower patch length	13
Upper patch width	6.2
Upper patch length	7
Patch thickness	0.009
Aperture length	9
Aperture width	1.02
Microstrip length	20.1
Microstrip width	0.82
Inner length of cavity	23
Inner width of cavity	25
Lower cavity height	1.2
Thickness of polymer rim	1.1
Upper cavity height	1.2
LCP film thickness	0.1



(a)



(b)

Figure 3.40 Schematic of the microstrip fed micromachined aperture coupled subarray antenna device. The top view of the apertures and feed lines on the substrate surface corresponding to (a) is shown in (b). $W_{tp}=7$ mm, $L_{tp}=6.2$ mm, $L_{ip}=7.4$ mm, $W_{ip}=13$ mm, $L_s=20.1$ mm, $W_s=3.3$ mm, $W_a=9$ mm, $L_{sep}=6.8$ mm, $W_{sep}=4.6$ mm, $L_r=26$ mm, $W_r=28$ mm

Figure 3.40 shows the cross-sectional and top view of the device. The design and modelling work for optimizing the antenna device was carried using the principles outlined in Section 3.5. A microwave PCB material (AD300A, Arlon MED) was used as the substrate. The dielectric constants of the LCP film, the SU8 polymer and the microwave substrate are 3.5, 4.2 and 3 while the corresponding loss tangents are 0.0026, 0.042 and 0.003 respectively. The dimensions of the polymer rim were chosen so as to achieve high efficiency and compact size for the stacked antenna in the simulation. The device was expected to operate at the operation frequency of range 10 to 16 GHz with a wide bandwidth of about 6 GHz. To form a stacked micromachined quad antenna subarray device, the device consists of a double cladded microwave PCB substrate and five

suspended patches. The device is fed through a microstrip and the intermediate patch element on a thin LCP substrate is excited through an aperture in the ground plane. The top layer consists of four patch elements separated by optimum distances as shown in Figure 3.40 (b). Micromachined polymer rim spacer forms an air cavity between the ground and the intermediate patch layer. A similar micromachined polymer rim configuration supports the top subarray patch elements. The top patch and the middle patch width are approximated by Equations 3.29 and 3.30. For this CPW fed stacked micromachined aperture coupled antenna device configuration, the top patch elements and the aperture were designed to be in close resonance while the microstrip line stub and the lower patch was used as the impedance tuning element for wideband operation. Fine impedance tuning was achieved by adjusting the dimensions of the lower patch. The aperture length was chosen to have a close resonance with that of the patches and the width was about one tenth of the length. The heights of the air cavities were chosen based on a trade-off between the bandwidth and the challenges for fabrication. The length of the feed line was then varied to obtain maximum bandwidth. The lengths of the top radiating patch elements were fixed owing to the space limitations. In order to obtain fixed band performance, the length of the aperture and the microstrip line were adjusted to tune the band of operation. Fine impedance tuning was achieved by adjusting the dimensions of the lower patch. The dimensions of the SU8 rims were determined to obtain a small footprint and higher antenna efficiency for the resultant antenna devices. It was necessary to carry out several iterations of the above steps to obtain an optimized antenna structure for high gain wideband operation. Table 3.8 and Table 3.9 show the electrical properties of the substrate and the design parameters for the microstrip fed micromachined aperture coupled subarray antenna.

Figure 3.41 shows the electric and magnetic fields for the microstrip fed micromachined aperture coupled subarray antenna structure at 9.82 GHz. The fields are plotted in vector and scalar form. The field plots show that at the frequency of interest 9.82 GHz which is the efficient radiating frequency for the antenna structure, the fields satisfies the TM_{100} mode at this resonant frequency. The plot also shows that on the ground plane, there are also electric and magnetic fields that correspond to the propagating quasi-TEM (transverse electromagnetic mode) mode on the microstrip transmission line underneath the ground plane. The electric and magnetic fields also indicate that there is reduced backward

radiation that corresponds to these fields and there by increasing the front to back ratio of the radiation pattern.

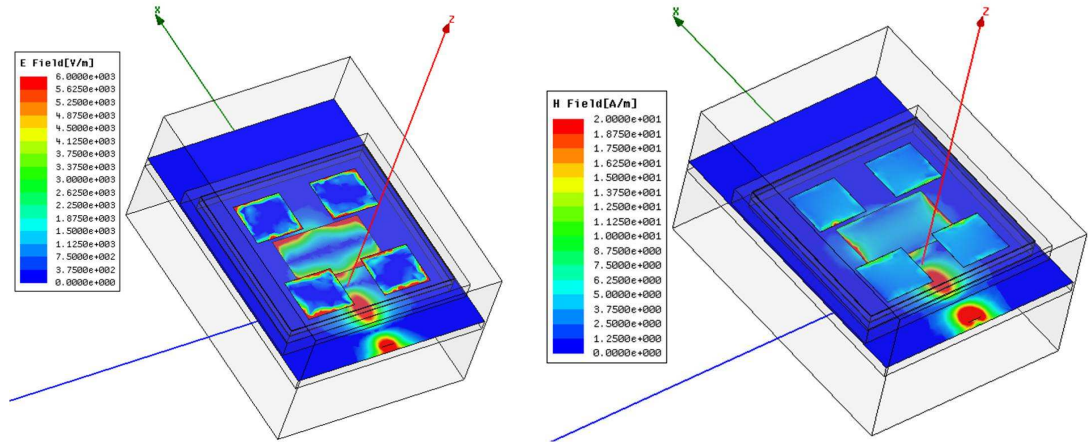


Figure 3.41 Field model showing the scalar (a) electric and (b) magnetic fields for the microstrip fed micromachined aperture coupled subarray antenna device at 13 GHz

3.8.2 Results and discussion

3.8.2.1 S parameters and study of the bandwidth

To determine the performance of micromachined subarray antenna device, the reflection coefficient (S_{11}) and VSWR parameters are plotted to determine the -10 dB bandwidth after optimising the antenna performance. The reflection coefficient (S_{11}) parameters are plotted as a function of frequency as shown in Figure 3.42.

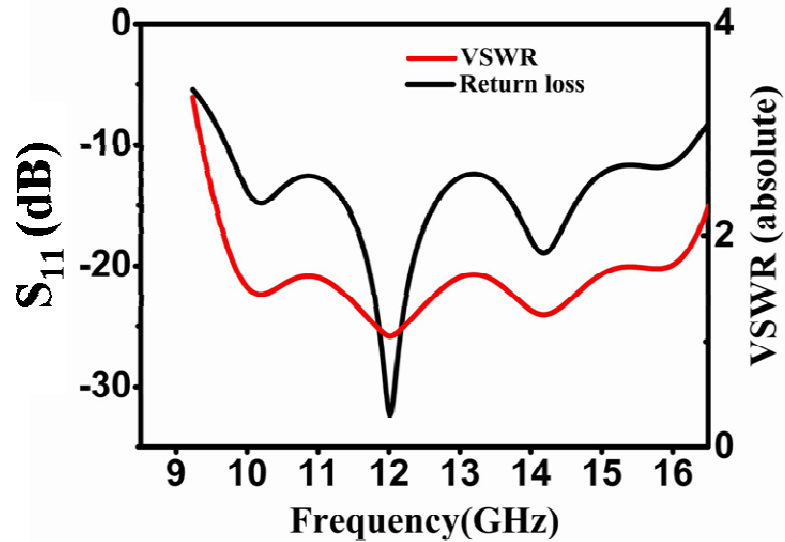


Figure 3.42 Simulated reflection coefficient and the VSWR parameters for the optimized microstrip fed micromachined aperture coupled subarray antenna

The impedance parameters are plotted in Figure 3.43. It can be seen from the plot that the reflection coefficient (S_{11}) is lower than -10 dB from around 9.72 GHz to 16.3 GHz and the VSWR is lower than a value of 2. The plot also shows that the reflection coefficient (S_{11}) is less than -5 dB from around 9.5 GHz to 16.5 GHz that corresponds to attenuation or a loss of ~ 30% of RF power. The impedance plot shows that the real and total magnitude of the impedance lies in between 25 to 80 Ω and the imaginary oscillated from capacitive to inductive and is in between -35 to 20 Ω . The bandwidth for the antenna device is about 6.5 GHz. The lower patch, the top four patches function as the resonators and the coupling between all these elements have resulted in a wide bandwidth device.

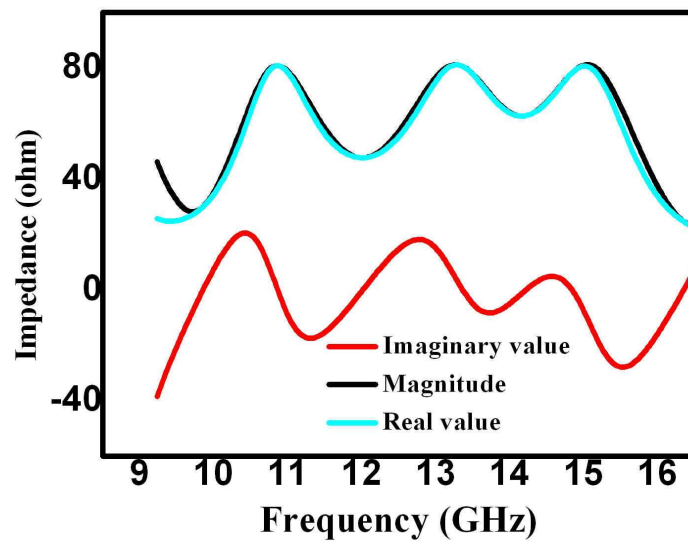


Figure 3.43 Simulated impedance parameters for magnitude, real and imaginary values for the optimized microstrip fed micromachined aperture coupled subarray antenna

3.8.2.2 Normalised radiation patterns

Figure 3.44 shows the 2D and 3D far field patterns for the microstrip fed micromachined subarray antenna device. The normalised radiation patterns for the E plane and H plane are plotted at different frequencies. Figure 3.45 shows the polar radiation pattern curves for the frequency value of 9.5 GHz to 16.5 GHz. The E plane curve shows that there is a significant side lobe in the front side which is seen at 14.5 GHz increasing with frequency and maximizes at 16 GHz. The radiation plots also show that there is significant backward radiation for frequencies below 10.5 GHz and above 15.5 GHz. The minimum backward radiation for both E plane and H plane is around -12 dB in relative magnitude within the radiation bandwidth.

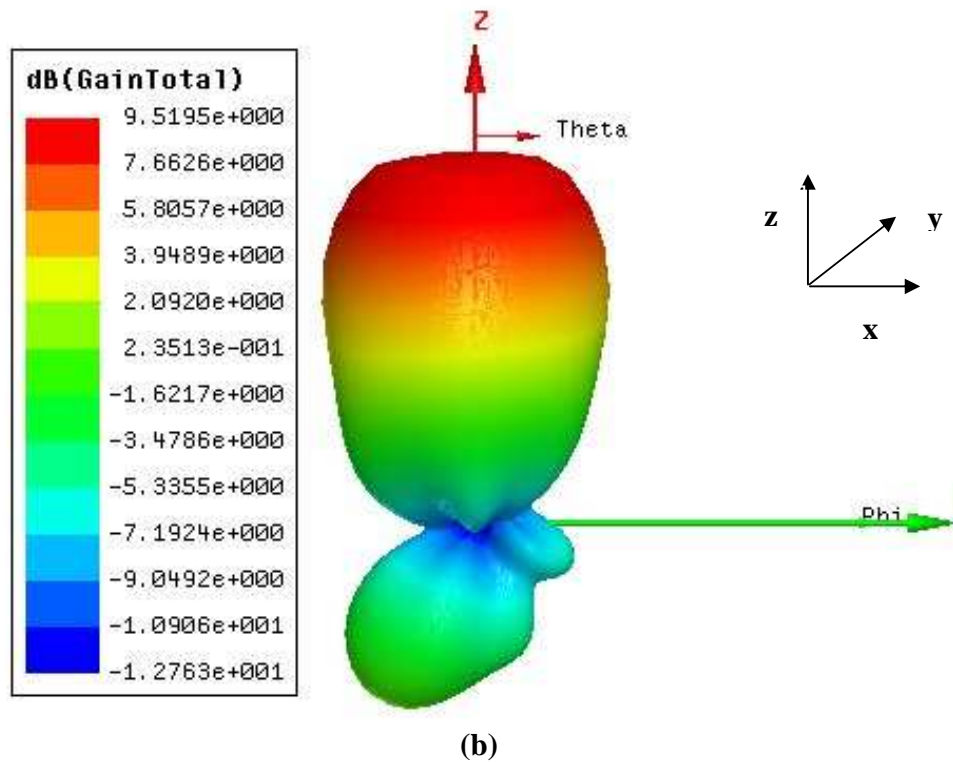
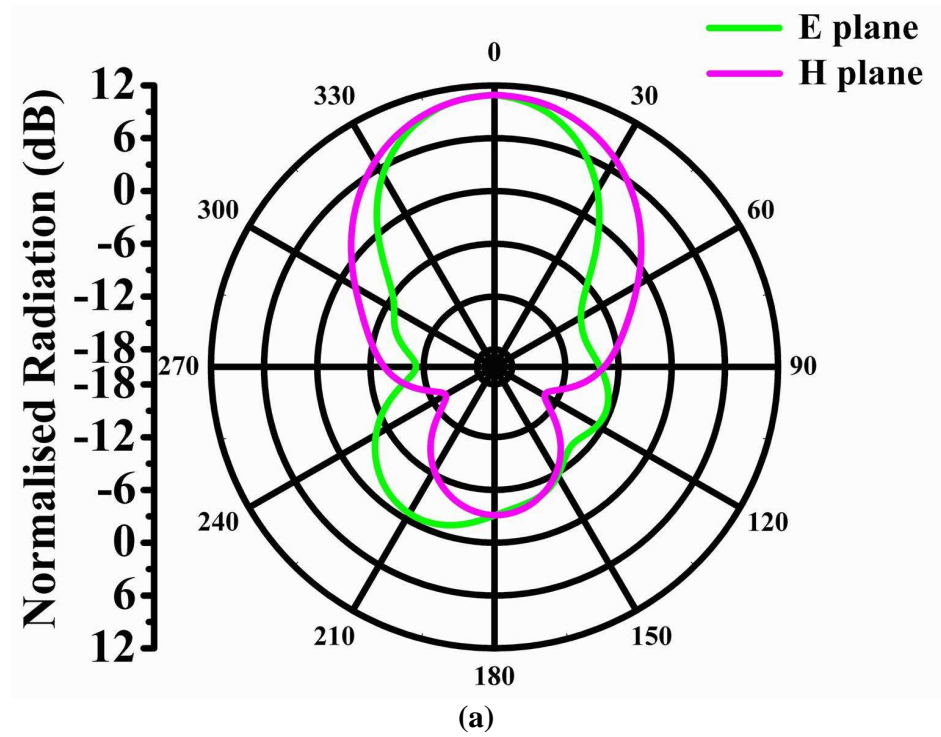


Figure 3.44 (a) 2D radiation patterns in E (x-z) plane and H (y-z) plane and (b) 3D radiation pattern at 11 GHz for the microstrip fed micromachined aperture coupled subarray antenna

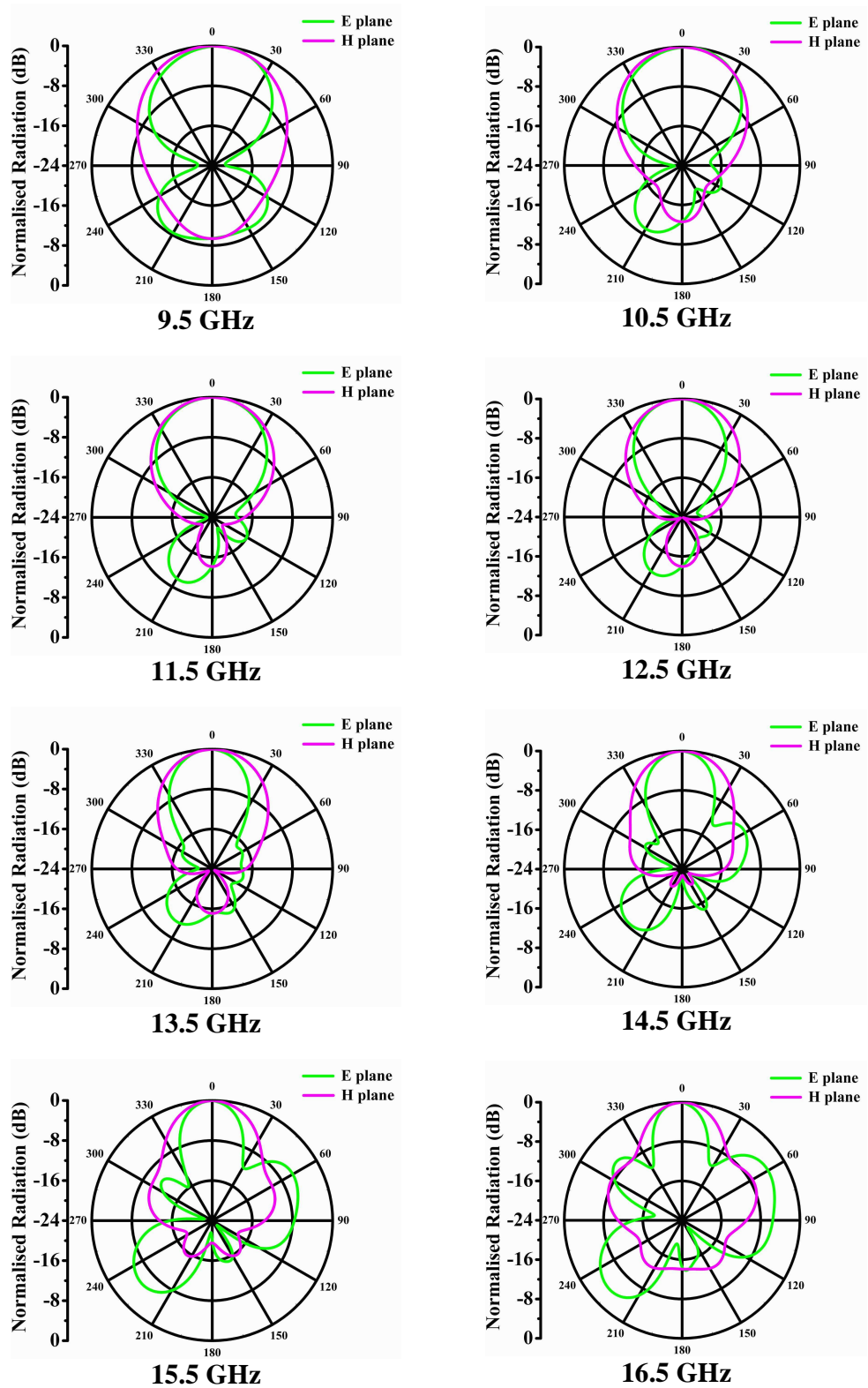


Figure 3.45 Simulated normalized E and H plane radiation patterns at different frequencies for the microstrip fed micromachined aperture coupled subarray antenna

It can also be seen from Figure 3.45 that the backward radiation in the E plane for the antenna device varies from -8 dB at 9.5 GHz to around -12 dB at 13.5 GHz, and increases again to around -8 dB at 16.5 GHz. It can be concluded that the microstrip fed micromachined aperture coupled subarray antenna device has an improved front to back ratio over a micromachined aperture coupled stacked antenna device. However the side lobes in forward radiation are increased.

3.8.2.3 Directivity and gain

Figure 3.46 shows the directivity, gain and efficiency for the microstrip fed micromachined subarray antenna device with respect to frequency from 9.5 GHz to 16.5 GHz.

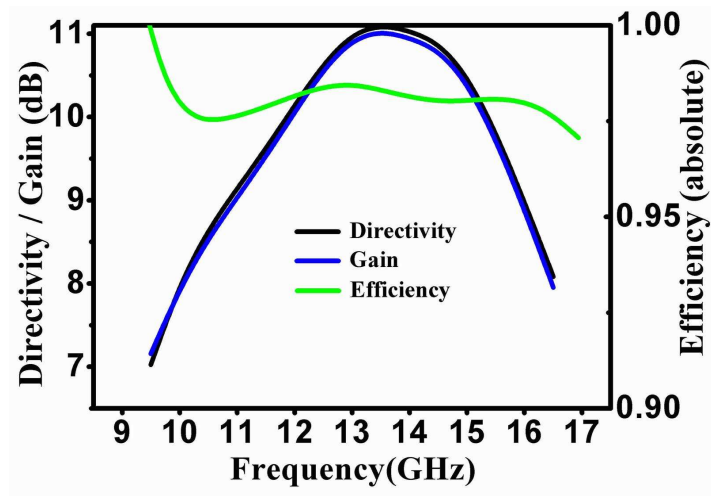


Figure 3.46 Simulated gain, directivity and radiation efficiency of the microstrip fed micromachined aperture coupled subarray antenna device

It can be seen from the plot the gain curve follows the directivity curve suggesting almost 100 % radiation efficiency within the radiation bandwidth region. The gain and efficiency increases from about ~ 7 dBi at 9.5 GHz to ~ 11.2 dBi at 14 GHz and then fall back below 8 dBi beyond 15.5 GHz. The variation of directivity and gain over the radiation bandwidth is around 4 dBi. The radiation efficiency is about 0.975 for the entire radiation bandwidth.

3.9 SUMMARY

Electromagnetic analysis techniques for micromachined aperture coupled patch antenna devices are presented in this chapter. The detailed design and simulation of several micromachined antenna devices were discussed

A bandwidth of 2.3 GHz (17%) is obtained for microstrip fed micromachined aperture coupled patch antenna device. The peak antenna gain is 8.3 dBi. The antenna radiation patterns show that there is significant backward radiation and significant side lobes in the E plane. The backward radiation pattern for both the E plane and H plane for the aperture coupled device is around -8 dB and also increases with frequency. The effects of different dimensions of the polymer rim are studied for the change in bandwidth and the gain of the antenna device. The gain, directivity and efficiency variance is minimal for the dimensions of 16 mm \times 16 mm and 20 mm \times 20 mm while a reduction is observed for the dimensions of 12 mm \times 12 mm. A bandwidth of 3.74 GHz (40%) is obtained for the microstrip fed micromachined aperture coupled stacked antenna device and thus almost doubled with respect to the non stacked antenna device. The peak antenna gain is 7.8 dBi. The minimum backward radiation is also decreased for both E plane and H plane and is around -12 dB within the radiation bandwidth. The variance of directivity and gain within the radiation bandwidth is below 1 dBi while it varies significantly out of the radiation bandwidth.

A bandwidth of 3.29 GHz (39%) is obtained for the CPW fed micromachined aperture coupled stacked antenna device with a peak antenna gain of 7.6 dBi. The minimum backward radiation for both E plane and H plane is around -17 dB in magnitude within the radiation bandwidth. It can thus be concluded that this micromachined aperture coupled stacked antenna device possesses an improved front to back ratio in terms of radiation than with a microstrip fed micromachined aperture coupled antenna device. A CPW feed also facilitates the easy integration of the antenna device with other surface mount passive devices. For comparison, FR4 and PTFE based stacked CPW antenna designs with similar dimensions as that of the CPW antenna are also designed and optimized for impedance matched performance. It was seen that there is little difference between gain values of the stacked patch antenna based multiplayer PTFE material and the devices with suspended patch elements since the dielectric loss is low in both designs. However, the micromachined device possessed a larger bandwidth. The performance of the FR4 based multilayer antenna is much poor due to the well known lossy behaviour of the FR4 material beyond the GHz frequency region.

Table 3.9 Summary of the antenna parameters for the micromachined aperture coupled antenna devices

Micromachined antenna device	Bandwidth (GHz)	Bandwidth (%)	Gain (dBi)
Microstrip fed single patch device	2.3	17	8.3
Microstrip fed stacked patch device	3.74	40	7.8
CPW fed aperture stacked patch antenna device	3.29	39	7.6
Microstrip fed subarray device	6.58	50	11.2

A bandwidth of 6.58 GHz (50%) is obtained for the microstrip fed micromachined aperture coupled subarray antenna device with a peak antenna gain of 11.2 dBi. The minimum backward radiation for both E plane and H plane is around -12 dB within the bandwidth. The micromachined sub array antenna device thus posses better bandwidth and gain than the other micromachined antenna devices. The drawback for this antenna device is variance of directivity and gain with in the radiation bandwidth of around 4 dBi. The radiation efficiency varies from about 0.91 to close to 0.99 for all of the micromachined antenna devices. Table 3.10 summarises the antenna parameters for the micromachined aperture coupled antenna devices.

CHAPTER 4 FABRICATION AND ASSEMBLY

4.1 INTRODUCTION

The design and simulation of micromachined aperture coupled antenna devices was presented in Chapter 3. This chapter describes the construction of the antenna devices using microfabrication and microassembly methods. Polymer rims were fabricated to create air gaps between the patch and the substrate in order to achieve wide band and high efficiency antennas. The antenna structures were fabricated in layers and assembled using the micromachined polymer spacers. Low cost materials like SU8, polyimide film and LCP substrate were used for the fabrication of the micromachined aperture coupled antenna devices. The feeding and aperture features were fabricated on microwave substrates while the radiating patch elements were fabricated on the polyimide and LCP substrates. UV lithography techniques (for SU8) followed by microassembly techniques have been used to produce the micromachined devices.

4.2 UV PHOTOLITHOGRAPHY

UV photolithography is the process extensively used for the manufacture of the electronic integrated circuits to transfer the physical layout pattern from a photomask to a photoresist layer deposited on the surface of a substrate. The photolithographic process involves the following steps (a) substrate preparation (b) spin coating (c) soft bake (d) exposure (e) hard bake (f) development [94, 130]. The sequence of steps involved will differ with the kind of photoresist employed, with the end application and the various MEMS (Micro Electro Mechanical Systems) fabrication methods used.

The flow chart in Figure 4.1 shows the sequence of steps that were involved in photolithographic process. The baked photoresist films were exposed through a photomask which changes the solubility of the photoresist in the suitable developer solution. In the case of positive photoresist, the UV exposed areas dissolve while the unexposed areas are retained. In the case of the negative photoresist, the UV exposed areas are cross-linked or hardened while the unexposed areas are dissolved. After development, the pattern on the photomask or its negative was produced in the photoresist film. The photolithographic

process involved ultra thick photoresist layers of tens of microns to millimetres. The photolithographic processes outlined above are described in Appendix A2.

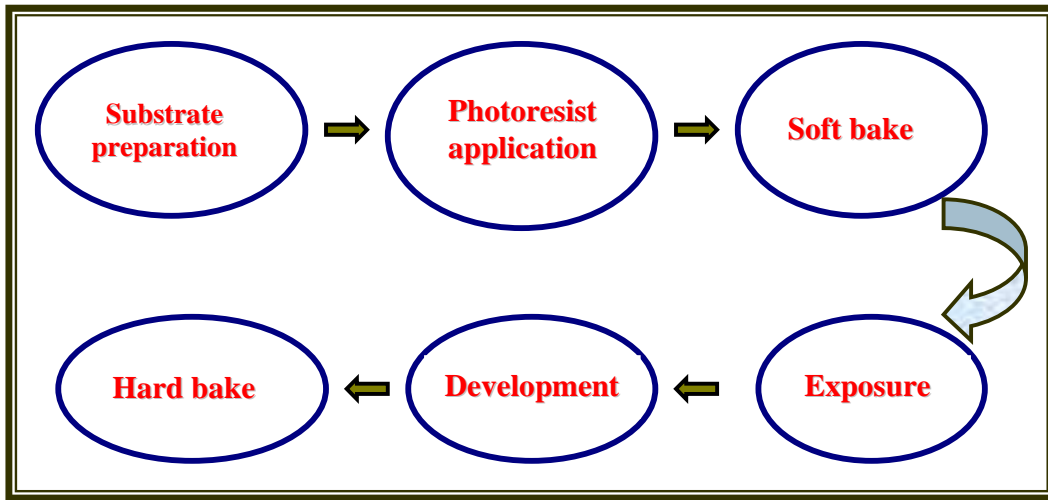


Figure 4.1 Sequence of steps involved in a photolithographic process

4.3 MATERIALS FOR MICROMACHINED ANTENNA DEVICES

4.3.1 SU8

SU8 is a negative, epoxy-type, near-UV photoresist based on EPON SU8 epoxy resin (Shell Chemical) that was originally developed and patented (US Patent No. 4882245 (1989)) by IBM [131, 132]. The chemical structure of the Bisphenol A Novolak epoxy oligomer, contained in SU8 is shown in Figure 4.2 [130]. Eight reactive epoxy functionalities allow a high degree of cross-linking after photo-activation. It has an exposure window in the i-line region of the UV spectrum. The SU8 photoresist can be used to produce films as thick as 2 mm with an aspect ratio more than 20 using spin coating and standard contact lithography equipment. Other methods such as blade coating and casting can be used to produce thicker SU8 films. The SU8 polymer is a well known as a micromachining material for MEMS applications. It is a low cost material, easy to deposit in thick films by spin coating or spreading, low processing temperature ($\sim 110^{\circ}\text{C}$) and chemically inert. A wide range of film thicknesses from microns to millimetres can be obtained by modifying the composition of the chemical formulations for film deposition. The thick film and high aspect ratio capabilities have made the SU8 polymer an ideal material for the spacer rims for the antenna devices. The RF properties of the SU8 material are studied recently from 1 GHz to up to 40 GHz.

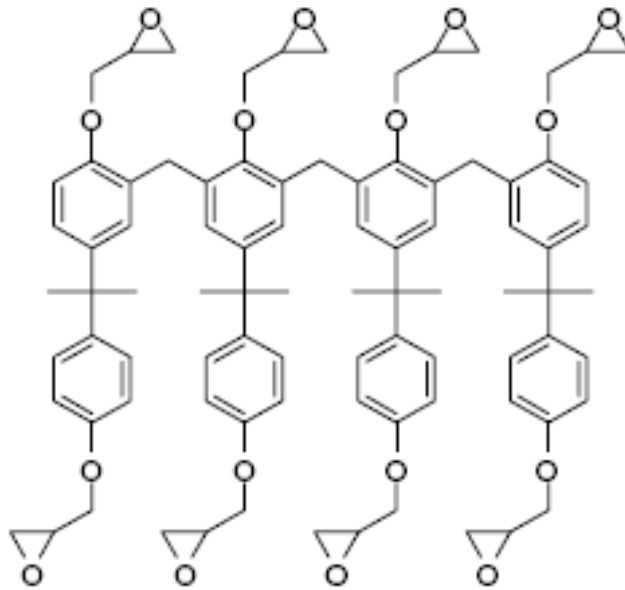


Figure 4.2 Chemical structure of the Bisphenol A Novolak epoxy oligomer contained in SU8 formulation. [130]

4.3.2 Thin film substrates

4.3.2.1 Polyimide film

Polyimide film was used as a substrate material for fabrication of the patch elements and the supporting SU8 rim structures for the micromachined aperture coupled antenna devices. The polyimide film used is from DuPont Kapton film with thickness of 125 μm . This low-cost flexible film has excellent thermal and mechanical properties for this application [120]. To facilitate the patch fabrication using UV photolithography and SU8 patterning, a large polyimide sheet was sheared into circular sheets of 3" diameter and then attached onto the 3" glass wafers by gluing it with spin coated AZ 9260 photoresist. Before attachment, both the polyimide sheets and the glass wafers were cleaned using the cleaning method introduced previously. The AZ 9260 photoresist was spin coated onto the glass wafer with a spin velocity of 5000 rpm for gluing the polyimide sheet onto the glass wafer. After baking the wafer on a hotplate at 80°C for 20 minutes, the polyimide sheet was attached onto the glass wafer. The glass wafer provides mechanical support to the polyimide film for photoresist deposition, exposure and electroforming if required.

4.3.2.2 Liquid Crystal Polymers

Liquid crystal polymers was another thin film carrier material for fabrication of the antenna patch elements and SU8 supporting rim structures for the micromachined aperture coupled

antenna devices. This low-cost flexible film has excellent thermal and mechanical properties for this application [133].

The unique properties of liquid crystal polymers (LCP) arise from their rigid, rod-like molecules that maintain a crystalline order even in the liquid or melt phase. The first commercial LCP was a lyotropic (solution processed) polymer from which DuPont developed KevlarB fibre in 1965 [134].

4.4 OVERVIEW OF ANTENNA FABRICATION AND ASSEMBLY

All of the antenna layers were fabricated with the microfabrication methods. A MEMS based fabrication process was implemented to obtain precision metal patterns on the substrates with the aim of reducing metal losses at higher frequencies. Electrical properties of the substrate and package materials are critical in the design of microwave circuits and devices. Selection of materials with lower permittivity and loss tangent was essential for packaging of antenna based systems.

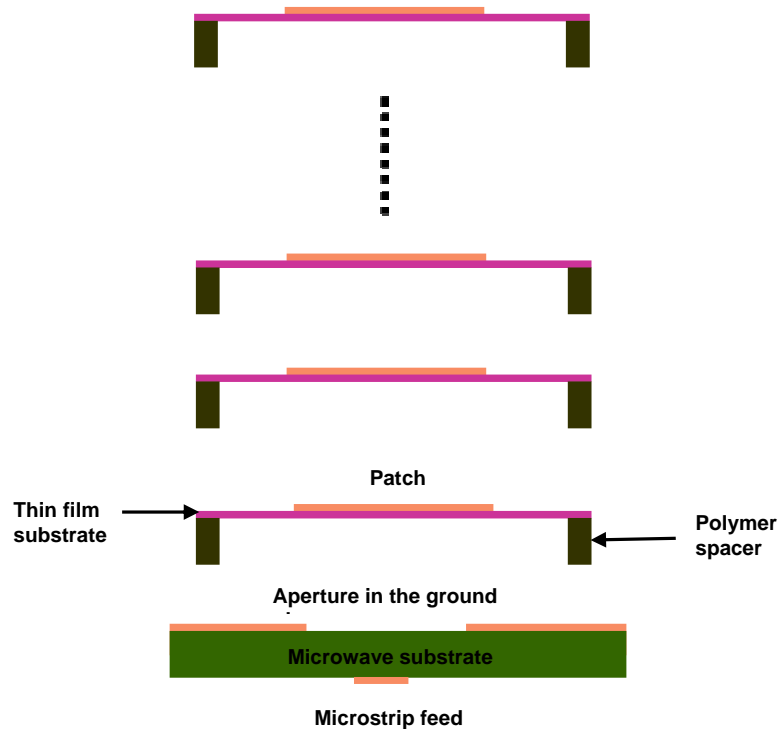


Figure 4.3 Illustration of the assembly method for fabrication of a generalised micromachined antenna device.

The materials used for the fabrication of micromachined aperture coupled antenna devices were chosen such that the antenna devices could potentially be integrated into a microwave

system using MMIC (Monolithic Microwave Integrated Circuits), SMT (Surface Mount Technology), SIP (System in a Package) and SOP (System on a Package) based approaches. Potentially the MMIC can be inserted in the air cavity of the micromachined aperture coupled antenna devices. Figure 4.3 shows the schematic of the layers for a micromachined aperture coupled antenna device with multiple patches to illustrate the low temperature fabrication method. For example, In order to produce a microstrip fed aperture coupled micromachined antenna device, the process flow was followed. The feeding and coupling structures were produced on a PCB substrate using the conventional PCB technology or a microfabrication method for devices requiring high resolution metal lines and aperture structures.

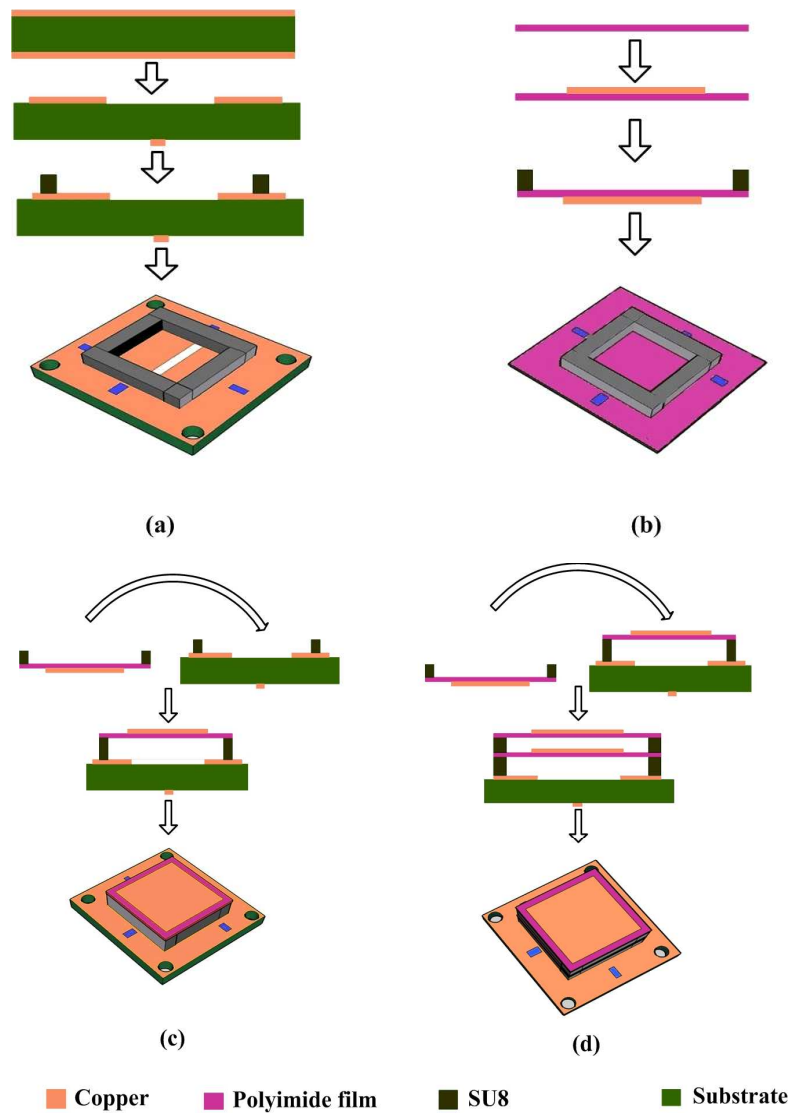


Figure 4.4 Schematic of the fabrication flow on (a) microwave substrate (b) polyimide film (c) assembly of the first patch (d) assembly of the second patch

The patch elements and the supporting micromachined polymer structures were fabricated on thin film polymer substrates. Polyimide and liquid crystal polymer thin films were suitable materials as the substrates for supporting the patches. After fabrication of the patch, the millimetre thick polymer structure for supporting the thin film substrate was fabricated using a surface micromachining method based on UV lithography. An additional polymer spacer was fabricated on the PCB substrate in order to produce a larger air gap between it and the polymer substrate about it. In this case the two spacers should be matched. The layers of the antenna were then aligned and bonded together to produce a stacked patch antenna device. Figure 4.4 shows the process steps for producing the micromachined antenna devices presented in Chapter 3.

The micromachined aperture coupled antenna devices utilised the free-standing patch elements to achieve high efficiency and improved bandwidth and the key process to achieve this is the assembly of the fabricated polymer rims. The fabricated substrate layers were assembled using a low temperature polymer bonding process to form high performance antenna devices. This was a new method for creating antenna devices with suspended patch elements. Flip chip assembly of the patch onto the microwave substrate was achieved by bonding the polymer rim on the patch to the corresponding one on the microwave substrate. The bonding process was carried out manually on a hotplate. Figure 4.4 (c) and (d) illustrates the process steps for assembly of a microstrip fed aperture coupled micromachined antenna device. A thin layer of SU8-5 solution was applied to the top surface of the polymer rims as the bonding material for antenna assembly. The polyimide film supporting the lower patch was attached to the substrate by bonding of the SU8 rim on the polyimide film to the corresponding one on the base substrate. Then the polyimide film with the top patch was attached to the polyimide substrate of the lower patch by bonding the SU8 rim to the polyimide film. Precision alignment marks on the polyimide films (transparent) and the base substrate were used to facilitate the accurate alignment of the layers. The bonding process could be carried out on a hotplate or on a flip chip bonder. Table 4.1 shows the composition of SU8-5 solution.

Table 4.1 The composition of the SU8-5 photoresist.

Composition	Percentage
SU8 resin	60.9%
Gamma-Butyrolactone liquid	21.1%
Photo initiator	6%

The assembly was heated to 55°C and maintained at this temperature for 10 minutes for bonding the two polymer rims together. After patch assembly, an SMA connector was attached to the microstrip and ground plane on the microwave substrate to obtain an antenna device for RF characterization. The assembly process for the microstrip fed micromachined aperture coupled stacked antenna device is illustrated in Figure 4.4(c) and (d). The polyimide film supporting the lower patch was attached to the substrate by bonding the SU8 rim on the polyimide film to the corresponding one on the base substrate. Then the polyimide film with the top patch was attached to the polyimide substrate of the lower patch by bonding the SU8 rim to the polyimide film. Precision alignment marks on the polyimide films and the base substrate were used to facilitate the accurate alignment of different layers. After the assembly process a micromachined stacked patch antenna device was obtained. For RF characterization, an SMA connector was attached to the microstrip and ground plane on the microwave substrate. Other micromachined aperture coupled antenna devices are assembled with the similar process as outlined for the microstrip fed micromachined aperture coupled stacked antenna device.

4.5 PHOTOMASK DESIGN

Photomasks were required for UV photolithography for the micromachined aperture coupled antenna devices. Photomasks were designed for fabrication of the feeding lines, apertures on the ground planes, SU8 polymer rims and the radiating patch elements for the all of the micromachined aperture coupled antenna devices as described in Chapter 3.

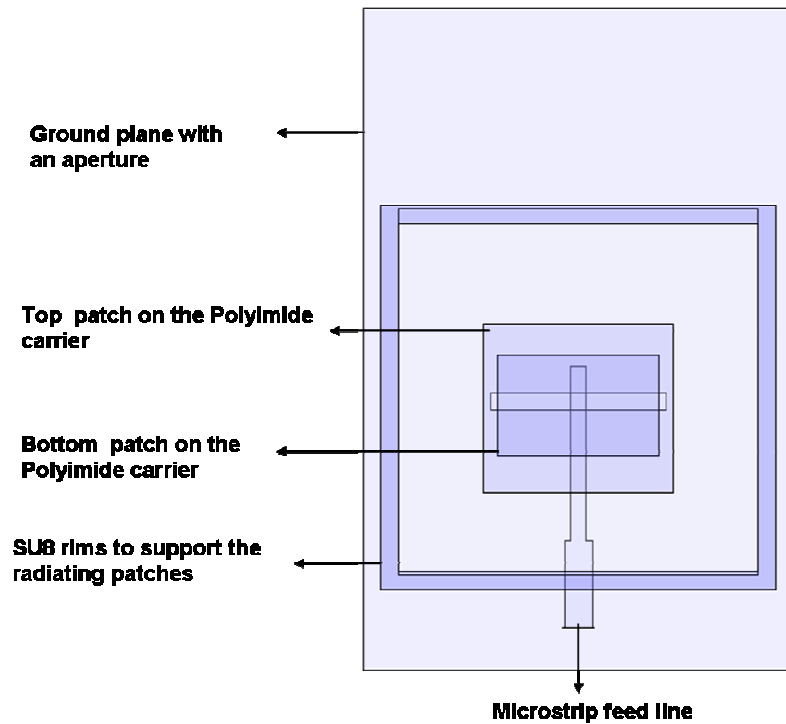


Figure 4.5 Schematic of the microstrip fed micromachined aperture coupled antenna device from the top view

In the case of the CPW fed micromachined aperture coupled antenna device, the CPW feeding line and the ground plane were on the same side of the substrate. This device reduced the need of an extra mask. Figure 4.5 shows the schematic of the microstrip fed micromachined aperture coupled antenna device from the top view. Figure 4.6 shows the schematics of the photomask designs for microstrip fed micromachined aperture coupled antenna device. For the SU8 polymer rims, photomasks for negative photoresist were designed. Four photomasks were produced for microstrip fed micromachined aperture coupled antenna devices. The first photomask contained the pattern of the microstrip feed line. The second photomask contained the pattern of the aperture on the top side of the base substrate. The third photomask contained the patterns for fabrication of the patch elements on polyimide substrate. The fourth photomask contained the patterns for fabrication of SU8 polymer rims on the polyimide and base substrate. The photomasks were designed for microfabrication on 3" glass and silicon wafers using a positive tone photoresist.

Figure 4.7 shows the schematics of the photomask designs for the CPW fed micromachined stacked antenna device. Four photomasks were designed and produced. The first photomask contained the patterns of the aperture and the ground on the top side of the base substrate. The second photomask contained the patterns for fabrication of the patch element on LCP substrate for the upper layers. The third photomask contained the patterns for fabrication of the patch element on LCP substrate for the lower layer. The fourth photomask contained the patterns for fabrication of SU8 polymer rims on the LCP and base substrates. A software package, Tanner L-Edit, was used to design the photomasks. L-Edit comprised of an integrated circuit layout editor that employed various drawing and editing tools in order to produce a schematic of the mask with precision in nanometres. The designed photomask patterns were printed onto flexible mylar substrates using a high-resolution (up to 64,000 dpi) plotter. The transparent areas in the film allowed the UV light to pass through the photomask, while the non transparent (black) areas in the film served as the UV absorption layer, blocking the UV light.

In L-Edit, each mask layout was drawn in a separate cell. To merge different mask layout, the layout in one cell could be superimposed on another cell by a process called a cell instance. To begin the mask drawing process, the default design unit in micron was used. The mask designs were drawn in units of microns for better precision. The boolean operations such as AND, OR and XOR were employed to obtain complex shapes such as the apertures on the ground plane and the CPW feed line etc. The masks were drawn in the positive mode in the case of metallic patterning and in negative mode for the SU8 polymer rim. The masks were drawn in the positive mode initially and in negative mode using the boolean operations. The track length and width of the alignment marks were 1 mm and 500 μm respectively. Alignment marks were important in the photomask design because the different layers could be built on one substrate or on different substrates and subsequently assembled to obtain a device. Four alignment marks were positioned at the corners of each photomask. The alignment marks ('+') were used for the microstrip fed micromachined aperture coupled antenna device while a negative version of this symbol was used for the photomasks for the CPW fed device as shown in Figure 4.7.

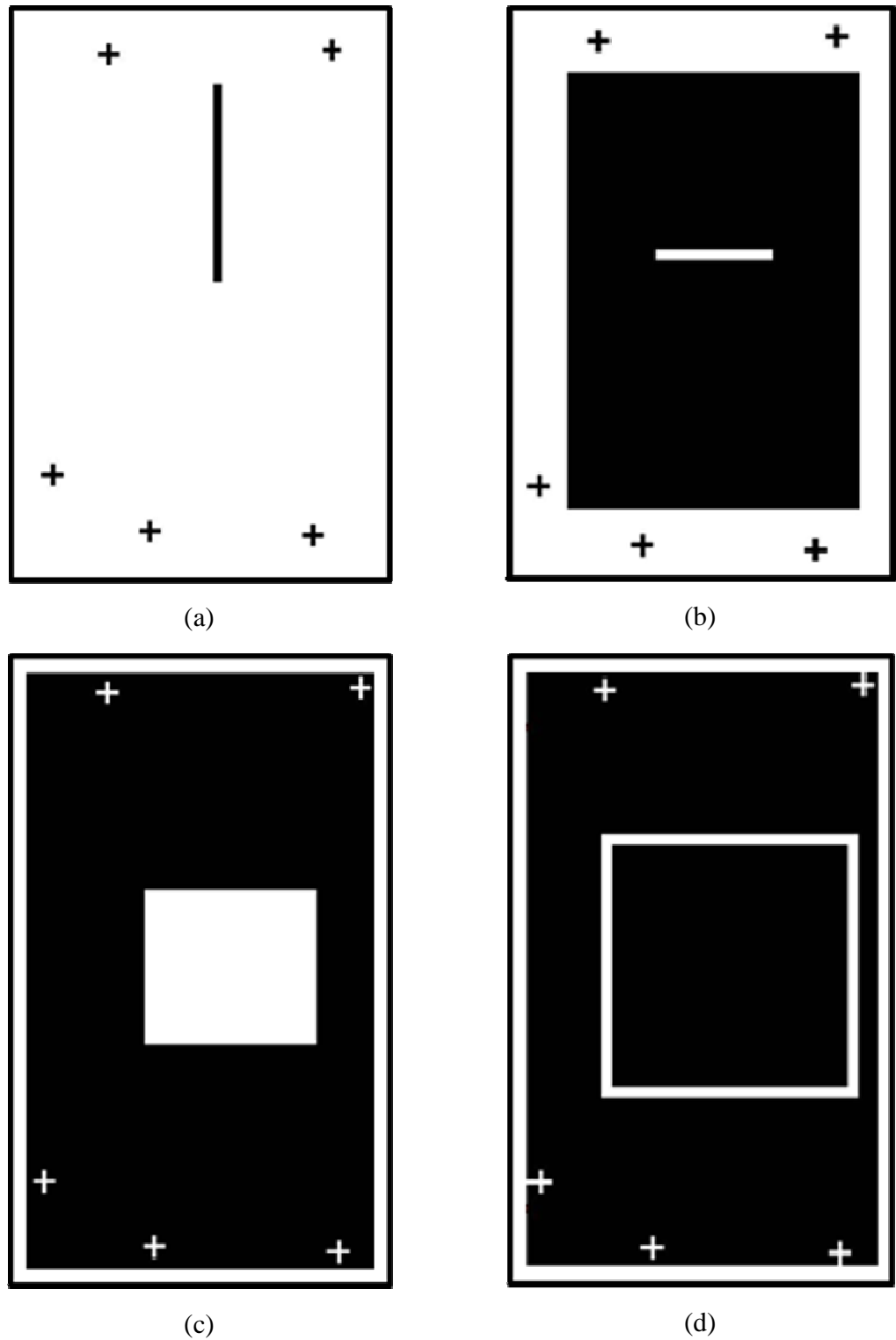


Figure 4.6 Schematic of the photomask designs for fabrication of the microstrip fed micromachined aperture coupled antenna device with the alignment marks. The photomasks shown are for (a) Microstrip feed line, (b) Ground plane and the aperture (c) Patch element and (d) Polymer rim

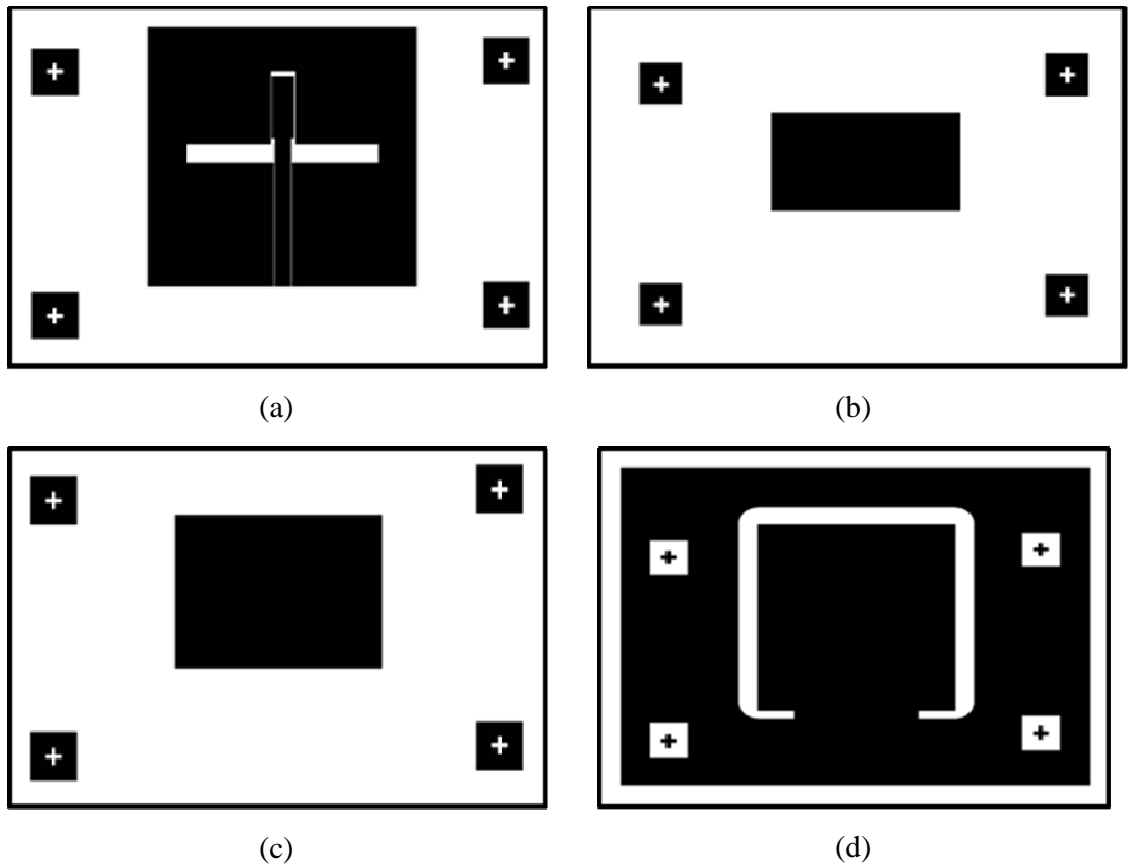


Figure 4.7 Schematic of the photomask designs for fabrication of the CPW fed micromachined aperture coupled stacked antenna device. The photomasks shown are for (a) CPW feed line, ground plane and the aperture (c) Top patch element and (d) Polymer rim.

The alignment marks used for the CPW design could result in better alignment accuracy of layers during UV exposure and also during the assembly process as it was a distinctive combination of square and ('+') alignment mark. For printing the mask, the CAD (computer aided design) was transferred on to a mylar film. The photomasks in L-Edit were exported to a design file of GDSII format. The GDSII file was converted into a Gerber file using the CAD file format conversion software, LinkCAD. The photomask was printed by an external photomask supplier, JD Photo-Tools Ltd.

4.6 FABRICATION

The design dimensions used for the fabrication of the micromachined aperture coupled antenna devices have been described in Chapter 3. Figure 4.5 shows the schematic of the microstrip fed micromachined aperture coupled antenna device from the top view. From the schematic it can be seen that the dimensions of the base substrate is larger than

polyimide substrate used for supporting the patch element. If the dimensions of the base substrate were similar in dimensions as that of the polyimide substrate in order to design compact antennas, this would result in a reduction in antenna efficiency. The micromachined aperture coupled antenna devices were to be fabricated on a 3 inch wafer and two devices could fit in single 3 inch wafer. In order to facilitate the RF characterisation of the antenna devices after fabrication, care has been taken in the design for the SMA probes to slide well on to the microstrip or the CPW lines by allowing adequate spacing from the SU8 polymer rim. Adequate microstrip and CPW line widths have also been designed in order to match the central pin of the SMA connector.

4.6.1 Fabrication of microstrip feed and aperture on the base substrate

Commercial microwave substrates Arlon (AD300A) and Taconic (TLY-3-0200-CH/CH) were used as the base substrates for fabrication of the micromachined aperture coupled antenna devices. Low-cost sodium silicate (glass) substrates were used as carriers for the thin film substrates in the fabrication process. For the fabrication of the microstrip structure, one AZ 9260 photoresist layer was used and for the fabrication of the aperture in the subsequent processing step, the other one was used to protect the copper layer on the other side of the substrate. The copper layer was electrodeposited using ferric chloride based copper etchant after UV photolithography of the photoresist layer. Acetone was then used to strip away the photoresist layers on both sides of the substrate. For fabrication of the aperture, the above process was repeated. For the CPW fed micromachined aperture coupled stacked antenna device, the CPW feed and the aperture were fabricated on the same side of the Taconic substrate. Figure 4.8 shows the schematic of the fabrication steps.

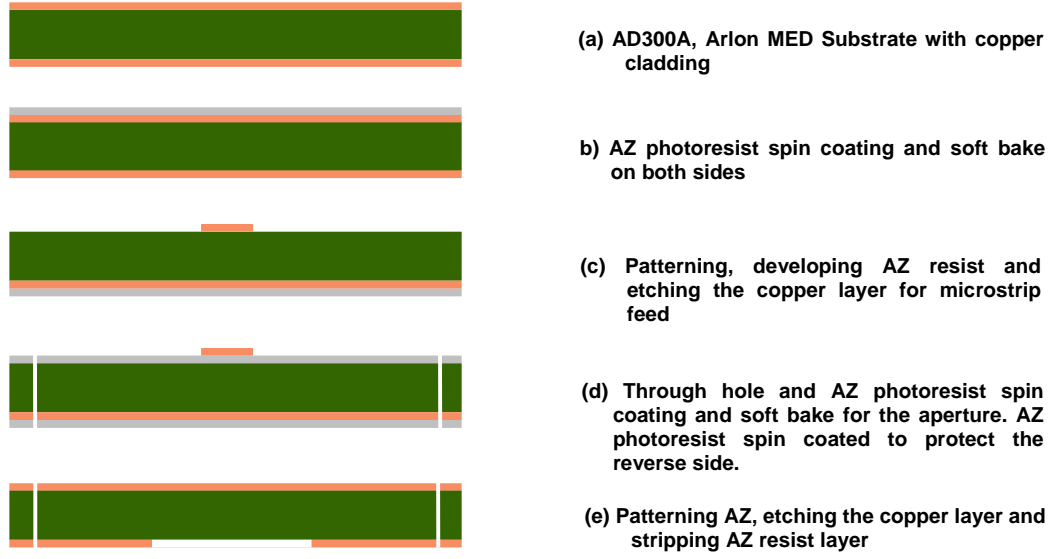


Figure 4.8 Process flow of substrate fabrication for the microstrip fed micromachined aperture coupled antenna device

4.6.1.1 Photoresist deposition

The glass wafers and the microwave substrates were cleaned to ensure that they were free of contaminants and moisture. The wafer cleaning process was carried out using an ultrasonic bath (Grant MXB14). The glass wafers were mounted on a wafer holder and placed in a beaker containing de-ionised water (DI water) mixed with detergent. A commonly used detergent for wafer cleaning, Decon 90, was used. The concentration of the detergent liquid was 10 ml/L. The substrates were cleaned in the ultrasonic bath for one hour at 30°C. After the ultrasonic cleaning, the substrates were rinsed in DI water for one hour under the same ultrasonic conditions. Then the wafers were taken out from the beaker and dried using compressed dry nitrogen. The wafers were ready for fabrication of the antenna devices as described in the following sections. After cleaning and drying, both sides of the substrate were deposited with a photoresist layer. Deposition of the AZ 9260 [135] photoresist layer onto the seed layer of a carrier wafer was carried out as described in Section 4.2.3. The AZ 9260 photoresist was sensitive to the ultraviolet light of the spectrum from 320 nm to 410 nm, so a UV filter was not necessary. The spin conditions are summarised in Table 4.4.

4.6.1.2 Soft bake

Soft bake for the photoresist was carried out on a hotplate. The hotplate provided a well controlled temperature and heat distribution to bake the photoresist film. The substrate wafer coated with the photoresist film was placed on the hotplate and baked at the temperature of 80°C for the required duration. The solvent in the photoresist was driven out from the resist film by thermally activated solvent diffusion and evaporation. The solvent diffusion rate is a function of the solvent concentration in the resist and the baking temperature. After soft bake, the solvent contained in the photoresist was removed and a solid photoresist film with a flat surface was produced on the substrate wafer. After deposition, the substrate wafer was left at room temperature for 10 minutes to allow the air bubbles trapped in the resist film to propagate to the surface in order to eliminate the formation of defects in the photoresist layer after baking. Also, AZ 9260 required a certain amount of water for the photochemical reaction to take place during the UV exposure process. Therefore an adequate delay of the UV exposure was necessary for the wafer to cool down to the room temperature and to allow the re-hydration of the photoresist. The wafer was kept in the standard clean room environment after soft bake to allow the resist to absorb enough water from the air.

4.6.1.3 UV exposure

After the spin coating, relaxing and soft baking, the photoresist film on the substrate wafer was exposed to UV light through a photomask to transfer the patterns of microstrip feed and the aperture from the photomask into the photoresist film. The UV exposure of the photoresist film was carried out on a UV mask aligner (Mask Alignment and Collimated UV Exposure System, Model 152, Tamarack Scientific Co. Inc) as outlined in Section 4.2.5. The polyester photomask with the pattern of the microstrip feed line structures were placed on the photomask holder with its film side facing the wafer. The photomask was held in place by turning on the vacuum at the photomask holder. The mask aligner had a built-in UV intensity sensor and a timer for controlling the exposure dose.

4.6.1.4 Development and copper etch

Post exposure bake was not required for the AZ 9260 photoresist. The photoresist development was a process in which the photoresist is selectively removed, wherein the selection came from the UV exposure. AZ 400K (AZ electronic materials, Clariant Corporation) was the developer for the development of the exposed AZ 9260 photoresist

film. It was diluted using de-ionised water (1:3) to make up the developer solution. Careful control was necessary to ensure a well defined microstrip line.

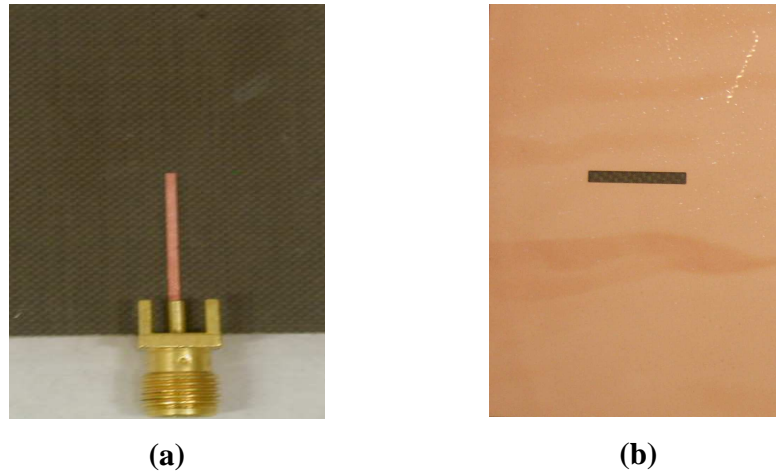


Figure 4.9 Optical images of (a) a feeding microstrip and (b) a coupling aperture on a substrate after fabrication for the microstrip fed micromachined aperture coupled antenna device

The substrate wafer with the photoresist film was immersed into the developer solution in a petri dish. The dish was shaken gently by hand to increase the rate of development. The development was monitored by visual inspection or on a ZYGO interferometer. After the photoresist development and removal, the substrate wafer was removed from the petri dish, rinsed with de-ionised water and blown dry with compressed nitrogen gas. The exposed copper was etched in a ferric chloride based etching bath as described in Section 4.2.7. The remaining photoresist layer was then removed by immersing the substrate in acetone. For alignment of the microstrip to the aperture to be fabricated on the opposite side of the substrate in the subsequent fabrication process, precision holes were drilled at the corners of the substrate using a mechanical drilling method. Then both sides of the substrate were coated with a photoresist layer for fabrication of the coupling aperture and protection of the microstrip line. The same photoresist patterning and metal etching processes as for the microstrip were repeated to obtain the aperture on the ground plane. The process flow of substrate fabrication for the microstrip fed antenna device is summarized in Figure 4.8. Figure 4.9 shows the images of the fabricated microstrip line and aperture on the substrate for the microstrip fed micromachined aperture coupled antenna device.

4.6.1.5 Optimisation of photolithographic parameters for AZ 9260 photoresist

The patterned photoresist film worked as a mould for electroforming and etching processes in order to obtain conductor patterns for the microstrip fed micromachined aperture coupled antenna device. The parameters of soft bake, exposure UV energy dose and developing time were closely interrelated to determine the quality of the photoresist film [135, 136].

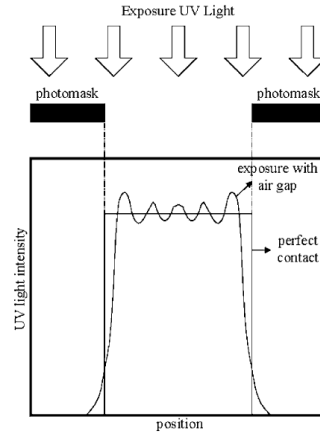


Figure 4.10 Optical diffraction patterns by various exposure situations reproduced from [136]

Various defects rose in the photoresist film due to inappropriate photolithographic parameters and hence the electroformed or etched metallic structures deviated from the original design. Therefore optimisation of the photolithographic parameters was crucial for obtaining better photoresist films for electroplating or etching purposes. The manufacturer's guide of AZ 9260 did not give any explicit photolithographic parameters for processing the AZ 9260 photoresist films of $\sim 10\ \mu\text{m}$ of thickness. They were determined and optimised through experimentation. For film thickness of $10\ \mu\text{m}$, soft baking at 80°C for less than 3 minutes was inadequate. Fully exposed AZ 9260 photoresist released large volume of nitrogen gas in the photochemical reaction. Ideally it diffused through the resist to the film surface without forming bubbles. However in the case of rich solvent remaining in the photoresist film, the nitrogen gas generated during exposure was trapped in the film to form bubbles inside the film. Bubbles formed at the interface of the photoresist film and the substrate reduced the adhesion of the film to the substrate. The trapped bubbles also changed stress distribution in the photoresist film and hence caused cracks in the film. Soft baked time was increased in steps of 2 minutes keeping the exposure and development times constant at $500\ \text{mJ}/\text{cm}^2$ and 2.5 minutes. It was found that a soft bake period of 10

minutes at 80°C for the film thickness of 9 µm gives better features after exposure and development and to reduce cracking in the AZ film after exposure.

Table 4.2 Optimisation of photolithographic parameters for AZ 9260 photoresist

	Insufficient	Excessive
Soft bake	Mask contamination Air bubbles creation Photoresist film delamination after hard bake	Excessive development after exposure Broaden pattern due to the radiation profile
Exposure	Excessive resist development after hard bake Broadened pattern due to excessive radiation intensity	Excessive stresses and possible delamination during development.
Development	Photoresist residues Metal delamination	Over development and rough sidewalls Delamination of the developed structures

UV dose parameters of 400 mJ/cm² recommended by the data sheet of the AZ 9260 photoresist were used initially and were found to produce undeveloped feature after development. The strategy to find the appropriate UV energy dose for exposure was similar to that for bake time optimisation. The resultant photoresist structures were inspected under the optical microscope to determine if the exposure intensity was insufficient or excessive. The UV energy dose was then increased or decreased accordingly in the subsequent photolithographic experiments until an optimised value was found. Insufficient exposure resulted in excessive developing time and slanted side walls. The cross-sectional schematic in Figure 4.10 shows the intensity distribution of the UV light through an aperture of a photomask in the photoresist film. The UV intensity at the bottom of the resist film was lower than the intensity near the surface due to the absorption and diffraction of the UV light by the photoresist. When the exposure time was insufficient, the photoresist near the bottom of the film was unable to absorb enough UV energy dose to complete the full photochemical reaction. The exposure parameters are optimised first starting with initial 3 minutes soft bake and 2.5 minutes development and then the soft bake

parameters are optimised. An optimised value for UV exposure of 500 mJ/cm^2 is found to be adequate for the microstrip feed and aperture features. Table 4.2 shows the optimised photolithographic parameters for AZ 9260 photoresist.

4.6.2 Fabrication of patch elements on thin film substrates

Polyimide and LCP films were used as thin substrates for fabricating patch elements for the micromachined aperture coupled antenna devices. As the polyimide film substrates did not have a copper cladding layer, a copper foil of $9 \text{ }\mu\text{m}$ of thickness from Taconic was laminated on the substrate for patch fabrication. Electroplating technique was used to fabricate the patch on a polyimide substrate of $125 \text{ }\mu\text{m}$ (Dupont) of thickness for the microstrip fed micromachined aperture coupled antenna device. For the other antenna devices, the etching method after photoresist patterning was used. Figure 4.11 shows the process flow for fabrication of the patch elements on a thin film substrate sing the etching approach.

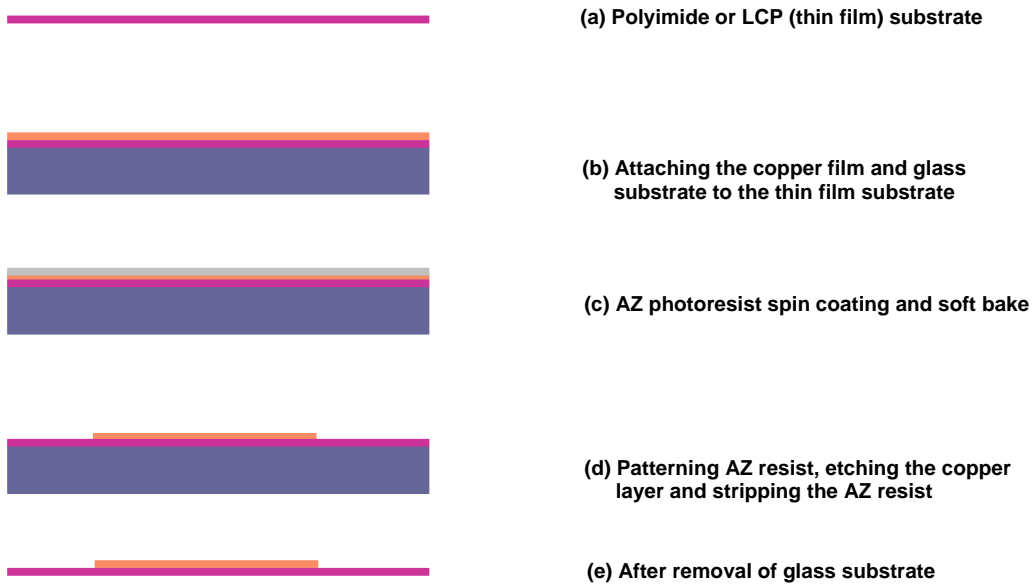


Figure 4.11 Fabrication flow for the suspended patch elements for the micromachined aperture coupled antenna devices

After deposition of thin layers of titanium and copper on the polyimide substrate using the electron beam deposition method as described in Section 4.2.4.1, a layer of photoresist film was deposited on the substrate using the same process as described previously. The photoresist material was spin coated on the thin film substrates directly without the electron beam deposition for the etching based fabrication method. The photoresist layer was then

patterned to expose the area of the copper film for patch fabrication. In order to produce a film of thickness of about 8 μm for the patch, electroplating was carried out in a copper plating bath by using a current density of 1 A/dm^2 for the microstrip fed micromachined aperture coupled antenna device. The photoresist films were then removed for fabrication of the polymer supporting rim. Several patches can be fabricated on a polymer film. The alignment marks were fabricated at the same time as that for the patches.

4.6.3 Fabrication of micromachined spacers

In order to obtain SU8 rims on the base and thin film substrates, surface micromachining of the SU8 film by photolithography was carried out. The millimetre thick polymer spacer rims were fabricated on the thin film substrates after patch fabrication using the polymer surface machining method. Polymer micromachining, a process where high aspect ratio polymer structures are fabricated out of a thick polymer film on a substrate was utilized for fabricating the SU8 polymer rims. Photo-imageable SU8 epoxy polymer was used to produce the polymer structures on the substrate layers for constructing the microstrip fed micromachined aperture coupled antenna device. In order to create a large air gap between the microwave substrate and the suspended patch above it for the microstrip fed devices, a pair of matching spacer rims were fabricated, one on each of the microwave and the film substrate respectively. Fabrication of the millimetre thick SU8 spacer rims on the rigid Arlon MED and Taconic substrates were found to be more challenging than the thin film substrates and thus an optimized process for soft baking was developed. Delamination of the SU8 spacer rims from the substrate could occur after the fabrication process due to the higher interfacial stress built up in the baking process prior to photolithography. The increased stress was caused by the larger CTE mismatch between the SU8 layer and the rigid microwave PCB substrate than the film substrate.

Table 4.3 Composition of the SU8-100 solution.

Composition	Percentage
SU8 resin	72.9%
Gamma-butyrolactone liquid	21.1%
Photoinitiator	6%

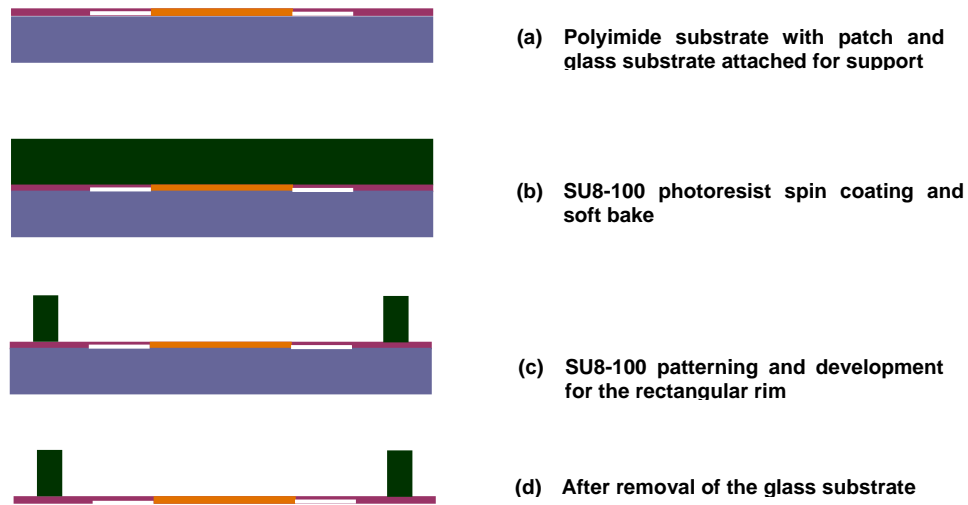


Figure 4.12 Fabrication flow for the SU8 polymer rim for the microstrip fed micromachined aperture coupled antenna device

However this problem was solved by careful control of the temperature profile in the soft baking process, a smooth temperature profile in the heating and cooling processes is required [137]. The SU-100 polymer solution was prepared in house in order to fabricate millimetre thick polymer spacers. The composition of the solution is given in Table 4.3. The dimensions and fabrication parameters for the polymer rims for various antenna designs are outlined in Table 4.4 and Table 4.5. Figure 4.12 shows the process flow for fabrication of SU8 spacer rims on the substrate layers for antenna assembly. The required spacer thickness for each antenna layer was obtained by controlling the spin speed and time in the deposition of the SU8 layer. The thin film or base substrate was cleaned prior to the application of the photoresist by placing the spinning chunk at 4000 rpm. Acetone was applied to the substrate first followed by Isopropanol. The process was repeated if any visible particles were found on the wafer.

4.6.3.1 Spin coating

Spin coating of the thick photoresist layer was done by applying SU8 on to the base substrate or thin film substrate using a normal pipette at ambient temperature. Approximately an amount of 12-15 mL of SU8-100 was dispensed on to the centre of the substrate or thin film for uniform coating. The substrate or thin film was spun at different spin velocities and ramp (acceleration) rates. The wafer was spun at 70 rpm, 30 r/s, 20 s for the initial spin cycle. The spread cycle parameters and the smoothing cycle parameters are

given in Table 4.4 and Table 4.5 in order to achieve various thicknesses for various micromachined aperture coupled antenna devices. Any bubbles larger than ~2 mm of diameter were removed using tip of a spatula. The edge bead on the wafer was removed by using the outer edge of the pipette. This was achieved by resting the pipette's outer edge on the edge of the wafer and manually rotating the wafer on the spin chuck. The wafer was then removed from the spin chuck and the SU8 photoresist allowed to planarize on a level surface for 30 minutes to 1 hour.

4.6.3.2 Prebake

After the application of the photoresist for the purpose of soft baking of the SU8 photoresist, an initial temperature of 65°C was used for 5 minutes and then ramped up to 95°C linearly in 5 minutes. Thereafter the temperature of the hot plate was maintained at 95°C. The duration for various thicknesses is provided in Table 4.4 and Table 4.5. It is important that at which the actual temperature of the hot plate was set to, as a slight change in temperature or baking time could cause a huge difference in the behaviour of the photoresist film. Figure 4.13 shows the temperature profile in the prebake process for SU8 films.

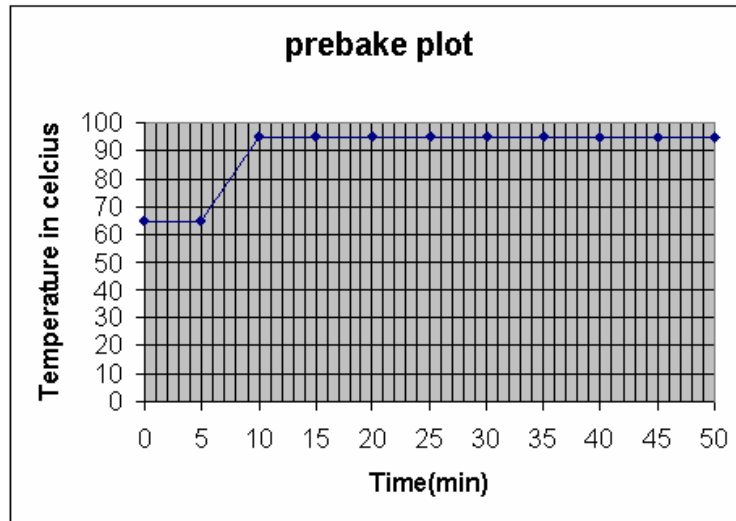


Figure 4.13 Temperature verses time plot for the prebake process for SU8 wafer.

The tilting angle for the wafer to be baked was to be considered in order to achieve uniform film thickness. A small tilting angle from the horizontal plane could introduce a significant difference of thickness at different ends of a wafer as depicted in Figure 4.14. The difference in height between the two polymer rim ends can be given by

$$\Delta H = a \sin(\theta) \quad (4.1)$$

For example if θ equal to 0.25° and for a polymer rim of dimensions $20 \text{ mm} \times 20 \text{ mm}$, the difference in height would be around $87 \text{ }\mu\text{m}$. It has been found that this variation in height would not affect the performance of the antenna performance. The 0.25° of tilt was within the sensitivity limit of a spirit based levelling tool used for the hotplates.

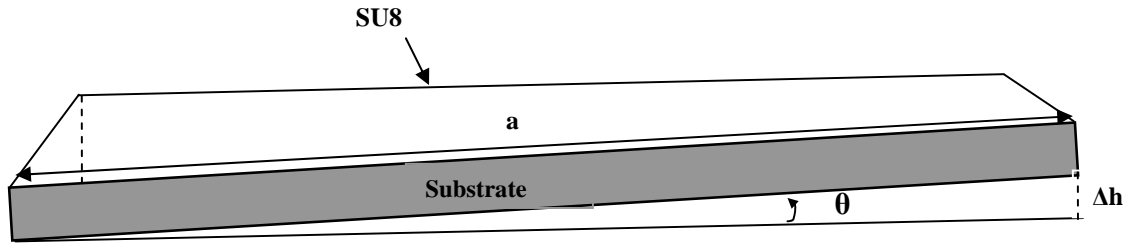


Figure 4.14 Illustration of tilted wafer and uneven SU8 photoresist

4.6.3.3 UV exposure

After soft baking, the film was exposed to the i-line (365 nm) of the UV source on a mask aligner using the photomask with the patterns of the spacer rims. The process was outlined in section 4.2.4.4. Higher absorbance was seen at shorter wavelengths than at longer wavelengths when the UV absorption spectrum of the unexposed SU8 resist was observed with a spectrometer. The change in absorbance of UV light during exposure was also observed to increase at shorter wavelengths. The longer wavelength components of the UV radiation source penetrated further down and exposed the bottom part of an SU8 film. For this reason, a UV filter was used to cut out the light below 365 nm of wavelength during exposure.

4.6.3.4 Post bake and development

After exposure the wafer was baked at 65°C on the hot plate. The SU8 layer was developed in the EC (Microchem Inc) solvent to remove the unexposed SU8 during the photolithographic exposure. Mild agitation provided by a magnetic stirrer was used to reduce the development time and improve the quality of the resultant SU8 structures as described in Section 4.2.6. The details of the post bake process are shown in Table 4.4 and Table 4.5.

Table 4.4 Processing steps and parameters for fabrication of AZ 9260 films for copper patterning and SU8 polymer rim for the micromachined aperture coupled antenna devices

	AZ 9260	SU8-100 (a)
Spin Coating	Initial spin: 70 rpm, 30 r/s, 20 sec	Initial spin: 70 rpm, 30 r/s, 20 sec
	Spread: 1000 rpm, 200 r/s, 20 sec	Spread: 1000 rpm, 200 r/s, 5 sec
	Smoothing: 2500 rpm, 400 r/s, 20 sec	Smoothing: 650 rpm, 2000 r/s, 45 sec
Delay	5 minutes	5 minutes
Soft bake	10 minutes at 80°C	65°C for 5 minutes and 95°C for 5 hr and 45 min
Delay	45 minutes	1 hour
Exposure dose	500 mJ/cm ²	2800 mJ/cm ²
Post bake	-	65°C for 2.5 minutes
Development	2.5 minutes	~ 15 minutes in stirring bath
Film thickness	~ 10 µm	~ 750 µm
Copper etching time	1 minute	-

Table 4.5 Processing steps and parameters for fabrication of SU8 polymer rims for the micromachined aperture coupled antenna devices

	SU8-100 (b)	SU8-100 (c)	SU8-100 (d)	SU8-100 (e)
Spin Coating	Initial spin: 70 rpm, 30 r/s, 20 sec	Initial spin: 70 rpm, 30 r/s, 20 sec	Initial spin: 70 rpm, 30 r/s, 40 sec	Initial spin: 70 rpm, 30 r/s, 20 sec
	Spread: 500 rpm, 100 r/s, 5 sec	Spread: 500 rpm, 100 r/s, 5 sec	Spread: 500 rpm, 100 r/s, 5 sec	Spread: 500 rpm, 100 r/s, 5 sec
	Smoothing: 500 rpm, 100 r/s, 50 sec	Smoothing: 465 rpm, 100 r/s, 50 sec	Smoothing: 715 rpm, 100 r/s, 60 sec	Smoothing: 450 rpm, 100 r/s, 50 sec
Delay	5 minutes	5 minutes	5 minutes	5 minutes
Soft bake	65°C for 5 minutes and 95°C for 6 hr and 15 minutes	65°C for 5 minutes and 95°C for 6 hr 15 minutes	65°C for 5 minutes and 95°C for 5 hr 45 min	65°C for 5 minutes and 95°C for 6 hr 45 minutes
Delay	1 hour	1 hour	1 hour	1 hour
Exposure dose	3000 mJ/cm ²	3200 mJ/cm ²	2800 mJ/cm ²	3300 mJ/cm ²
Post bake	65°C for 3.5 minutes	65°C for 4 minutes -	65°C for 2.5 minutes -	65°C for 5 minutes -
Development	~ 30 minutes in stirring bath	~ 30 minutes in stirring bath	~ 30 minutes in stirring bath	~ 30 minutes in stirring bath
Film thickness	~ 1000 µm	~ 1150 µm	~ 680 µm	~ 1200 µm

4.6.3.5 Optimisation of parameters for SU8 photoresist

Soft-baking time, exposure dose, post exposure bake and the development time are the major contributors to the internal film stress of 50%, 30%, 15% and 5% respectively [138]. Solvent removal in the soft baking process in general lead to volume shrinking and mechanical stress within the photoresist films.

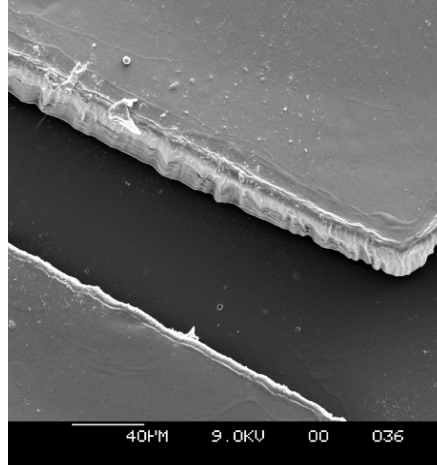


Figure 4.15 Illustration of SU8 layer peel off from the substrate due to excessive stresses during prebake.

The accumulated stress increased with increasing film thickness and dimensions and when the stress reached a critical point, and then the resist layer would peel off from the substrate wafer and in some cases complete delamination could occur due to weaker adhesion. There is a trade off between the soft bake time and the quality of the features for the SU8 photoresist. In general, the soft-baking time determined the final solvent content of the resist. Short soft-baking interval would leave a soft photoresist layer with some residual solvents that is less prone to internal stress for the remaining processing steps. On the other hand, high residual solvent during soft bake produced extra air bubbles during post-exposure baking resulting in the collapse of SU8 features after development due to lower mechanical stability at the bottom of the film as a result of the soft photoresist at the bottom [139]. If the photoresist was over baked and hard, cross-linking in the irradiated/exposed areas would be hindered. As a result, an optimum soft-baking time was to be optimized for each particular photoresist / thickness and application. Figure 4.15 illustrates the SU8 layer peel off from the substrate due to excessive stresses during prebake.

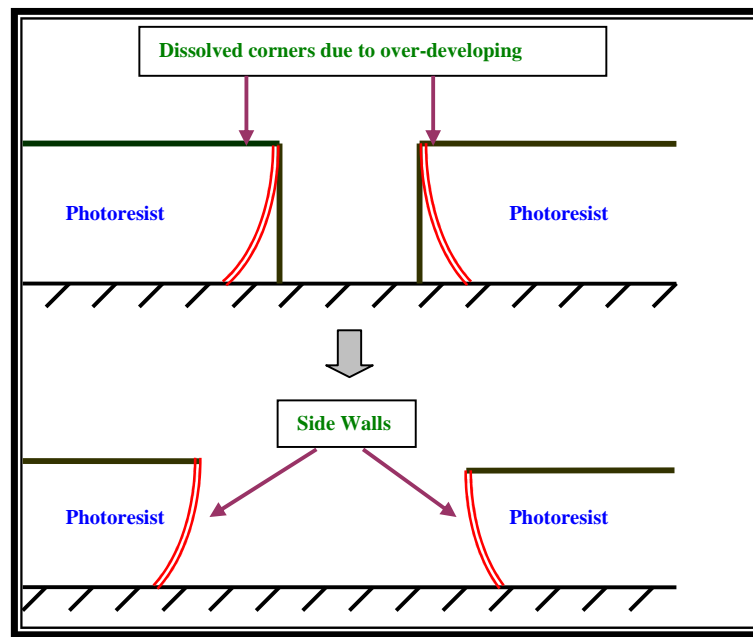


Figure 4.16 Illustration of the excessive development in the SU8 photoresist film

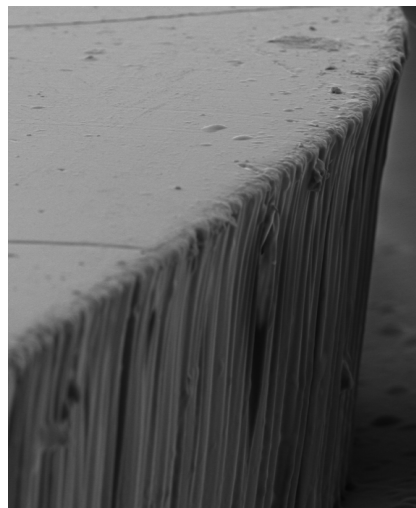


Figure 4.17 Photograph of a excessively developed SU8 polymer side wall

In the case of spin coated SU8 photoresist layers of up to 2 mm of thickness, the solvent content varied from 10.4% at the top to 5.4% at the bottom of the photoresist film [130]. The solvent evaporated quickly at the beginning of the soft baking because of the very high solvent concentration and less at the bottom resulting in delamination of the developed structures. If the wafer was baked at slightly higher temperature or for higher time intervals, then the solvents in the photoresist would evaporate completely making it unusable. On the other side if it was baked at lower temperatures or for shorter intervals of

time, then the photoresist would not be hard enough to be applicable for exposure. Finally, optimum development time was crucial for obtaining better side walls and SU8 films without over development that would result in peel off and reduced bond strength with the substrate. Figure 4.16 and Figure 4.17 illustrate the excessive development process in the SU8 photoresist film and a photograph of an excessively developed SU8 polymer side wall.

4.7 ANTENNA ASSEMBLY

The packaging method employed to assemble the micromachined aperture coupled antenna devices is illustrated in Section 4.4. The micromachined aperture coupled antenna devices utilised the free-standing patch elements to achieve high efficiency and improved bandwidth. Figure 4.18 shows optical images of microstrip fed micromachined aperture coupled antenna device using the assembly process outlined in Section 4.4.

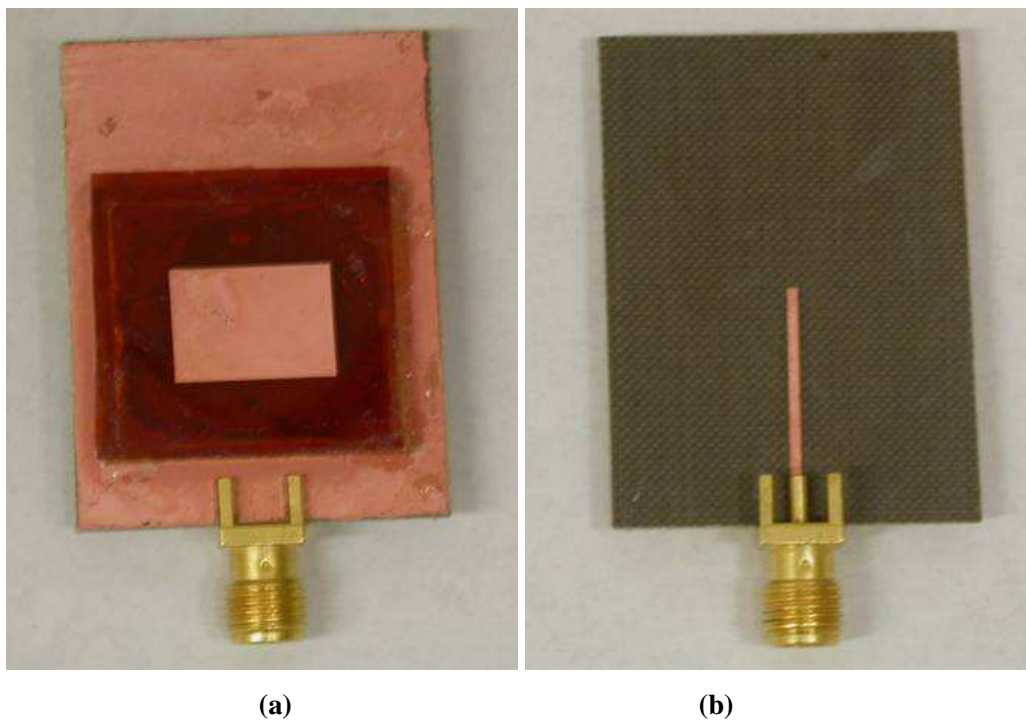


Figure 4.18 (a) Photograph of the fabricated microstrip fed micromachined aperture coupled antenna device after assembly. (b) Photo graph of the back side of the fabricated antenna

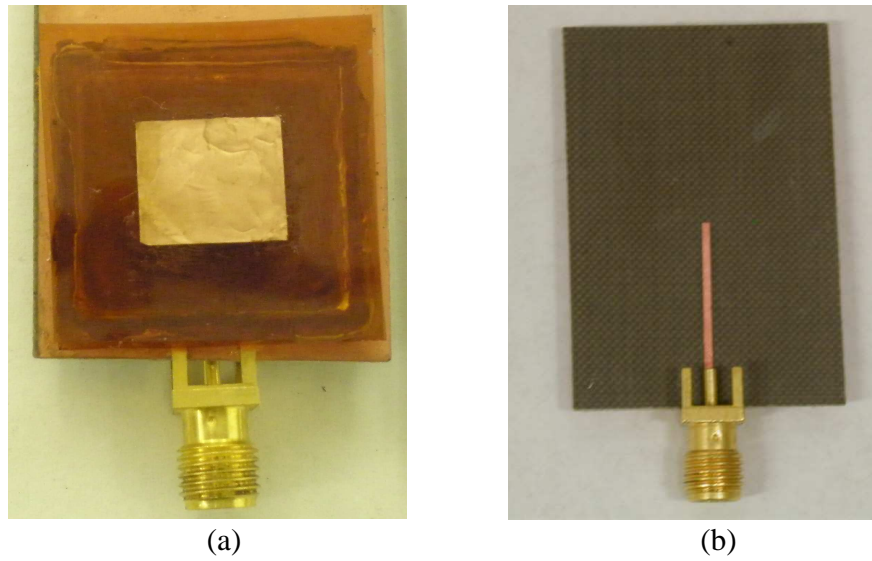


Figure 4.19 (a) Optical picture of the front side of a fabricated antenna (b) Optical picture of the reverse side of the antenna

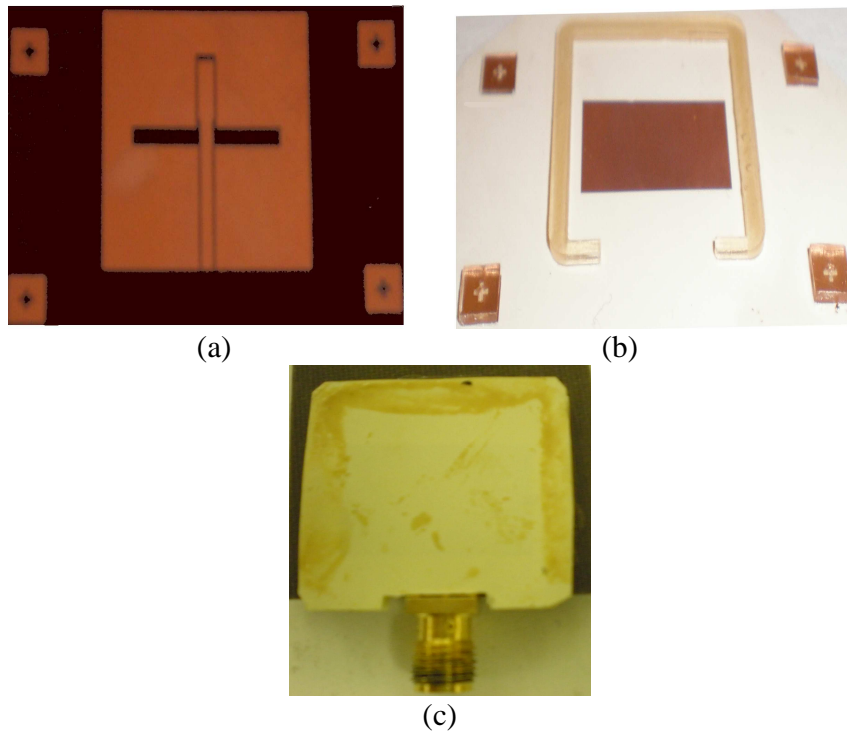


Figure 4.20 (a) Photograph of a fabricated CPW line and aperture on the PTFE substrate, (b) Optical picture of a patch and a SU8 polymer rim on a LCP substrate and (c) Optical picture of an assembled device after stacking three patch layers on the PTFE base substrate

The most critical parameters determining the quality of the bonding were the thickness uniformity of the SU8 rims, the amount of SU8-100 solution applied to the surface of the

SU8 rims and the bonding pressure and temperature. SU8 rims with good surface uniformity could be obtained using an optimized fabrication process. The amount of SU8-100 liquid for bonding was determined by minimizing void formation and at the same time reducing the overflow of the material during bonding. A good bonding temperature was 65°C which was just above the glass transition temperature (64°C) of the SU8 material but not high enough to cause significant overflow as the viscosity changed rapidly around the glass temperature [140]. Figure 4.19 shows optical images of microstrip fed micromachined aperture coupled stacked antenna device with three stacked patch elements.

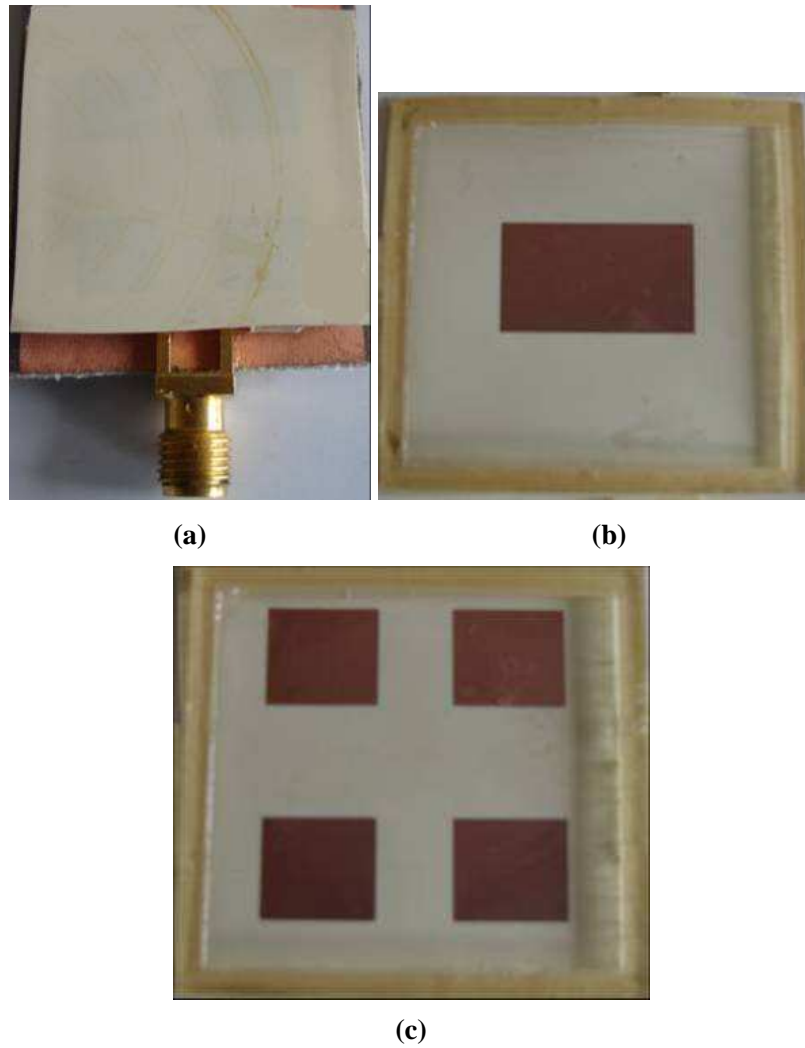


Figure 4.21 (a) Photograph of the microstrip fed micromachined aperture coupled stacked quad antenna after assembly. (b) Photograph of the lower patch element on LCP film and (c) Photograph of the upper quad array patch element on LCP film

Figure 4.20 shows optical pictures of the CPW fed antenna device with three stacked patch elements. Figure 4.20 (a) shows the CPW line and the coupling aperture fabricated on

PTFE substrate prior to the assembly of the patches. Figure 4.20 (b) shows a picture of the bottom patch and a SU8 polymer rim on a LCP substrate. The opening of 15 mm in length in the SU8 rim was used to facilitate the attachment of an SMA connector to the ground and the CPW line on the base substrate for RF characterization. Figure 4.20 (c) shows the assembled device after stacking three patch layers on the PTFE base substrate. The metal patch elements were fabricated on the lower surface of the LCP substrate for better protection. Figure 4.21 shows optical images of microstrip fed micromachined aperture coupled stacked quad antenna device.

4.8 SUMMARY

Micro-fabrication and micro-assembly methods have been developed to fabricate high performance MEMS based antenna devices. The antenna structures were fabricated in layers and assembled using micromachined polymer spacers. Low cost materials like SU8, polyimide film, LCP substrate were employed for the fabrication of the micromachined aperture coupled antenna devices. The feeding and aperture features were fabricated on the microwave substrates while the radiating patch elements fabricated on the polyimide and LCP substrates. A UV lithography technique was developed with a positive photoresist (AZ 9260) for obtaining better conductor patterns with electrodeposition and etching techniques. Polymer rims were used to obtain air cavities between the patch and the substrate for high gain operation. The thermal stress due to the CTE (coefficient of thermal expansion) mismatch between the SU8 polymer rims and the substrate materials was minimised in the fabrication process using optimised prebake and post bake parameters in order to eliminate the delamination of the SU8 structures from the substrates. The fabricated substrate layers were assembled using a low temperature polymer bonding process to form high performance antenna devices. Precision alignment marks on the polyimide films (transparent) and the base substrate were used to facilitate the accurate alignment of the layers. After antenna assembly, SMA connectors were attached to the conductor lines in the microwave substrates to obtain antenna devices for RF characterization. The use of low cost polymer for cavity construction had a significant advantage over the micromachined silicon in producing millimetre scale air gaps for high gain operation.

CHAPTER 5 MICROWAVE MEASUREMENTS AND CHARACTERISATION

After the fabrication and assembly of the micromachined antenna devices, microwave characterisation of the devices is carried out using a network analyser for reflection and radiation measurements. Transmission measurements were conducted to determine the antenna gain and radiation pattern for the antenna devices. Radiation measurements that include antenna gain and radiation pattern were carried out in an anechoic chamber using the far field method. The reflection coefficient, impedance and the radiation characteristics are presented followed by discussion and comparison of the devices.

5.1 THE EXPERIMENTAL METHOD

5.1.1 Reference plane and calibration method

5.1.1.1 *Reference plane*

The reflection and transmission characteristics of the antenna devices were measured using a HP 8510B network analyser for obtaining various antenna parameters. The network analyser is described in Appendix A3. For microwave measurements, the travelling waves or the voltage ratios are a function of position on the transmission lines. Any change in the cross-section of the transmission line will give rise to a reflection and the generation of evanescent modes. It is therefore necessary to be able to specify a reference plane which is appropriately at a sufficient length of uniform transmission line.

5.1.1.2 *TRL calibration*

The accuracy of a microwave measurement system is greatly influenced by the components of the measurement setup, such as coaxial cables, SMA connectors and coplanar probes. Calibration is an error correction procedure to remove the parasitic effects of the components of the measurement setup. The frequency range of the microwave measurement was set appropriately with sufficient bands outside the simulation results. A TRL calibration is employed for both one port and two port calibrations by following the instructions displayed on the screen of the network analyser. One port calibration is sufficient for the S_{11} measurements but two port calibration is necessary for radiation measurements [141]. A total of ten measurements are made to quantify eight unknowns in three steps for the two port calibration. The “thru” step consists of the test ports connected

together directly (zero length thru) or with a short length of transmission line (non zero length thru) and the transmission frequency response and port match are measured in both directions by measuring all four S-parameters. The “reflect” step consists of open and/or short circuits connected to each test port and measured (S_{11} and S_{12}). The line step consists of a short transmission line (different in length from thru) inserted between port 1 and port 2 and the frequency response and port match are measured in both directions by measuring all four S parameters. After the above steps, the calibration is completed and the network analyser computes the errors associated with the connectors, cables and the probes according to the measured characteristics of the three standards. In the subsequent measurements, these errors will be automatically removed from the measurement results.

5.1.1.3 The SMA connector

The interface dimensions for SMA connectors are listed in MIL-STD 384A. The SMA connector is widely used in many applications for its cost-effective feature; however it is not suitable for precision metrology. It is a semi-precision connector that has limitations with the solid plastic dielectric and potential damage to the plug pin. The SMA connector is widely used for characterizing the microwave devices but not suitable for repeated connections [141]. Destructive interference may result if the contacts protrude beyond the outer conductor mating planes and so care should be taken while connecting the SMA connectors.

5.2 ANTENNA RADIATION MEASUREMENTS

Antenna measurements and testing methods have been evolving for many years. Antenna anechoic chambers have been developed for the purpose of measuring the radiation patterns of antennas independent of their operational environment.

5.2.1 Anechoic chambers

There are two basic types of anechoic chambers, the rectangular and the tapered designs. A rectangular anechoic chamber is usually designed to simulate free-space conditions. In order to reduce the reflected energy level, high-quality absorbing material is used on surfaces which would otherwise reflect energy directly towards the test region as shown in Figure 5.1. The actual width and height required depend on the magnitude of the errors (due to reflections) that can be tolerated and the characteristics of the absorbing material

used to line the walls. Additionally the room width and the size of the source antenna should be chosen such that no part of the main lobe of the source antenna is incident upon the sidewalls, ceiling, and floor.

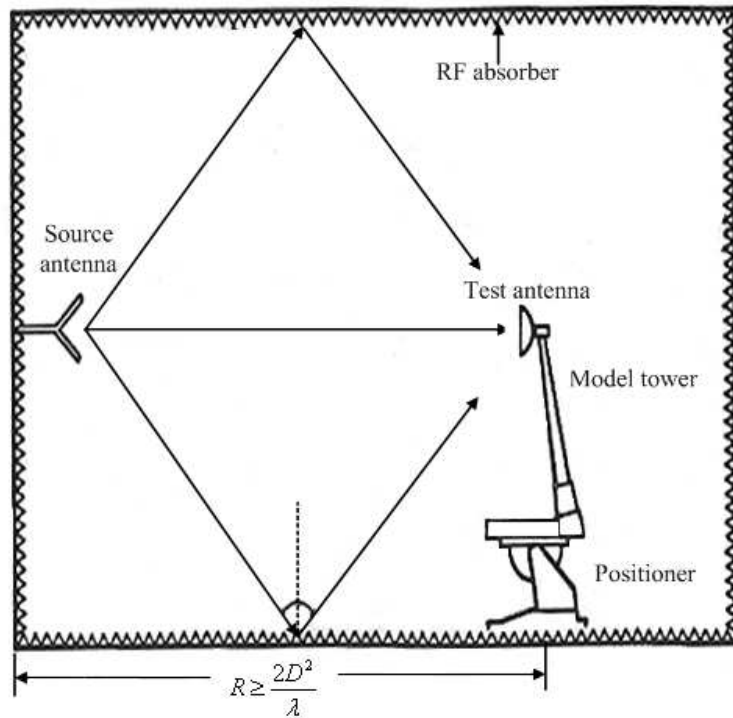


Figure 5.1 A typical rectangular anechoic chamber [141]

5.2.2 Far field measurements

The far field approach is the simplest method for electrically small antennas since it does require a large separator between the transmitting and receiving antennas. The dimensions of the micromachined antenna devices are relatively small; the separation distance for the far field measurements can be set between 1 to 2 metres. Patterns are obtained in 2D at a time and there is no need to measure the phase. On the other hand, the far field pattern and other data such as gain and directivity are obtained readily without much computer processing. The limitations of this method are that it has a limited angular coverage (with accuracy) and the method is subject to environmental conditions such as temperature and humidity. The three most widely used techniques in the far field test method are

- Elevated range
- Ground reflection range
- Compact range

The compact range measurement technique was used for the radiation measurement of the micromachined antenna devices. A three antenna gain measurement method was used for the microstrip fed micromachined aperture coupled antenna device in order to validate the gain of the standard gain horn antennas used and to measure the gain of the antenna device in E and H plane. The gain transfer method was used to measure the antenna gain at bore sight for the rest of the micromachined antenna devices. Radiation pattern measurements in the E and H plane are performed by measuring the S_{21} parameters between the 20 dBi FlannTM standard gain antenna and the AUT with the setup shown in Figure 5.2.

5.2.2.1 Three antenna gain measurement method

The far field measurement for antenna characterisation is based on the Friis transmission formula, which states that for a two-antenna system as shown in Figure 5.2, the power received at a matched load connected to the receiving antenna is given by [142, 143]

$$P_r = P_0 G_A G_B \left(\frac{\lambda}{4\pi R} \right)^2 \quad (5.1)$$

where P_r is the power received, P_0 is the input power of the transmitting antenna, G_A is the power gain of the transmitting antenna, and G_B is the power gain of the receiving antenna [144]. λ is the wavelength at which the gain is measured and R is the distance between the transmitting and receiving antennas. This form of the transmission formula implicitly assumes that the antennas are polarization matched for their prescribed orientations and that the separation between the antennas is such that the far-field conditions are met. The Friis transmission formula can be written in logarithmic form, from which the sum of the gains, in decibels, of the two antennas can be written as

$$(G_A)_{dB} + (G_B)_{dB} = 20 \log \left(\frac{4\pi R}{\lambda} \right) - 10 \log \left(\frac{P_0}{P_r} \right) \quad (5.2)$$

In order to determine the power gain of the antennas, the parameters R and $10 \log P_0/P_r$ are measured first and then $(G_A)_{dB}$ is computed. This method is referred to as the two-antenna method because of the use of two identical antennas. However if antennas A and B are not identical type, it requires a third antenna to determine the gain. Antenna types vary with the physical structure and electromagnetic design that include monopole, dipole, reflector, horn, yagi, slot and patch antennas [142, 143]. In the case where three antennas are used, three sets of measurements are performed using all combinations of three antennas [145, 146]. The result is a set of three simultaneous equations as follows.

$$(G_A)_{dB} + (G_B)_{dB} = 20\log\left(\frac{4\pi R}{\lambda}\right) - 10\log\left(\frac{P_0}{P_r}\right)_{AB} \quad (5.3)$$

$$(G_A)_{dB} + (G_C)_{dB} = 20\log\left(\frac{4\pi R}{\lambda}\right) - 10\log\left(\frac{P_0}{P_r}\right)_{AC} \quad (5.4)$$

$$(G_B)_{dB} + (G_C)_{dB} = 20\log\left(\frac{4\pi R}{\lambda}\right) - 10\log\left(\frac{P_0}{P_r}\right)_{BC} \quad (5.5)$$

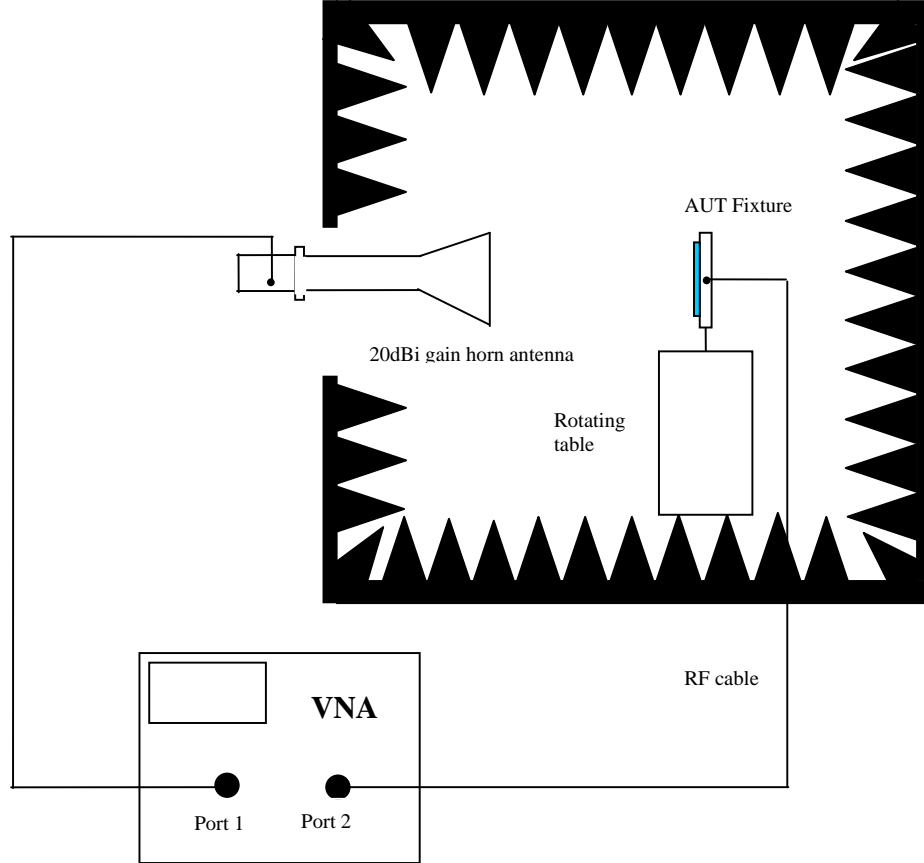


Figure 5.2 Schematic showing the far field set up

From these equations the gains of all of the three antennas can be determined. The instrumentation layout shown in Figure 5.2 can be used for the measurement of gain using the two-antenna or three-antenna methods. Calibration adjustments are made to the coupling network between the source and the transmitting antenna, so that the power measured at the transmit test point and the power fed into antenna A can be accurately related. The two antennas are arranged in a bore-sighted configuration so that they are properly aligned and oriented. For the three antenna method, a FlannTM standard gain antenna of 20 dBi gain was used as the gain standard. Another standard gain antenna

(Microwave Instruments Limited) of gain of 15 dBi was used as another standard gain antenna. A full two port calibration was carried out to shift the calibration reference plane to the ends of the connectors that fed the AUT (antenna under test) and the standard gain horns. The S_{21} readings for the configurations AB, AC and BC were taken from 0° to 180° in steps of 5° for the E and H planes. The data was transferred to an excel sheet where the absolute S_{21} values are substituted for the P_o and P_r for equations (5.3) – (5.5). These equations are solved to obtain the gain of the AUT.

5.2.2.2 Gain-transfer method

In the gain-transfer method, comparison of a test antenna and that of a standard gain antenna is performed in order to measure the unknown power gain. Ideally the test antenna is illuminated by a plane wave which is polarization matched to the plane wave, and the received power is measured into a matched load. The micromachined aperture coupled antennas and the standard gain antennas are linearly polarised. Polarization match for the H plane measurements is achieved by matching the vertical polarisation (electrical field varying in vertical direction with respect to ground) of the micromachined antenna device with the vertical polarisation for the horn antenna (probe feed direction). A horizontal polarisation is matched for the E plane measurements. The test antenna is replaced by a gain standard, leaving all other conditions the same. The received power into its matched load is again measured. From the Friis transmission formula it can be shown that the power gain (G_T) dB of the test antenna, in decibels, is given by

$$(G_T)_{dB} = (G_S)_{dB} + 10 \log \left(\frac{P_T}{P_S} \right) \quad (5.6)$$

where $(G_S)_{dB}$ is the power gain of the gain-standard antenna, P_T is the power received with the test antenna, and P_S is the power received with the gain-standard antenna. One method of achieving this exchange between test and gain-standard antennas is to mount the two antennas back to back on either side of the axis of an azimuth positioner. With this configuration the antennas can be switched by a 180° rotation of the positioner. Measurements are taken to position the antennas so that they will be in the same location when switched. In order to reduce the reflections in gain standard's vicinity, usually absorbing material is required immediately behind the gain standard which might perturb the illuminating field. The reflection coefficients of all the components shall be measured as a function of frequency so that corrections can be made to the measured power gain.

The ideal conditions required for power-gain measurements can be summarised as follows [145]:

- (1) Antenna range: Free-space conditions, uniform plane-wave field at the receiving antenna.
- (2) Antennas: Impedance matched, aligned and properly bore sighted, in addition the antennas should be suitably polarization matched.
- (3) Equipment operation: Components, ideal and impedance matched, single sinusoidal frequency, single waveguide mode, stable generator and receiver, adequate sensitivity and dynamic range

A flann standard gain antenna of 20 dBi gain was used as gain standard in the receiving mode. Another standard gain antenna (Microwave Instruments Limited) of 15 dBi of gain is used as the transmitting antenna. The second standard gain antenna is used instead of a standard dipole antenna in the transmitting mode due to the inherent low gain of a standard dipole. A low gain dipole will give lower S_{21} values and reduced sensitivity. Figure 5.3 shows the far field measurement system in the anechoic chamber to measure the antenna radiation pattern and gain. The standard gain antenna and the AUT are mounted on a rotating stage. The rotating stage is a 360 degree rotating column with precise relative angle output on a marker screen. The reference antenna was mounted on a stationary and stable flat form facing the AUT or the gain standard. A two-port calibration was used to shift the reference plane at the ends of the connectors that feed the AUT and the standard gain horns. An on/off switch is located on the controlling column to take the readings manually for a shift in angle of 1 degree or more. A 25 dB RF power amplifier along with an isolator was used to amplify the signal from the network analyser. It is anticipated that an absolute power level value of the amplifier is not necessary as the antenna measurements for the gain and radiation pattern involves the relative transmission values. The gain of the amplifier is taken from the manufacturer's data sheet but not calibrated. The AUT and the reference antenna were placed with a separation distance of about 1 metre. The transmission coefficient S_{12} was recorded for every five degree of angle shift and subsequently converted into the absolute values. The E plane and the H plane for the antenna are defined in terms of the orientation of the AUT with respect to reference antenna as shown in Figure 3.12(a). The data is transferred to an excel sheet where in the absolute

S_{21} values are substituted for the P_T and P_S in Equation (5.6) for finding the gain of the AUT. To obtain the normalised radiation pattern the S_{21} values obtained from the standard gain antenna and the AUT with respect to the reference antenna device are normalised.

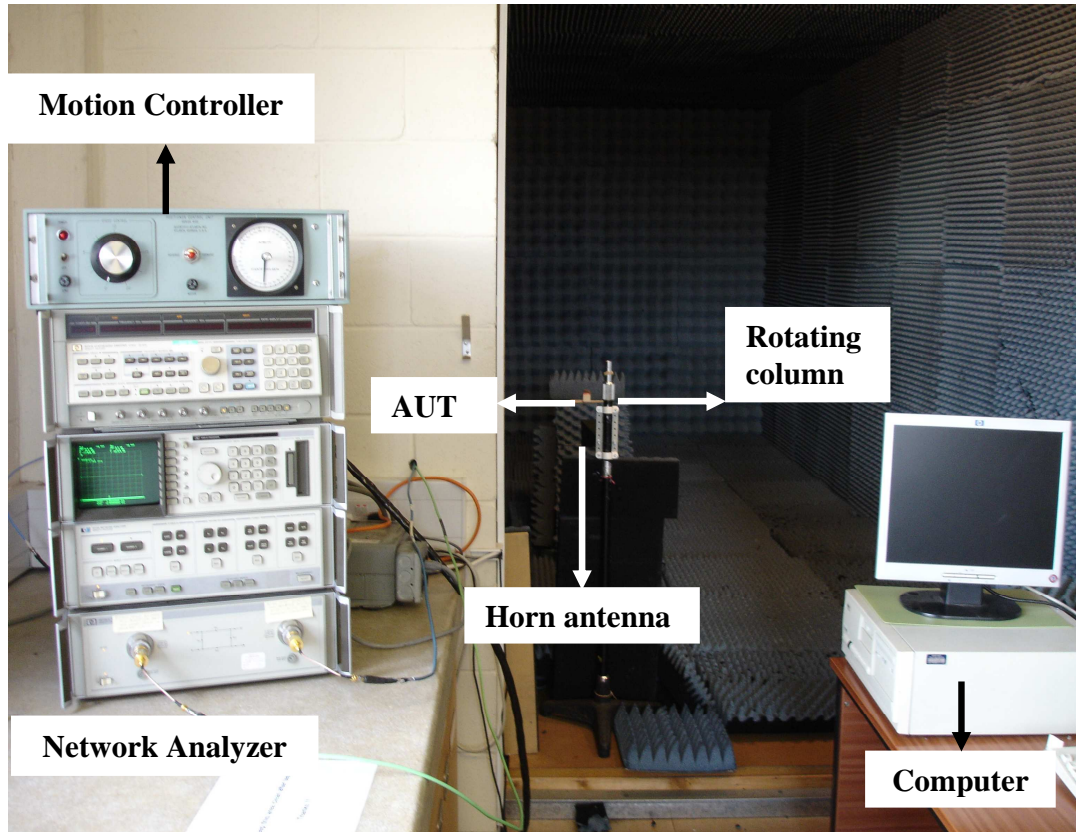


Figure 5.3 Photograph of the far field measurement system in the anechoic chamber to measure the antenna radiation pattern and gain

5.3 RESULTS

The radiation patterns which were measured using the methods described in section 5.3 are plotted as polar plots and compared with the simulation results presented in Chapter 3. The three-antenna method was used to measure the absolute gain of the single patch micromachined antenna device while the gain comparison technique was used for the rest of the antenna devices.

5.3.1 Microstrip fed micromachined aperture coupled patch antenna device

Figure 5.4 shows the measured results for the reflection characteristics (S_{11}) of the microstrip fed micromachined aperture coupled patch antenna device. The measured results are plotted as a function of frequency from 10 to 15.5 GHz. It can be seen from the

plot that the return loss is lower than 10 dB from around 12 GHz to 14.3 GHz for the simulation and from 12.1 GHz to 14.7 GHz for the measurements. The -10 dB bandwidth of the device is determined to be 19% from the measured results. The corresponding simulated bandwidth of the antenna is 2.3 GHz or 17%. The wide bandwidth of this single patch micromachined antenna device is due to the resonance effects of the TM_{10} resonance of the radiating patch and the parasitic resonance of the aperture in the ground plane of the antenna device.

The device exhibits a wide bandwidth as a result of the coupling between the patch and the aperture resonances. The difference in the measurements to the simulation can be primarily due to the SU8 material dielectric constant as outlined in Section 3.5. In order to demonstrate this, the antenna device is simulated for various dielectric constant values and it can be seen from the reflection coefficient curve obtained as shown in Figure 3.22 that the measurement curve follows more closely to the simulation curve. The shift in the measurement curve from the simulated curve can also be due to the tolerances (fabrication errors) in polymer rim thickness as presented in Section 3.5.5 and due to smaller contributions (usually <1 dB) [141] from measurement uncertainties, numerical inaccuracies in simulation, measurement and inaccuracies due to the SMA connector as the SMA connector is not calibrated until the connecting pin. The bandwidth for the single patch micromachined antenna device is due to the multiple resonance effects that include the TM_{10} resonance of the top radiating patch and the resonance of the aperture in the ground plane of the antenna device.

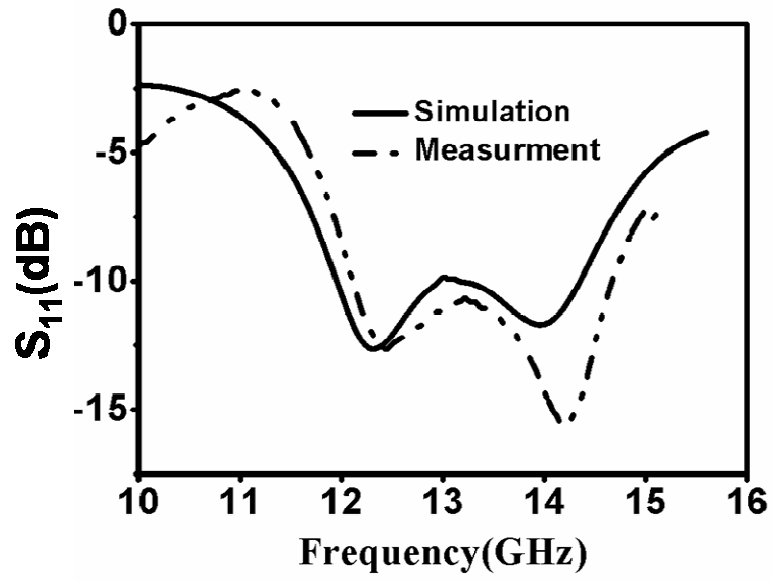


Figure 5.4 Simulation and measurement results of the return loss for the microstrip fed micromachined aperture coupled patch antenna device

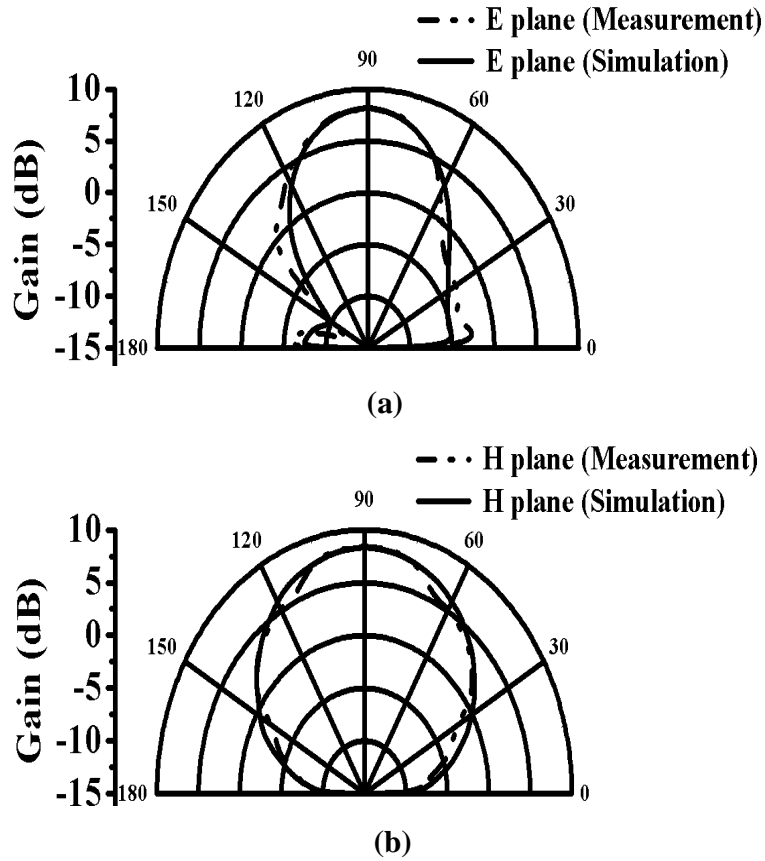


Figure 5.5 Simulated and measured E-plane (a) and H-plane (b) radiation patterns for microstrip fed micromachined aperture coupled patch antenna device at 12.1 GHz

Figure 5.5 shows the gain-factor results for the microstrip fed micromachined aperture coupled patch antenna device. The gain of the antenna device at broadside is about 8.3 dBi at 12.1 GHz. The E-plane patterns show that there are significant side lobes and it can be seen from Chapter 3.3 that the predicted radiation efficiency for the device is 98% based on the simulation results using HFSS. The measured H plane radiation pattern is symmetric while the E plane is almost symmetric except at the angles near 0° and 180° respectively. This can be attributed to the radiation from the microstrip line and the aperture in the ground plane. The beam width and the radiation patterns agree well with the simulation results. It can be seen that the gain of the device has been improved over the conventional microstrip patch antenna as presented in Section 2.2. The gain of the conventional patch antenna with a dielectric constant of 10.2 and at same resonant frequency was about 4.7dBi while the gain of the microstrip fed micromachined antenna device was 8.6 dBi. From Table 2.1, it can be seen that the decrease in gain is primarily due to decrease in radiation efficiency and directivity for a higher permittivity substrate. Thus from Table 2.1 and from Sections 2.2.4 and 2.2.5, by having a low dielectric constant primarily air or an air cavity between the patch and the substrate (by using a polymer rim) an improvement in the antenna gain and bandwidth can be achieved.

5.3.2 Microstrip fed micromachined aperture coupled stacked antenna device

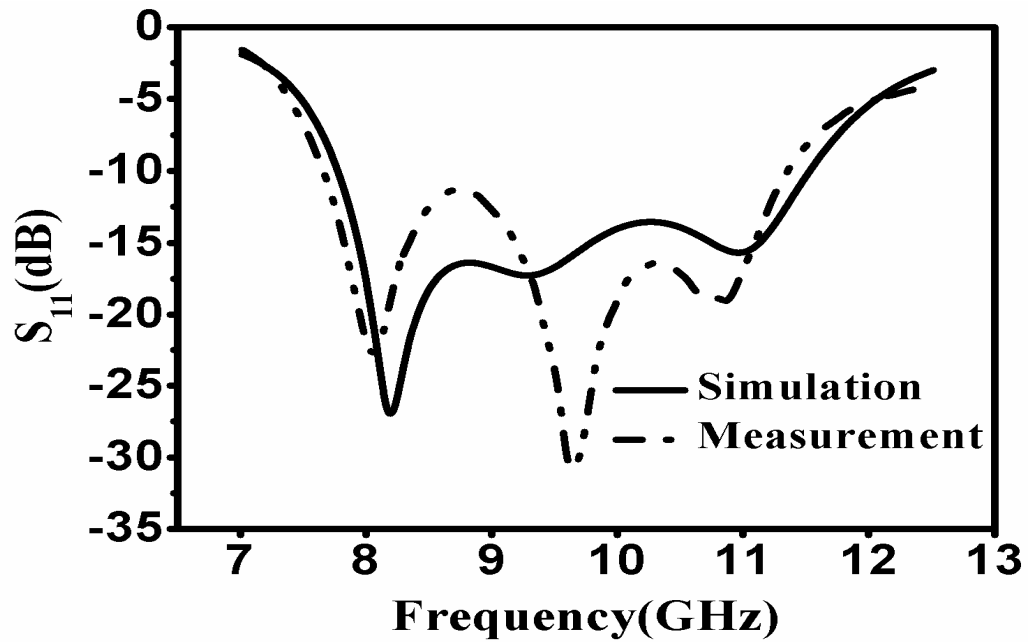


Figure 5.6 Simulation and measurement results of the reflection coefficient for the microstrip fed micromachined aperture coupled stacked antenna device

Figure 5.6 shows the measured and simulated results of the reflection characteristic (S_{11}) of the microstrip fed micromachined aperture coupled stacked antenna device. The return loss parameters are plotted as a function of frequency from 7 to 12.5 GHz. It can be seen from the plot that the return loss is lower than 10 dB from around 7.785 GHz to 11.525 GHz for the simulation and from around 7.675 GHz to 11.375 GHz for the measured results. The corresponding bandwidth of the antenna is 3.74 GHz or $\sim 40\%$ for the simulation and 3.7 GHz or $\sim 39\%$ for the measurements. The increase in bandwidth for this stacked micromachined patch antenna device is due to the micromachined polymer rim, multiple resonance effects that include the TM_{10} resonances due to both magnetic and electric coupling (outlined in Section 3.3.1) between the top radiating patch and the aperture in the ground plane of the antenna device. In order to demonstrate this, the antenna device is simulated with the lower patch removed and keeping the rest of the dimensions and materials constant. The reflection coefficient curve due to this is shown in Figure 5.7. It can be seen from the curve that the -10 dB bandwidth does not vary much ($<2\%$) by removing the lower patch while the impedance matching is degraded. Thus, the wide bandwidth is only due to the coupling mechanism between the aperture and the top radiating patch that includes both magnetic and electric coupling.

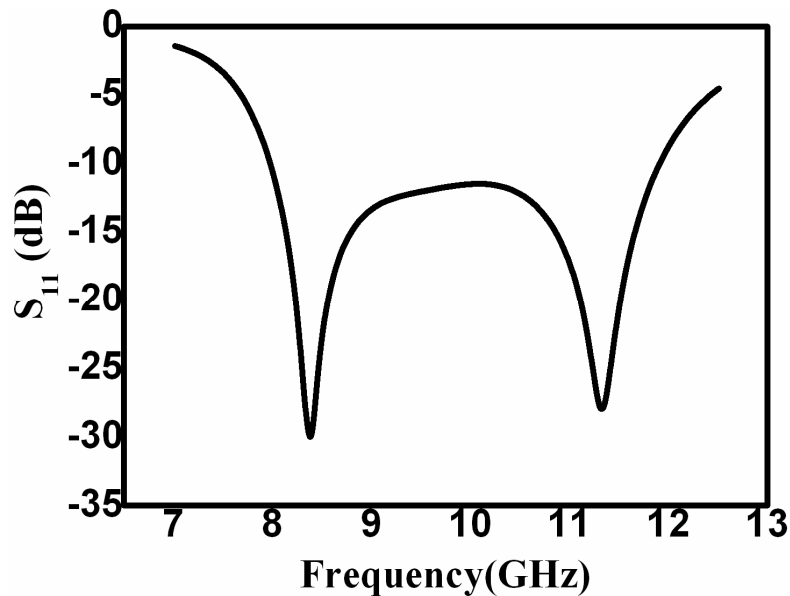


Figure 5.7 Simulation results of the reflection coefficient for the microstrip fed micromachined aperture coupled stacked antenna device with the lower patch removed.

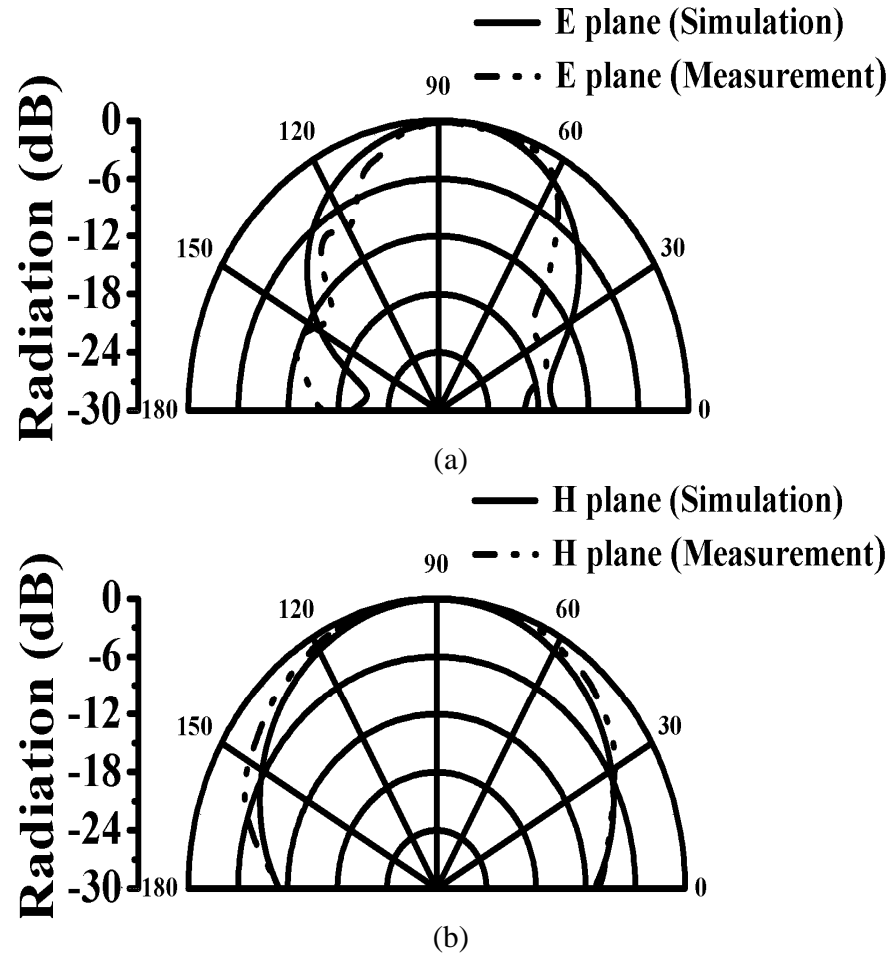


Figure 5.8 Simulated and measured E-plane (a) and H-plane (b) radiation patterns for the microstrip fed micromachined aperture coupled stacked antenna device at 9.5 GHz

It can be seen from Figure 5.6 that the measured results agree well with that of the simulation in terms of the -10 dB bandwidth apart from the disagreement with respect to the frequency shift of antenna resonances after -10 dB in reflection coefficient. The difference in the measurements to the simulation can be primarily due to the SU8 material dielectric constant and due to fabrication tolerances in the heights of the polymer rim as outlined in Section 3.5. As the stacked micromachined patch configuration is relatively complex in construction when compared to the simple micromachined aperture coupled antenna configuration it is hard to quantitatively determine the contribution of each effect although the effects of the polymer rim characteristics and its dimensions can be understood from the computer simulations for a simple antenna configuration as presented in Section 3.3. The shift in the measurement curve from the simulated curve can also be due to smaller contributions (usually <1 dB) [141] from measurement uncertainties,

numerical in accuracies in simulation, measurement and inaccuracies due to the SMA connector as the SMA connector is not calibrated until the connecting pin. Figure 5.8 shows the normalized antenna radiation pattern results for the microstrip fed micromachined aperture coupled stacked antenna device. The gain of the antenna is about 7.8 dBi at ~ 10.5 GHz. The E-plane patterns show that there are small side lobes. The measured E and H plane radiation patterns are symmetric. The small side lobe between 160° and 180° can be attributed to the microstrip line and the aperture in the ground plane. The beam widths and the co-polarised radiation patterns agree well with the simulation patterns. The back radiation associated with the antenna device is reduced by introducing an air cavity underneath the bottom patch substrate while the Q-factor and the bandwidth of the antenna device remains the same.

5.3.3 CPW fed micromachined aperture coupled stacked antenna device

Figure 5.9 shows the measured and simulated results of the reflection characteristic (S_{11}) for the CPW fed micromachined aperture coupled stacked antenna device. The return loss parameters are plotted as a function of frequency from 5.5 to 11 GHz. It can be seen from the plot that the return loss is lower than -10 dB from around 6.73 GHz to 10.02 GHz for the simulation and from around 6.425 GHz to 10.05 GHz for the measured results. The corresponding bandwidth of the antenna is 3.29 GHz or $\sim 39.2\%$ for the simulation and 3.6 GHz or $\sim 44\%$ for the measurements. The difference in the measurements to simulated results can be attributed primarily to the manufacturing tolerance in the height of the polymer rims, material characteristics of the polymer rims and partly due to the SMA discontinuities. This is because the calibration is performed until the end of the coaxial cables but not to the end of the probe of the SMA connector. The device exhibits a wide bandwidth as a result of coupling between the top two patches and the aperture resonances, while the lower patch improves the reflection coefficient for the antenna device. For this device, the top two patches appear to be strongly coupled. In order to demonstrate this, the antenna device is simulated with the lower patch and the middle patch elements removed and the reflection coefficient curves due to this is shown in Figure 5.10. It can be seen from the curves that the -10 dB bandwidth does not vary much with the lower patch removed while it varies substantially with the middle patch element removed.

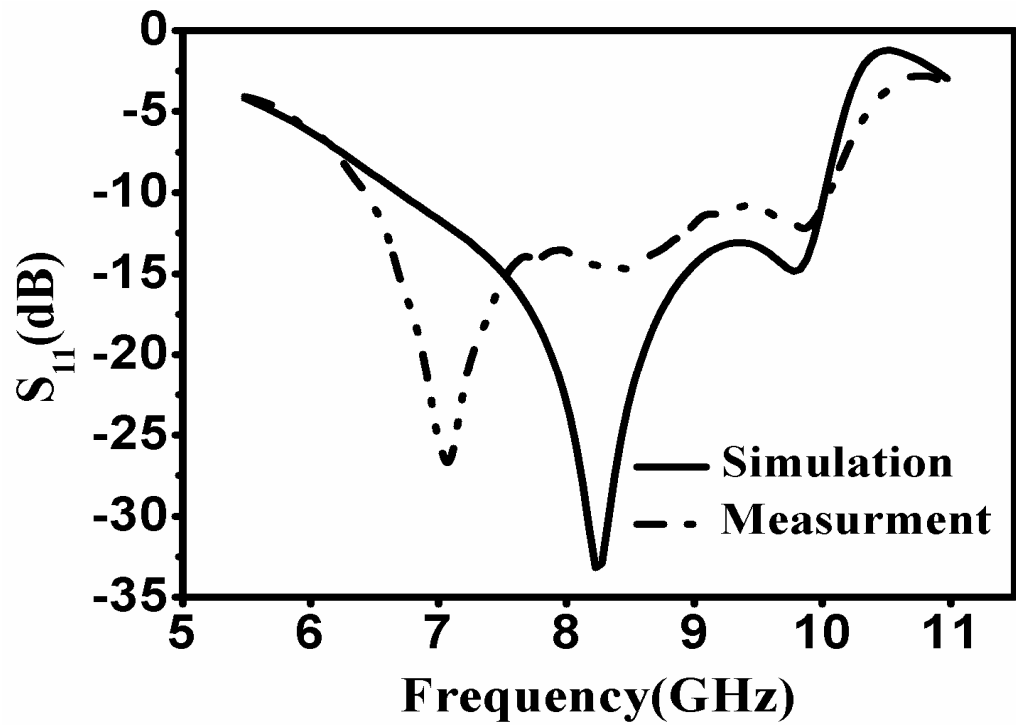


Figure 5.9 Simulation and measurement results of the reflection coefficient for the CPW fed micromachined aperture coupled stacked antenna device

Figure 5.11 shows the normalized antenna radiation results for the CPW fed micromachined aperture coupled stacked antenna device. The gain of the antenna is about 7.6 dBi at ~ 10 GHz. The E and H plane radiation patterns show that the side lobes are reduced significantly when compared to the microstrip fed antenna device and it can be seen from the simulation results in Section 3.5 that this antenna device has much less back radiation as a result of the CPW feed configuration and thus forming a so called substrate independent antenna configuration [84]. The thin film LCP substrate has negligible effect on the performance of the device as shown in the results. The measured H plane radiation pattern is symmetric while the E plane is almost symmetric except for the occurrence of nulls at 180° respectively. This can be attributed to the radiation from the CPW line configuration and the non presence of CPW Line at 180° and the aperture in the ground plane. The beam widths and the co-polarised radiation patterns agree well with the simulation patterns.

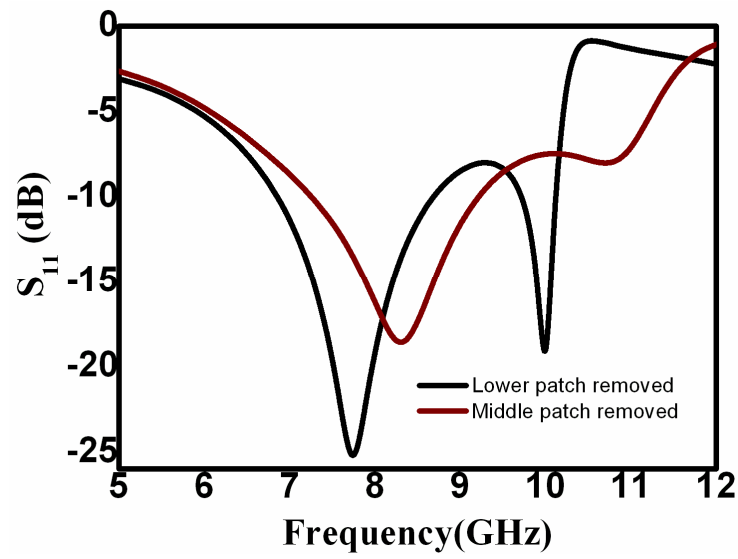


Figure 5.10 Simulation results of the reflection coefficient for the CPW fed micromachined aperture coupled stacked antenna device with the lower and middle patch elements removed

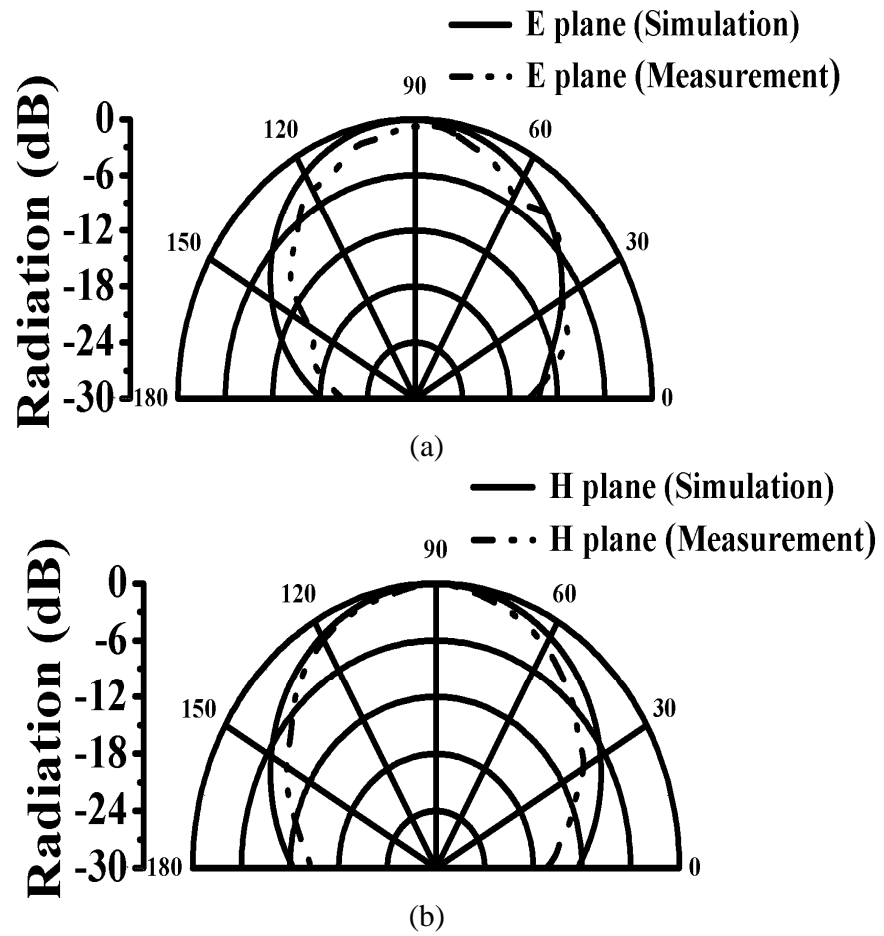


Figure 5.11 Simulated and measured E-plane (a) and H-plane (b) radiation patterns for CPW fed micromachined aperture coupled stacked antenna device at 10 GHz

From Table 2.1, it can be seen that by increasing the height of air cavity, the patch antenna directivity and gain decreases minimally. Thus, the lower gain of the antenna device can be attributed to the height of the polymer rims and is slightly higher than the microstrip feed stacked antenna configuration. The results obtained from the microstrip fed and CPW fed micromachined antenna devices are comparable to that of the foam based antenna devices [25].

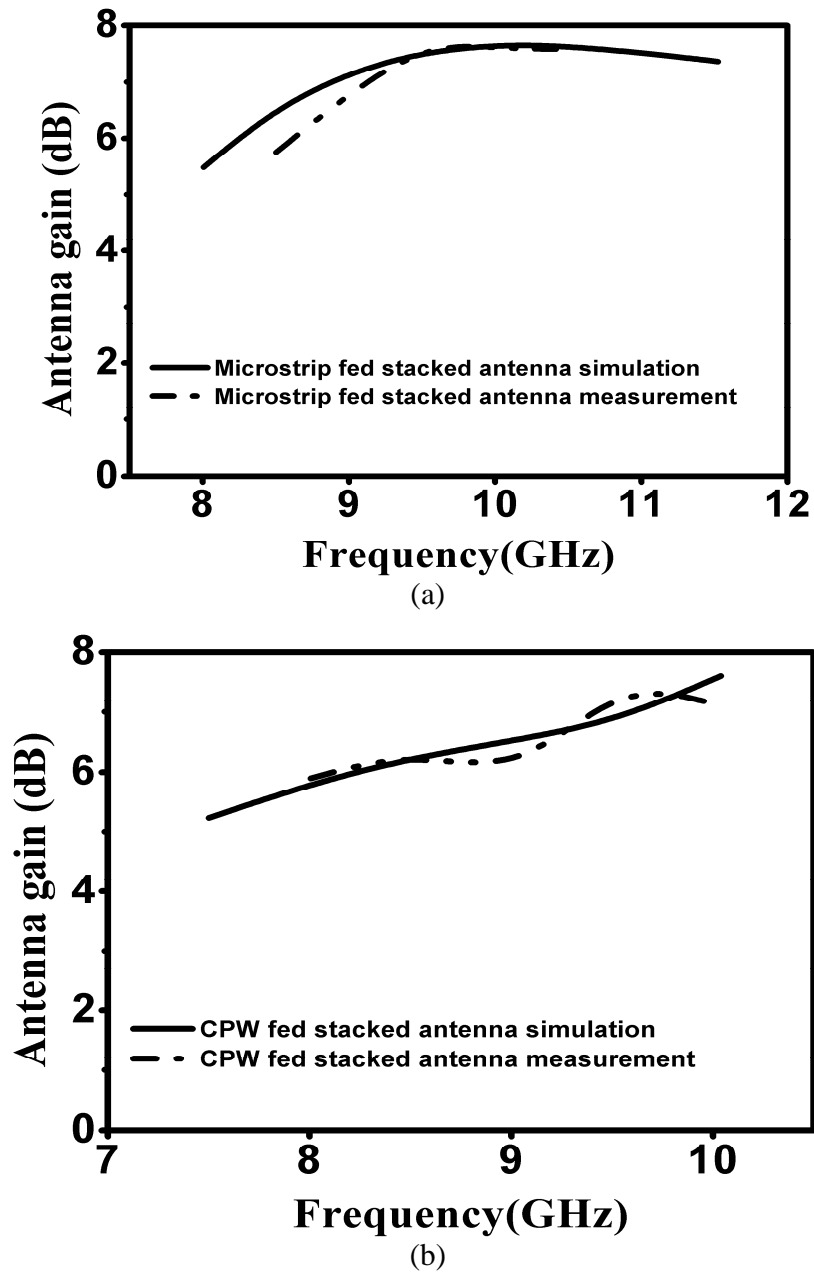


Figure 5.12 Frequency dependent peak gain for (a) microstrip fed and (b) CPW fed stacked patch antenna with respect to frequency

Figure 5.12 shows the results of gain variation as a function of frequency over the operation bandwidth for each of the microstrip and CPW fed stacked aperture coupled micromachined antenna devices. The measured results agree well with that of simulation. The gain varies from 5dBi at ~ 7 GHz to around 7.8 dBi at ~ 10.5 GHz for the microstrip fed device. For the CPW fed device the gain varies from 5dBi at ~ 7 GHz to around 7.6 dBi at ~ 10 GHz. Thus high gain has been realised over a wide bandwidth for the devices.

5.3.4 Microstrip fed micromachined aperture coupled subarray antenna device

Figure 5.13 shows the measured and simulated results of the reflection characteristic (S_{11}) of the microstrip fed micromachined aperture coupled subarray antenna device. The return loss parameters are plotted as a function of frequency from 9.2 to 16.6 GHz. It can be seen from the plot that the return loss is lower than 10 dB from around 9.72 GHz to 16.3 GHz for the simulation and from around 9.6 GHz to 15.81 GHz for the measured results. The corresponding bandwidth of the antenna is 6.58 GHz or ~ 50.5% for the simulation and 6.21 GHz or ~ 48.8% for the measurements. A wide bandwidth was obtained as a result of coupling between the patch, the aperture resonances and the quad array.

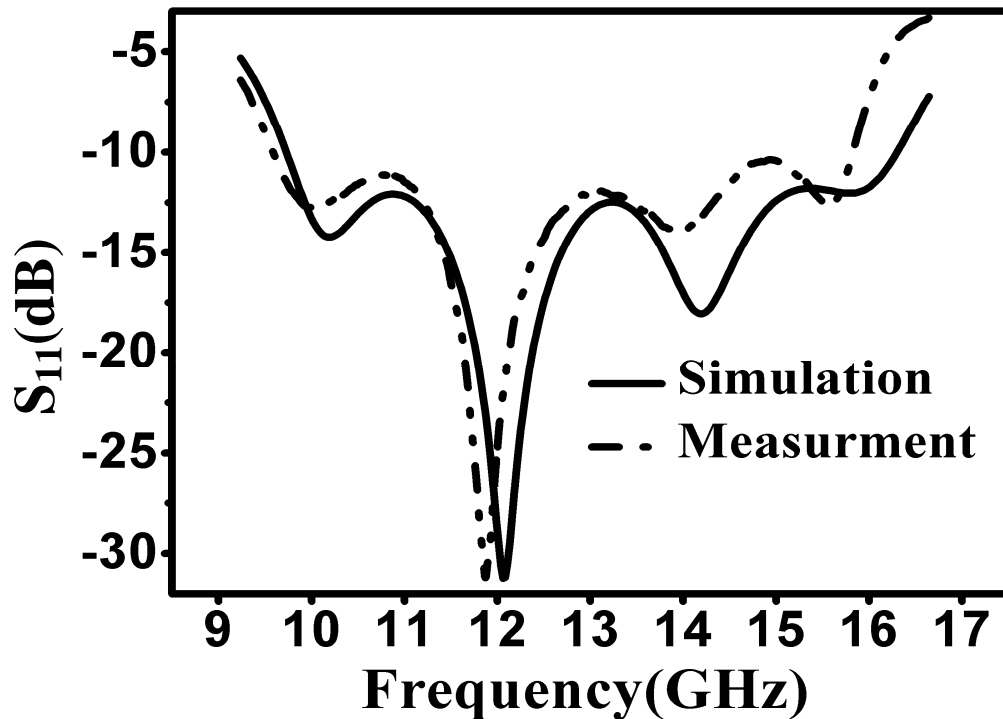


Figure 5.13 Simulation and measurement results of the reflection coefficient for the microstrip fed micromachined aperture coupled subarray antenna device

Figure 5.14 shows the normalized antenna radiation pattern results for the microstrip fed micromachined aperture coupled subarray antenna device. The measured peak gain of the antenna was observed to be 10 dBi. The predicted maximum gain of this device is ~ 11.5 dBi at 13.5 GHz. The thin film LCP substrates have negligible effect on the performance of the device as shown in the results. The beam widths and the co-polarised radiation patterns agree well with the simulation patterns.

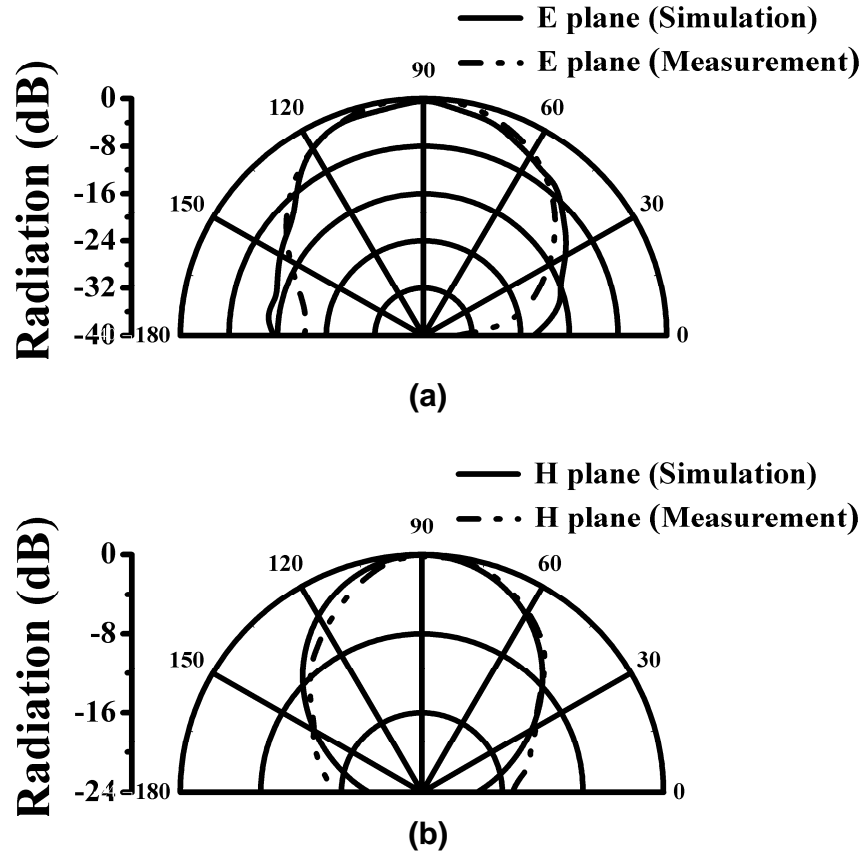


Figure 5.14 Simulated and measured E-plane (a) and H-plane (b) radiation patterns for the microstrip fed micromachined aperture coupled subarray antenna device at 12 GHz

5.4 SUMMARY

The measurement of reflection coefficient, radiation pattern and radiation gain have been realized for the micromachined antenna devices by appropriate RF measurement techniques. Two different radiation measurement techniques have been employed that includes the three antenna method and gain comparison methods. Good agreement between the experimental results and theoretical results was obtained. From the measurement results, it is concluded that the lossy effect of the SU8 polymer, the polyimide

and LCP supporting substrates is minimal due to the low dielectric loss tangents and this has been verified by simulations with Ansoft HFSS as the electrical properties of these materials are also included in the simulations as presented in Chapter 3. Thus these materials could be employed extensively for producing stacked antenna device with increased accuracy of aligning the stacked layers.

Table 5.1 Comparison of the measured antenna parameters for the micromachined antenna devices and the simulated conventional patch antenna device

Micromachined antenna device	Bandwidth (GHz)	Bandwidth (%)	Gain (dBi)
Microstrip fed micromachined aperture coupled patch antenna device (Figure 3.8)	2.5	19	8.3
Microstrip fed micromachined aperture coupled stacked antenna device (Figure 3.26)	3.7	39	7.8
CPW fed micromachined aperture coupled stacked antenna device (Figure 3.32)	3.6	44	7.6
Microstrip fed micromachined aperture coupled subarray antenna device (Figure 3.40)	6.21	48.8	10
Calculated and simulated conventional patch antenna with width/length ratio of the patch equal to that of the microstrip fed micromachined aperture coupled patch antenna device and with air as a dielectric and thickness = 1.5 mm (calculated values shown in Table 2.1) (Figure 2.3)	Calculated		
	1.116	8.59	9.75
	HFSS simulation		
	0.991	7.63	9.29
Simulated conventional patch antenna with width/length ratio of the patch equal to that of the microstrip fed micromachined aperture coupled patch antenna device and $\epsilon_r=10.2$ (Rogers RO3010 TM) and thickness = 1.5 mm as shown in Table 2.1) (Figure 2.3)	Calculated		
	0.198	1.53	4.7
	HFSS simulation		
	0.175	1.35	4.4

The deviation of the measured results from the simulations can be due to the uncertainties in the measurement of S_{21} (power), reflections, the dimensions (separating distances of the antenna devices), the non-similarity of the antenna types and the SMA connector reliability. Errors in the measured radiation pattern or antenna gain can also be expected owing to the RF cable acting as a secondary radiator driven by the surface currents on the conducting surface of the AUT (usually <1 dB) [141]. The shape of the main lobe of the radiation

pattern can be measured accurately while the minima and the back lobe radiation suffered from the dynamic range achieved as the directivity of the small antennas are relatively small (less than 9 dBi). Table 5.1 compares the measured antenna parameters for the micromachined antenna devices. A simulated bandwidth of 2.3 GHz (17%) is obtained for microstrip fed micromachined aperture coupled patch antenna device while the measured bandwidth is 2.5 GHz (19%) is obtained. The peak measured antenna gain is 8.3 dBi. A simulated bandwidth of 3.74 GHz (40%) is obtained for the microstrip fed micromachined aperture coupled stacked antenna device while the measured bandwidth is 3.7 GHz (39%) is obtained. The bandwidth thus almost doubled with respect to the simple microstrip fed aperture coupled antenna device. The peak antenna gain is 7.8 dBi. For the CPW fed micromachined aperture coupled stacked antenna device, a simulated bandwidth of 3.29 GHz (39%) is obtained while the measured value is 3.6 GHz (44%). The simulated and measured bandwidth values for the microstrip fed micromachined aperture coupled subarray antenna device are 6.58 GHz (50%) and 6.21 GHz (48.8%) respectively. A maximum peak gain of 10 dBi at 12 GHz has been measured for the micromachined aperture coupled quad array antenna device. A peak-gain of 7.8 dBi was obtained at the frequency of 10.5 GHz for the microstrip fed stacked antenna device and 7.6 dBi at ~10 GHz for the CPW fed device. The calculated and simulated parameters of a conventional patch antenna device presented in Section 2.2 with two different relative dielectric constants air ($\epsilon_r=1$) and Rogers RO3010TM ($\epsilon_r=10.2$) have also been presented in Table 5.1 for comparison. From Table 5.1, it can be seen that the bandwidth for the micromachined aperture coupled antenna devices have increased significantly when compared to the conventional patch antenna device with similar W/L ratio of the patch element. The simulated antenna efficiencies for the micromachined has an average value of 99.5% which is comparable (99.9%) obtained with that of an air filled conventional patch antenna device.

CHAPTER 6 CONCLUSIONS

6.1 CONCLUSIONS

The contribution of the thesis is primarily related to the micromachining approach that can be used to achieve a low dielectric constant low loss region under the patch element to increase in radiation efficiency and bandwidth. A micromachining approach based on photolithography and metal deposition techniques for integrated CMOS-technology compatible solution has been developed where in the RF active devices on the CMOS chip can potentially be integrated on to the common substrate used to fabricate the passive devices like antennas and filters. The design, fabrication, assembly and characterization of microstrip and CPW fed micromachined aperture coupled single and stacked patch antenna devices has been presented in the thesis. A high gain planar antenna using a frequency selective surface (FSS) and operating at a frequency of 60 GHz has also been studied for high gain operation. The simulation results for the FSS based antenna device show low reflection coefficient and good radiation characteristics with a gain of 25 dBi at around 60 GHz and an antenna efficiency of more than 95%.

The design and simulation of the suspended micromachined antenna devices was carried out using an electromagnetic field simulation software package (Ansoft HFSS). The reflection coefficient (S_{11}), radiation pattern, gain, directivity and efficiency for each of the antenna devices were studied in order to obtain optimised devices. A polymer rim (SU8) was used to create a sealed air cavity between the substrate layers. The slot (aperture) based feeding method along with the stacked patch elements improves bandwidth using the coupling effects of the aperture and the stacked patch elements. It has been verified that a tolerance of SU8 polymer thickness of 100 μm is acceptable for variance in bandwidth and gain. The effect of SU8 polymer rim dimensions on the S_{11} results and the radiation efficiency for the microstrip fed micromachined aperture coupled patch antenna device was studied and an optimum polymer rim dimensions identified. Bandwidths of 2.3 GHz (17%), 3.74 GHz (40%), 29 GHz (39%), 6.58 GHz (50%) were obtained for microstrip fed, microstrip fed stacked, CPW fed, microstrip fed quad array micromachined aperture coupled patch antenna devices respectively from the modelling. The corresponding gain values are 8.3 dBi, 7.8 dBi, 7.6 dBi, 11.2 dBi respectively. The minimum backward radiation

for both E plane and H plane is around -8 dB, -12 dB, -17 dB, and -12 dB for the antenna devices respectively. The radiation efficiency is in between 0.91 to close to 0.98 for all of the micromachined antenna devices. In comparison, the best antenna radiation efficiency obtained for the micromachined antenna devices from the literature review presented in Chapter 2 are 64% for silicon micromachining, 97.4% for polymer micromachining (similar to the process used for the micromachined aperture coupled antenna devices), 73.3% for the synthesised substrates and 60% for the micromachined glass. The effect of SU8 material properties and the SU8 polymer rim dimensions is studied for a simple microstrip fed micromachined aperture coupled antenna device by simulating the antenna devices with various material properties. The simulation results show that the antenna impedance (reflection coefficient) characteristics vary substantially with the polymer rim height and the dielectric constant of the SU8 material while other characteristics like antenna gain, efficiency, directivity and -10 dB bandwidth remains almost constant. The tolerances in the fabrication of SU8 polymer rims of the order of 100 μ m are possible as presented in Section 4.6. Thus, in order to reduce this fabrication tolerances other methods such as direct casting technique should be explored [147].

Micro-fabrication and micro-assembly methods have been developed to fabricate the antenna devices. The antenna structures are fabricated in layers and assembled using micromachined polymer spacers. Low cost materials like SU8, polyimide film, LCP substrate are employed for the fabrication of the micromachined aperture coupled antenna devices. The polymer based stacked assembly is used for air suspended radiating patches as well as for antenna module packaging. The feeding and aperture features are fabricated on to the microwave substrates while the radiating patch elements are fabricated on to the polyimide and LCP substrates. A UV lithography technique has been developed with a positive photoresist (AZ 9260) for obtaining better conductor patterns with electrodeposition and etching techniques. UV lithography techniques (for SU8) followed by microassembly techniques have been employed for the micromachined cavities on the different kinds of substrates. The fabricated substrate layers are assembled using a low temperature polymer bonding process to form high performance antenna devices. After patch assembly, in order to obtain an antenna device for RF characterization, an SMA connector was attached to the microstrip and ground plane on the microwave substrate.

The measurement of reflection coefficient, radiation pattern and radiation gain have been realized for these micromachined antenna devices with appropriate RF measurement techniques. The antenna bandwidth and gain factor of the micromachined antenna devices obtained from RF measurements. Measured bandwidths of 2.5 GHz (19%), 3.7 GHz (39%), 3.6 GHz (44%), 6.21 GHz (48.8%) were obtained for microstrip fed, microstrip fed stacked, CPW fed, microstrip fed quad array micromachined aperture coupled patch antenna devices respectively. Good agreement between the experimental results and theoretical results was obtained. From the measurement results, it is concluded that the lossy effect of the SU8 polymer, the polyimide and LCP supporting substrates is minimal and hence these materials could be employed extensively for producing stacked antenna device with increased accuracy of aligning the stacked layers. The peak measured antenna gain is 8.3 dBi at 12.1 GHz for the microstrip fed micromachined aperture coupled patch antenna device. A peak-gain of 7.8 dBi was obtained at the frequency of 9.5 GHz for the microstrip fed stacked antenna device and 7.6 dBi at ~10 GHz for the CPW fed device. A maximum peak gain of 10 dBi at 12 GHz has been measured for the micromachined aperture coupled quad array antenna device. The measured bandwidth of the microstrip fed micromachined aperture coupled quad array antenna device was thus, almost a factor of 5 larger than the figure of 10.5% obtained for the probe fed micromachined antenna device [84]. Comparison of the measured gain and bandwidth of the stacked micromachined antenna device and that of a conventional aperture coupled antenna devices for a comparable profile dimensions shows a significant enhancement in antenna gain performance particularly in the multi-GHz, and millimetre wave frequency region and an improvement in % bandwidth [32]. A similar kind of improvement is observed with other micromachined approaches [84].

The stacked antenna device configurations presented in this thesis have resulted in doubling the antenna bandwidth while the gain is reduced by 0.5 dBi when compared to the simple aperture coupled antenna configuration. The stacked quad array configuration had increased the bandwidth by 2.5 times while the gain is increased by about 3 dBi (radiation efficiency unchanged). This shows that the antenna device performance is enhanced on the expense of the complexity in aligning and bonding the fabricated layers in order to obtain the stacked antenna configurations. For the mass manufacture, this complexity can be reduced by a camera based robotic machines. The developed fabrication process provides

an alternative low cost packaging process as compared to the conventional LTCC and PCB technology. The suspended antennas are lightweight and can be easily fabricated with micromachining of the SU8 photopolymer. The method of fabrication has potential applications in the emerging field of UWB networks, WLAN networks at 60 GHz, automotive collision radar and terahertz antenna devices. The stacked single antenna devices can also be used to fabricate antenna arrays for high gain applications. The fabrication process developed can be used for constructing other passive devices such as high performance filters at millimetre wave and terahertz frequency regimes. New ultra thick photoresists that does not necessarily need post baking process could pave the way for cost effective fabrication of these antenna devices [148].

6.2 FUTURE WORK

In a typical communication device, an antenna occupies a significant portion of the area of the device. It is envisaged that the micromachined antenna devices will potentially find applications in miniature sensor networks, large array planar antenna devices, on chip communication antenna systems in the X band, millimetre wave and terahertz frequency regimes. Certain applications like the miniature sensor networks operating at millimetre wave frequencies and beyond will potentially need a compatible encapsulation and assembly process for the RFICs and the antenna device. Potentially, the micromachined antenna devices can be realised in to the emerging 3-D packaging approaches often referred to as SIP (System-in-Package) and SOP (System-on-package) to provide major opportunities in both miniaturization and integration for advanced and portable wireless packages. The micromachining concept for antenna fabrication facilitates the integration of RFIC chips in the air cavity underneath the patch elements.

In the work described in this thesis, single element and a quad-element micromachined suspended micromachined antenna devices were produced. In the future, the suspended micromachined antenna devices and the associated arrays of these devices can be integrated with RFIC chips to investigate the improvement of the performance of the communication systems using the micromachined antenna devices. Thus, it will be interesting to study the integration capability of this assembly approach in the future. The reliability and robustness of the suspended micromachined antenna devices should be further investigated. The reliability of the micromachined antenna devices containing suspended structures is a

concern in general. The vibration, shock and thermal cycling test etc can be carried out in the future to study the reliability of the suspended micromachined antenna devices. Shear test can be carried out to investigate the bond strength of the supporting polymer rims. The thermal stress due to the CTE (coefficient of thermal expansion) mismatch between the SU8 polymer and the substrate materials should be accommodated in the fabrication process so as to eliminate the potential delamination of the SU8 structures from the substrates.

APPENDIX

A1 A MICROMACHINED FSS BASED ANTENNA DEVICE

A1.1 Introduction

There has been a growing interest in utilizing the unlicensed 60 GHz band due to the benefits of wide bandwidth, the maximized frequency reuse, and the short wavelength that allows very compact passive devices [149]. Multilayer low-temperature cofired ceramic (LTCC) based System-on-Package (SoP) technology has already been implemented on terminals for mobile communications or wireless local area networks (WLANs). Although the LTCC based antenna systems have been realized at the 60 GHz band, they suffer from low gain and low efficiency coupled with complex feeding networks. They may also suffer from low resolution metal printing techniques such as screen and stencil printing resulting in poor device performance.

A high gain planar antenna using a suspended frequency selective surface (FSS) and operating at a frequency of 60 GHz has been investigated. Using micromachining technology, the dimensions of the polymer ring spacer can be controlled precisely to provide the required air gap between the FSS layer and the ground plane to obtain high performance. Although the principle of operation of a micromachined FSS based antenna device is different to the micromachined patch antenna devices presented earlier in the thesis the fabrication process for this antenna device is similar to that presented in Chapter 4. Thus, it is anticipated that the fabrication techniques for the micromachined aperture coupled antenna devices can be used for the micromachined FSS based antenna devices. The principle of operation, the modelling of the antenna device and initial measurement results are presented in this appendix.

A1.2 Review of FSS based partially reflective arrays and antennas

G. V. Trentini *et al* introduced the partial reflecting sheet arrays for antenna applications for the first time in 1956 [150]. Multiple reflections of electromagnetic waves between two planes were studied, and the increase in directivity that results from a partially reflecting sheet in front of an antenna was investigated at a wavelength of 3.2 cm. The device relied on the ‘electromagnetic transparency’ of an inductive frequency-selective surface (FSS) in

its pass band and as a result weak leaky-wave action was observed due to multiple reflections between the FSS and the ground plane. The outer diameter and over-all length of the antenna devices were 1.88λ and 0.65λ respectively. The device showed half-power beam widths of 34° and 41° in the E and H planes respectively, and a gain of approximately 14 dB. It was shown that larger systems could produce considerably greater directivity but that their efficiency would be poor.

J. R. James *et al* [151] reported further beam forming properties that result from having multiple FSS's in conjunction with a low-gain primary aperture. High gain antenna devices by the use of frequency selective surfaces as partially reflecting sheets have been continuously developed in the recent years. Feresidis *et al* have developed a high gain planar antenna using optimized partially reflective surfaces as shown in Figure A.1 [152].

The high gain planar antenna was developed using an optimized partially reflecting surface (PRS) placed in front of a waveguide aperture at around 14.5 GHz with a maximum gain of 21.9 dBi and a 1.2% bandwidth for an array size of 17×17 . The device was constructed using a foam board based spacer. A ray based analysis was employed to describe the operating principle of the antenna and to qualitatively predict the antenna performance. Full-wave simulations were carried out using a commercially available software tool (Microstripes). The effect of the finite PRS size on the antenna performance (directivity and side lobe level) was also studied.

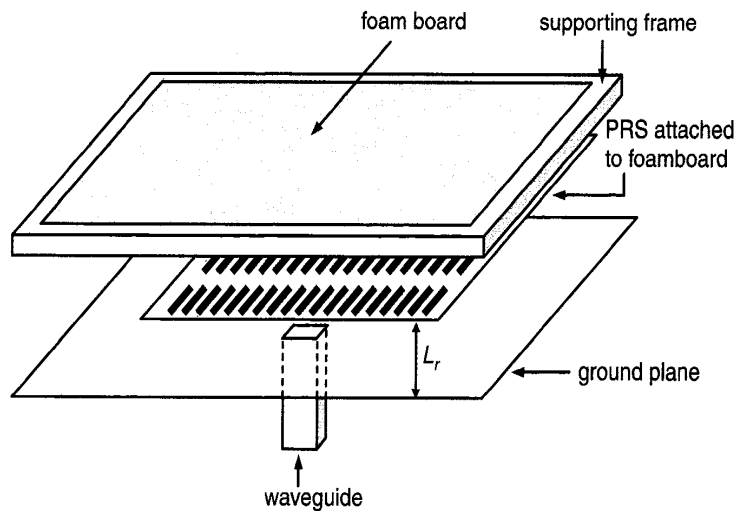


Figure A.1 Schematic showing the FSS based antenna and the principle of operation [152]

Low profile antenna devices have been developed by the same group by employing artificial magnetic conductors [153-155] and an array antenna device with increased element spacing [156]. Further variations of these antenna devices have been developed [157-160] with an optimized antenna device obtained using a multi-feed based design. A high gain antenna device for multi-spot coverage has been developed by Chantalat *et al* [157]. On the other hand, antenna devices have been developed for base station antennas applications such as the omni directional [161, 162] and sectoral antenna devices [163].

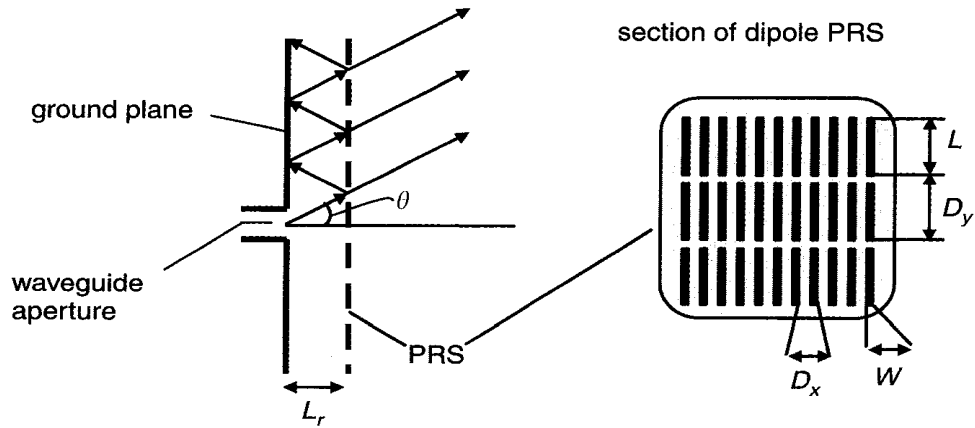


Figure A.2 FSS based antenna device with multiple reflections between PRS screen and the ground plane [152]

The leaky-wave behaviour is illustrated in Figure A.2, showing a ray emitted at angle θ from the primary aperture, progressively reflecting between the conducting ground plane and parallel FSS. The complex reflection coefficient $R(\theta) \exp [j \phi(\theta)]$ at the FSS is a function of both θ and the FSS geometry. L_r is the resonant distance between the PRS and the ground plane. If $f(\theta)$ is the angular distribution of rays from a primary antenna, then an approximate formula for the radiation pattern $P(\theta)$, based on the summation of rays, is [150-152]

$$P(\theta) = \frac{|1 - R^2(\theta)| f^2(\theta)}{1 + R^2(\theta) - 2R(\theta) \cos \left[\phi(\theta) - x - \frac{4\pi L_r}{\lambda_0} \cos \theta \right]} \quad (6.1)$$

where $\phi(\theta)$ is the reflection coefficient phase of the FSS interface and $P(\theta)$ is maximum when the following condition is satisfied.

$$\phi(0) - \pi - \frac{4\pi L_r}{\lambda_0} = 2N\pi \quad \text{or} \quad (6.2)$$

$$L_r = \left(\frac{\phi(0)}{\pi} - 1\right) \frac{\lambda_0}{4} + N \frac{\lambda_0}{2}, \quad \text{where } N = 0, 1, 2, \dots$$

The gain of the antenna device is given by

$$G = \frac{P}{F} = \frac{1+R}{1-R} \quad (6.3)$$

While the bandwidth is given by

$$BW = \frac{\Delta f_{1/2}}{f_0} = \frac{\lambda}{2\pi L_r} \frac{1-R}{\sqrt{R}} \quad (6.4)$$

Thus by knowing the complex reflection coefficient, one can estimate the gain and bandwidth for these kinds of antenna devices. The complex reflection coefficient can be measured experimentally for any periodic FSS geometry with two standard gain horn antennas.

A1.3 Design and modelling

A1.3.1 Software tool for electromagnetic design and simulation

Figure A.3 shows the schematic of the antenna device based on metamaterial (FSS) and micromachining techniques. FSS based Fabry-Perot cavity antenna device for high directivity form as a basis for this antenna device. In order to reduce loss and to produce a low profile device, the FSS structure is placed on a thin polymer film. The micromachined ring spacer is used to position and suspend the thin polymer film above the ground plane. A waveguide-fed aperture in the ground plane is used to provide excitation of the cavity. The design of the FSS was carried out using method of moment code by analyzing the reflectivity of the FSS structure. The FSS is then incorporated into the antenna structure for device design and modelling using MicrostripesTM [164] a time domain based electromagnetic (EM) simulation package. CST MICROSTRIPESTM (CST MS) is a powerful 3D simulation software which uniquely employs the Transmission Line Matrix (TLM) method to solve Maxwell's equations in the time domain, a highly efficient numerical method. The TLM matrix is coupled with a GUI (Graphical user interface) and an optimal meshing algorithm. The design process follows five steps:

1. Define the geometry using a solid modeller or import the geometric model from another CAD package.

2. Assign the material properties to the geometry
3. Exciting the port or a plane wave excitation
4. Define the results such as S_{11} , impedance, radiation patterns etc
5. Solving the Maxwell equations with the efficient time domain solver based on the TLM (Transmission Line Matrix) for accurate broadband results.

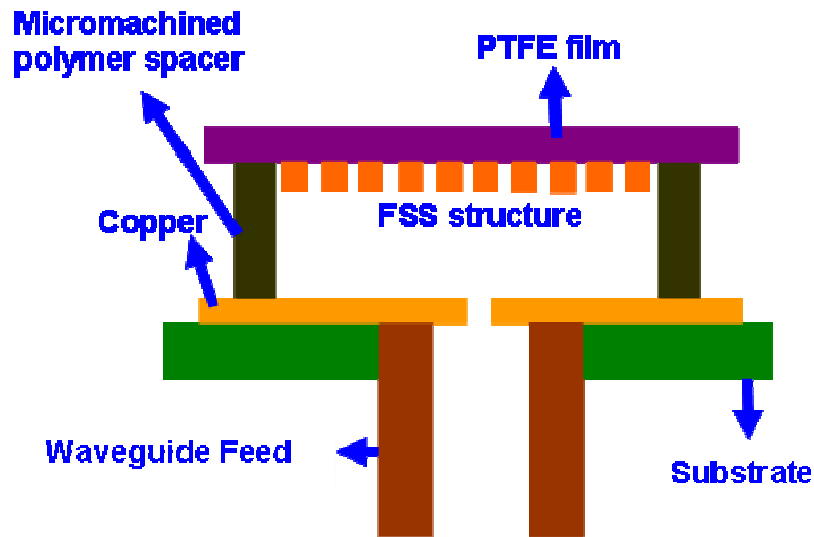


Figure A.3 Schematic of the cross-sectional view of the antenna design for 60 GHz operation.

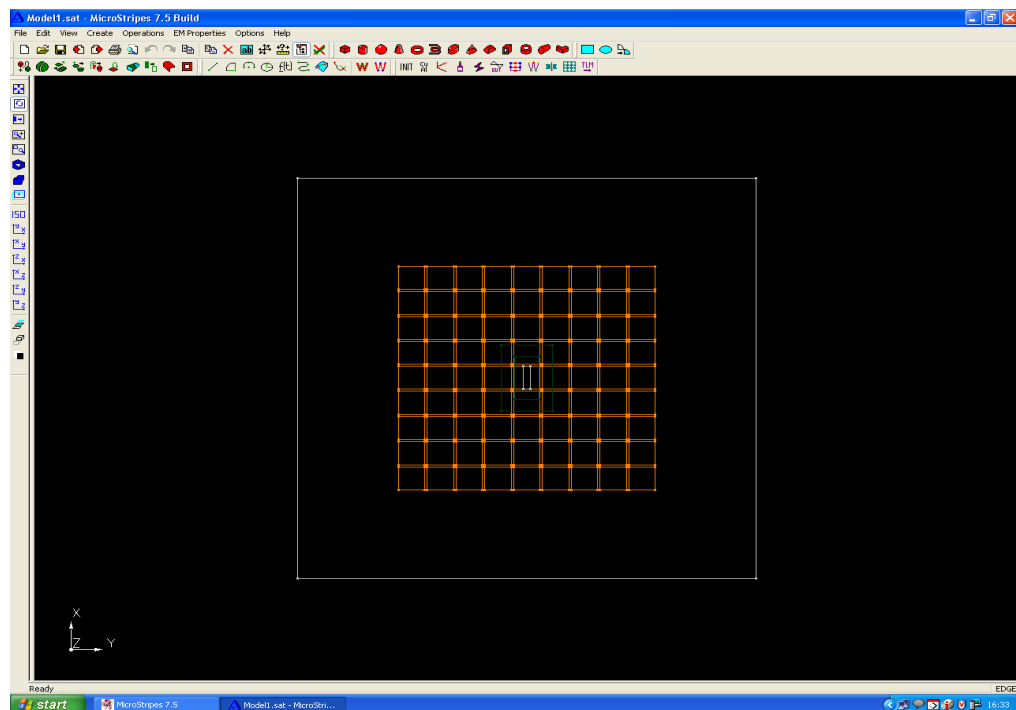


Figure A.4 Layout of the micromachined FSS based antenna device in solid modeller within the MicrostripesTM package[164]

CST MICROSTRIPES™ has a model builder that can be used to create solid geometry while Boolean operations, library parts, sweeps and transformations are also available to aid the geometry creation. Within CST MICROSTRIPES™ models can be excited in a variety of ways such as by ports and plane waves. Ports, which can be waveguide, coaxial, microstrip, stripline, co-planar, slotline or wire source, can be specified anywhere within the workspace and do not have to be coincident with the boundaries. The excitation is an impulse in the time domain and the resulting output (impulse response) can then be convolved with user definable waveforms producing results as if the model had been excited with said waveform. The size of the largest and smallest cells in the mesh has a significant effect on the accuracy and speed of the simulation, and therefore requires careful consideration. The 3D-TLM simulator considers the electromagnetic field to be uniform within each cell. The Automesher chooses the default cell-size to be 1/10 of the free-space wavelength at the requested maximum model frequency, or 5% of the model size, whichever is the smaller. The Automesher also always takes into account material properties and reduces the cell-size within dielectric bodies. In general, it will take at least two time steps for the electromagnetic wave to cross any cell in any direction - so that the time-step depends critically on the smallest dimension of any cell. Thus, the largest dimension of any cell limits the frequency range and the smallest dimension of any cell limits the time-step. Finally, a Fourier transform module is used to transform time domain output from the solver into the frequency domain. The actual integral is as follows [164]

$$G(f) = \int_{t_1}^{t_2} g(t) e^{-i(2\pi ft)} dt \quad (6.5)$$

Where $g(t)$ is the time domain response and $G(f)$ is the frequency domain response. Now

$$\Delta f = \frac{1}{nT} \quad (6.6)$$

The spacing between frequency samples, Δf is a constant chosen to ensure that the frequency domain data appears smooth when plotted as a graph. nT is the number of time steps.

A1.3.2 Results and analysis

The micromachined FSS based antenna design shown in Figure A.4 was designed for 60 GHz operation. The polymer film containing the FSS structure is supported by a

micromachined polymer ring spacer above the ground plane. Table A.1 gives the dimensions and electrical properties for the micromachined FSS based antenna device.

Table A.1 Dimensions and electrical parameters for the micromachined FSS based antenna device

Parameter	
Array size of FSS	17×17
Patch dimension	2.2 mm
Height of cavity	2.6 mm
Dimension for coupling aperture	2.1mm × 0.4mm
Outer dimensions of cavity	44.5 × 44.5 mm
Taconic substrate thickness	0.25 mm
SU8 polymer rim thickness	2.6 mm
PTFE	0.125 mm
Copper thickness	0.009 mm
Dielectric constant of SU8	3.2
Dielectric constant of PTFE film	3.2
Dielectric constant of Taconic TM TLY-5 substrate	2.2
Loss tangent of SU8	0.043
Loss tangent of PTFE film	0.005
Loss tangent of Taconic TM TLY-5 substrate	0.0009

The design procedure of the antenna device is similar to that described previously [150]. The FSS structure contains an array of 19x19 square elements of copper printed on a PTFE film of thickness 0.25 mm including the copper cladding of 18 µm and dielectric constant 2.2 respectively. The dimension of each element is 2.2mm × 2.2mm and the separation between the adjacent elements is 150 µm. The design and optimisation of the FSS structure was carried out using the method of moment code. The analysis is based on Floquet's theorem and assumes an array of infinite size [152]. The optimum design parameters and the resultant electromagnetic characteristics of the antenna device were obtained using the Microstripes EM simulation package by optimising the design. The initial SU8 polymer thickness and thereby the height of the cavity is given approximately by Equation (6.2).

The dimensions of the coupling aperture and the thickness of the SU8 polymer rim are optimised for better bandwidth and antenna gain.

The height of the polymer ring was determined to be 2.6 mm for the device to operate at 60 GHz. The internal dimensions of the ring are 48mm x 48mm and the wall thickness of the ring is 2.5 mm. The size of the coupling aperture is 2.1mm x 0.4mm. Figure A.5 shows the reflection characteristic of the antenna. The return loss is better than -10 dB at the design frequency, and with a -10dB bandwidth of 2%.

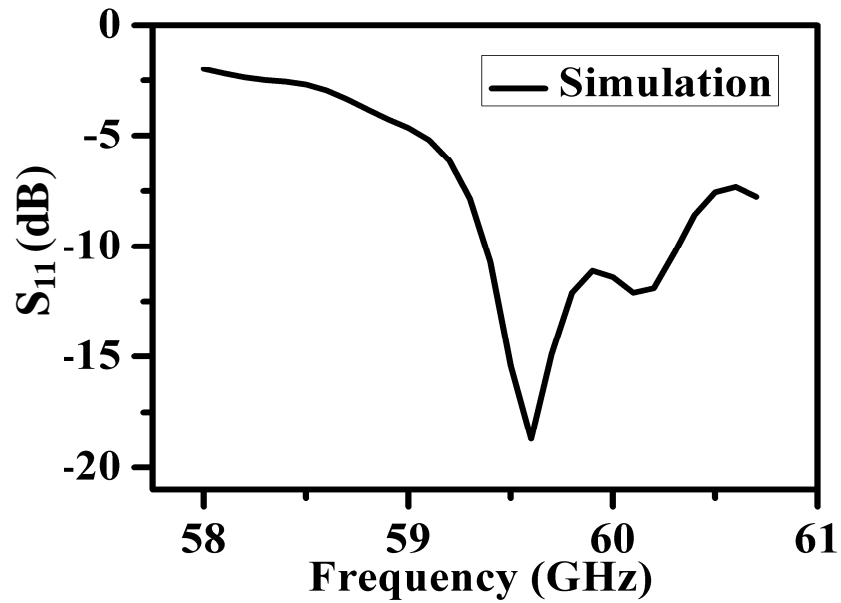


Figure A.5 Simulation results of reflection coefficient (S_{11}) for the micromachined FSS based antenna device

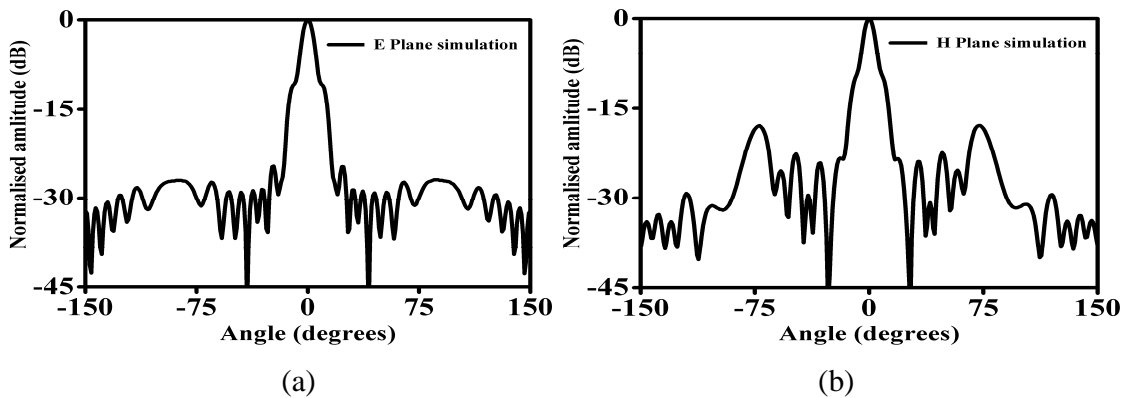


Figure A.6 Simulated radiation patterns of the micromachined FSS based antenna device at 60 GHz

Figure A.6 shows the E plane and H plane radiation characteristics. The side lobes are less than -28 dB in the E plane and -15 dB in the H plane respectively. The higher side lobes in the H plane are attributed to the diffracted fields due to the finite size of the PRS, which was limited to about $8.9 \times 8.9\lambda$ in order to reduce the computational requirements. The radiation bandwidth of the antenna is about 1.5%. The radiation bandwidth is defined as the bandwidth over which the gain of the antenna varies at about 3 dB from the peak. The design was optimised for both optimum bandwidth and gain. However, as is well known for this type of antenna there is a clear trade-off between these two parameters. Figures A.7 and A.8 show the 3D radiation profiles of the micromachined FSS based antenna device at two different frequencies. Figure A.9 shows a 3D radiation profile of the antenna device when a solid layer of SU8 is used as the spacer. Thus, it can be seen that the antenna gain varies from 23.561 dBi at the centre frequency of 60.25 GHz to 16.5 dBi at 58.54 GHz (band limit) while the material loss increases from 0.13 dB to 0.75 dB.

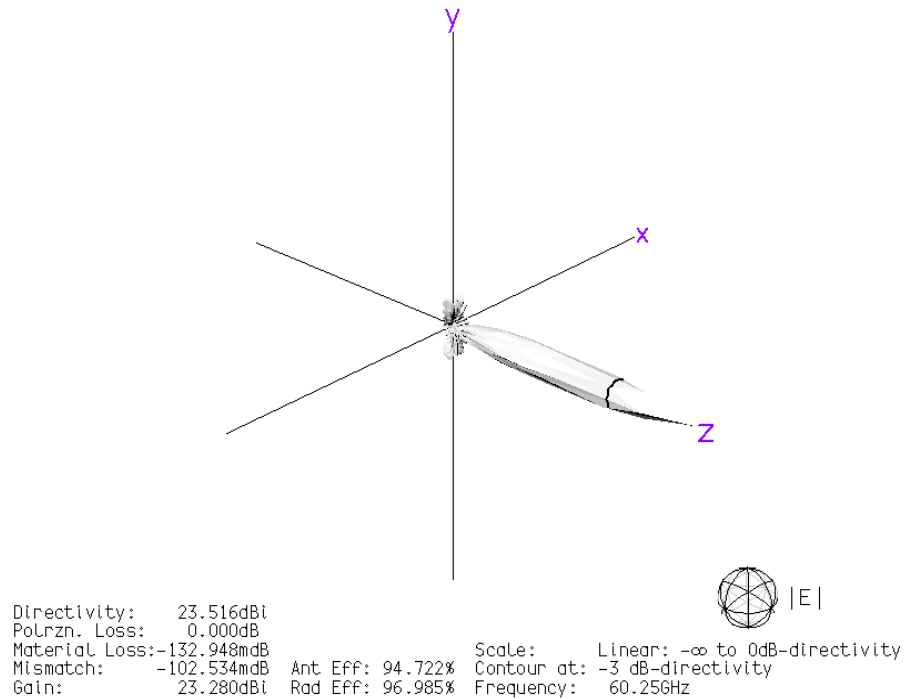


Figure A.7 Simulation of the 3D radiation profile for the micromachined FSS based antenna device at 60.25 GHz

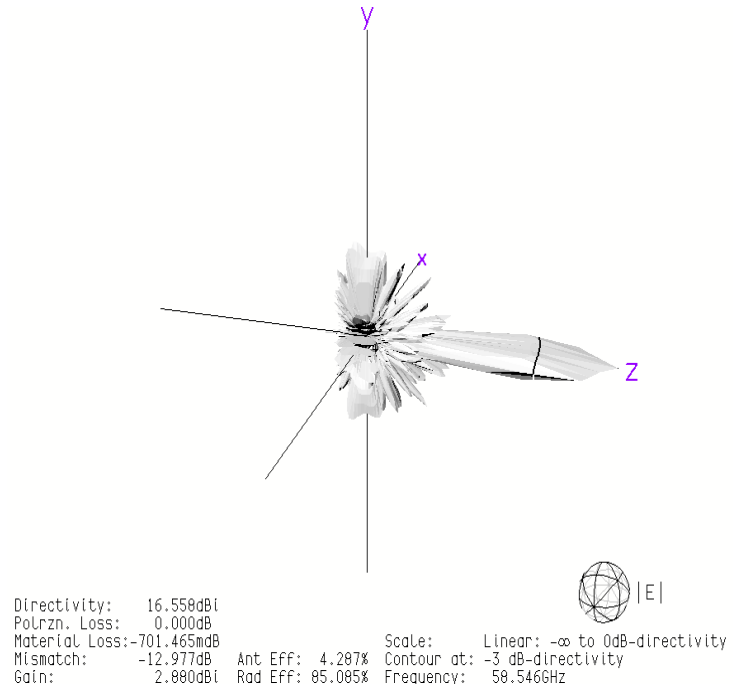


Figure A.8 3D radiation profile for the micromachined FSS based antenna device at 58.54 GHz

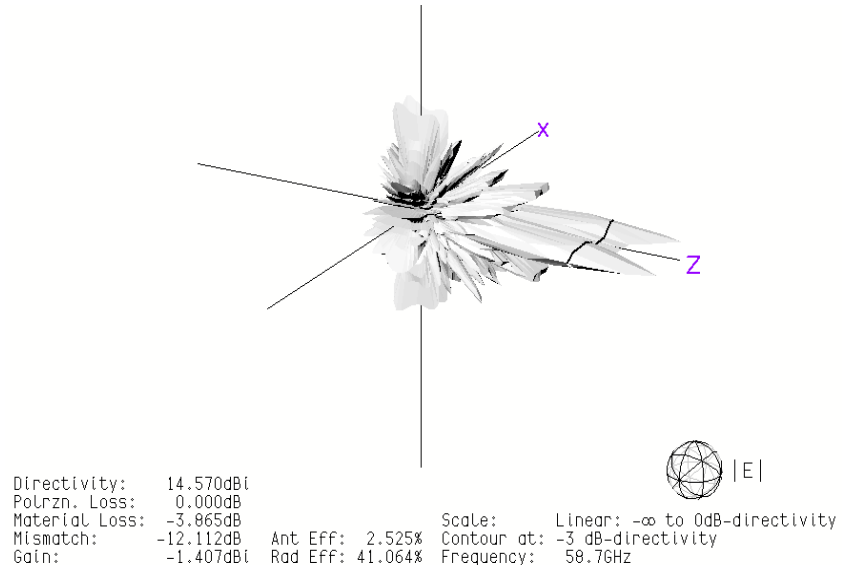


Figure A.9 3D radiation profile for the micromachined FSS based antenna device with SU8 filled inside the cavity

The full wave simulation gives a material loss of around 3.8 dB for SU8 filled cavity at the centre frequency which shows that one should refrain from using SU8 material as a substrate for these kinds of antenna devices.

A1.4 Fabrication and assembly

The antenna device was fabricated using the MEMS based microfabrication and microassembly techniques described in chapter 4. Figure A.10 outlines the fabrication flow for the micromachined FSS based antenna device. The FSS structure was fabricated on a thin copper foil laminated on a thin film, low loss polymer substrate. After deposition of a photoresist layer by spin coating, the photoresist is patterned using a photomask to define the FSS structure.

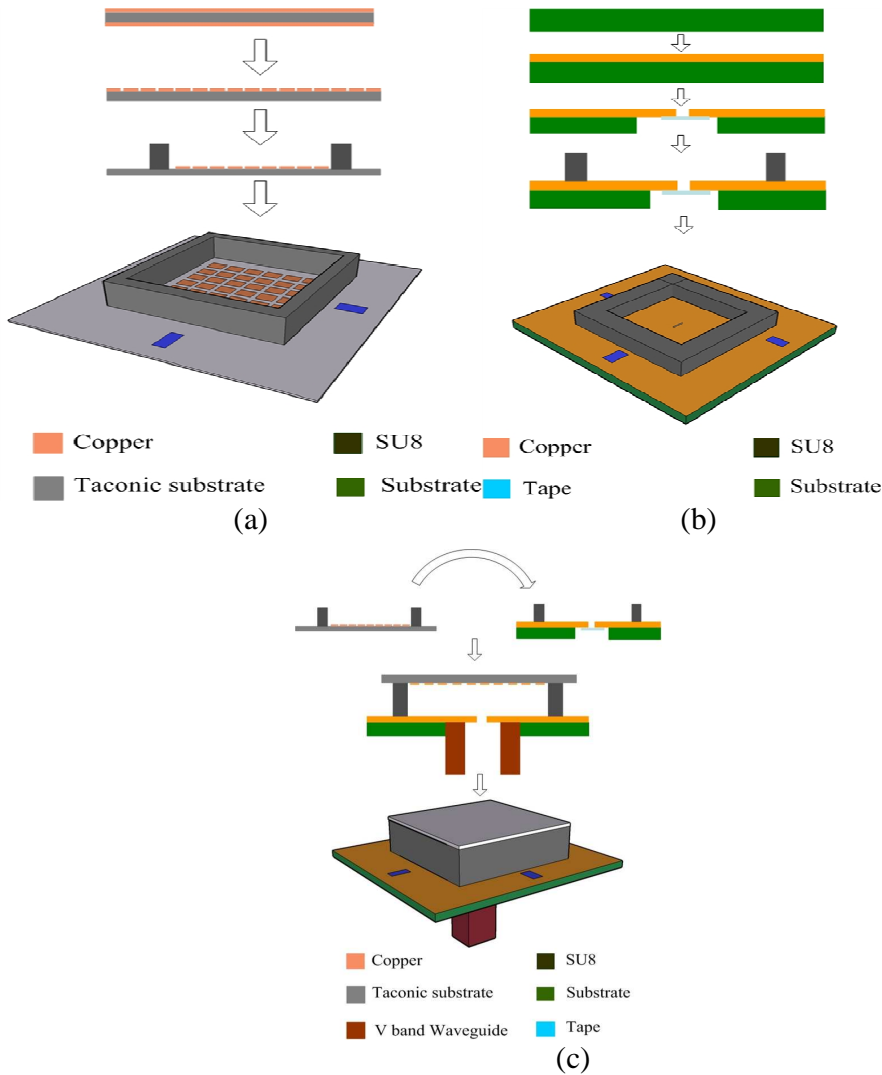


Figure A.10 Schematic of the fabrication flow for the micromachined FSS based antenna device on (a) microwave substrate (b) Taconic substrate (c) antenna assembly.

The exposed copper layer is then removed by wet etching followed by photoresist removal to obtain the FSS structure containing arrays of square copper elements. The coupling aperture on the ground plane was fabricated using a similar method. The supporting

polymer rim was produced by bonding two identical SU8 based polymer ring structures that were produced on the FSS and ground plane substrates respectively. The SU8 rim structures are fabricated by surface micromachining of thick film SU8 epoxy layer as illustrated in Chapter 4. The height and wall thickness of each of the rims were 1.3 mm and 2.5 mm respectively. To facilitate the coupling of the waveguide to the antenna device for EM characterization, alignment marks were produced on the ground plane substrate by precision mechanical machining. Figure A.11 shows the photographs of the fabricated antenna device.

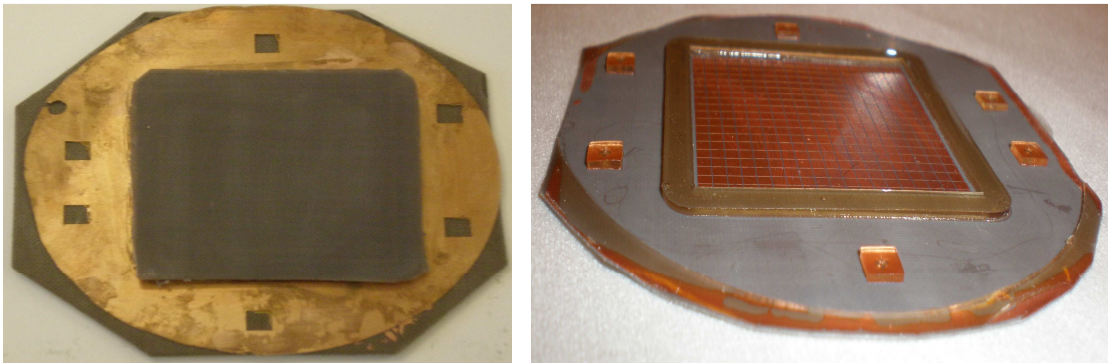


Figure A.11 (a) Photograph of the micromachined FSS based antenna device after assembly (b) Photograph showing the FSS layer on the Taconic substrate along with the SU8 polymer rim

A1.5 Measurement

Initial measurements for antenna device were performed for radiation characteristics but not for the reflection characteristics as a vector network analyser is required. The far field test setup for the work is shown in Figure A.12. A 20 dBi FlannTM standard gain horn was used as a reference antenna. An Agilent 83557A mm-wave source module was used to drive the standard gain horn antenna. An 8350/83550A sweep oscillator was used as a frequency source to drive the millimetre wave module. A U85026A WR-19 waveguide detector from 40 GHz to 60 GHz was connected to an Agilent 8757 scalar network analyser to obtain the scalar transmission parameters. A waveguide flange end from the detector was connected to the V band waveguide that feeds the micromachined antenna device (AUT). A gain of about 12 dBi was obtained using the gain comparison technique as described in Chapter 5.

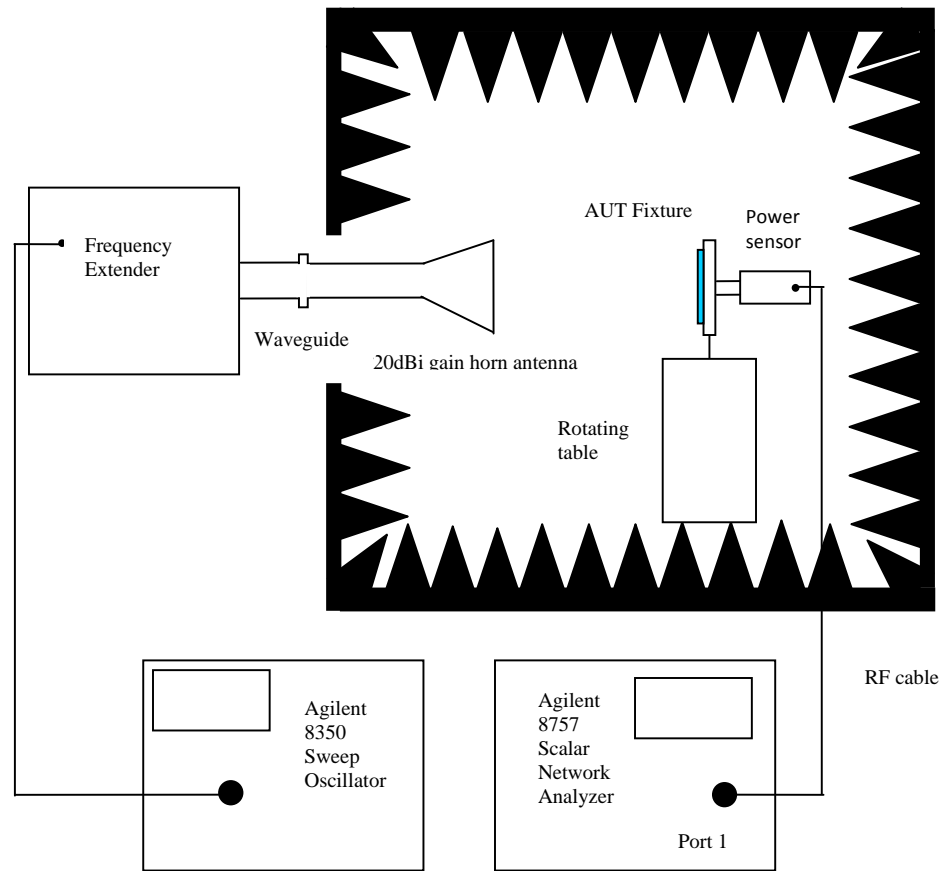


Figure A.12 Schematic showing the far field set up for the micromachined FSS based antenna device

The lower value of the measured gain can be attributed to the misalignment of the waveguide feed to the aperture. The waveguide feed is a FlannTM V band waveguide that is machined and glued to the copper plate on the Taconic substrate. Any misalignment during the fixture and the smoothness of the machined waveguide are the sources of error during measurements. The lower measured gain can also be due to the measurement technique used where a scalar network analyser is employed and the reflection parameters were not measured to take into account any serious mismatches at the measured frequency.

A1.6 Summary

A high-gain micromachined FSS based antenna device has been successfully designed and modelled for V band operation. The simulation results show low reflection coefficient and good radiation characteristics with a gain of 25 dBi at around 60 GHz and an antenna

efficiency of more than 95% have been achieved. The antenna device was constructed. Preliminary measurements of antenna radiation pattern, S_{11} parameter and gain were carried out. The initial results show a gain of about 12 dBi for the device, lower than the expected value of 25 dBi. Further investigations are necessary in order to improve the measurement setups to determine the performance of the device, in particular better control of coupling between the feeding waveguide and the aperture of the ground plane.

A2 FABRICATION

A2.1 Thin film deposition

Conductor patterning on substrates can be achieved by either thin film deposition followed by electroplating or chemical based etching of a metal film. The metal features tend to possess rough side walls and non-uniform feature sizes for the patterns obtained using the chemical etching process.

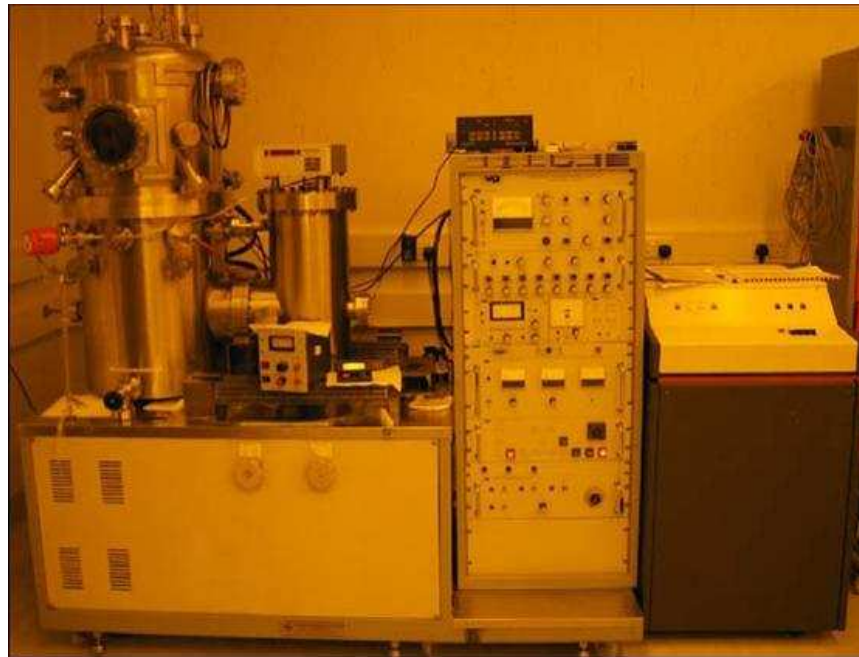


Figure A.13 Photograph of the electron beam evaporator

The thin film deposition was used in the thesis work for producing seed layers on non-metallic polymer thin film substrates for patch fabrication. The thin-film metal layers were deposited by vacuum evaporation using an electron beam based deposition facility. Figure A.13 shows a photograph of the electron beam evaporator. Titanium and Copper thin films were used as the adhesive and seed layer respectively.

A2.2 Spin coating

Spin coating, spray coating and blade coating are the three main methods for deposition of photoresist layers on wafers in microfabrication [94]. The spin coating method was used for deposition of thick film photoresist layers for fabrication of antenna devices. The spin coating can produce uniform photoresist films owing to the control of the polymer spaces

and patches for construction of antenna devices. The method consists of an initial spread cycle and a high speed spin cycle. The photoresist was coated onto the substrate wafers to produce a uniform photoresist film of the desired thickness. A commercial spin coater (Brewer Science, Model 100) was used for this purpose. Figure A.14 shows a photograph of the spin coater.



Figure A.14 Photograph of the spin coating machine

The photoresist deposition process comprised of three steps: dispensing, spreading and smoothing respectively. In the dispensing step, the carrier wafer was rotated at a low speed for dispensing the photoresist onto the carrier wafer. In the spreading cycle, the carrier wafer was accelerated to a higher spin speed to spread the photoresist to cover the whole wafer. In the final smoothing cycle, the carrier wafer was spun at accelerated high speeds to avoid the formation of photoresist bead at the edge of the wafer and to form a smooth photoresist film. The spin speeds, acceleration and spin time were programmed for each of the cycles described above. A negative photoresist (SU8) was used for fabrication of the polymer rims. The photoresist used for patch fabrication was AZ 9260 (AZ electronic materials, Clariant Corporation), which is a positive tone photoresist.

A2.3 Soft baking

Soft baking is the process of removing solvents in the photoresist film prior to UV exposure [94]. After spin coating and the subsequent relaxation period, the wafer was soft baked on

a hotplate levelled with less than a 0.1° of inclination. The wafer was then removed from the hotplate and left horizontally on a levelled surface to prevent the AZ / SU8 photoresist layers from flowing. Figure A.15 shows a photograph of the plate setup for pre-baking of the photoresist layers.



Figure A.15 Photograph of the hot plate setup for pre-baking of the photoresist films

A2.4 UV exposure

The mask aligner, Tamarack used for photolithography is shown in Figure A.16. It consists of a collimated broadband UV exposure system with manual controls for alignment. The UV light source employed a 2000 W Hg arc lamp, which has a typical UV spectrum of g-line (436 nm), h-line (405 nm) and i-line (365 nm). The AZ9260 photoresist is sensitive to the i-line and h-line (320 ~ 410 nm) while the SU8 photoresist is sensitive to the i-line of the spectrum. The Tamarack mask aligner provided a touch screen display interface. Most of the operations for mask alignment and UV exposure were carried out through the touch screen. The substrate wafer coated with the photoresist film could be mounted onto the vacuum chuck of the mask aligner and held in place by vacuum.

The UV light from the Hg arc lamp was collimated to expose an area of about 10 cm in diameter (4" wafers). The mask alignment could be performed in both contact and proximity modes. For the work described in this thesis, proximity exposure was used as the features are relatively large. Diffraction of UV-light occurs at the air gap between the photomask and the photoresist layer. This can be minimized by filling an index-matching

material such as glycerol on the photomask [130]. A Cargille refractive index matching liquid has been used to improve the features of the SU8 photoresist [130, 165, 166]. Feature sizes of $6\text{ }\mu\text{m}$ and $1150\text{ }\mu\text{m}$ in height (aspect ratio > 190) with high quality sidewalls were demonstrated.

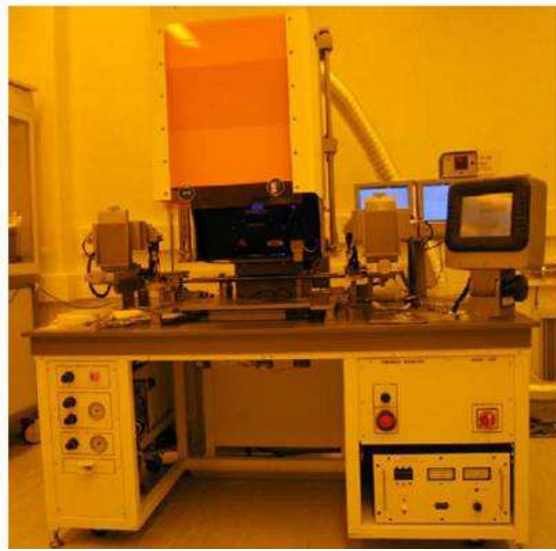


Figure A.16 Photograph of the Tamarac UV exposure system

A2.5 Development

Several methods for development of an UV exposed photoresist layer exist such as solvent based stirring or spinning, jet and spray based. The solvent based stirring approach is the most widely used development technique wherein the stirring effect enhances diffusion that increases the development rate. If the UV exposed wafer or substrate is downward oriented, then this improves development of high aspect ratio (HAR) structures, because it allows the gravitational force to aid in the chemical solubility of photoresist [130, 167]. Megasonic and ultrasonic agitations frequencies use well above the vibration modes of the resist structures (typically 0.1 to 10 MHz) to agitate the developer. SU8 structures ranging from $20\text{ }\mu\text{m}$ to 1.5 mm in height and with aspect ratios up to 50 have been reported [130]. The disadvantage is that ultrasonic waves and megasonic waves can cause cracking and debonding of the photoresist layer. Spray development and jet development are the recent developed techniques for HAR structures using the SU8 photoresist [168]. In spray development, a spray nozzle is used to create small droplets of developer that are sprayed on the wafer uniformly. In jet development, the developer is directed in specific locations at elevated pressure to force fresh developer into deeper, less accessible parts of the pattern.

Spray development doesn't have selectivity while jet development can selectively remove soluble photoresist to create HAR structures.

For the fabrication of the micromachined aperture coupled antenna devices, a combination of the stirring and ultrasonic method was used. The SU8 coated wafers after exposures were developed in the PGMA solution in an ultrasonic bath for less than a minute and then further developed with the stirrer system. The stirrer system consisted of a hotplate with a magnetic bead stirrer. The wafer to be developed was placed in PGMA solution on the stirrer system at 25°C. The solution was stirred with the help of a magnetic bead at ~100 rpm. The polymer rims fabricated for the microstrip fed stacked and simple antenna devices are of around 1.2 mm thick and 1 mm wide thus having an aspect ratio of 1.2 while for the CPW fed antenna device is 1.1 mm and 2 mm in width possessing an aspect ratio of 1.6. It was found that this level of aspect ratio gives better mechanical stability for the SU8 polymer rim owing to the large feature sizes of the polymer rims (typically around 20 mm×20 mm). Although, SU8 is known for achieving high aspect ratios (>190) this is true only for smaller feature sizes (<0.1 mm×0.1 mm) and as the feature sizes get larger like that for the polymer rims than problems like adhesion to the substrate and uniform development (due to uniform exposure dose) will arise.

A2.6 Copper etch

A copper etch tank (Bungard Jet 34 d) [169] as shown in Figure A.17(a) was used to etch the copper layers after the UV-lithography process in order to produce conductor patterns on metallised substrates. The etching solution was prepared by dissolving 350 g of sublimate in 1 litre of cold water using a heat proof container and stir with a non-metallic tool as shown in 4.6(b). It should be noted that the preparation process should not be carried out in the etching tank due to the exothermic reaction. Ferric chloride tends to deposit a mud of copper chloride in the solution tank. This can be eliminated by adding small portions of chloric acid to the used (but never to the fresh) liquid.



(a)



(b)

Figure A.17 (a) Bungard Jet 34 d spray etching machine, (b) Ferric chloride solution with 50 g/l in the spray etch machine [169]

Table A.2 Physical and thermal properties of SU8 photoresist

Characteristics	Value
Maximum modulus of elasticity (E)	4.95 +/- 0.42 GPa
Bi-axial modulus of elasticity ($E/(1 - \nu)$)	5.18 +/- 0.89 GPa
Poisson ratio	0.22
Film stress	19 – 16 Mpa
Max stress	34 Mpa
Max sheer	0.009
Plastic domain limit	'no' plastic domain observed
Friction coefficient (μ)	0.19
Maximum bond strength	20.7 +/- 4.6 MPa
Glass temperature (T_g)	~50 °C
Thermal expansion coefficient	$52 \pm 5.1 \text{ ppm K}^{-1}$ at 95 °C
Polymer shrinkage	7.5%

Table A.3 Physical and thermal properties of DuPont Kapton polyimide film from Kapton® HN [120]

Characteristics	Value at 23°C
Tensile Strength	231 MPa
Elongation	72 %
Poisson ratio	0.34
Tensile Modulus	2.5 GPa
Density	1.42 gm/cc
Coefficient of Friction, static	0.63
Heat Sealability	not heat sealable
Thermal Coefficient of Linear	20 ppm/°C
Shrinkage	0.17% at 150°C
Flammability	94V0

Table A.4 Physical and thermal properties of liquid crystal polymer (LCP) [133].

Dimensional stability	MD (%)	-0.06
	CMD (%)	-0.03
Peel Strength	N/mm (lbs/in)	0.95(8.52)
Initiation Tear Strength, min	Kg(lbs)	1.4(3.1)
Tensile Strength	MPa(Kpsi)	200(29)
Tensile Modulus	MPa(Kpsi)	2255(327)
Density	gm/cm ² , Typical	1.4
Coefficient of Thermal Expansion CTE (30°C to 150°C)	X ppm/°C	17
	Y ppm/°C	17
	Z ppm/°C	150
Solder Float, method B(288°C)		PASS
Melting Temperature	°C	315
Relative Thermal Index - RTI	Mechanical °C	190
	Electrical °C	240
Thermal Conductivity	W/m/°K	0.2
Thermal Coefficient of z., -50°C to 150°C	ppm/°C	(+)24

A3 THE NETWORK ANALYSER

Network analysers are used to measure components, devices and circuits by looking at a known signal in terms of frequency and are described as stimulus-response systems [141]. The reflection and transmission characteristics of the antenna devices were measured using a HP 8510B network analyser for obtaining various antenna parameters. A network analyser can provide much higher accuracy than a spectrum analyser. Spectrum analysers on the other hand are used to measure signal characteristics on unknown signals.

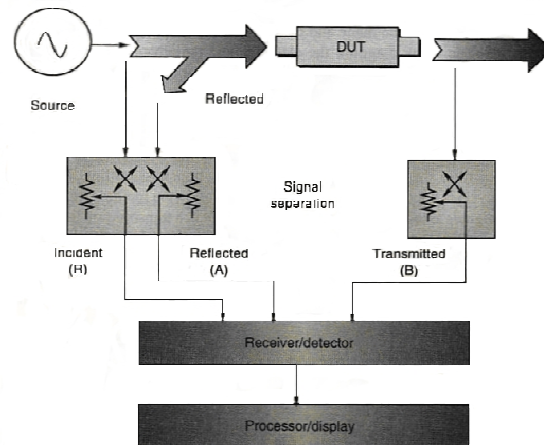


Figure A.18 General block diagram of a network analyzer [141]

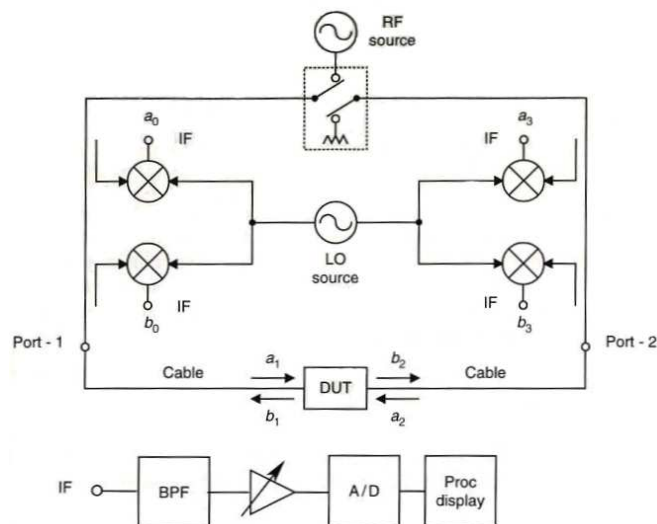


Figure A.19 Schematic of an S-parameter measurement system [141]

Spectrum analysers are usually a single channel receivers without a source and have a much wider range of IF bandwidths than a network analyser. Interpreting the results is much easier with a network analyser than a spectrum analyser [141]. Figure A.18 shows a block diagram of a network analyser illustrating the main signal processing parts while Figure A.19 shows the schematic of an S-parameter measurement system. The four main elements of a network analyser are:

- A source to provide a stimulus
- Signal separation devices
- A receiver for detecting the signals
- A processor and display for calculating and showing the results.

For a modern vector network analyser, a source is a synthesised sweeper; a signal separation device is a directional coupler while a tuned receiver is used for signal detection. Finally, a sampler is used to sample the time slices of detected signal and send to A/D and then to the display.

REFERENCES

- [1] D. M. Pozar, "Microstrip antennas," *Proceedings of the IEEE*, vol. 80, pp. 79-91, 1992.
- [2] S. Bruni, A. Neto, and F. Marliani, "The Ultrawideband Leaky Lens Antenna," *IEEE Trans. Antennas Propagat.*, vol. 55, pp. 2642-2653, 2007.
- [3] E. Benner and A. B. Sesay, "Effects of antenna height, antenna gain, and pattern downtilting for cellular mobile radio," *Vehicular Technology, IEEE Transactions on*, vol. 45, pp. 217-224, 1996.
- [4] I. Papapolymerou, R. Franklin Drayton, and L. P. B. Katehi, "Micromachined patch antennas," *IEEE Trans. Antennas Propagat.*, vol. 46, pp. 275-283, 1998.
- [5] R. B. Waterhouse, "Stacked patches using high and low dielectric constant material combinations," *IEEE Trans. Antennas Propag.*, vol. 47, pp. 1767-1771, 1999.
- [6] N. Z. N. Chen, "Wideband microstrip antennas with sandwich substrate," *IET, Microwaves, Antennas & Propagation*, vol. 2, pp. 538-546, 2008.
- [7] K. Carver and J. Mink, "Microstrip antenna technology," *IEEE Trans. Antennas Propag.*, vol. 29, pp. 2-24, 1981.
- [8] G. A. Deschamps, "Microstrip microwave antennas," in *3rd USAF Symposium on Antennas*, 1953.
- [9] H. Gutton and G. Baissinot, "Flat aerial for ultra high frequencies," French patent no. 703113, Patent, 1955.
- [10] E. V. Byron, "A new flush-mounted antenna element for phasedarray application," in *Phased-Array Antenna Symposium*, 1970, pp. 87-192.
- [11] R. E. Munson, "Single slot cavity antennas assembly," U.S. Patent No. 3713 162 Patent, Jan. 23, 1973.
- [12] J. Q. Howell, "Microstrip antennas," in *IEEE Digest, Antennas and Propagation Society International Symposium*, SOC., Williamsburg, VA, December 1972, pp. 177-180.
- [13] G. W. Garvin, R. E. Munson, L. T. Ostwald, and K. G. Schroeder, "Low profile electrically small missile base mounted microstrip antennas," in *IEEE Digest, Antennas and Propagation Society International Symposium*, Urbana, IL, June 1975, pp. 244-247.
- [14] J. Q. Howell, "Microstrip antennas," *IEEE Trans. Antennas Propagat.*, vol. AP-23, pp. 90-93, January 1975.
- [15] H. D. Weinschel, "Progress report on development of microstrip cylindrical arrays for sounding rockets," Physics and Science lab, New Mexico State University, Las Cruces, 1973.
- [16] G. G. Sanford, "Conformal microstrip phased array for aircraft tests with ATS-6," in *Proc. Nat. Electronics Conf.*, Oct. 1974, pp. 252-257.
- [17] J. R. James and P. S. Hall, *Handbook of microstrip antennas* London: IEE - Peter Peregrinus, Ltd, 1989.
- [18] I. J. Bahl and P. Bhartia, *Microstrip Antennas*. Dedham MA, : Artech House, 1980.
- [19] D. M. Pozar, "Microstrip antenna aperture-coupled to a microstripline," *Electronics Letters*, vol. 21, pp. 49-50, 1985.
- [20] D. Pozar, "A Review of Aperture Coupled Microstrip Antennas: History, Operation, Development, and Applications," in [Online]. Available: <http://www.ecs.umass.edu/ece/pozar/aperture.pdf>, May 1996.

- [21] J.-F. Zürcher, "The SSFIP: A global concept for high performance broadband planar antennas," *Electron letters*, vol. 24, pp. 1433-1435, 1988.
- [22] S. D. Targonski and R. B. Waterhouse, "An aperture coupled stacked patch antenna with 50% bandwidth," in *IEEE Digest, Antennas and Propagation Society International Symposium*, 1996, pp. 18-21, vol.1.
- [23] F. Croq and A. Papiernik, "Large bandwidth aperture-coupled microstrip antenna," *Electronics Letters*, vol. 26, pp. 1293-1294, 1990.
- [24] F. Croq and A. Papiernik, "Stacked slot-coupled printed antenna," *Microwave and Guided Wave Letters, IEEE*, vol. 1, pp. 288-290, 1991.
- [25] F. Croq and D. M. Pozar, "Millimeter-wave design of wide-band aperture-coupled stacked microstrip antennas," *Antennas and Propagation, IEEE Transactions on*, vol. 39, pp. 1770-1776, 1991.
- [26] J. Wang, R. Fralich, C. Wu, and J. Litva, "Multifunctional aperture coupled stacked antenna," in *IEEE Digest, Antennas and Propagation Society International Symposium, 1991*, 1991, pp. 727-730, vol.2.
- [27] D. M. Pozar and S. M. Duffy, "A dual-band circularly polarized aperture-coupled stacked microstrip antenna for global positioning satellite," *Antennas and Propagation, IEEE Transactions on*, vol. 45, pp. 1618-1625, 1997.
- [28] S. D. Targonski, R. B. Waterhouse, and D. M. Pozar, "Design of wide-band aperture-stacked patch microstrip antennas," *IEEE Trans. Antennas Propag.*, vol. 46, pp. 1245-1251, 1998.
- [29] S. T. Rowe and R. B. Waterhouse, "Broadband CPW fed stacked patch antenna," *Electronics Letters*, vol. 35, pp. 681-682, 1999.
- [30] R. B. Waterhouse, "Design and performance of large phased arrays of aperture stacked patches," *IEEE Trans. Antennas Propag.*, vol. 49, pp. 292-297, 2001.
- [31] E. Nishiyama, M. Aikawa, and S. Egashira, "Three-element stacked microstrip antenna with wide-band and high-gain performances," in *IEEE Digest, Antennas and Propagation Society International Symposium*, 2003, pp. 900-903, vol.2.
- [32] S. Mestdagh, R. Walter De, and G. A. E. Vandenbosch, "CPW-fed stacked microstrip antennas," *Antennas and Propagation, IEEE Transactions on*, vol. 52, pp. 74-83, 2004.
- [33] C. R. Trent and T. M. Weller, "Design and tolerance analysis of a 21 GHz CPW-fed, slot-coupled, microstrip antenna on etched silicon," in *IEEE Digest, Antennas and Propagation Society International Symposium*, 2002, pp. 402-405, vol.1.
- [34] W. S. T. Rowe and R. B. Waterhouse, "Reduction of backward radiation for CPW fed aperture stacked patch antennas on small ground planes," *IEEE Trans. Antennas Propag.*, vol. 51, pp. 1411-1413, 2003.
- [35] R. N. Simons and R. Q. Lee, "Coplanar waveguide aperture coupled patch antennas with ground plane/substrate of finite extent," *Electronics Letters*, vol. 28, pp. 75-76, 1992.
- [36] R. Q. Lee and R. N. Simons, "Coplanar-waveguide aperture-coupled microstrip patch antenna," *Microwave and Guided Wave Letters, IEEE*, vol. 2, pp. 138-139, 1992.
- [37] D. R. Jackson, "Microstrip Antennas," in *Antenna Engineering Handbook*, J. L. Volakis, Ed., 4 ed: McGraw Hill Professional, 1993.
- [38] D. R. Jackson and N. G. Alexopoulos, "Simple approximate formulas for input resistance, bandwidth, and efficiency of a resonant rectangular patch," *Antennas and Propagation, IEEE Transactions on*, vol. 39, pp. 407-410, 1991.

- [39] E. O. Hammerstad, "Equations for Microstrip Circuit Design," in *Microwave Conference, 1975. 5th European*, 1975, pp. 268-272.
- [40] A. Ghannam, C. Viallon, D. Bourrier, and T. Parra, "Dielectric microwave characterization of the SU-8 thick resin used in an above IC process," in *Microwave Conference, 2009. EuMC 2009. European*, 2009, pp. 1041-1044.
- [41] M. I. Ali, K. Ehata, and S. Ohshima, "Single-feed superconducting circularly polarized microstrip array antenna for direct-to-home receiving system," *Superconductor Science and Technology*, vol. 13, pp. 1095-1100, 2000.
- [42] C. Hsi-Tseng, K. Li-Ruei, and H. Chieh-Sheng, "Subsystem embedded microstrip antennas and its performance evaluation," in *IEEE Digest, Antennas and Propagation Society International Symposium*, 2007, pp. 936-939.
- [43] I. J. Bahl, S. S. Stuchly, and M. A. Stuchly, "A Microstrip Antenna for Medical Applications," in *Microwave Symposium Digest, 1980 MTT-S International*, 1980, pp. 358-360.
- [44] R. A. Yogi, S. A. Gangal, R. C. Aiyer, and R. N. Karekar, "Microwave ring resonator as a novel bio-material moisture sensor," *Sensors and Actuators B: Chemical*, vol. 50, pp. 38-44, 1998.
- [45] V. F. Fusco and J. A. C. Stewart, "An integrated X-band microstrip movement sensor and its application in a microprocessor-based alarm system," *Journal of Physics E: Scientific Instruments*, vol. 17, pp. 359-362, 1984.
- [46] K. Hamaguchi, Y. Shoji, H. Ogawa, H. Sato, K. Tokuda, Y. Hirachi, T. Iwasaki, A. Akeyama, K. Ueki, and T. Kizawa, "A Wireless Video Home-link Using 60GHz Band: Concept and Performance of the Developed System," in *European Microwave Conference, 2000. 30th*, 2000, pp. 1-4.
- [47] C. Karnfelt, P. Hallbjorner, H. Zirath, and A. Alping, "High gain active microstrip antenna for 60-GHz WLAN/WPAN applications," *Microwave Theory and Techniques, IEEE Transactions on*, vol. 54, pp. 2593-2603, 2006.
- [48] G. D. Lange, B. R. Jacobson, and H. Qing, "Micromachined millimeter-wave SIS-mixers," *Applied Superconductivity, IEEE Transactions on*, vol. 5, pp. 1087-1090, 1995.
- [49] J. Navarro, J. McSpadden, and C. Kai, "Experimental study of inverted microstrip for integrated antenna applications," in *IEEE Digest, Antennas and Propagation Society International Symposium*, 1994, pp. 920-923, vol.2.
- [50] G. Kristensson, P. Waller, and A. Derneryd, "Radiation efficiency and surface waves for patch antennas on inhomogeneous substrates," *IEE Proceedings on Microwaves, Antennas and Propagation*, vol. 150, pp. 477-483, 2003.
- [51] S. M. Duffy and M. A. Gouker, "Experimental comparison of the radiation efficiency for conventional and cavity backed microstrip antennas," in *IEEE Digest, Antennas and Propagation Society International Symposium*, 1996, 1996, pp. 196-199 vol.1.
- [52] A. S. Elmezughi, W. S. T. Rowe, and R. B. Waterhouse, "Cavity backed hi-lo stacked patch antennas," in *Antennas and Propagation Society International Symposium, 2008. AP-S 2008. IEEE*, 2008, pp. 1-4.
- [53] D. Pozar, "Considerations for millimeter wave printed antennas," *Antennas and Propagation, IEEE Transactions on*, vol. 31, pp. 740-747, 1983.
- [54] J. R. Aguilar, M. Beadle, P. T. Thompson, and M. W. Shelley, "The microwave and RF characteristics of FR4 substrates," in *Low Cost Antenna Technology (Ref. No. 1998/206), IEE Colloquium on*, 1998, pp. 2/1-2/6.

- [55] I. Wolff, "Design and Technology of Microwave and Millimeterwave LTCC Circuits and Systems," in *Signals, Systems and Electronics, 2007. ISSSE '07. International Symposium on*, 2007, pp. 505-512.
- [56] W. Sang-Hyuk, S. Yong-Bin, S. In-Sang, C. Sung-Hoon, I. S. Koh, L. Yong-Shik, and Y. Jong-Gwan, "Package-level integrated antennas based on LTCC technology," *IEEE Trans. Antennas Propag.*, vol. 54, pp. 2190-2197, 2006.
- [57] S. Koulouridis, G. Kiziltas, Z. Yijun, D. J. Hansford, and J. L. Volakis, "Polymer - Ceramic Composites for Microwave Applications: Fabrication and Performance Assessment," *Microwave Theory and Techniques, IEEE Transactions on*, vol. 54, pp. 4202-4208, 2006.
- [58] J. A. Rogers, Z. Bao, K. Baldwin, A. Dodabalapur, B. Crone, V. R. Raju, V. Kuck, H. Katz, K. Amundson, J. Ewing, and P. Drzaic, "Paper-like electronic displays: Large area, rubber stamped plastic sheets of electronics and electrophoretic inks" *Proc. Nat. Acad. Sci.*, vol. 98, pp. 4835-4840, 2001.
- [59] D.-H. Hwang, S. T. Kim, X.-C. Li, B. S. Chuah, J. C. DeMello, R. H. Friend, S. C. Moratti, and A. B. Holmes, "New luminescent polymers for LEDs and LECs," *Proc. Macromolecular Symp.*, vol. 125, pp. 111-120, 1998.
- [60] S. A. Bokhari, J. R. Mosig, and F. E. Gardiol, "Radiation pattern computation of microstrip antennas on finite size ground planes," *Microwaves, Antennas and Propagation, IEE Proceedings H*, vol. 139, pp. 278-286, 1992.
- [61] Y. Yashchyshyn and J. W. Modelski, "Rigorous analysis and investigations of the scan antennas on a ferroelectric substrate," *Microwave Theory and Techniques, IEEE Transactions on*, vol. 53, pp. 427-438, 2005.
- [62] B. Hunt and L. Devlin, "LTCC for RF modules," in *IEE Seminar Proc. Packag. Intercon. Microw. mm-Wave Freq.*, 2000, pp. 5/1-5/5.
- [63] R. Popielarz, C. K. Chiang, R. Nozaki, and J. Obrzut, "Dielectric properties of polymer/ferroelectric ceramic composites from 100 Hz to 10 GHz," *Macromolecules*, vol. 34, pp. 5910-5915, 2001.
- [64] P. Kyung-Wook, C. Sungdong, and H. Jni-Gul, "Novel epoxy/BaTiO₃ composite embedded capacitor films embedded in organic substrates," in *Proceedings of International IEEE Conference on the Asian Green Electronics*, 2004, pp. 68-73.
- [65] H. Windlass, P. M. Raj, D. Balaraman, S. K. Bhattacharya, and R. R. Tummala, "Colloidal processing of polymer ceramic nanocomposite integral capacitors," *Electronics Packaging Manufacturing, IEEE Transactions on*, vol. 26, pp. 100-105, 2003.
- [66] G. Kiziltas, D. Psychoudakis, J. L. Volakis, and N. Kikuchi, "Topology design optimization of dielectric substrates for bandwidth improvement of a patch antenna," *Antennas and Propagation, IEEE Transactions on*, vol. 51, pp. 2732-2743, 2003.
- [67] E. Apaydin, D. Hansford, S. Koulouridis, and J. L. Volakis, "Integrated RF circuits design and packaging in high contrast ceramic-polymer composites," in *Antennas and Propagation Society International Symposium, 2007 IEEE*, 2007, pp. 1733-1736.
- [68] N. Kingsley, G. E. Ponchak, and J. Papapolymerou, "Reconfigurable RF MEMS Phased Array Antenna Integrated Within a Liquid Crystal Polymer (LCP) System-on-Package," *Antennas and Propagation, IEEE Transactions on*, vol. 56, pp. 108-118, 2008.

- [69] C. Lugo, Jr. and J. Papapolymerou, "Electronic switchable bandpass filter using PIN diodes for wireless low cost system-on-a-package applications," *IEEE Proceedings - Microwaves, Antennas and Propagation*, vol. 151, pp. 497-502, 2004.
- [70] K. I. Shinotani, P. M. Raj, M. Seo, S. Bansal, H. Sakurai, S. K. Bhattacharya, and R. Tummala, "Evaluation of alternative materials for system-on-package (SOP) substrates," *Components and Packaging Technologies, IEEE Transactions on*, vol. 27, pp. 694-701, 2004.
- [71] D. C. Thompson, O. Tantot, H. Jallageas, G. E. Ponchak, M. M. Tentzeris, and J. Papapolymerou, "Characterization of liquid crystal polymer (LCP) material and transmission lines on LCP substrates from 30 to 110 GHz," *Microwave Theory and Techniques, IEEE Transactions on*, vol. 52, pp. 1343-1352, 2004.
- [72] S. K. Koul, "Design and development of passive and active RF Components using MEMS technology," in *International Workshop on Physics of Semiconductor Devices*, 2007, pp. 670-675.
- [73] W. H. Chow, A. Champion, and D. P. Steenson, "A precision micromachining technique for the fabrication of hybrid millimeter wave circuits and sub-assemblies," in *Microwave Symposium Digest, 2004 IEEE MTT-S International*, 2004, pp. 345-348 Vol.1.
- [74] E. D. Marsh, J. R. Reid, and V. S. Vasilyev, "Gold-Plated Micromachined Millimeter-Wave Resonators Based on Rectangular Coaxial Transmission Lines," *Microwave Theory and Techniques, IEEE Transactions on*, vol. 55, pp. 78-84, 2007.
- [75] J. R. Reid and R. T. Webster, "A 55 GHz Bandpass Filter Realized With Integrated TEM Transmission Lines," in *Microwave Symposium Digest, 2006. IEEE MTT-S International*, 2006, pp. 132-135.
- [76] F. Hou, J. Zhu, Y.-W. Yu, and J. Wu, "Millimeter-wave design of aperture-coupled micromachined patch antennas," in *Microwave and Millimeter Wave Technology, 2008. ICMWT 2008. International Conference on*, 2008, pp. 1401-1404.
- [77] E. Ojefors, H. Kratz, K. Grenier, R. Plana, and A. Rydberg, "Micromachined Loop Antennas on Low Resistivity Silicon Substrates," *Antennas and Propagation, IEEE Transactions on*, vol. 54, pp. 3593-3601, 2006.
- [78] H. Kratz and L. Stenmark, "Micromachined S-band patch antenna with reduced dielectric constant," in *Solid-State Sensors, Actuators and Microsystems, 2005. Digest of Technical Papers. TRANSDUCERS '05. The 13th International Conference on*, 2005, pp. 1088-1091 Vol. 1.
- [79] M. Abdel-Aziz, H. Ghali, H. Ragaie, H. Haddara, E. Larique, B. Guillon, and P. Pons, "Design, implementation and measurement of 26.6 GHz patch antenna using MEMS technology," in *Abdel-Aziz*, 2003, pp. 399-402, vol.1.
- [80] G. P. Gauthier, J. P. Raskin, L. P. B. Katehi, and G. M. Rebeiz, "A 94-GHz aperture-coupled micromachined microstrip antenna," *IEEE Trans. Antennas Propagat.*, vol. 47, pp. 1761-1766, 1999.
- [81] T. Ryo-ji and F. Kuroki, "High Permittivity Tape Transmission Line Embedded in Low Dielectric Support at Millimeter-Wave Frequencies," in *Microwave Conference, 2007. KJMW 2007. Korea-Japan*, 2007, pp. 189-192.
- [82] K. Jeong-Geun, L. Hyung Suk, L. Ho-Seon, Y. Jun-Bo, and S. Hong, "60-GHz CPW-fed post-supported patch antenna using micromachining technology," *Microwave and Wireless Components Letters, IEEE*, vol. 15, pp. 635-637, 2005.
- [83] P. Bo, Y. Yoon, J. Papapolymerou, M. M. Tentzeris, and M. G. Allen, "Design and fabrication of substrate-independent integrated antennas utilizing surface

- micromachining technology," in *Microwave Conference Proceedings, 2005. APMC 2005. Asia-Pacific Conference Proceedings*, 2005, p. 4 pp.
- [84] B. Pan, Y. K. Yoon, G. E. Ponchak, M. G. Allen, J. Papapolymerou, and M. M. Tentzeris, "Analysis and Characterization of a High-Performance Ka-Band Surface Micromachined Elevated Patch Antenna," *Antennas and Wireless Propagation Letters, IEEE*, vol. 5, pp. 511-514, 2006.
 - [85] P. Bo, Y. Yoon, J. Papapolymerou, M. M. Tentzeris, and M. G. Allen, "A high performance surface-micromachined elevated patch antenna," in *IEEE Digest, Antennas and Propagation Society International Symposium*, 2005, pp. 397-400, vol. 1B.
 - [86] P. Bo, Y. Yoon, P. Kirby, J. Papapolymerou, M. M. Tentzeris, and M. Allen, "A W-band surface micromachined monopole for low-cost wireless communication systems," in *Microwave Symposium Digest, 2004 IEEE MTT-S International*, 2004, pp. 1935-1938 Vol.3.
 - [87] P. Bo, L. Yuan, G. E. Ponchak, J. Papapolymerou, and M. M. Tentzeris, "A 60-GHz CPW-Fed High-Gain and Broadband Integrated Horn Antenna," *Antennas and Propagation, IEEE Transactions on*, vol. 57, pp. 1050-1056, 2009.
 - [88] N. A. Murad, M. J. Lancaster, P. Gardner, M. L. Ke, and Y. Wang, "Micromachined H-plane horn antenna manufactured using thick SU-8 photoresist," *Electronics Letters*, vol. 46, pp. 743-745.
 - [89] M. V. Lukic and D. S. Filipovic, "Integrated cavity-backed ka-band phased array antenna," in *IEEE Digest, Antennas and Propagation Society International Symposium*, 2007, pp. 133-136.
 - [90] M. Lukic, K. Kim, Y. Lee, Y. Saito, and D. S. Filipovic, "Multi-physics design and performance of a surface- micromachined Ka-band cavity backed patch antenna," in *ISBMO/IEEE MTT-S International Conference Microwave and Optoelectronics*, 2007, pp. 321-324.
 - [91] Y. H. Cho, K. Sung-Tek, C. Wonkyu, H. Man-Lyun, C. Pyo, and K. Young-Se, "A frequency agile floating-patch MEMS antenna for 42 GHz applications," in *IEEE Digest, Antennas and Propagation Society International Symposium*, 2005, pp. 512-515, Vol. 1A.
 - [92] J. Wang, Y. Cai, T. Ativanichayaphong, M. Chiao, and J. C. Chiao, "Fabrication techniques and RF performances of transmission lines on polymer substrates," in *Microelectronics: Design, Technology, and Packaging II*, Brisbane, Australia, 2005, pp. 60351M-9.
 - [93] L. L. W. Leung, K. J. Chen, X. Huo, and P. C. H. Chan, "On-Chip Microwave Filters on Standard Silicon Substrate Incorporating a Low-k BCB Dielectric Layer," in *European Microwave Conference, 2002. 32nd*, 2002, pp. 1-4.
 - [94] K. F. Tong, K. Li, and T. Matsui, "Performance of Millimeter-wave Coplanar Patch Antennas on Low-k Materials," *PIERS (2005)*, vol. 1, pp. 46-47, 2005.
 - [95] G. P. Gauthier, A. Courtay, and G. M. Rebeiz, "Microstrip antennas on synthesized low dielectric-constant substrates," *Antennas and Propagation, IEEE Transactions on*, vol. 45, pp. 1310-1314, 1997.
 - [96] P. M. Mendes, A. Polyakov, M. Bartek, J. N. Burghartz, and J. H. Correia, "Integrated chip-size antennas for wireless microsystems: Fabrication and design considerations," *Sensors and Actuators A: Physical*, vol. 125, pp. 217-222, 2006.
 - [97] C. U. Huang, I. Y. Chen, H. J. H. Chen, C. F. Jou, and S. R. S. Huang, "Compact 3D-MEMS-meander monopole antenna," *Electronics Letters*, vol. 41, pp. 1149-1151, 2005.

- [98] T. Baras and A. F. Jacob, "Manufacturing Reliability of LTCC Millimeter-Wave Passive Components," *Microwave Theory and Techniques, IEEE Transactions on*, vol. 56, pp. 2574-2581, 2008.
- [99] S. H. Wi, J. S. Kim, N. K. Kang, J. C. Kim, H. G. Yang, Y. S. Kim, and J. G. Yook, "Package-Level Integrated LTCC Antenna for RF Package Application," *IEEE Trans. Adv. Packag.*, vol. 30, pp. 132-141, 2007.
- [100] W. Chia-Chun, C. Chun-Fu, and C. Shyh-Jong, "Development of a Compact Low-Temperature Co-Fired Ceramic Antenna Front-End Module," *Microwave Theory and Techniques, IEEE Transactions on*, vol. 56, pp. 2483-2492, 2008.
- [101] Y. P. Zhang, J. J. Wang, Q. Li, and X. J. Li, "Antenna-in-Package and Transmit - Receive Switch for Single-Chip Radio Transceivers of Differential Architecture," *Circuits and Systems I: Regular Papers, IEEE Transactions on*, vol. 55, pp. 3564-3570, 2008.
- [102] K. Schuler, Y. Venot, and W. Wiesback, "Innovative material modulation for multilayer LTCC antenna design at 76.5 GHz in radar and communication applications," in *Microwave Conference, 2003. 33rd European*, 2003, pp. 707-710 vol.2.
- [103] A. Shamim, M. Arsalan, L. Roy, M. Shams, and G. Tarr, "Wireless Dosimeter: System-on-Chip Versus System-in-Package for Biomedical and Space Applications," *Circuits and Systems II: Express Briefs, IEEE Transactions on*, vol. 55, pp. 643-647, 2008.
- [104] D. M. Pozar and D. H. Schaubert, "A review of CAD for microstrip antennas and arrays," in *Microstrip antennas*, ed: IEEE Press, 1995.
- [105] J. F. Lee, D. K. Sun, and Z. J. Cendes, "Full-wave analysis of dielectric waveguides using tangential vector finite elements," *Microwave Theory and Techniques, IEEE Transactions on*, vol. 39, pp. 1262-1271, 1991.
- [106] M. El Yazidi, M. Himdi, and J. P. Daniel, "Analysis of aperture-coupled circular microstrip antenna," *Electronics Letters*, vol. 29, pp. 1021-1022, 1993.
- [107] M. Himdi, J. P. Daniel, and C. Terret, "Analysis of aperture-coupled microstrip antenna using cavity method," *Electronics Letters*, vol. 25, pp. 391-392, 1989.
- [108] M. Himdi, J. P. Daniel, and C. Terret, "Transmission line analysis of aperture-coupled microstrip antenna," *Electronics Letters*, vol. 25, pp. 1229-1230, 1989.
- [109] M. Himdi, O. Lafond, S. Laignier, and J. P. Daniel, "Extension of cavity method to analyse aperture coupled microstrip patch antenna with thick ground plane," *Electronics Letters*, vol. 34, pp. 1534-1536, 1998.
- [110] K. Jeong Phill and P. Wee Sang, "Analysis and network modeling of an aperture-coupled microstrip patch antenna," *Antennas and Propagation, IEEE Transactions on*, vol. 49, pp. 849-854, 2001.
- [111] A. K. Bhattacharyya, Y. M. M. Antar, and A. Ittipiboon, "Full wave analysis of an aperture-coupled patch antenna," *Electronics Letters*, vol. 27, pp. 153-155, 1991.
- [112] K. Jeong Phill and P. Wee Sang, "An improved network modeling of slot-coupled microstrip lines," *Microwave Theory and Techniques, IEEE Transactions on*, vol. 46, pp. 1484-1491, 1998.
- [113] K. C. Gupta, R. Garg, I. Bahl, and P. Bhartia, *Microstrip Lines and Slotlines*, 2nd ed. Norwood, MA: Artech House, 1996.
- [114] H. Pues and A. van de Capelle, "Accurate transmission-line model for the rectangular microstrip antenna," *Microwaves, Optics and Antennas, IEE Proceedings H*, vol. 131, pp. 334-340, 1984.

- [115] "Ansoft HFSS™ 3D Full-wave Electromagnetic Field Simulation " in [Online]. Available: <http://www.ansoft.com/products/hf/hfss/>.
- [116] S. Din Kow, Z. Cendes, and L. Jin-Fa, "Adaptive mesh refinement, h-version, for solving multiport microwave devices in three dimensions," *Magnetics, IEEE Transactions on*, vol. 36, pp. 1596-1599, 2000.
- [117] D.-K. Sun, J.-F. Lee, and Z. Cendes, "Construction of Nearly Orthogonal Nedelec Bases for Rapid Convergence with Multilevel Preconditioned Solvers," *SIAM Journal on Scientific Computing*, vol. 23, pp. 1053-1076, 2001.
- [118] G. S. Kirov, A. Abdel-Rahman, G. Nadim, and A. S. Omar, "Impedance matching improvement for a class of wideband antennas," *IEEE Antennas Propagat. Mag.*, vol. 46, pp. 98-101, 2004.
- [119] P. Sullivan and D. Schaubert, "Analysis of an aperture coupled microstrip antenna," *Antennas and Propagation, IEEE Transactions on* vol. 34, pp. 977-984, 1986.
- [120] W. Dupont Inc., DE, "Summary of Properties for Kapton Polyimide," [Online]. Available: http://www2.dupont.com/Kapton/en_US/index.html.
- [121] J. R. Thorpe, D. P. Steenson, and R. E. Miles, "High frequency transmission line using micromachined polymer dielectric," *Electronics Letters*, vol. 34, pp. 1237-1238, 1998.
- [122] "Data Sheet for AD 300A PTFE, (Woven Fiberglass/ Micro-Ceramic Filled Laminate for RF & Microwave Printed Circuit Boards)," Arlon Materials for Electronics (MED), a Division of Bairnco Corp., Orlando, FL, [Online]. Available: <http://www.ctsind.com.sg/arlon.html>.
- [123] S. Lucyszyn, "Comment on Terahertz time-domain spectroscopy of films fabricated from SU-8," *Electronics Letters*, vol. 37, p. 1267, 2001.
- [124] F. D. Mbairi and H. Hesselbom, "High frequency design and characterization of SU-8 based conductor backed coplanar waveguide transmission lines," in *Advanced Packaging Materials: Processes, Properties and Interfaces, 2005. Proceedings. International Symposium on*, 2005, pp. 243-248.
- [125] J.-S. Hong and M. J. Lancaster, "Aperture-Coupled Microstrip Open-Loop Resonators and Their Applications to the Design of Novel Microstrip Bandpass Filters," *Microwave Theory and Techniques, IEEE Transactions on*, vol. 47, pp. 1848-1855, 1999.
- [126] "Data sheet for TLY RF & Microwave Laminate, Woven fiberglass fabric coated with PTFE interleaved with thin sheets of pure PTFE," Taconic, specializing in coating of glass fabrics with PTFE, [Online]. Available: <http://www.taconic-add.com/pdf/tly.pdf>.
- [127] S. M. Duffy, D. M. Pozar, and F. Colomb, "An aperture coupled five element subarray," in *IEEE Digest, Antennas and Propagation Society International Symposium, 1994* 1994, pp. 1828-1831 vol.3.
- [128] K. F. Tong, T. M. Au, K. M. Luk, and K. F. Lee, "Wideband two-layer five-patch microstrip antennas," in *IEEE Digest, Antennas and Propagation Society International Symposium*, 1995, pp. 2112-2115, vol. 4.
- [129] H. Legay and L. Shafai, "New stacked microstrip antenna with large bandwidth and high gain," *Microwaves, Antennas and Propagation, IEE Proceedings -*, vol. 141, pp. 199-204, 1994.
- [130] A. D. Campo and C. Greiner, "SU-8: a photoresist for high-aspect-ratio and 3D submicron lithography," *Journal of Micromechanics and Microengineering*, vol. 17, pp. R81-R95, 2007.

- [131] H. Lorenz, M. Despont, N. Fahrni, N. LaBianca, P. Renaud, and P. Vettiger, "SU-8: a low-cost negative resist for MEMS," *Journal of Micromechanics and Microengineering*, vol. 7, pp. 121-124, 1997.
- [132] J. M. Shaw, J. D. Gelorme, N. C. LaBianca, W. E. Conley, and S. J. Holmes, "Negative photoresists for optical lithography," *IBM J. Res. Dev.*, vol. 41, 1997.
- [133] ULTRALAM® 3000, Liquid Crystalline Polymer Circuit Material, Double-Clad Laminates [Online]. Available: <http://www.rogerscorp.com/documents/730/acm/ULTRALAM-3000-LCP-laminate-data-sheet-ULTRALAM-3850.aspx>
- [134] E. C. Culbertson, "A new laminate material for high performance PCBs: liquid crystal polymer copper clad films," in *Electronic Components and Technology Conference, 1995. Proceedings., 45th*, 1995, pp. 520-523.
- [135] "AZ electronic materials technical support form," in *Microchemicals GmbH*, [Online]. Available: http://www.microchemicals.com/photoresist/photoresist_az_9260.htm.
- [136] Y. J. Chuang, F. G. Tseng, and W. K. Lin, "Reduction of diffraction effect of UV exposure on SU-8 negative thick photoresist by air gap elimination," *Microsystem Technologies*, vol. 8, pp. 308-313, 2002.
- [137] J. N. Patel, B. Kaminska, B. L. Gray, and B. D. Gates, "PDMS as a sacrificial substrate for SU-8-based biomedical and microfluidic applications," *Journal of Micromechanics and Microengineering*, vol. 18 pp. 0960-1317, 2008.
- [138] R. L. Barber, M. K. Ghantasala, R. Divan, K. D. Vora, E. C. Harvey, and D. C. Mancini, "Optimisation of SU-8 processing parameters for deep X-ray lithography," *Microsystem Technologies*, vol. 11, pp. 303-310, 2005.
- [139] C. Becnel, Y. Desta, and K. Kelly, "Ultra-deep x-ray lithography of densely packed SU-8 features: II. Process performance as a function of dose, feature height and post exposure bake temperature," *Journal of Micromechanics and Microengineering*, vol. 15, pp. 1249-1259, 2005.
- [140] S. Tuomikoski and S. Franssila, "Free-standing SU-8 microfluidic chips by adhesive bonding and release etching," *Sensors and Actuators A: Physical*, vol. 120, pp. 408-415, 2005.
- [141] R. Collier and D. Skinner, *Microwave Measurements*, 3 ed. London: Institution of engineering and technology, 2007.
- [142] D. M. Pozar, *Microwave Engineering* 3rd edition ed.: John Wiley & Sons Inc, 2004.
- [143] J. D. Kraus, *Antennas*, 2 ed.: McGraw-Hill 1988.
- [144] "IEEE standard test procedures for antennas," *ANSI/IEEE Std 149 -1979*, 1979.
- [145] G. E. Evans, *Antenna Measurement Techniques*. Norwood, MA: Artech House Publishers 1990.
- [146] C. A. Balanis, "Antenna theory analysis and design," New-york:Wiley, Ch.16, pp. 858-874, 1997, pp. 858-874.
- [147] B. Charles and et al., "Ultra-deep x-ray lithography of densely packed SU-8 features: I. An SU-8 casting procedure to obtain uniform solvent content with accompanying experimental results," *Journal of Micromechanics and Microengineering*, vol. 15, p. 1242, 2005.
- [148] A. Sayah, V. K. Parashar, and M. A. M. Gijs, "LF55GN Photosensitive Flexopolymer: A New Material for Ultrathick and High-Aspect-Ratio MEMS Fabrication," *Microelectromechanical Systems, Journal of*, vol. 16, pp. 564-570, 2007.

- [149] D. Y. Jung, W. I. Chang, and C. S. Park, "A system-on-package integration of 60 GHz ASK transmitter," in *Radio and Wireless Symposium, 2006 IEEE*, 2006, pp. 151-154.
- [150] G. V. Trentini, "Partially reflecting sheet arrays," *IRE Trans. Antennas Propag.*, vol. 4, pp. 666-671, 1956.
- [151] J. R. James, S. J. A. Kinany, P. D. Peel, and G. Andrasic, "Leaky-wave multiple dichroic beamformers," *Electronics Letters*, vol. 25, pp. 1209-1211, 1989.
- [152] A. P. Feresidis and J. C. Vardaxoglou, "High gain planar antenna using optimised partially reflective surfaces," *Microwaves, Antennas and Propagation, IEE Proceedings -*, vol. 148, pp. 345-350, 2001.
- [153] A. P. Feresidis, G. Goussetis, W. Shenhong, and J. C. Vardaxoglou, "Artificial magnetic conductor surfaces and their application to low-profile high-gain planar antennas," *Antennas and Propagation, IEEE Transactions on*, vol. 53, pp. 209-215, 2005.
- [154] J. R. Kelly, T. Kokkinos, and A. P. Feresidis, "Analysis and Design of Sub-Wavelength Resonant Cavity Type 2-D Leaky-Wave Antennas," *Antennas and Propagation, IEEE Transactions on*, vol. 56, pp. 2817-2825, 2008.
- [155] S. Wang, A. P. Feresidis, G. Goussetis, and J. C. Vardaxoglou, "Low-profile resonant cavity antenna with artificial magnetic conductor ground plane," *Electronics Letters*, vol. 40, pp. 405-406, 2004.
- [156] J. R. Kelly and A. P. Feresidis, "Array Antenna With Increased Element Separation Based on a Fabry Perot Resonant Cavity With AMC Walls," *Antennas and Propagation, IEEE Transactions on*, vol. 57, pp. 682-687, 2009.
- [157] R. Chantalat, C. Menudier, M. Thevenot, T. Monediere, E. Arnaud, and P. Dumon, "Enhanced EBG Resonator Antenna as Feed of a Reflector Antenna in the Ka Band," *Antennas and Wireless Propagation Letters, IEEE*, vol. 7, pp. 349-353, 2008.
- [158] N. Guerin, S. Enoch, G. Tayeb, P. Sabouroux, P. Vincent, and H. Legay, "A metallic Fabry-Perot directive antenna," *Antennas and Propagation, IEEE Transactions on*, vol. 54, pp. 220-224, 2006.
- [159] L. Leger, T. Monediere, and B. Jecko, "Enhancement of gain and radiation bandwidth for a planar 1-D EBG antenna," *Microwave and Wireless Components Letters, IEEE*, vol. 15, pp. 573-575, 2005.
- [160] C. The Nan and J. S. Chaou, "Tapered partially reflective surface antenna," in *IEEE Digest, Antennas and Propagation Society International Symposium*, 2007, pp. 369-372.
- [161] H. Chreim, E. Pointereau, B. Jecko, and P. Dufrane, "Omnidirectional Electromagnetic Band Gap Antenna for Base Station Applications," *Antennas and Wireless Propagation Letters, IEEE*, vol. 6, pp. 499-502, 2007.
- [162] G. K. Palikaras, A. P. Feresidis, and J. C. Vardaxoglou, "Cylindrical electromagnetic bandgap structures for directive base station antennas," *Antennas and Wireless Propagation Letters, IEEE*, vol. 3, pp. 87-89, 2004.
- [163] A. R. Weily, K. P. Esselle, T. S. Bird, and B. C. Sanders, "Linear array of woodpile EBG sectoral horn antennas," *IEEE Trans. Antennas Propag.*, vol. 54, pp. 2263-2274, 2006.
- [164] "CST MICROSTRIPES™, 3D electromagnetic simulation tool," in [Online]. Available: <http://www.cst.com/Content/Products/MST/Solver.aspx>.

- [165] R. Yang and W. Wang, "A numerical and experimental study on gap compensation and wavelength selection in UV-lithography of ultra-high aspect ratio SU-8 microstructures," *Sensors and Actuators B: Chemical*, vol. 110, pp. 279-288, 2005.
- [166] C.-M. Cheng and R.-H. Chen, "Key issues in fabricating microstructures with high aspect ratios by using deep X-ray lithography," *Microelectronic Engineering*, vol. 71, pp. 335-342, 2004.
- [167] C.-M. Cheng and R.-H. Chen, "Development behaviours and microstructure quality of downward-development in deep x-ray lithography," *Journal of Micromechanics and Microengineering*, vol. 11, pp. 692-696, 2001.
- [168] S. Natarajan and et al., "Large-area, high-aspect-ratio SU-8 molds for the fabrication of PDMS microfluidic devices," *Journal of Micromechanics and Microengineering*, vol. 18, p. 045021, 2008.
- [169] Bungard, "Etching machines, Jet 34d, Features and technical data," [Online]. Available:http://bungard.de/index.php?option=com_content&view=article&id=20&Itemid=34&lang=english.